Molecular Vapor Deposition for Next Generation Functional Coatings

Daniel Gillard

December 2024

Abstract

As humanity delves further into the 21st Century the adoption of next generation technologies in areas such as the transport, computer processing and more recently the development of AI has led to a huge increase in the demand for energy. This demand has led to the increasing use of fossil fuels for generation which produce greenhouse gases such as carbon dioxide contributing to the ever growing issue of global warming. One promising solution to effectively reduce the use of fossil fuels in these areas is the use of renewable energy; this can generate electrical energy with minimal greenhouse gas production and enable the electrification of transport.

Due to the inconsistent rate of energy generation from renewable sources (as they rely on the external environment to work) there is a demand for high capacity storage solutions to store energy when it is in excess for use when generation is limited by these external factors. These high capacity energy storage systems will also allow for a more effective way to electrify transport. These systems include high capacity batteries and fuel cells. Currently these batteries are expensive and require large amounts of comparatively rare elements to manufacture. The Molecular Vapor Deposition (MVD 300) by KLA is an effective tool to uniformly coat high aspect ratio structures with a thin film of the coating material. These coatings commonly used in next generation technologies such as hydrophobic coatings for micro mechanical electrical systems (MEMs) applications. This work has investigated MVD thin films including Zinc Oxide and Aluminium oxide for application such as electrode coatings in batteries as well as metallic Platinum (Pt) coatings for catalysis.

Thin film coatings are playing a critical role in enabling next generation technologies and are becoming increasingly common as technology progresses. Their use is essential in field like semiconductors, optics, energy storage and biomedical devices where just a few nanometres of coated material can greatly benefit the function of these devices by allowing precise control over a devices properties. This work has investigates MVD thin films including Zinc Oxide and Aluminium oxide for application such as electrode coatings in batteries as well as metallic Platinum (Pt) coatings for catalysis.

Declarations

This work has not previously been accepted in substance for any degree and is not being concurrently submitted in candidature for any degree.

[redacted]

08/10/24

signed

Date

Statement 1

This thesis is the result of my own investigations, except where otherwise stated. Other sources are acknowledged by footnotes giving explicit references. A bibliography is appended.

[redacted]

08/10/24

signed

Date

Statement 2

I hereby give consent for my thesis, if accepted, to be available for electronic sharing.

[redacted]

08/10/24

signed

Date

Statement 3

The university's ethical procedures have been followed and, where appropriate, that ethical approval has been granted.

[redacted]

08/10/24

signed

Date

Acknowledgements

I would first of all like to acknowledge Swansea university and the materials and manufacturing academy (M2A) management team for providing me with the opportunity to undertake this project and the ongoing support I have received throughout it. I would also like to acknowledge the engineering and physical sciences research council (EPSRC), UKRI and my sponsoring company KLA for providing the funding for my salary and for the equipment and chemicals that have been essential for me to undertake my research. I'd like to thank KLA company representatives including Dr Huma Ashraf and Dr Jacob Mitchell for the Monday morning 'scrums' that have allowed me to collaborate with the company. The Monday morning scrum always put me a good mindset to start the week so thank you for this.

I'd like to also mention the Postdocs and PhDs in Serena energy storage group including Iain Aldous, Haytham Hussein, Ashley willow, Arturas Adomkevicius and Sajad Kiani who have provide consistent support with practical and theoretical aspects of my project and have allowed me to further my knowledge about the world of batteries. I'd like to throw a special mention to Anton Marusenko from this group who allowed me to use and build on alot of his data for the lithium ion work in Chapters 5 and 6. Given the complications I have had to with regards to lab access, finishing would not have been possible without this data. Thanks must go to my sister Emma who helped with writing the python codes to analyse data from battery cycling, without her great suggestions data analysis would have taken alot longer to undertake. Finally i'd like to thank my friends and family including Mum, Dad, Emma, my housemate Cameron, Kallum and Tobias for all their emotional support and encouragement throughout my EngD.

Thanks must also be extended to my academic supervisors Professors Owen Guy and Serena Margadonna for guidance and support throughout the course of my EngD and without whom this would not be possible.

As well as Swansea i'd like to extend my gratitude towards Cardiff Catalysis Institute, more specifically Tom Davies, Liam Bailey and Stuart Taylor who performed SEM characterisation and the propene oxidation experiments which made up a large section in chapter 7 of my thesis.

Finally thanks have to go to Klaudia Rejnhardt and Greg Burwell who performed all of the materials development for all of these MVD thin films that I have tested. Without them non of this work would be possible.

Contents

1 Introduction **1**

1.1 MVD for battery technology 2

1.2 MVD in catalysis 2

1.3 MVD scale up potential for lithium anodes 3

Bibliography 5

2 literature review **6**

2.1 Coating processes 6

2.1.1 Chemical vapor deposition 6

2.1.2 Atomic layer deposition 7

2.1.3 Molecular Layer Deposition 8

2.1.4 combining Atomic Layer Deposition and Molecular Layer Deposition 9

2.1.5 Molecular Vapor Deposition 10

2.1.6 Current products 11

2.1.7 MVD 300 a KLA tool 12

2.2 Batteries 13

2.2.1 Electrode processes basic fundamentals 14

2.2.2 Sodium vs Lithium 15
2.2.3 Solid metal anode batteries 17
2.2.4 Zero excess anode free batteries 17
2.2.5 Current research - copper current collector 19
2.3 ALD and MLD for batteries 21
2.3.1 The Solid Electrolyte Interphase 22
2.4 Al_2O_3 coatings 23
2.4.1 Coatings function and selection Al_2O_3 24
2.5 ZnO coatings 25
2.5.1 Coatings function and selection ZnO 28
2.6 MVD platinum 29
2.7 Catalysis 30
2.7.1 Hydrogen as a fuel 31
2.7.2 Hydrogen fuel cell technology 31
2.7.3 Proton exchange membrane hydrogen fuel cell technology (PEMFC) 32
2.7.4 PEM water electrolysis cell 34
2.8 Aims, structure and Hypothesis of this thesis 35
Bibliography 37

3 Materials and methodology **50**
3.1 materials and preparation 50
3.1.1 Coin cell parts 50
3.1.2 Copper foil 50
3.1.3 Celgard separator 51
3.1.4 Sodium preparation 51

3.1.5 Lithium preparation 51

3.1.6 Making the electrolyte 51

3.1.7 Karl fisher titration 52

3.2 Battery section 53

3.2.1 coin cells assembly 53

3.2.2 Molten lithium infusion into ZnO coated carbon electrodes 55

3.3 electrochemical testing methods and equipment 55

3.3.1 Redox reactions 55

3.3.2 Chronopotentiometry 57

3.3.3 Cyclic Voltametry 59

3.3.4 Platinum catalysis experiments propene oxidation 60

3.4 Coatings materials and methods 61

3.4.1 Methodology Al_2O_3 coatings 62

3.4.2 Methodology ZnO coatings 64

3.4.3 Methodology Pt coatings 64

3.4.4 Thickness calculation 65

3.4.5 Kurt J Lesker physical vapour deposition (PVD) 75 system 65

3.5 characterisation 66

3.5.1 Spectroscopic ellipsometry 66

3.5.2 X-ray photoelectron spectroscopy (XPS) 67

3.5.3 scanning electron microscopy(SEM) 69

3.5.4 Transmission electron microscopy (TEM) 70

3.5.5 Energy dispersive X-ray (EDX) 72

3.5.6 Focused ion beam (FIB) 72

3.5.7 Optical microscopy 73
3.5.8 Insitu optical microscopy 74
Bibliography 75

4 Lithium anode free 78

4.1 introduction 78
4.2 Deposition 79
4.3 Characterisation Al_2O_3 layer on Cu 79
4.3.1 Visual confirmation 80
4.3.2 Ellipsometry 81
4.3.3 SEM characterisation 81
4.3.4 Cross sectional EDX 82
4.3.5 XPS of Al_2O_3 83
4.4 Cycling half cells 86
4.4.1 Investigating how coating thickness affects the deposition of lithium 98
4.5 Conclusion and future work 102
Bibliography 104

5 ZnO for lithiophillic carbon electrodes 106

5.1 introduction 106
5.2 Deposition 106
5.3 characterisation 107
5.3.1 SEM 107
5.3.2 XPS 108
5.4 electrochemical infusion of lithium into the carbon matrix insitu 110

5.5 Prelithiation of carbon by molten metal . . . 116
5.5.1 Li infusion into carbon current collectors . . . 116
5.5.2 Charge-discharge lithium infused electrodes ZnO - DOL electrolyte . . . 118
5.6 Conclusion and future work . . . 123
Bibliography . . . 125

6 Al_2O_3 coatings on copper for anode free sodium ion batteries 126
6.1 Introduction . . . 126
6.1.1 Nucleation overpotential . . . 127
6.1.2 Cyclic voltametry . . . 128
6.1.3 Charge-discharge . . . 129
6.1.4 A look into the reason for these charge discharge graphs . . . 138
6.1.5 XPS crossectional analysis . . . 141
6.1.6 Investigating the incomplete stripping dilemma . . . 148
6.2 Conclusion and future work . . . 151
Bibliography . . . 154

7 MVD platinum metal coatings 155
7.1 introduction . . . 155
7.2 Characterisation of nanoparticles . . . 155
7.2.1 TEM . . . 158
7.2.2 XPS . . . 164
7.3 Propene to CO_2 conversion . . . 166
7.4 Conclusion and future work . . . 169
Bibliography . . . 170

8 Summary **172**

8.1 Summary of research 172

8.2 industrial scalability 174

Bibliography 175

9 Appendix **176**

9.1 Table showing target markets for ALD tools (table 2.1) 176

9.2 2.5nm Al_2O_3 repeat Li- Cu 177

9.3 45nm Al_2O_3 coated half cell charge discharge 178

9.4 sodium electrodeposition onto copper around edges 179

9.5 Python code - for obtaining values for CE and hysteresis 180

9.6 List of Conferences 184

List of Figures

1.1 (a)-(c) CAD showing the contraption designed for housing lithium pouch cell anodes for coatings, (d) CAD drawing of the MVD chamber. 4

2.1 Schematic showing an example Atomic layer deposition process of Aluminium oxide using precursors TMA and water 8

2.2 Schematic showing a combination of Atomic layer deposition and Molecular layer deposition to create an Alucone film using Ethylene glycol and TMA 9

2.3 Schematic highlighting the fundamental components within a battery. 14

2.4 Bar chart showing Lithium- ion battery cell demand worldwide in 2022, with a forecast to 2030 (in gigawatt-hours) [52] 15

2.5 Bar chart showing the prediction of demand for raw materials required in batteries from 2020 to 2030 16

2.6 Schematic highlighting (a) the mechanism for dendrite formation on a solid metal electrode, (b) how ideal plating and stripped would take place. 23

2.7 Schematic highlighting the concept of Al_2O_3 for enhancing the wettability of solid lithium electrodes [84] 24

2.8 Schematic highlighting the affect of lithium plating of a carbon fibre with an ALD ZnO process vs an SOL ZnO coating [99] 26

2.9 Schematic highlighting one method for depositing platinum metal by ALD using $MeCpPtMe_3$ precursors and O_2 plasma 29

2.10 Schematic highlighting the reduced activation energy pathway a catalyst provides for a system with examples of each stage of the reaction. 30

2.11 Schematic showing the structure of a PEMFC hydrogen fuel cell 33

3.1 Image (left) showing Karl Fisher titration setup used to determine water content of the electrolyte. Image (right) shows electrolyte with molecular sieves in container. 53

3.2 Diagram showing schematic representation of the coin cell format used throughout this thesis vs the real components layed out ready to be assembled 54

3.3 Graph showing show CE is calculated. (a) represents the constant application of current. (b) represents how the voltage response varys with time when the current is kept constant 58

3.4 Graph showing an example (a) the nucleation overpotential and (b) the hysteresis 58

3.5 Cyclic voltamograms including (a) the linear potential sweep with time (b) the current response to the potential sweep of Na plating on the Cu electrode 59

3.6 3 electrode EL- cell used with a schematic highlighting the components of the cell 60

3.7 Image showing the MVD 300 by KLA and the exposed chamber in which the deposition takes place (right) 61

3.8 Schematic highlighting the different working parts of the MVD vapor delivery system . . . 63

3.9 Schematic highlighting the components of the Kurt J Lesker PVD system 66

3.10 Schematic highlighting the components of a spectroscopic ellipsometer (left) image of the J.A. Woolam M-2000 ellipsometer (right) 67

3.11 Schematic highlighting the components of a XPS tool 68

3.12 Schematic highlighting the XPS sample transfer holder (left), image showing the XPS sample transfer holder (right) 68

3.13 Schematic showing the components of an SEM (left), image showing the Zeiss Evo SEM used for the majority of SEM imaging in this thesis (right) 69

3.14 image showing the SEM holder used by Kammrath Weiss closed (left) and open (right) . . . 70

3.15 Schematic highlighting the structure of a TEM (left), image of TEM (right) 71

3.16 Image showing the oxford EDX used for mapping throughout this thesis (left), EDX map of an example sample (right), the different colors highlight different elements 72

3.17 image showing the FIB lamellar cross section mounted ready for SEM analysis 73

3.18 example microscope image take of group 1 metal deposition for this thesis (left), image of the Keyence microscope used for this thesis (right) 74

3.19 Schematic and image showing setup used for insitu optical microscopy experiments 74

4.1 Image showing the experimental setup for how copper substrates were coated by MVD using stainless steel baffles to stop sample movement 80

4.2 Image showing visually the change in thickness of Al_2O_3, as the thickness increases the sample appears darker 80

4.3 Images showing SEM of the various Al_2O_3 coated samples. (a) shows a top down images of the copper with the Al_2O_3 coated copper, (b) shows the FIB cross section of the Cu/Al_2O_3 substrate, (c) shows the cross section of an Si/(pvd)Cu/Al_2O_3 coated sample 82

4.4 Figure showing (a) the EDX maps of the copper substrate with Al_2O_3 layer of the surface. (b),(c) and (d) shows the copper, Oxygen and Aluminium peaks respectably 83

4.5 XPS spectra showing (a) the fitted C1s peak for a 5.0nm Al_2O_3 coated copper sample, (b) the overlayed Al2P and Cu3p peaks for bare, 2.5, 5.0 and 10.0nm Al_2O_3 coated samples, (c) the fitted O1s peak for a 5nm Al_2O_3 coated sample, (d) the fitted Al2p and Cu3p peak for a 5nm Al_2O_3 coated sample 85

4.6 (a) graph showing the nucleation over-potential for lithium plating on bare, 2.5, 5.0, 10.0, 15.0,20 and 27.5nm Al_2O_3 (b) bar chart showing the comparison of the nucleation overpotential values 87

4.7 graphs a-aiii displaying charge-discharge data for uncoated Cu half cell. (b) graph showing CE data. (c) graph showing Hysteresis 88

4.8 graphs (a-aiii) displaying charge-discharge data for uncoated 2.5nm Al_2O_3 coated half cell. . 89

4.9 graphs (a-aiii) displaying charge-discharge data for uncoated 5.0nm Al_2O_3 coated half cell. (b) graph showing CE data. (c) graph showing Hysteresis 90

4.10 graphs (a-aiii) displaying charge-discharge data for uncoated 10.0nm Al_2O_3 coated half cell. (b) graph showing CE data. (c) graph showing Hysteresis 91

4.11 graphs (a-aiii) displaying charge-discharge data for uncoated 15.0nm Al_2O_3 coated half cell. (b) graph showing CE data. (c) graph showing Hysteresis 92

4.12 graphs (a-aiii) displaying charge-discharge data for uncoated 20.0nm Al_2O_3 coated half cell. (b) graph showing CE data. (c) graph showing Hysteresis 93

4.13 graphs (a-aiii) displaying charge-discharge data for uncoated 27.5nm Al_2O_3 coated half cell. (b) graph showing CE data. (c) graph showing Hysteresis 94

4.14 Figure showing the coulombic efficiency of uncoated Cu, 5.0, 10.0, 15.0, 20.0 and 27.5nm Al_2O_3 overlayed for ease of interpretation 95

4.15 Bar chart showing the cycle life of each cell for ease of comparison 96

4.16 Figure showing the CE of uncoated Cu, 5.0, 10.0, 15.0, 20.0 and 27.5nm Al_2O_3 overlayed for ease of interpretation 97

4.17 Optical and SEM images showing the $1mAh/cm^2$ of lithium plating at a current rate of $1mA/cm^2$ for Al_2O_3 coated copper half cells. These include thicknesses of (a)- (aii) bare copper, (b)-(bii) 2.5nm, (c)-(cii) 5.0nm, (d)-(dii) 15.0nm and (e)-(eii) 27.5nm Al_2O_3. 100

4.18 optical and SEM images showing how the deposition of lithium changes from non mossy to mossy depending on the location on the electrode. (a) shows optical image of copper with markers highlighting regions where plating is non mossy (red) and mossy (green). (ai) and (aii) show SEM images of areas take on the lines highlighted in (a). (aiii) shows low magnification SEM images of areas including regions of mossy and non mossy growth. . . . 101

5.1 SEM and optical images showing the charaterisation of ZnO. (a) highlights the optical changes as the coating thickness is increased, (b) SEM showing the fibrous carbon structure of the electrodes uncoated, (c) SEM showing high magnification of an electrode fibre without any coating, (d) SEM showing the ZnO deposition onto the fibrous carbon electrode. 108

5.2 XPS showing the electrodes after being coated with MVD ZnO. (a) C1s spectra, (b) O1s spectra, (c) Zn2p spectra 109

5.3 graphs showing the GCD of the MVD ZnO coated fibrous carbon electrodes of thicknesses including (a) uncoated, (b) 2.5nm ZnO, (C) 15.0nm ZnO and (d) 27.5nm ZnO 113

5.4 Graphs showing the CE data from the MVD ZnO coated fibrous carbon electrodes of thicknesses including (a) uncoated, (b) 2.5nm ZnO, (C) 15.0nm ZnO, (d) 27.5nm ZnO and (e) showing the overlayed data 114

5.5 Bar chart showing the number of cycles to failure for the ZnO coated carbon half cells, failure was determined when the CE was less that 80% 115

5.6 Microscope images showing the lithiation of ZnO coated carbon images (a),(b) and (c) show the experimental setup. Images (d),(e) and (f) show the lithiation at 0, 5minutes and 60 minutes respectively 115

5.7 camera images highlighting the molten infusion of lithium into a fibrous carbon electrode (left) and a ZnO coated fibrous carbon electrode (right) 117

5.8 Graph showing GCD results of the molten lithium infused carbon samples in half cell format,(a) Li-Li cell, (b) LiC- Li cell, (c) 50nm ZnOLiC cell 119

5.9 Overlayed GCD results of the molten lithium infused carbon samples with some exploded sections of the graph for more detailed analysis 120

5.10 CE data from the Molten lithium GCD cycling. (a) Li-Li cell, (b) LiC-Li cell, (c) 50nm ZnOLiC cell and (d) which highlights the overlayed results 121

5.11 Hysteresis data from the Molten lithium GCD cycling. (a) Li-Li cell, (b) LiC-Li cell, (c) 50nm ZnOLiC cell, (d) overlayed hysteresis at the end of cycling and (e) which highlights the overlayed results 122

6.1 (a) figure showing the nucleation overpotential of sodium electrodeposition on uncoated, 15nm Al_2O_3 coated copper and 45nm Al_2O_3 coated copper, (b) bar chart highlighting overpotential values for each sample more clearly 128

6.2 Graph showing 3 electrode CV of sodium electrodeposition and stripping on copper 129

6.3 (a) Graphs highlighting the GCD results of sodium electrodeposition onto copper, (b) hysteresis and (c) CE 131

6.4 Photograph and SEM images of sodium electrodeposition onto an uncoated copper substrate 132

6.5 (a) Graphs highlighting the GCD results of sodium electrodeposition onto copper coated with 15nm Al_2O_3, (b) hysteresis and (c) CE 133

6.6 Photograph and SEM images of sodium electrodeposition onto a copper substrate with 15nm Al_2O_3 on the surface 134

6.7 (a) Graphs highlighting the GCD results of sodium electrodeposition onto copper coated with 45nm Al_2O_3, (b) hysteresis and (c) CE 135

6.8 Photograph and SEM images of sodium electrodeposition onto a copper substrate with 45nm Al_2O_3 on the surface 136

6.9 Figure showing (a) hysteresis of the 3 thickness overlayed (b) Coulombic efficiency of the 3 thicknesses overlayed 137

6.10 schematic showing the layout of the copper used for insitu- optical microscopy experiments . 138

6.11 microscope images highlighting the deposition of sodium onto copper at 300 second intervals starting at 300 seconds (a), 600 seconds (b), 900 seconds (c), 1200 seconds (d), 1500 seconds (e) and ending on 1800 seconds (f). 139

6.12 Image showing the exploded image of insitu optical microscopy experiment at 1800 seconds highlighting the different sites mentioned in the text 140

6.13 schematic highlight cross section of electrodeposition onto copper highlighting the different layers that are expected to be etched through 141

6.14 Microscope images with square highlighting the rough area for where the XPS etch took place. 142

6.15 XPS spectra showing the Cu2p peak (blue) and Al2P peak (red) at 3000 second intervals throughout the XPS etch 144

6.16 EDX image highlighting the elements including sodium, aluminium and copper on a 15nm Al_2O_3 coated copper sample which had sodium electro deposited onto it 145

6.17 XPS spectra highlighting the Na1s peak at 0 seconds and 24000 seconds 146

6.18 Figure showing (a) GCD response for uncoated copper with a voltage but no time cutoff, (b) zoomed in cycle highlighting oscillation and (c) CE response. 148

6.19 Figure showing (a) cell stopped on an oscillation, (b) opened and the electrode observed and (c) SEM analysis 149

6.20 Image showing sodium deposits in the separator after sodium electrodeposition had occurred 149

6.21 Schematic highlighting the idea for why the noisy response was observed on the stripping cycle of cell 150

7.1 SEM images showing Platinum growth as a function of cycle number (a) 5 cycles, (b) 10 cycles, (c) 15 cycles, (d) 25 cycles, (e) 30 cycles and (f) 35 cycles respectively on Si/SiO_2 wafer pieces 157

7.2 TEM images showing platinum nanoparticle deposition on RGO TEM grids. Images (a) and (b) show 30 cycles of deposition whilst images (c) and (d) show 35 cycles of deposition. . . 159

7.3 TEM and optical images showing platinum nanoparticle deposition to ceramic monoliths before being used for propene oxidation catalysis experiments. (a) images of the ceramic monoliths, (b), (c) and (d) TEM micrographs of the platinum nanoparticles deposited on the monoliths at different magnifications. 160

7.4 Graph showing PSD analysis of nanoparticles on RGO TEM grids (a) comparing 35 MVD cycles and 30 MVD cycles, (b) comparing probability distribution of particles 161

7.5 Graph showing PSD analysis of nanoparticles on ceramic monoliths. (a) highlights PSD, (b) highlights 162

7.6 Graphs highlighting the results of the XPS of platinum nanoparticles (a) widescans, (b) C1s, (c) O1s and (d) Pt4f 165

7.7 Graph highlighting the conversion of propene to CO_2. Sample were repeatedly tested highlighting the 3 consecutive runs. 166

7.8 Graph showing the Propene to CO_2 oxidation of platinum nanoparticles after being reduced in a furnace at 500^oC 168

9.1 repeat results - (a) Graphs highlighting the GCD results of sodium electrodeposition onto copper coated with 2.5nm Al_2O_3, (b) hysteresis and (c) CE 177

9.2 figure highlighting the 45nm Al_2O_3 cycled by GCD vs lithium counter electrode 178

9.3 Images highlighting the electrodepsoition of active mass around the edge of copper substrates 179

List of Tables

2.1 Table showing various different ALD tools from different companies and their capabilities (parameters including N/a indicate that the sources do not mention this parameter) 12

2.2 An overview of lithium ion batteries for electric vehicles [38, 39] 13

2.3 Table showing some research articles highlighting sodium anode free cells that function by electrodeposition of sodium onto copper 19

2.4 Table showing some research articles highlighting lithium anode free cells that function by electrodeposition of lithium onto copper 20

2.5 Table showing different research articles highlighting the application of zinc oxide for lithiophillic 2D carbon current collectors. 27

2.6 Different types of hydrogen fuel cell technologies and their operating parameters [116] . . . 32

7.1 Table showing how this research compares to platinum deposited by ALD for other studies . 163

9.1 Table showing application of ALD systems highlighted in table 2.1 176

Abbreviations

MVD	Molecular layer deposition
PVD	Physical vapor deposition
CVD	Chemical vapor deposition
CV	Cyclic voltametry
XPS	X-Ray photoelectron spectroscopy
SEM	Scanning electron microscopy
EDX	Energy dispersive X-ray
PEM	proton exchange membrane
TMA	Tri-methylaluminium
DEZ	Di-ethyl zinc
ALD	Atomic layer deposition
PeALD	Plasma enhanced atomic layer deposition
MLD	Molecular layer deposition
CVD	Chemical vapor deposition
CE	Coulombic efficiency
SEI	solid electrolyte interphase
PEM	Proton exchange membrane
VDM	Vapor delivery module
GPC	Growth per cycle
RGO	Reduced graphene oxide
TEM	Transmission electron microscopy
IPA	Isopropyl alcohol
DI	Deionised

GCD	Galvanostatic charge discharge
MEMS	Micro-electromechanical systems
ITO	Indium tin oxide
PSD	Particle size distribution
MOF	Metal-organic framework
SAM	Self assembling monolayer
FDTS	heptadecafluoro-1,1,2,2- tetrahydrodecyltrichlorosilane
FOTS	tridecafluoro-1,1,2,2-tetrahydrooctyltrichlorosilane
GPC	Growth per cycle

Chapter 1

Introduction

Molecular Vapor Deposition (MVD) is a versatile thin-film deposition technique capable of forming organic, inorganic, hybrid, and metallic coatings, making it suitable for a wide range of applications. While techniques such as Physical Vapor Deposition (PVD), Chemical Vapor Deposition (CVD), Atomic Layer Deposition (ALD), and Molecular Layer Deposition (MLD) are commonly used, MVD offers unique advantages—particularly in its capability to deposit ultrathin, conformal films at relatively low temperatures. Beyond these, solution-based chemical methods such as sol-gel coating, dip coating, and electroless plating have also been employed by various authors [1]. However, these techniques often suffer from limitations such as poor conformality on complex geometries, incomplete surface coverage, or limited control over film thickness and composition. Due to being the most similar to MVD, PVD, CVD and MLD will be expanded on in chapter 2.

Presently, the market boasts over 100 MVD systems with more than 50 in commercial applciations, predominantly serving a niche market in hydrophobic/hydrophilic coatings for MEMs devices. This thesis looks to explore novel applications for the KLA MVD 300 tool, aiming to assess its viability in these fields and potentially position it as a competitive option for applications in these markets. The primary sectors of interest include battery systems, with a secondary focus on nanoparticle deposition for catalysis applications.

1.1 MVD for battery technology

In 2022, the battery market had witnessed a valuation of \$85 billion, with projections indicating a substantial surge to \$400 billion by 2030, as forecasted by Fleischmann *et al* [2]. This valuation encompasses various segments such as raw material mining, refining processes, active materials production, cell manufacturing, battery pack assembly, and the growing recycling sector. The exponential growth is fueled by escalating demand, particularly evident in the lithium-ion battery sector, poised to increase from 700 GWh in 2022 to a staggering 4700 GWh by 2030, according to Fleischmann *et al* [2]. Some applications for lithium ion battery technology include the transport sector, portable electronic devices such as mobile phones, grid storage and aviation.

This surge in demand is propelled by several factors, notably the intensifying global scrutiny on fossil fuel usage due to their adverse environmental impact, underscored by the commitments outlined in the Paris Agreement of 2015 [3]. Currently, the battery landscape is witnessing a wave of innovation, with promising technologies such as anode-free battery systems and lithium-sulfur configurations emerging from research laboratories. These technologies offer advantages over more conventional counterparts, promising significant advancements in the markets, (see sections 2.2.3 and 2.2.4 for more details regarding this).

However, one persistent challenge plaguing these innovative battery designs is the stability of their electrodes, particularly the anode. MVD coatings hold the potential to address this challenge, potentially leading to breakthroughs in anode coatings and presenting a new market opportunity for KLA, whose core business is in semiconductor inspection and metrology.

This thesis concentrates on, 1) the application of Al_2O_3 coatings to stabilize electrodeposition processes in anode-free batteries and 2) ZnO coatings to enhance the lithiophilicity of 3D carbon anodes. By delving into these applications, the thesis aims to not only contribute to the advancement of battery technologies but also to explore avenues for KLA's entry into these growing market segment.

1.2 MVD in catalysis

In addition to the surging demand for batteries as a primary energy storage solution, the utilization of hydrogen as an alternative fuel holds immense promise for environmental benefits, as mentioned in section 2.7.1. Presently, Proton Exchange Membrane (PEM) technology stands out as a front runner in hydrogen fuel cell research, with a market size of $2.1 billion in 2021. This figure is projected to increase to $22.73 billion by 2028. [4].

Molecular Vapor Deposition (MVD) processes, particularly for depositing platinum metal, have undergone optimization through the PhD work of Klaudia Rejnhard [5]. Building upon this foundation, this thesis looks to further explore the use of this platinum deposition technique, with a specific focus on catalysis applications for hydrogen fuel cell technology. Preliminary research was focused on using the nanoparticles as a catalyst for propene oxidation, assessing the efficiency of the MVD platinum nanoparticles in catalytic process. Through strategic research and innovation, the long-term vision is to integrate MVD technology into the growing market of hydrogen fuel cell technology, driving sustainable progress and environmental stewardship.

1.3 MVD scale up potential for lithium anodes

The KLA MVD 300 stands out for its ability to efficiently produce coated products in batches, offering a practical advantage for industrial applications. This capability was explored in a theoretical analysis of MVD's potential in depositing Al_2O_3 for solid lithium metal anodes. The study, conducted in collaboration with OXIS Energy, highlighted the interest in MVD technology due to its batch production capability. However, it's worth noting that OXIS Energy faced financial difficulties and went into administration in May 2019. Despite this, the exploration of MVD's batch production potential remains pertinent for enhancing manufacturing efficiency in various industries.

Based on OXIS Energy's commercial demand of 100,000 anodes annually, and considering the lithium anodes' dimensions of 60mm x 100mm, a concept for a sample holder was devised to facilitate MVD coating, as illustrated in Figure 1.1. The design features a bracket (Figure 1.1a) comprising a two-part system with a recess to securely hold each electrode, accommodating 10 electrodes per bracket. A cradle (Figure 1.1c) was then developed with 20 slots for 20 brackets, enabling the coating of 200 electrodes per batch. This assembly fits into the chamber depicted in Figure 1.1d.

Assuming a coating thickness of 14nm Al_2O_3, based on preliminary research by Kozen *et al* [6], basic calculations indicate that the MVD system could theoretically process 219,000 anodes annually if operated continuously. This output exceeds the required amount by over 2 times, despite the relatively slow

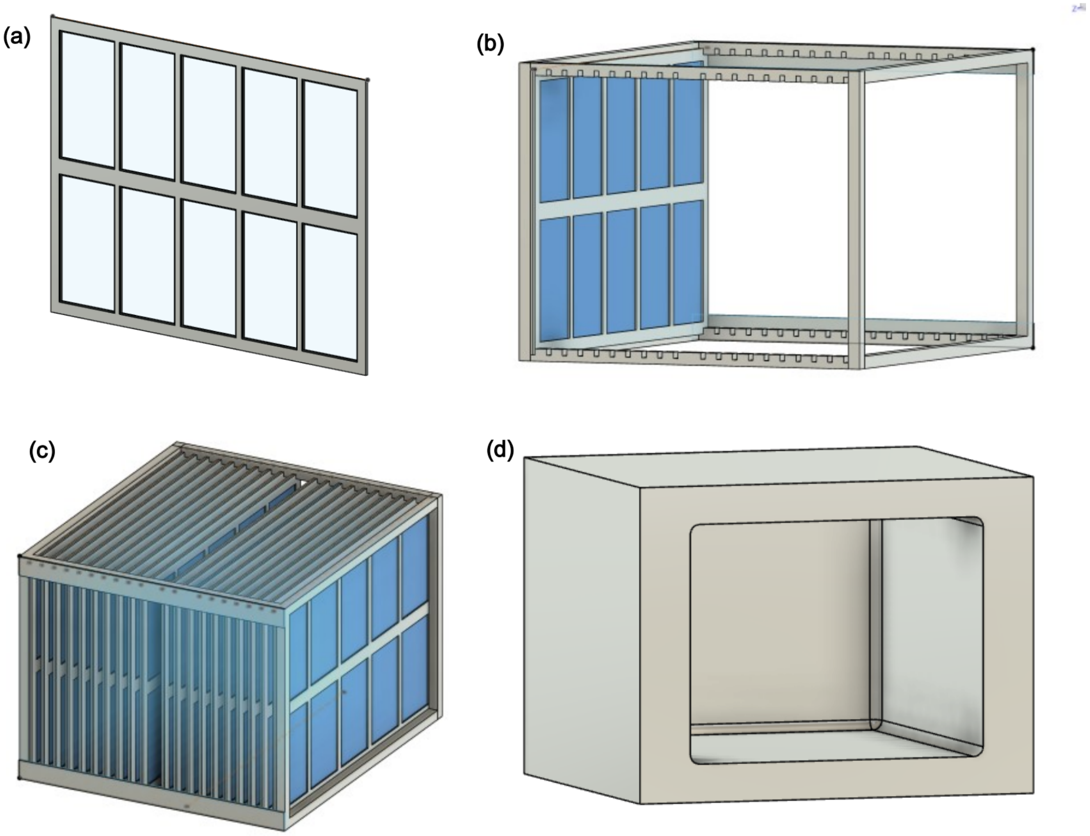

Figure 1.1: (a)-(c) CAD showing the contraption designed for housing lithium pouch cell anodes for coatings, (d) CAD drawing of the MVD chamber.

coating process of Al_2O_3. However, achieving this level of throughput would necessitate extensive process optimization to ensure precise precursor dosing, especially given the heavy loading of electrodes in this scenario. Thus, while promising, this estimation remains speculative and subject to further optimization and refinement.

Bibliography

[1] Rointan F Bunshah. *Handbook of deposition technologies for films and coatings: science, applications and technology*. William Andrew, 1994.

[2] Jakob Fleischmann, Mikael Hanicke, Evan Horetsky, Dina Ibrahim, Sören Jautelat, Martin Linder, Patrick Schaufuss, Lukas Torscht, and Alexandre van de Rijt. Battery 2030: Resilient, sustainable, and circular. *McKinsey & Company*, pages 2–18, 2023.

[3] Benjamin Jones, Viet Nguyen-Tien, and Robert JR Elliott. The electric vehicle revolution: Critical material supply chains, trade and development. *The World Economy*, 46(1):2–26, 2023.

[4] Fortune Business Insights. Market research report. *Fortune Business Insights*, pages 2021–2028, 2021.

[5] Klaudia rejnhard. *Advanced Functional Coatings for Integrative Semiconductor Materials and Devices*. PhD thesis, Swansea university, 2022.

[6] Alexander C Kozen, Chuan-Fu Lin, Alexander J Pearse, Marshall A Schroeder, Xiaogang Han, Liangbing Hu, Sang-Bok Lee, Gary W Rubloff, and Malachi Noked. Next-generation lithium metal anode engineering via atomic layer deposition. *ACS nano*, 9(6):5884–5892, 2015.

Chapter 2

literature review

2.1 Coating processes

Although many coating processes exist, this section will concentrate on MVD and its derivatives. The aim is to outline these processes and comment on the advantages and limitations that come with them. As well as this, an analysis of current products that exist in the market will be outlined and compared.

2.1.1 Chemical vapor deposition

Like ALD and MLD, Chemcial Vapor Deposition (CVD) is a method of epitaxially growing a functional coating on a surface using gas phase precursors. Although it is unclear when the process first came into being, it is likely that the first CVD processes date back to the early 19th century with John Howarth who used the process to create carbon black as a pigment. Since then the technique has developed into a widely used process capable of depositing metals and non metal compounds alike [1, 2, 3]. CVD works by purging the working chamber with precursor gases which react in the vapour phase on the surface of the heated substrate to form a solid deposit. The reaction on the surface is dependent on the kinetics of the gases and the mass transfer of reactants onto the surface of the substrate, this ultimately governs the transport process and thereforee is used to control the rate of the reaction [4].

2.1.2 Atomic layer deposition

Atomic layer deposition (ALD) is a technique developed in the 1970s by Tuomo Suntola in Finland, originally known as atomic layer epitaxy. Unlike conventional Chemical Vapor Deposition (CVD) techniques, ALD applies thin functional coatings to substrate surfaces through self-limiting chemical reactions in a layer-by-layer manner, utilizing two or more precursor gases which are diluted in a nitrogen carrier gas. There are several advantages to coating using ALD. Firstly, it offers precise control over thin film thickness, with each layer typically in the order of angstroms thick, although this can vary depending on the molecule or compound being coated. Additionally, ALD allows gas-phase reactants to penetrate into very small features such as trenches and channels, making it suitable for high aspect ratio structures. The self-limiting nature of ALD, combined with purge/pulse cycles of precursor gases, ensures non-statistical deposition. This means that all active sites on the substrate are filled during each pulse/purge cycle, resulting in a more uniform coating with fewer pinhole defects. Furthermore, the sequential separation of precursor gases in ALD eliminates the possibility of gas-phase reactions that could lead to the formation of granular precipitates, thereby enhancing the quality of the deposited films [5].

The process initially demonstrated by Tuomo Suntola was primarily aimed at growing high-quality polycrystalline Zinc sulphide (ZnS) films for electroluminescent display panels [6]. However, over time, the versatility of ALD has led to its application in a wide range of fields. Today, ALD is used for coating various films, opening up its potential for diverse applications, including aluminium oxide passivation layers for battery components [7], aluminium oxide coatings as gate dielectrics for field-effect transistors [8], ultrathin ALD TiO_2 coatings for photoanodes in dye-sensitized solar cells [9], aluminium oxide and titanium dioxide coatings for corrosion protection of stainless steel [10], and ruthenium oxide coatings for electrochemical activation in supercapacitor applications [11]. These examples represent just a fraction of the many applications where ALD is now utilized. Its versatility, precise control over film thickness, and ability to deposit uniform coatings have made ALD a valuable tool in various industries, ranging from electronics to renewable energy and beyond.

One particular material that features throughout this thesis is Al_2O_3. A commonly used method to deposit Al_2O_3 is using precursor materials Tri-methylaluminium (TMA) and water which was first demonstrated by Higashi *et al* [12]. Figure 2.1 demonstrates the reaction between TMA and water to epitaxially grow Al_2O_3. The reaction can be represented by 2 stages seen by equation 1 and 2, equation 1 represents the self terminating reaction that occurs between surface hydroxyl groups and the TMA molecule forming methane as a bi-product. equation 2 represents the self termination reaction that occurs between water and the surface species creating the first atomic layer of Al_2O_3. This reaction can be repeated until the desired film thickness has been reached. (The following schematic assumes Al_2O_3 is also the substrate) [13, 14].

$$AlOH + Al(CH_3)_3 -> Al - O - Al(CH_3)_2 + CH_4 \tag{2.1}$$

$$Al - O - Al(CH_3)_2 + 2H_2O -> Al - O - Al(OH)_2 + 2CH_4 \tag{2.2}$$

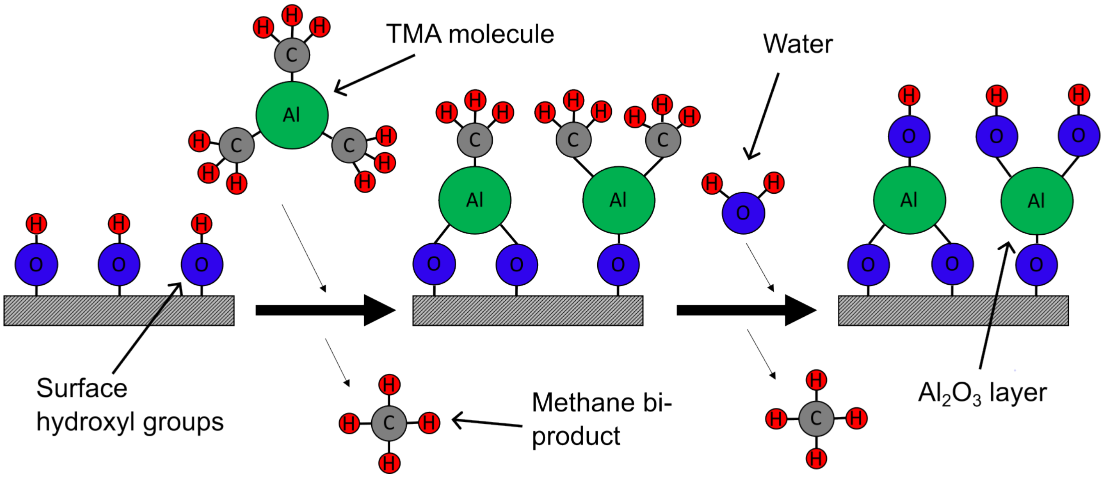

Figure 2.1: Schematic showing an example Atomic layer deposition process of Aluminium oxide using precursors TMA and water

2.1.3 Molecular Layer Deposition

Molecular Layer Deposition (MLD) is an extension of ALD, the techniques primarily describes the epitaxy of organic layers. The process works by removing the oxidising precursor from the system and replacing it with an organic linker or by adding molecular fragments to the film [15, 16]. The technique first appeared in Japan during the 1990's where several groups developed condensation polymerization reactions for producing organic polymers, one instance of this work includes reacting pyromellitic dianhydride (A) and 2,4 - diaminomitrobenzene or 4,4 - diaminodiphenyl to produce a 100 angstrom thick film that is self terminating

[17]. Since the discovery of the technique many organic compounds have been deposited by MLD, some of these include polyamide, polyimide, polyurethane and polythiourea [18, 19, 20].

2.1.4 combining Atomic Layer Deposition and Molecular Layer Deposition

In addition to purely organic or non-organic films, the processes of MLD and ALD can be combined to create hybrid organic-metallic films, such as the widely studied metalcones. Metalcones utilize a combination of organic linkers found in MLD coating processes, such as Ethylene glycol, and metal precursors like trimethyl aluminium, which react together by a ligand exchange forming Alucone, see figure 2,2 for a schematic representation on the formation of Alucone [21, 15].

A significant advantage of hybrid ALD and MLD films is the ability to tune their properties by leveraging desirable traits from either process. For instance, films can be made more flexible with reduced density and lower cost, thanks to the organic linkers present in MLD processes. This flexibility and versatility represent a key selling point for these hybrid films, offering tailored solutions that may not be achievable with purely non-organic compounds [21].

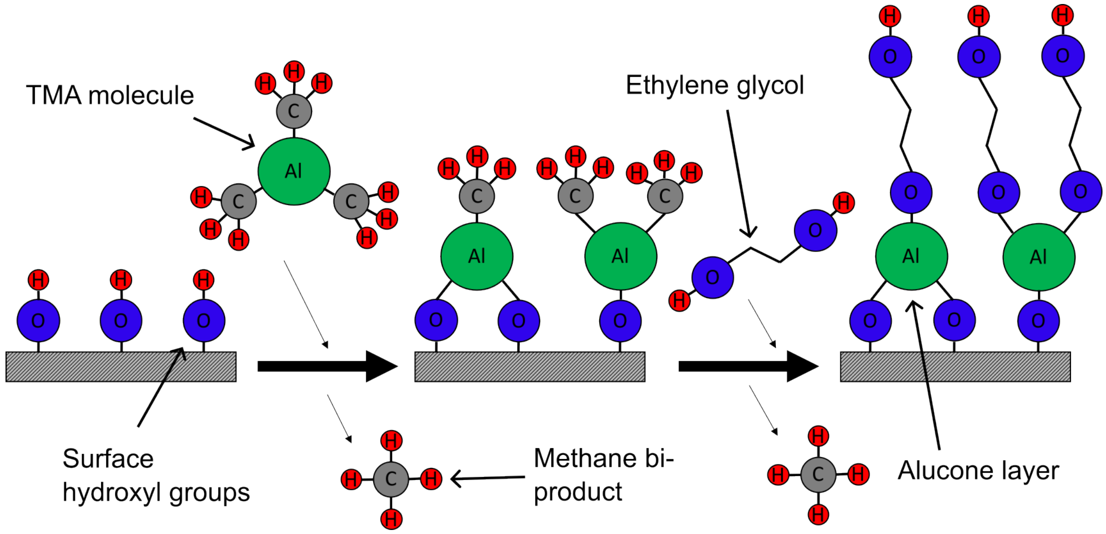

Figure 2.2: Schematic showing a combination of Atomic layer deposition and Molecular layer deposition to create an Alucone film using Ethylene glycol and TMA

2.1.5 Molecular Vapor Deposition

MVD is a deposition technique which combines the principles of CVD and ALD. The use of two or more differing precursors is similar to an ALD system however the pump purge sequencing which differs from conventional continuous flow through ALD technology lends itself more towards a CVD process [22, 5]. As well as this, MVD processes differ as they don't require the use of a nitrogen carrier gas for delivery of precursor to the sample, as suggested by Burwell *et al* [22] this could reduce the mean free path of a precursor molecule to active site on sample allowing for high quality films to be deposited at lower temperature. Generally typical ALD Al_2O_3 processes require in excess of 250^oC to deposit good quality films [23, 24].

There is a growing pool of research around MVD coatings which highlight the versatility of the deposition process. Burwell *et al* successfully deposited stoichiometric Al_2O_3 as low as 100^oC using a thermal MVD process which opens up the potential to coat high quality materials onto substrates that are temperature sensitive. Ben-sasson *et al* used an MVD process to coat dielectric layers for vertical organic field effect transistors, the group reported uniform films characterized by high dielectric properties with thicknesses ranging between 1.2 and 24nm [25]. Kobrin *et al* used MVD to deposit self assembling monolayer (SAM) films of heptadecafluoro-1,1,2,2- tetrahydrodecyltrichlorosilane (FDTS) and tridecafluoro-1,1,2,2-tetrahydrooctyltrichlorosilane (FOTS). By depositing a seed layer, the group was able to create a more robust film with better immersion and thermal stability then more typical liquid based synthesis methods[26].

2.1.6 Current products

This section provides an overview of various ALD, MLD, CVD, and MVD hybrid tools currently available in the market. Table 2.1 outlines the capabilities of these tools, detailing key features such as the number of precursor delivery lines, which enable the deposition of material stacks, and the range of operating temperatures. Additionally, the table highlights the types of deposition processes supported, the chamber sizes (which influence the industrial feasibility of each tool), the ability to utilize plasma or ozone, and the uniformity of coatings—a critical indicator of process quality. Selecting the appropriate precursor enables the deposition of materials using many of the deposited techniques listed.

Product	**Company**	**delivery lines**	**deposition potential**	**plasma/ ozone potential**	**temperature potential**	**throughput**	**uniformity**	**target markets**	**Ref**
NLD-4000	Nanomaster	up to 7X50cc ampules	ALD	Plasma	up to 400C substrate heater	1x 8inch Si wafer compatible	less then 1 Angstrom	A (appendix)	[27]
Flex-Al	Oxford instruments	up to 10 ampules (100-500 grams)	ALD (1 x hybrid mentioned)	Plasma(300 or 600 watts)	30C- 550C temperature range	cassete of 8 inch Si wafers	less then +- 2% uniformity	B (appendix)	[28]
MVD 300	SPTS (a KLA company)	4x25cc ampules	MVD, ALD, MLD and CVD (Aspect ratio 1:3500)	Plasma	35C - 150C (substrate heater compatible)	cassete of 12 inch Si wafers (up to 25)	N/a	C (appendix)	[29]
Genesis ALD system	E+R group	N/a	ALD	N/a	up to 250C	Roll to Roll 10 meters per minute (max).	N/a	D (appendix)	[30]
Gemstar 8	Arradiance	6x150cc ampules	ALD	Ozone	25C-300C (400C heated chuck)	Cassete of 8 inch Si wafers (up to 9)	less then +- 2% (bath wafer) 1% (simgle wafer)	E (appendix)	[31]
ALD 150LX9-	Kurt J lesker	6xgas lines	ALD (Aspect ratio 1:2500)	Plasma	up to 250C (500C heated chuck)	single 6 inch wafer	less than +- 1% (thermal & plasma)	F (appendix)	[32]
Pheonix system	Veeco	4 x gas,liquid or solid precursor lines	ALD	no	up to 285C	Cassete of 12 inch wafers (up to 40)	less than +- 2% Al_2O_3	G (appendix)	[33]
Savannah	Veeco	up to 6 x 50ml ampules	ALD (Aspect ratio 1:2000)	Ozone potential	up to 400C (S100)	1 x 12 inch wafer compatible	less than 1% Al_2O_3	H (appendix)	[34]
P-300B	Picosun	4 x seperate inlets	ALD	Ozone	50-500C	casset of 8 inch wafers (up to 25)	less than 1% A	I (appendix)	[35]
SVT assosciates	Northstar ALD-P-200B	8 x precursor lines	ALD	energy enhanced	up to 500C	1 x 12 inch wafer	less than +- 1% (Al_2O_3)	J (appendix)	[36]

Table 2.1: Table showing various different ALD tools from different companies and their capabilities (parameters including N/a indicate that the sources do not mention this parameter)

2.1.7 MVD 300 a KLA tool

After conducting some analysis on the following products that are based off of ALD or MLD derivatives, the MVD 300 offers some bespoke advantages over it competitors. Firstly, the quoted aspect ratio of the MVD is much higher at 1:3500 which makes it the best option for coating non uniform features present on substrates, e.g structured or porous objects. Furthermore, the lack of a carrier gas means that high quality coatings such as Al_2O_3 can be produced at low temperatures making the process very good for coating temperature sensitive substrates which is highlighted by Burwell *et al* [22].

2.2 Batteries

”A battery is one or more electrically connected electrochemical cells having terminals/contacts to supply electrical energy”. Batteries convert electrical energy by reduction and oxidation of chemical species at the anode and cathode within a cell. Many different types of batteries exist but can be categorised under two distinct titles which are primary and secondary cells. Primary cells are single use batteries that cannot be recharged whilst secondary cells can be recharged [37]. Each individual battery technology contains different materials and has individual strengths and weaknesses. However the fundamental inner workings are the same. See table 2.2 for examples of different battery technology.

Battery type	Cycle life	Nominal voltage (V)	Self discharge	Energy density Wh/kg	Overcharge tolerance
Lead acid	200-300	2	Low	30-50	High
Nickle Cadmium	1500	1.25	Moderate	45-80	Moderate
Nickle metal hydride	300-500	1.25	High	60-120	Low
Lithium ion	900-2000	3.6	Very low	250-300	Very low

Table 2.2: An overview of lithium ion batteries for electric vehicles [38, 39]

Figure 2.3 shows the typical format of a common secondary rechargeable battery cell. The anode is the negative electrode of the cell. Whilst the anode material depends heavily on the on the battery type, for commonly used lithium ion batteries this is normally a carbon based material such as graphite, for sodium ion batteries this tends to be hard carbon, due to sodium’s inability to form graphite intercalation compounds under moderate conditions [40, 41, 42]. The cathode is the positive electrode of the battery and usually consists of a layered ionic solid with a crystal structure capable of containing active ions by intercalation [43]. The electrolyte bridges the electrodes and conducts active ions between them. It must be carefully selected to be compatible with system. For lithium ion batteries typically organic solvents are used as they allow for a wide voltage window and are relatively stable in the presence of lithium when compared to aqueous solvents found in lead acid batteries as an example. The separator acts as a barrier between the anode and cathode which is an electrical insulator, this prevents the electrodes from touching preventing unwanted short circuits from occurring [44].

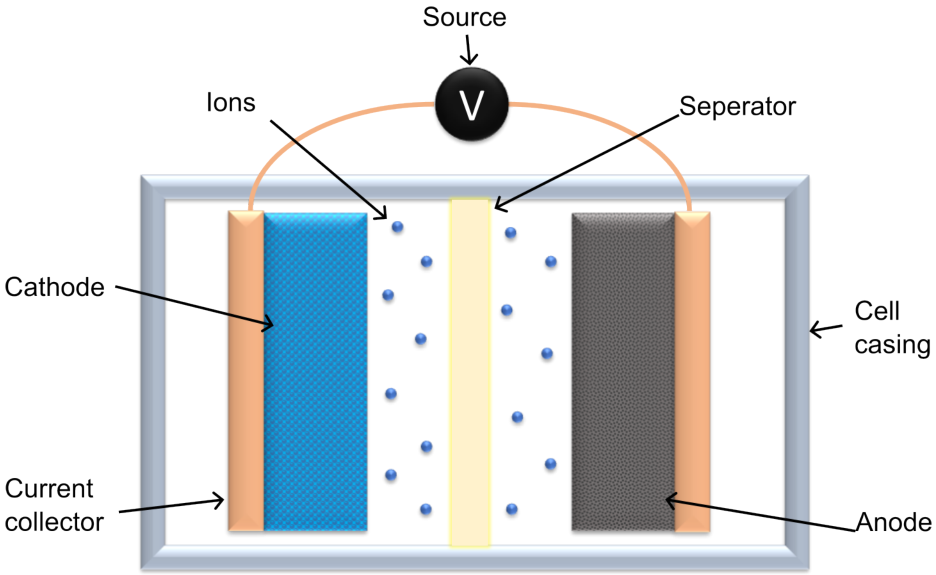

Figure 2.3: Schematic highlighting the fundamental components within a battery.

2.2.1 Electrode processes basic fundamentals

Electrode processes work by in situ chemical reactions which usually involve the transfer of charge at the interphase between the solid and solution phase of a system. A typical reaction involves a solid metal electrode being oxidised thus losing an electron and dissolving into the adjacent solution as an ion. Electrode processes can be seen in all aspects of everyday life from extensive use in battery technology through to the inconvenient rusting of metal appliances and architecture [45, 46, 47]. Although fundamentally for the given references the electrode processes occur in the same way, for the purpose of this thesis electrode processes for battery technology will be the focus.

2.2.2 Sodium vs Lithium

One ongoing argument is the feasibility on continuing to use lithium as the active mass inside of batteries in the markets for battery technology, some of these markets include electric vehicles, portable electronic devices and stationary storage [48]. Due to the ever increasing adverse climate affects caused by the combustion of fossil fuels, the world is looking for greener alternatives for achieving net zero emissions to allow for a more sustainable future in which the electrification of transport and storage for renewable energy plays an important role [49, 50]. As expected this has been met with a massive up scaling of the manufacturing of lithium ion batteries which is predicted to increase exponentially up to 4700 Gwh in 2030 from a value of 700 Gwh in 2022. This can be seen more clearly from the graph in figure 2.4 [49, 51, 52].

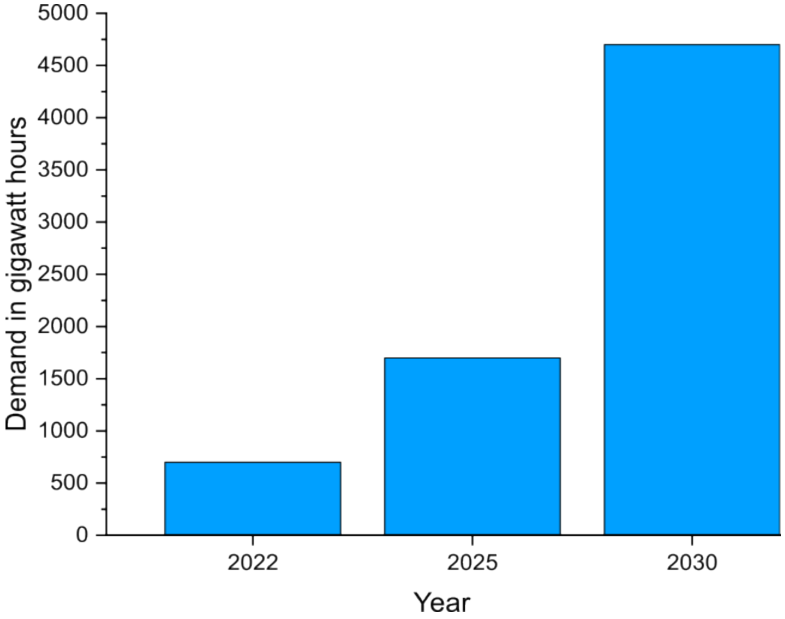

Figure 2.4: Bar chart showing Lithium- ion battery cell demand worldwide in 2022, with a forecast to 2030 (in gigawatt-hours) [52]

With this massive increase in battery production there will also be a large increase of the demand for raw materials to manufacture them. These include copper, Lithium, Aluminium, Graphite, Nickel, Iron, Phosphorous, Manganese and Cobalt. The expected increase in demand can be seen in figure 2.5. A question lies as to is there enough raw materials to fuel the ever increasing demand or are alternatives to Li-ion batteries required. Focusing on the batteries active mass which is Lithium, whilst reserves of Lithium are

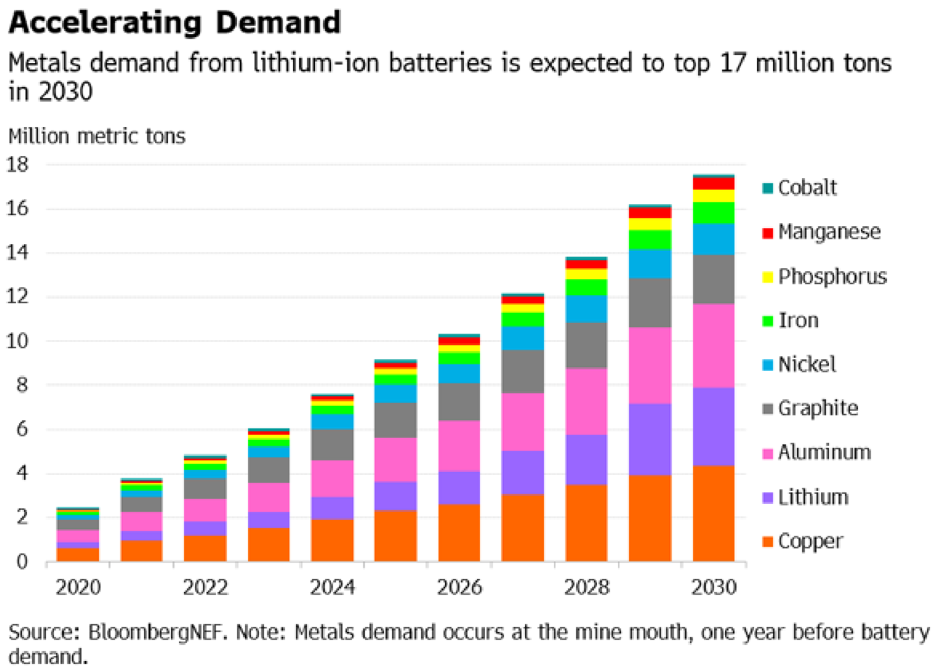

Accelerating Demand

Metals demand from lithium-ion batteries is expected to top 17 million tons in 2030

Source: BloombergNEF. Note: Metals demand occurs at the mine mouth, one year before battery demand.

Figure 2.5: Bar chart showing the prediction of demand for raw materials required in batteries from 2020 to 2030

an ongoing debate with some conservatives estimates suggesting only 31.1 million tonnes remain and other positive estimates suggesting 117 million tonnes remain. Dates are already being suggested as to when depletion may occur. Some articles suggests this may occur as soon as 2055[53, 54, 55]. It is worth noting that this value does not include lithium present in seawater due to process cost and that recycling lithium at this point in time is unfeasible due to its complexity. [56, 57]

Although debates are ongoing it is evident that the price of lithium is much higher then it once was, in 2010 1 metric tonne of lithium carbonate cost 5180 USD whilst its current price in 2022 is 37000 USD making it roughly 5 times more expensive this makes alternative technologies more attractive such as sodium ion batteries due to the much lower cost of sodium at 150USD and higher abundance in the earths crust (1180x that of lithium).[58, 59]. It is worth noting that the price of lithium is very volatile so may be different to when this was written. Historically sodium ion batteries have been paid little attention when compared to lithium namely due to the lower electrode potential vs the standard hydrogen electrode and higher atomic mass which consequently leads to a lower theoretical specific capacity and volumetric energy density of 1165 mah/g vs 3829 mah/g and 7420wh/l vs 4060wh/l respectively, however due to the ever increasing cost, Sodium ion is emerging as a potential lower cost alternative[60, 61].

2.2.3 Solid metal anode batteries

Unlike a conventional battery configuration that usually consists of a carbon-based anode vs a crystalline layered oxide cathode, in which intercalation bonds form during the reduction of active ions as the battery is charged, the use of a solid metal anode removes this conventional material and replaces it with a solid bulk substrate of active mass (Sodium or Lithium usually). During the charging of the cell, active ions in the electrolyte solution are electroplated onto the solid metal anode. The advantages of using a solid metal anode is that a much higher theoretical specific capacity is available. To put this into perspective, sodium has a theoretical specific capacity of 1165 mah/g and a low electrochemical potential of -2.71V vs the standard hydrogen electrode. The theoretical capacity of hard carbon anodes is between 300-400 mah/g which is roughly 4 times less then the solid sodium anode alternative [62, 60].

Although there are some significant benefits of the use of solid metal anodes, unfortunately there are some detrimental issues that limit the use of this cell structure on current technology. Firstly during the charge cycle of the batteries, ideally sodium would deposit as a homogeneous bulk substrate. However it tends to deposit forming needle like protrusions know as dendrites, these dendrites are detrimental to cell function causing instability in the SEI layer that will be highlighted in more detail in section 2.4.1.

2.2.4 Zero excess anode free batteries

The term anode free refers to the substitution of conventional carbon based material in batteries for alternative methods. One particular method removes all components from the anode current collector, active ions are electroplated directly onto the current collector during the charge cycle of the cell. During the discharge, the opposite happens, active ions are oxidised and stripped off of the current collector where they move through the electrolyte and intercalate back into the cathode material [63].

The imapact of removing the carbon based anode from the cell allows for an enhancement in the gravimetric and colorimetric energy density. One source highlighted mentions the graphite anode present in traditional lithium ion batteries represents 27.8% of the cell stack weight which corresponds to 46.1% of the stack thickness and removing this material would increase the gravimetric energy density by 38.5% which would correlate to a volumetric energy density increase of 85.5%. 1mAh/cm2 of electroplated lithium will lead to a change in thickness within that specific area on the electrode of 4.85µm. This equates to a volume expansion of 4.85x$10^{-4} cm^3$ when depositing 1mAh of capacity onto a current collector.

Furthermore by completely removing the conventional anode material and having a system that works entirely by electrodeposition on the charge cycle would mean that an excess of anode material is not required to allow for the charge and discharge of the cell which is typical for a conventional lithium ion setup [64].As well as this, removal of the conventional anode reduces the overall cost of the cell, one source by Yang *et al* puts the reduction in cost of a sodium anode free battery vs a conventional sodium ion at 19%, this is due to the complete removal of the coating and drying process used to create anodes as well as all of the solvents and processed materials required [65]. Finally by removing the anode you are bypassing the slow diffusion kinetics associated with the intercalation process and the detrimental effects of cycling anodes at high currents (more specifically hard carbon anodes for this reference) allowing for faster charging [66, 67].

The points above including, cost, volumetric energy density and high power capabilities are all common issues limiting current electric vehicles. The use of the anode free architecture can provide a better solution to all the problems mentioned. Whilst the principles of solid metal anodes and anode free cells are similar as they both work by electrodepostion of sodium, the anode free setup is more sensitive to the detrimental issues assosciated with the technology (dendrite growth etc). By removing the sodium anode material you are removing a infinite source for sodium ions therefore if a parasitic reactions occur, 'lost' sodium cannot be replaced by more from this bulk substrate on the anode which would cause cell capacity to diminish quickly. therefore stable electrodeposition is very important for this field [65].

2.2.5 Current research - copper current collector

Anode	Cathode	Electrolyte	cycle number	Date	Ref
Bare copper	$Na_3V_2(PO_4)_3$	4M NaFSI in DME	C rate test up to 4C 100 cycles in total	2016	[68]
Bare copper	Na counter electrode	4M NaFSI DME	300 cycles at 0.2, 0.5 and 1 $4mA/cm^2$ 99% for 0.5 and 1, 0.2 seemed unsable		
Bare copper	$Na_2Fe_2(CN)_6$	$1MNaBF_4$ in tetraglyme	100 cycles CE 76% (initial capacity 336 Wh/kg) charging C/5 discharge 1C	2018	[69]
Bare copper	Na counter electrode	$1MNaBF_4$ in tetraglyme	100 cycles CE 100% $0.5mA/cm^2$ charge $0.1mA/cm^2$ discharge		
Copper with PVDF &Bi layer	Na counter electrode	$1MNaPF_6$ in Diglyme	2500 cycles $1mA/cm^2$ 99.92% 1300 cycles $2mA/cm^2$ 99.95%	2021	[70]
Copper with PVDF &Bi layer	$Na_3V_2(PO_4)_3$	$1MNaPF_6$ in Diglyme	150 cycles 1C CE 99.7% CR 95.1%		
Bare copper	Na counter electrode	$1MNaPF_6$in Diglyme	300 cycles at $0.5mA/cm^2$ at $1mah/cm^2$ 99.9% CE	2015	[71]
Bare copper	Na counter electrode	$1MNaPF_6$ in Dimethyl ether	100 cycles at $1.0mA/cm^2$ at 1,2,3 mAh/cm^2 CE becomes unstable above $1mAh/cm^2$	2017	[72]
copper nanowires	Na counter electrode	$1MNaPF_6$ in Dimethyl ether	100 cycles at $1.0mA/cm^2$ at 1,2,3 mAh/cm^2 CE at 98% for all		
copper nanowires	$Na_3V_2(PO_4)_3$	$1MNaPF_6$in Dimethyl ether	200 cycles at with 99%CR		
Bare copper	Na counter electrode	$1MNaPF_6$ in Dimethyl ether	267 cycles low CE of 70% $1mA/cm^2$, $1mah/cm^2$	2023	[73]
copper with HCOONA layer	Na counter electrode	$1MNaPF_6$ in Dimethyl ether	840 cycles low CE of 99.9% $1mA/cm^2$, $1mah/cm^2$		
copper with HCOONA layer	$Na_3V_2(PO_4)_3$	$1MNaPF_6$ in Dimethyl ether	400 Cycles retaining 88.2% of its original capacity at 0.5C		
Bare copper	Na counter electrode	$1MNaPF_6$ in Dimethyl ether	200 cycles stable cycling CE rapidly fades to around 96 from 200-500 cycles $2mA/cm^2$, $3mah/cm^2$	2023	[74]
Bare copper	$Na_3V_2(PO_4)_3$	$1MNaPF_6$ in Dimethyl ether	100 cycles retaining 70% of its original capacity 0.5C		

Table 2.3: Table showing some research articles highlighting sodium anode free cells that function by electrodeposition of sodium onto copper

Anode	Cathode	Electrolyte	cycle number	Date	Ref
Copper with 8nm Al_2O_3	Li counter electrode	1M TFSI DDN	370 cycles $1mA/cm^2$ - $1mAh/cm^2$ 120 cycles $2mA/cm^2$ - $1mAh/cm^2$	2022	[75]
Copper with SnO_2, ZnO, uncoated Cu	Li counter electrode	1M TFSI DON	Failure within 150 cycles $1mA/cm^2$ - instantly $2mA/cm^2$		
Copper	LiS cathode	2 M lithium trifluoromethanesulfonate in 1,2- dimethoxyethane/1,3-dioxolane with 0.2M $LiNO_3$ additive	51.5% capacity retention over 100 cycles - C/10	2018	[76]
Copper	Li Counter electrode	1 M $LiPF_6$ in EC/DEC 1:1 v/v ratio	70 cycles CE drops to 20%	2019	[77]
Copper	Li Counter electrode	2 M $LiPF_6$ in EC/DEC 1:1 v/v ratio	100 cycles CE up at 95-100%		
Copper	$LiNi_1/3Mn_1/3Co_1/3O_2$ cathode	1 M $LiPF_6$ in EC/DEC 1:1 v/v ratio	30 cycles $0.2mA/cm^2$ CE drops to 80%		
Copper	$LiNi_1/3Mn_1/3Co_1/3O_2$ cathode	2 M $LiPF_6$ in EC/DEC 1:1 v/v ratio	100 cycles $0.2mA/cm^2$ CE up at 95-100%		
Copper	Li counter	3 m LiFSI in DOL:DME (1:1, v/v)	$2mA/cm^2$ $1.62mAh/cm^2$ CE around 99.9% for 1500 cycles	2019	[78]
Copper	LFP cathode	3 m LiFSI in DOL:DME (1:1, v/v)	$1mA/cm^2$ retained 78% of its discharge capacity after 40 cycles		

Table 2.4: Table showing some research articles highlighting lithium anode free cells that function by electrodeposition of lithium onto copper

As highlighted by table 2.3 research exists that incorporates copper as the functional anode in the system. Copper was selected as an anode material due to its inability to alloy with sodium and form an intermetallic phase at the interphase where the current collector meets the electrolyte which would physically changing it [79]. As well as this, the material has a very good electrical conductivity which strengthens its application as a current collector in batteries [80].

Cao *et al* Performed cycling of sodium onto copper and aluminium anode current collectors. The group tested 3 discharge currents including 0.2, 0.5 and 1 mA/cm^2 and reported a CE of 99% for 300 cycles in a 4M NaFSI DME electrolyte. The group highlight the presence of low CE at the start of cycling and this was due to parasitic reactions which improves rapidly as passivisation occurs [68].

Seh *et al* although primarily focused on cycling solid sodium metal electrodes performed some experiments where they cycle sodium onto copper using 1M $NaPF_6$ in diglyme. The group reported the stable plating and stripping of sodium up to 300 times maintaining a CE of 99.9% when a current of $0.5mA/cm^2$ was applied. Seh *et al* group obtain a hysteresis value for this ranging between 13.3 and 19.5mV indicating good kinetics [71].

Rudola *et al* cycled sodium onto copper using 1M $NaBF_4$ in tetraglyme and achieved 100% CE over 100 cycles of plating and stripping at a charging current of $0.5mA/cm^2$ and discharge current of $0.1mA/cm^2$.A voltage hysteresis of 40 mV on stripping and -10mV on plating was observed which shows insignificant polarisation. Interestingly the group precycle electrodes for 10 cycles between 0.0 and 1.0V at 5.0 microamps/cm^2 to remove any contamination from the electrode. As well as half cells the group cycled full cells of copper vs $Na_2Fe_2(CN)_6$ cathode and achieved 100 cycles with a capacity retention of 76% and a CE of 100% when the charging current was set to C/5 ($0.18mA/cm^2$) and discharge at 1C ($0.90mA/cm^2$).

As well as sodium showing promising research, lithium systems also exist (see table 2.5) which includes work performed by Hagos *et al* who cycle lithium copper half cells with different concentrations of $LiPF_6$ in EC/DEC 1:1 v/v ratio electrolyte. The group reported a cell with a cycle life of 70 cycles when the electrolyte has a concentration of $1MLiPF_6$ at a current rate of $0.2mA/cm^2$. This increased to 100 cycles at a concentration of 2M $LiPF_6$ maintaining a CE of 95%. The group also successful cycle full cells using a NMC cathode for up to 100 cycles, maintaining a CE of 95-100% when the electrolyte concentration was 2M [77].

2.3 ALD and MLD for batteries

Since 2006 MLD and ALD coatings have begun to appear in battery research. This research includes coatings for Anode and Cathode materials alike. Chae *et al* applied an MLD polymer coating consisting of (pentadlurophenylpropyl) trimethoxysilane (PFPPS) onto Lithium Nickel Manganese oxide (LNMO) powder which was 1-2nm thick. The cell outperformed the pristine Li/LMNO cell which lost 88% of its initial capacity in the first 100 cycles while the coated cathode retained it's initial capacity when discharged at 0.5C [81]. As well as MLD coatings, ALD coatings have been applied to cathode materials such as $Na_3V_2PO_4$ as demonstrated by Dong *et al*. The group used a typical ALD process for aluminium oxide using TMA and water to coat 4.5nm of amorphous material onto cathode active material which was then mixed into a slurry and cast into an electrode. The Al_2O_3 coated NVP electrode retained 89.8% of its original capacity after 100 cycles at 1C, as well as this the coated electrode displayed significantly better charge/discharge rate capabilities at higher C rates from 5C to 20 C where the uncoated NVP control cell capacity diminished rapidly [82].

ALD coatings for anode materials is another promising field of research. Loebl *et al* performed experiments depositing ALD Al_2O_3 and MLD/ALD hybrid metal-organic films of Alucone onto carbon fibre based anodes for enhancing the cyclability of the cells. The group reported that when 10 cycles of ALD Al_2O_3 were applied to the anode, the first cycle capacity retention was improved from 291 mah/g to 359mah/g cycle irreversible loss which equates to a 24% improvement. Thicker coatings of 20 and 30 cycles lowered the capacity when compared to uncoated materials. When compared to the ALD approach, MLD resulted in less improvement to reversible capacity and a greater loss of capacity [83]. As well as conventional carbon based anodes, ALD coatings have been applied to solid metal anodes which are becoming more prolific in research as highlighted in previous sections. Chen *et al* applied several thicknesses (10 and 20 cycles which equated to 2.5 and 4nm respectively) of ALD Al_2O_3 onto solid lithium metal anodes. The group reported the Al_2O_3 coated samples cycled for 2x longer duration when a current of $1mA/cm^2$ was applied to the electrode which maintained a CE as high as 98% [84].

Although Al_2O_3 is the most prominant coating used in this thesis, it is worth noting that many other materials have been coated to enhance the performance of batteries. Theses include Zinc oxide (ZnO) for stabalizing carbon based anodes [85], Aravindan *et al* utilise ALD Tin oxide (SnO_2) that is 58-60nm thick onto stainless steel substrates for enhancing the performance of lithium ion batteries [86]. Zhao *et al* applied a ALD V_2O_5 coating to nitrogen doped graphene as an anode material [87]. These are just a few of many materials that have been applied to the field

2.3.1 The Solid Electrolyte Interphase

The SEI is a passivisation layer that forms on the anode due to chemical and electrochemical reactions between the electrolyte and the anode. The SEI is a very important feature that exists in the battery and, depending on the composition of this layer it can be beneficial, preventing excess degradation of the electrolyte, limiting dendrite growth and minimizing the volume change within the cell whilst still allowing for fast transport of the active species [88, 89, 90]. Various strategies can be applied to tune the thickness, morphology and chemistry of this layer to optimise it for the desired system. This includes electrolyte additives, artificial SEI layers, engineering solvation structures and adopting super concentrated electrolytes [91, 92, 93, 94].

It is worth noting that although previously the benefits of the SEI are highlighted, the formation of this layer can also be detrimental to the cell. Dendrite growth can not only pierce the electrically insulating separator causing catastrophic failure by short circuit, but can also react with the organic electrolyte leading to the formation of more inorganic products that are typically present in the SEI [95]. The constant re-deposition and removal of dendrites leads to consistent fresh exposure of active material which further reacts with the organic electrolyte causing more SEI to form in an uncontrollable manner. This causes cell failure by consuming the finite volume of electrolyte within the cell whilst leaving behind a thick resistive SEI. This theory can be visualised by the schematic representation in figure 2.6 [96, 71].

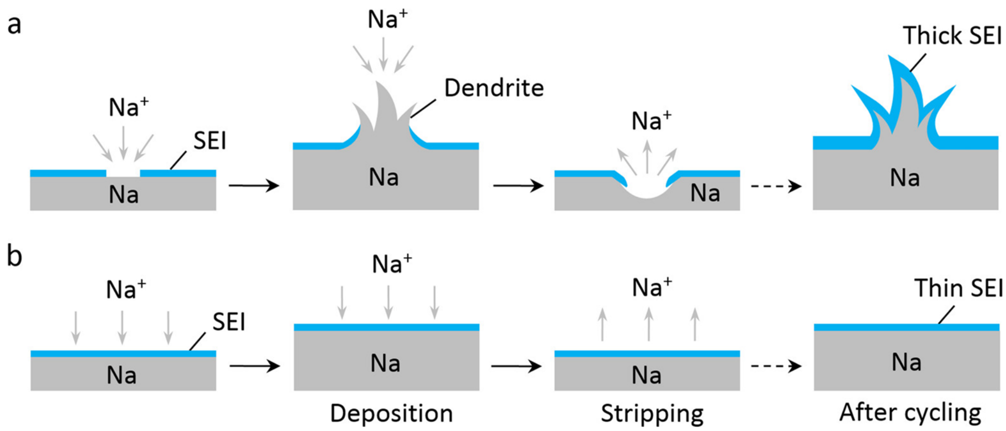

Figure 2.6: Schematic highlighting (a) the mechanism for dendrite formation on a solid metal electrode, (b) how ideal plating and stripped would take place.

2.4 Al_2O_3 coatings

The most accepted explanation for the function of the Al_2O_3 coating is that it acts as a artificial layer, which is an ion permeable barrier reducing the reaction between the solid metal anode and electrolyte, effectively preventing dendrite growth and improving the lifetime of the cell. Zhao *et al* provide evidence for this by performing XPS analysis on the sodium metal electrode. The group showed that the presence of inorganic Na_2O, NaF and RCH_2ONa from the O 1s and F 1s peaks is effectively decreased. These are typical compounds that are found in the solid electrolyte interphase for sodium batteries[97].

Looking back at the work performed by Chen *et al* who applied ALD coatings to solid lithium metal anodes, the group mention that the Al_2O_3 layer remains intact during lithium plating and stripping and that the layer acts to enhance the wettability of the lithium electrode to carbonate and ether based electrolytes

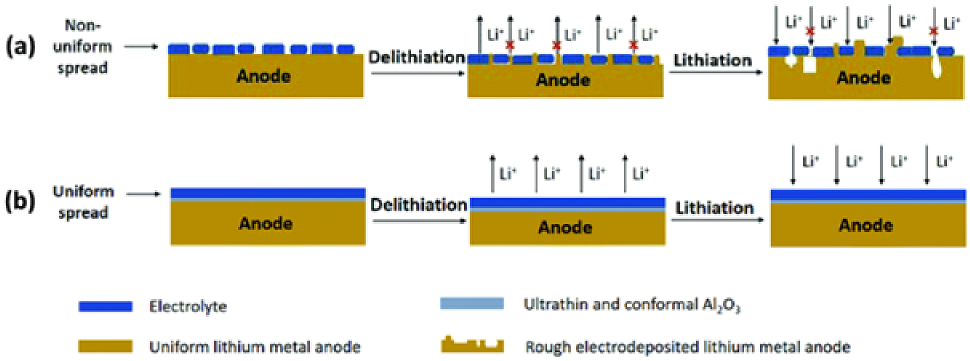

Figure 2.7: Schematic highlighting the concept of Al_2O_3 for enhancing the wettability of solid lithium electrodes [84]

which consequently allow the electrolyte to wet the electrode, thus forming a more uniform and stable solid electrolyte interphase. In order for this to function, the Al_2O_3 would have to remain ontop of the Lithium during cycling, which was proven by XPS. This more stable SEI reduces the consumption of electrolyte by exposure to fresh lithium as mentioned previously [71]. Figure 2.7 highlights the concept of the theory, the group suggest the presence of 'microscopic dry patches' on the surface of the electrode without the Al_2O_3 coating and, as a consequence dendrites, would deposit in these regions, which cause the electrolyte degradation. This is not the case for Al_2O_3 coated lithium. It is worth noting that this work was performed on a solid lithium electrodes [84].

More recently Oyakhire *et al* reported enhanced performance of Al_2O_3 coated copper samples when reversibly cycled against a lithium metal counter electrode and an NMC 532 cathode (results can be seen in table 2.4). The group propose the high resistance of the Al_2O_3 reduces the available nucleation sites for lithium coating promoting sparse nucleation of lithium deposits. The radial diffusion of lithium ions towards the nucleated deposits promotes lateral growth of lithium, resulting in dense low surface area lithium deposits. In contrast to previous studies the group mentioned the SEI formation is structurally similar for the different coatings which suggests the changes in lithium morphology stem from differences in substrate properties and not the SEI [75].

2.4.1 Coatings function and selection Al_2O_3

Al_2O_3 coatings were chosen due to their success in research when compared to other metal oxide coatings such as SnO_2. This could be due to the coatings ability to rapidly conduct sodium and lithium ions. Furthermore, Al_2O_3 precursors were available to be used at Swansea university and process optimization of the coatings had been performed prior to this research to ensure coatings were of good quality[75, 98].

The effectiveness of Al_2O_3 coatings is not yet fully understood, but several theories suggest key roles based on their properties. As an artificial SEI, the coating must be chemically stable, ionically conductive, and flexible to accommodate electrodeposition beneath it. If enhancing wettability, it must also be hydrophilic while maintaining those same properties to ensure continuous electrolyte contact. Alternatively, it may control lithium nucleation by introducing defects that promote sparse growth and limiting active ion availability to reduce uncontrolled deposition.

2.5 ZnO coatings

As seen in table 2.5, ZnO has been used as a functional coating to enhance the plating and stripping efficiencies of carbon based anodes. Zhao *et al* apply a ZnO coating by ALD to a carbon fibre anode matrix to enhance the lithiophilicity of the carbon fibres. This allows for molten lithium to be infused into the electrodes, creating an Li/C composite electrode with a flat surface to minimize the effective current density. By utilizing this technique the group were able to achieve a half cell that achieved 200 cycles at an impressive current of $5mA/cm^2$ and a capacity of $1mAh/cm^2$ with a low overpotential of 120mV. Whilst performing a C rate test, the group reported the ability of the electrode to be cycled at a staggering $25mA/cm^2$ [99, 8].

Zhao *et al* apply ZnO to carbon nanofibres by an electrospinning process which includes the use of zinc acetate in the precursor solution. The group achieved stable cycling for 300 hours at $2mA/cm^2$ with a capacity of $1mAh/cm^2$. Better still the group coupled their electrodes with LFP full cells and achieved superior cycing up to 10C during a rate test with a specific capacity of 155.6 mAh/g at 0.2C. [100, 99].

Yu *et al* present a novel approach wherein ZnO is integrated into a microcubic carbon framework via the in-situ pyrolization of multi-walled carbon nanotubes implanted with Zn-MOF. These structures serve as a three-dimensional host for a robust metallic Li Anode. Impressively, the team demonstrated an extended cycle life of 320 hours at $2.0mA/cm^2$, with an areal capacity of $1mAh/cm^2$, boasting a stable Coulombic Efficiency (CE) of 98.5% and reduced voltage polarization of just 28.0mV. Furthermore, when these anodes are coupled with LFP cathodes, they achieve notable results displaying 150 cycles at 1C, with a remarkable

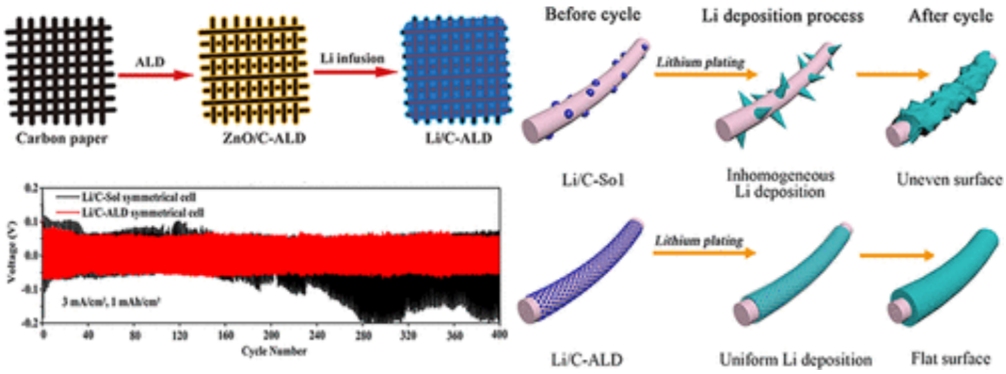

Figure 2.8: Schematic highlighting the affect of lithium plating of a carbon fibre with an ALD ZnO process vs an SOL ZnO coating [99]

capacity retention of 93.8%. Even under rigorous conditions, such as cycling up to 10C during a rate test, the full cells exhibit promising performance. This success is attributed to the utilization of high surface area carbon-based electrodes, enhancing both conductivity and mechanical strength. By mitigating localized current density and accommodating the high volume expansion associated with Li metal anodes, these electrodes significantly improve cycling and rate capabilities. Notably, the confinement of ZnO within the porous carbon cubes facilitates uniform nucleation for lithium metal deposition. This innovative strategy holds substantial promise for advancing lithium metal battery technology [101].

Anode	Cathode	Electrolyte	cycle number	Date	Ref
Carbon nanofibres	Li counter electrode	1, 3-dioxolane (DOL)/1, 2-dimethoxyethane (DME) (1/1, v/v) with 1M LiTFSI & 0.2M $LiNo_3$ additive	250 cycles (stopped) $1mA/cm^2$ for $1mAh/cm^2$	2021	[100]
line Carbon nanofibres @ZnO (electrospinning followed by heat treatment)	Li Counter electrode	1, 3-dioxolane (DOL)/1, 2-dimethoxyethane (DME) (1/1, v/v) with 1M LiTFSI & 0.2M $LiNo_3$ additive	1300 cycles $1mA/cm^2$ for $1mAh/cm^2$		
line Bare copper	Li counter electrode	1, 3-dioxolane (DOL)/1, 2-dimethoxyethane (DME) (1/1, v/v) with 1M LiTFSI & 0.2M LiNo3 additive	120 cycles (stopped) $1mA/cm^2$ for $1mAh/cm^2$		
line Carbon nanofibres @ZnO (electrospinning followed by heat treatment)	$LiFePO_4$	1, 3-dioxolane (DOL)/1, 2-dimethoxyethane (DME) (1/1, v/v) with 1M LiTFSI	rate capability 0.2C 156 mah/g with a CE 99.8%		
ZnO-C ALD	Li Counter electrode	1 M $LiPF_6$in EC/DEC(1:1 vol %)	400 cycles $3mA/cm^2$ at $1mAh/cm^2$ cycles up to $25mA/cm^2$	2020	[99]
ZnO-C-SOL	Li counter electrode	1 M $LiPF_6$in EC/DEC(1:1 vol %)	inconsistent voltage hysteresis throughout cycles stably up to $5mA/cm^2$		
Hollow carbon nanofibres (HCNF)	Li counter electrode	1 M $LiPF_6$ in ethyl methyl carbonate (EMC), dimethyl carbonate (DMC), and ethylene carbonate (EC) with a volume ratio of 1:1:1	$3mA/cm^2$ at $1mAh/cm^2$ for 1000 hours	2023	[99]
NHCNF - 5-ZnO (coaxial electrospinning)	Li Counter electrode		$3mA/cm^2$ at $1mAh/cm^2$ for 170 hours (stopped)		
Copper foil	Li counter electrode		$3mA/cm^2$ at $1mAh/cm^2$ for around 50 cycles (stopped)		
NHCNF-5-ZnO ($5mAh/cm^2$ Li pre-deposited)	LFP		154mah/g at 0.2C 120mah/g at 1C cycle life 150 cycles 1C CE 99.87%		
ZnO@ C-MWCNTs	Li counter electrode	The electrolyte was 1.0 M of lithium bis (trifluoromethanesulfonyl)-imide (LiTFSI) in 1,3-dioxolane (DOL) and 1,2-dimethoxyethane (DME) (volume ratio 1:1) with 1.0 wt % lithium nitrate ($LiNO_3$)	$3mA/cm^2$ at $1mAh/cm^2$ 250 cycles CE 99% consistent	2022	[101]
ZnO@C	Li counter electrode		$3mA/cm^2$ at $1mAh/cm^2$ 190 cycles (stopped) CE unstable past 100 cycles%		
copper foil	Li counter electrode		$3mA/cm^2$ at $1mAh/cm^2$ 90 cycles (stopped) CE rapidly decreases past 70 cycles%		
ZnO@C-MWCNTs	LFP		150cycles at 1C 93.9% capcity retention. Cycled up to 10C		

Table 2.5: Table showing different research articles highlighting the application of zinc oxide for lithiophillic 2D carbon current collectors.

2.5.1 Coatings function and selection ZnO

ZnO was selected for 2D carbon current collectors due to prior process optimisation and precursor availability at Swansea university. Furthermore, previous studies were performed by Zhao et al using ALD systems. Due to the MVD's ability to coat features with high aspect ratio conformally, ZnO was studied to compare ALD and MVD with the hypothesis MVD will provide more uniform coatings enhancing the cycle life of the batteries. Further information for how ZnO coatings function can be found in section 2.4.3 [99].

To highlight the mechanism from the previous section, The ZnO forms an alloy with lithium which has a larger binding energy with Li and a lower Li nucleation overpotential than carbon. This high binding energy signifies a strong interaction between Li and the LiZn alloy. The lower nucleation overpotential of the alloy when compared to carbon means the Li will preferentially deposit on the alloy. The high conformality of ALD has allowed for uniform deposition of ZnO causing uniform deposition of lithium during electrodeposition and therefore preventing the occurrence of dendrite growth [99, 8].

2.6 MVD platinum

The coatings mentioned have been very specific to metal oxides and metalcones, It is also possible to deposit metal by MVD as well. This section will focus on platinum metal deposited by MVD and how it can be applied to different applications.

Metal thin films and nanoparticles have been utilised in many areas of research including waveguide cladding for photonics, metal contacts for electronic device technologies, tuneable metal films for space applications and catalysis[102, 103, 104, 105].

Whilst many methods exist for depositing metal thin films and nanoparticles, examples include CVD and PVD, metal nanoparticles can also be deposited by ALD, which offer some bespoke advantages such as highly conformal coatings on high surface area porous solids. These surfaces are typical for catalyst applications [106, 105, 107, 108]. A common ALD process for deposition of platinum can be seen in figure 2.9 where Trimethyl(methylcyclopentadienyl)platinum(IV) ($MeCpPtMe_3$) is the precursor and either oxygen or oxygen plasma is introduced to combust the methyl groups of the $MeCpPtMe_3$ ligand leaving an atomic layer of platinum. A layer of Al_2O_3 is applied as an adhesion layer [109].

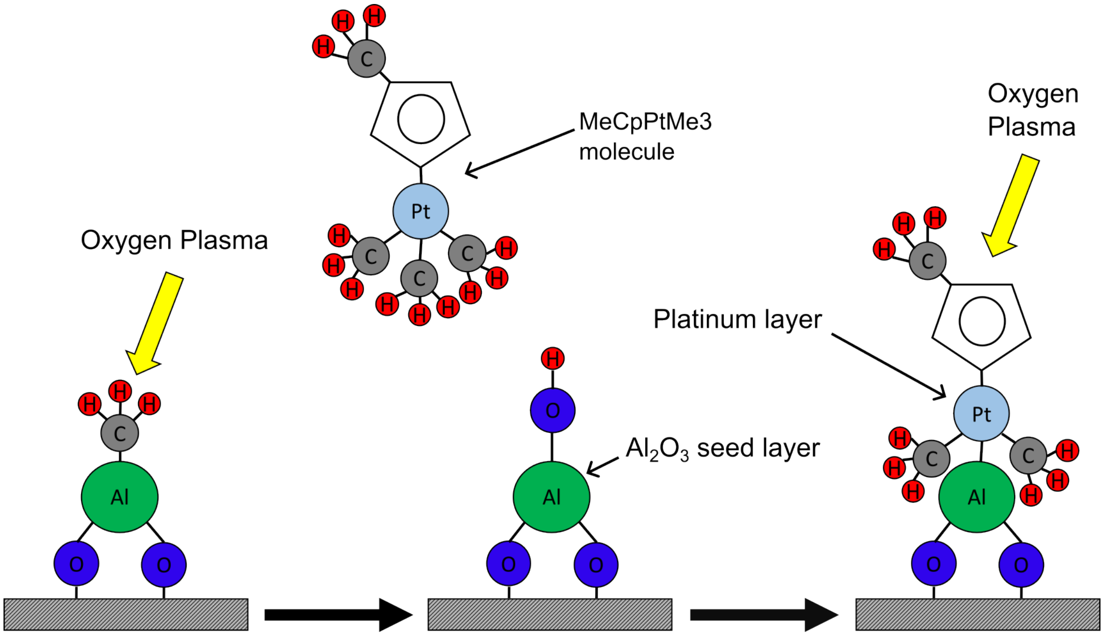

Figure 2.9: Schematic highlighting one method for depositing platinum metal by ALD using $MeCpPtMe_3$ precursors and O_2 plasma

2.7 Catalysis

A catalyst is a material that can open up a new reaction pathway for a chemical reaction via a lower activation energy. It does this by providing a partial bond which stabilises the transition state and compensates for part of the energy required to break a bond in the reactant before stabilisation by the newly formed bond takes over. The catalyst remains unchanged in the reaction. Addition of a catalyst you can increase the rate of reaction whilst reducing the energy required for the specific process. This makes catalysts desirable. Figure 2.10 shows the basic function of how a catalyst works. [110].

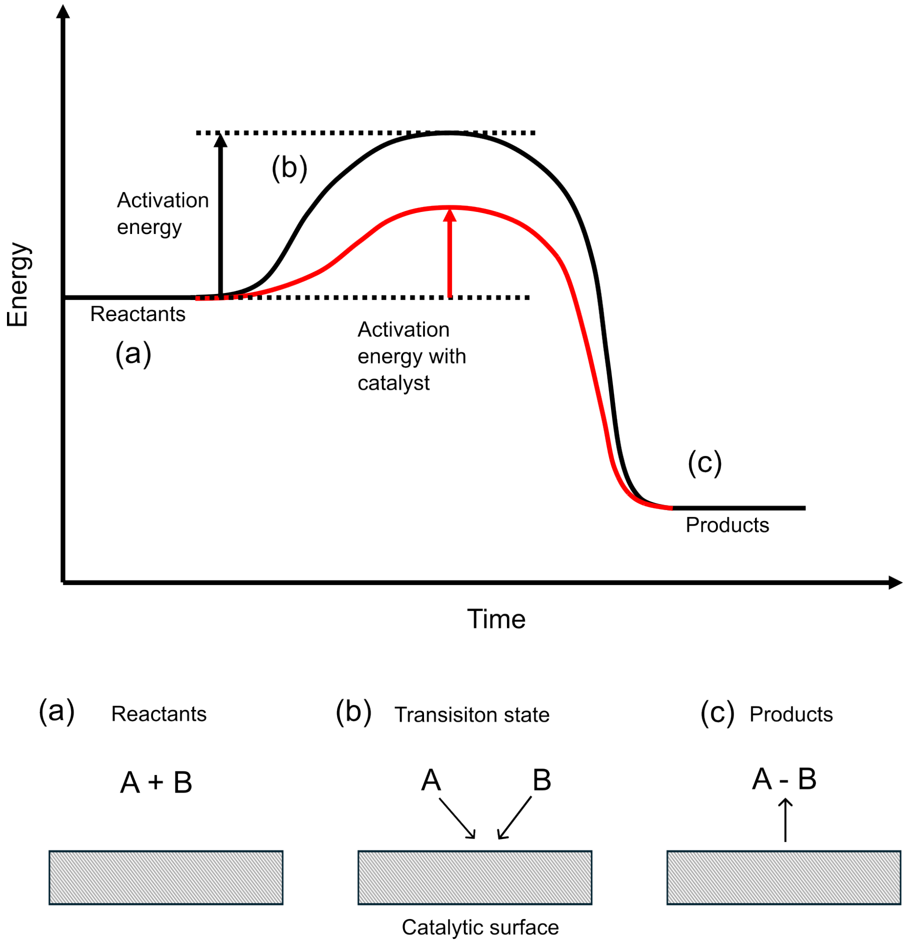

Figure 2.10: Schematic highlighting the reduced activation energy pathway a catalyst provides for a system with examples of each stage of the reaction.

Catalysts can be found in many different industries including Ammonia (NH_3) and syngas production, catalytic cracking of gas oil, synthesis of sulphuric and nitric acid, hydrogenation reactions and electrocatlaysis [111, 112, 113].

2.7.1 Hydrogen as a fuel

Over the past century, the automotive industry has heavily relied on the combustion of fossil fuels, notably the iconic internal combustion engine. The remarkable energy density of petrochemicals has enabled the production of vehicles with extensive ranges at relatively low costs, facilitating their widespread use due to their simplicity and quick refueling capabilities. However, ongoing governmental pressures seek to mitigate the global dependency on fossil fuels to combat the production of greenhouse gases such as CO_2, a byproduct of their combustion. These emissions not only degrade air quality but also contribute to climate change[114]. Oil and gas stand out as the predominant contributors to the global energy mix, collectively constituting over 84% of total global energy production, with oil alone representing 33% of this share. Notably, a substantial portion of this oil, approximately 65%, is consumed by the transport sector [115].

Hydrogen presents itself as an attractive alternative to fossil fuels owing to its high energy density by weight, surpassing gasoline by around 3 times, and yielding harmless combustion byproducts, mainly water. Currently, global hydrogen production stands at 50 million tonnes, predominantly sourced from nonrenewable energy (96%), with only a minor fraction (4%) derived from renewable sources. Despite its advantages, hydrogen faces challenges due to its low volumetric energy density, approximately 3000 times lower than gasoline, necessitating compression. This compression process demands expensive equipment and entails safety risks. Given that hydrogen exists as a gas at room temperature, any leaks in systems can lead to gas accumulation, posing significant safety concerns [116, 117].

2.7.2 Hydrogen fuel cell technology

Fuel cell technology provides as a new method to potentially replace the internal combustion engine. Although hydrogen fuel cell technology varies, the basic principles are similar and work by the conversion of hydrogen into electricity. See table 2.6 for examples of different major types of fuel cell technology, these include Proton exchange membrane (PEMFCs), alkaline fuel cells (AFCs) and Molten carbonate fuel cells (MCFCs) as a few examples.

-	PEMFCs	AFCs	PAFCs	MCFCs	SOFCs
Electrolyte charge carrier	Polymeric membrane H+	Potassium hydroxide OH-	Phosphoric acid H^+	Molten carbonate $CO_3 2-$	Ceramics O2-
Operating temperature	-40-120^oC (150-180^oC in high temp PEMFCs)	50-200^oC	150-220^oC	600-700^oC	500-1000^oC
Electrical efficiency	up to 65-72%	up to 70%	Up to 45%	Up to 60%	Up to 65 %
Primary fuel	H_2, reformed H_2, methanol in direct methanol fuel cells.	H_2 or cracked ammonia	H_2 or reformed H_2	H_2, biogas, or methane.	H_2, biogas or methane
Shipments in 2019	934.2MW	0MW	106.7 MW	10.2 MW	78.1 MW

Table 2.6: Different types of hydrogen fuel cell technologies and their operating parameters [116]

2.7.3 Proton exchange membrane hydrogen fuel cell technology (PEMFC)

From the technology in table 2.6 PEMFC fuel cells had the most shipments in 2019 (934.2MW). PEMFC is most suited to the electrification of transport applications which is a heavy focus of this thesis. The advantages of PEMFCs over other technology is the high efficiency (65-72%) of the system as well as modest operation temperatures ($-40^oC - 120^oC$) which allows them to operate in the climate conditions present in most countries [116] .

A PEMFC works by an electrolysis process. Hydrogen and Oxygen are supplied to the PEMFC. Hydrogen is oxidised at the anode and therefore loses an electron creating H^+ ions. This electron causes a current in the circuit which is the function of the fuel cell. At the cathode oxygen is reduced generating heat and water as bi products [118, 119]. in-between the electrodes is a acidic polymer electrolyte that is capable of conducting protons which allows for their exchange in between the electrodes [116]. Figure 2.11 shows the structure of a PEMFC hydrogen fuel cell.

An essential aspect of PEMFC technology involves the utilization of platinum metal as a catalyst. Typically, platinum nanoparticles are dispersed on the porous gas diffusion materials, often composed of carbon [120]. Nanoparticles are commonly placed on the cathode to facilitate the oxygen reduction reaction and on the anode to catalyze the hydrogen oxidation reaction [121, 122].

Atomic Layer Deposition (ALD) has emerged as a promising technique for depositing platinum nanoparticles on the PEMFC anode to enhance the hydrogen oxidation reaction, as demonstrated by Song *et al.* Their study showed that ALD-deposited nanoparticles (20 cycles) increased the surface area of the particles

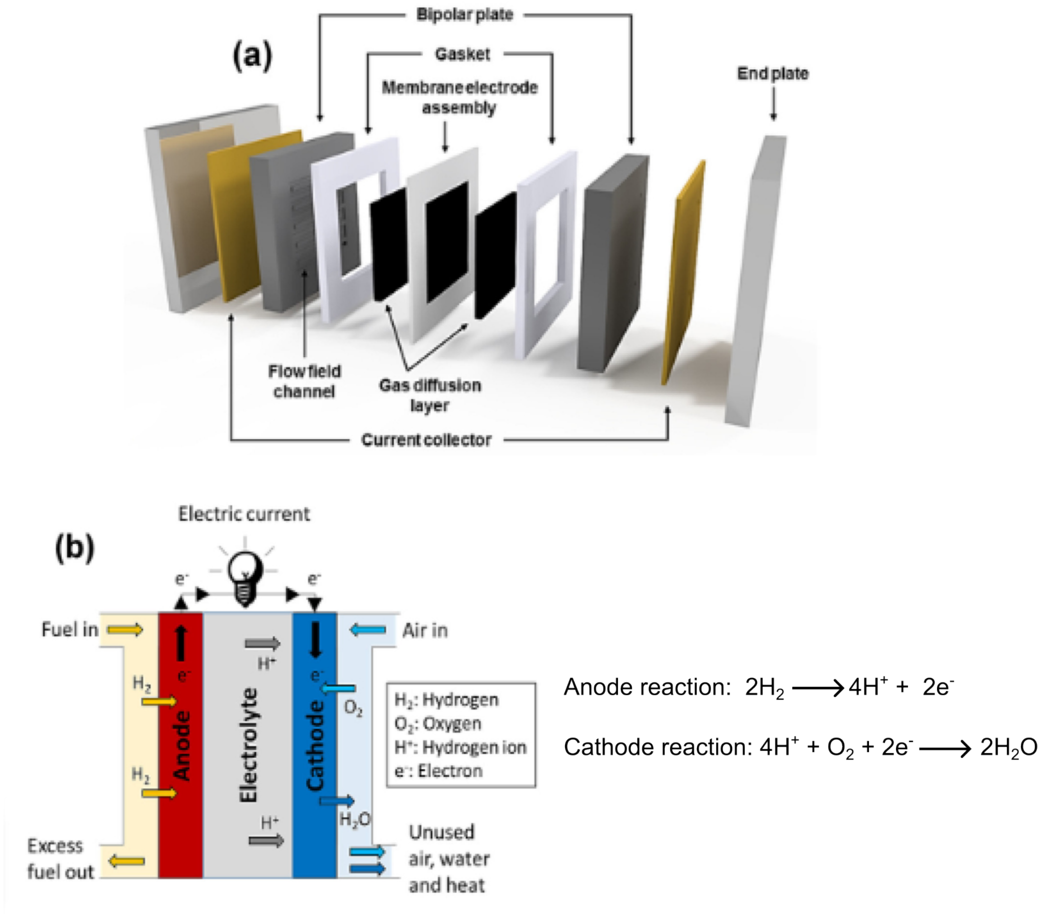

Figure 2.11: Schematic showing the structure of a PEMFC hydrogen fuel cell

to 155 m^2/g, which is three times higher than the commercial example of 50.3 m^2/g, while achieving an ultra-low platinum loading of 0.01 mg/cm^2. Previously, conventional electrode preparation methods yielded a minimum loading of 0.025 mg/cm^2 for the anode without compromising the kinetics of the hydrogen oxidation reaction [123, 124]. This advancement significantly enhances platinum dispersion, utilization, and durability, resulting in a superior electrode [122].

2.7.4 PEM water electrolysis cell

In addition to PEM fuel cells for hydrogen oxidation, PEM technology also finds applications in water electrolysis for hydrogen generation. As previously mentioned, the majority (96%) of global hydrogen production stems from fossil fuel refinement, with only a small fraction (4%) originating from renewable energy sources, primarily due to the limitations of current water electrolysis methods in terms of output and cost [125]. Nevertheless, technological advancements are paving the way for more cost-effective water electrolysis methods, including the utilization of Atomic Layer Deposition (ALD). Laube *et al* demonstrate the deposition of platinum catalysts on the cathode within a PEM setup using ALD. The group achieved a significant reduction in platinum loading to 0.28 mg/cm^2, down from commercial values ranging between 0.5 to 1.0 mg/cm^2, while maintaining promising performance. This reduction in loading holds the potential to decrease the overall cost of PEM systems, making them a more appealing option for hydrogen generation [126, 127].

2.8 Aims, structure and Hypothesis of this thesis

The aim of this thesis is to explore the applications of MVD coatings in new fields such as batteries and catalysis. Currently the SPTS MVD is a tool with only very bespoke market applications including hydrophobic coatings for MEMs. An ideal outcome for this thesis would be to show off the MVD tools capability of providing better outcomes for research being conducted in anode free batteries and catalysis systems due to its mechanisim for deposition compared to other processes, see section 2.1.5 for more detail. Depending on the success of the research, a bonus outcome could be opening a potential new market for tool and therefore generate revenue for my sponsoring company KLA.

In this literature review, the extensive research that has been performed on sodium ion and lithium ion anode free battery technology. Although many approaches have been taken to allow for stable cycling of these batteries for long periods of time, full cells are not commercially viable, with the best performance being 400 cycles at 0.5C retaining 88.2% of its original capacity as shown by wang *et al*. This indicates there are fundamental issues with regards to this particular battery technology[73]. As well as this, research has been conducted on PEM catalysis systems, which aim to revolutionise hydrogen fuel cells for cars as well as hydrogen generation by electrolysis as a more environmentally friendly substitute for fossil fuels.

In chapter 4, previously developed ALD Al_2O_3 coatings have been applied to zero excess anode free lithium ion batteries on copper. Current research however doesn't include the use of MVD as a deposition technique and doesn't investigate how the affect of changing the thickness of the coatings can affect the cycling performance, which is the aim of this chapter. The hypothesis is that there will be a sweet spot whereby the thickness of the material has an optimal affect on the cycle life of half cells. This will assist other researchers in selecting this value when coating their substrates. Additionally due to the higher aspect ratio the MVD has to offer compared to other ALD tools highlighted, MVD can offer better coating uniformity over the rough surface of the copper substrates, therefore half and full cells should outperform those reported in other research articles. Current research offers different explanations as to how the coatings specifically function so this will also be reported in this work.

In chapter 5, ZnO Coatings have been applied to 2D carbon current collectors. Research has been conducted in this field previously however, no MVD alternative has been attempted. The higher aspect ratio of the MVD compared to other techniques is particulary relavent in this application due to the 2D carbon substrate as the anode. It was hyspothesised that due to the enhanced capability of MVD for coating of structures, the MVD will enable more conformal coatings then conventional ALD tools. This will enhance the cyclability of cells created.

In chapter 6, currently no research articles have been published whereby Al_2O_3 coatings have been applied to copper substrates for Zero excess sodium anode free batteries. It is expected that similar to the lithium ion anode free work in chapter 4, the Al_2O_3 will enhance cyclability of the cells being tested and will therefore improve the performance of these batteries. The coating function will also specifically be studied to unlock information as to how it improves performance.

Chapter 7 details the novel MVD deposition of metallic platinum. The growth of these films has been studied at thin film levels and applied in model catalytic reactions to various areas within the field of catalysis to assess their performance.

Bibliography

[1] Anthony C Jones and Michael L Hitchman. *Chemical vapour deposition: precursors, processes and applications*. Royal society of chemistry, 2009.

[2] John Norman Pring and William Fielding. Clxxi.—the preparation at high temperatures of some refractory metals from their chlorides. *Journal of the Chemical Society, Transactions*, 95:1497–1506, 1909.

[3] Andrew R Barron. Cvd of sio2 and related materials: an overview. *Advanced materials for optics and electronics*, 6(2):101–114, 1996.

[4] Hugh O Pierson. *Handbook of chemical vapor deposition: principles, technology and applications*. William Andrew, 1999.

[5] Steven M George. Atomic layer deposition: an overview. *Chemical reviews*, 110(1):111–131, 2010.

[6] Tuomo Suntola and Jorma Antson. Method for producing compound thin films, November 15 1977. US Patent 4,058,430.

[7] Yoon Seok Jung, Peng Lu, Andrew S Cavanagh, Chunmei Ban, Gi-Heon Kim, Se-Hee Lee, Steven M George, Stephen J Harris, and Anne C Dillon. Unexpected improved performance of ald coated licoo2/graphite li-ion batteries. *Advanced Energy Materials*, 3(2):213–219, 2013.

[8] Ying Zhang, Wei Luo, Chengwei Wang, Yiju Li, Chaoji Chen, Jianwei Song, Jiaqi Dai, Emily M Hitz, Shaomao Xu, Chunpeng Yang, et al. High-capacity, low-tortuosity, and channel-guided lithium metal anode. *Proceedings of the National Academy of Sciences*, 114(14):3584–3589, 2017.

[9] Ting Shen, Jianjun Tian, Bo Li, and Guozhong Cao. Ultrathin ald coating on tio2 photoanodes with enhanced quantum dot loading and charge collection in quantum dots sensitized solar cells. *Science China Materials*, 10(59):833–841, 2016.

[10] E Marin, A Lanzutti, L Guzman, and L Fedrizzi. Corrosion protection of aisi 316 stainless steel by ald alumina/titania nanometric coatings. *Journal of coatings technology and research*, 8:655–659, 2011.

[11] Roseanne Warren, Firas Sammoura, Fares Tounsi, Mohan Sanghadasa, and Liwei Lin. Highly active ruthenium oxide coating via ald and electrochemical activation in supercapacitor applications. *Journal of Materials Chemistry A*, 3(30):15568–15575, 2015.

[12] GS Higashi and CG Fleming. Sequential surface chemical reaction limited growth of high quality aluminum oxide dielectrics. *Appl. Phys. Lett*, 55:1989, 1963.

[13] AC Dillon, AW Ott, JD Way, and SM George. Surface chemistry of al2o3 deposition using al (ch3) 3 and h2o in a binary reaction sequence. *Surface Science*, 322(1-3):230–242, 1995.

[14] EL Lakomaa, A Root, and T Suntola. Surface reactions in al2o3 growth from trimethylaluminium and water by atomic layer epitaxy. *Applied Surface Science*, 107:107–115, 1996.

[15] Yang Zhao and Xueliang Sun. Molecular layer deposition for energy conversion and storage. *ACS Energy Letters*, 3(4):899–914, 2018.

[16] Pia Sundberg and Maarit Karppinen. Organic and inorganic–organic thin film structures by molecular layer deposition: A review. *Beilstein journal of nanotechnology*, 5(1):1104–1136, 2014.

[17] Tetsuzo Yoshimura, Satoshi Tatsuura, and Wataru Sotoyama. Polymer films formed with monolayer growth steps by molecular layer deposition. *Applied physics letters*, 59(4):482–484, 1991.

[18] Paul W Loscutoff, Han-Bo-Ram Lee, and Stacey F Bent. Deposition of ultrathin polythiourea films by molecular layer deposition. *Chemistry of Materials*, 22(19):5563–5569, 2010.

[19] Takayuki Miyamae, Kiyomi Tsukagoshi, Osamu Matsuoka, Sadaaki Yamamoto, and Hisakazu Nozoye. Preparation of polyimide-polyamide random copolymer thin film by sequential vapor deposition polymerization. *Japanese journal of applied physics*, 41(2R):746, 2002.

[20] Frank Fug, Adrien Petry, Hendrik Jost, Aisha Ahmed, Mohammad Zamanzade, and Wulff Possart. Molecular layer deposition of polyurethane—polymerisation at the very contact to native aluminium and copper. *Applied Surface Science*, 426:133–147, 2017.

[21] Byoung H Lee, Byunghoon Yoon, Aziz I Abdulagatov, Robert A Hall, and Steven M George. Growth and properties of hybrid organic-inorganic metalcone films using molecular layer deposition techniques. *Advanced Functional Materials*, 23(5):532–546, 2013.

[22] Gregory Burwell, Klaudia Rejnhard, Jon Evans, Jacob Mitchell, Michael T Grimes, Matt Elwin, Ardalan Armin, and Paul Meredith. A low-temperature batch process for the deposition of high-quality conformal alumina thin films for electronic applications. *Advanced Engineering Materials*, 2023.

[23] Georgios P Gakis, Constantin Vahlas, Hugues Vergnes, Sandrine Dourdain, Yann Tison, Hervé Martinez, Jerôme Bour, David Ruch, Andreas G Boudouvis, Brigitte Caussat, et al. Investigation of the initial deposition steps and the interfacial layer of atomic layer deposited (ald) al2o3 on si. *Applied Surface Science*, 492:245–254, 2019.

[24] Corina Barbos, Danièle Blanc-Pelissier, Alain Fave, Claude Botella, Philippe Regreny, Geneviève Grenet, Elisabeth Blanquet, Alexandre Crisci, and Mustapha Lemiti. Al2o3 thin films deposited by thermal atomic layer deposition: Characterization for photovoltaic applications. *Thin Solid Films*, 617:108–113, 2016.

[25] Ariel J Ben-Sasson, Guy Ankonina, Michael Greenman, Michael T Grimes, and Nir Tessler. Low-temperature molecular vapor deposition of ultrathin metal oxide dielectric for low-voltage vertical organic field effect transistors. *ACS applied materials & interfaces*, 5(7):2462–2468, 2013.

[26] Boris Kobrin, Jeff Chinn, and W Ashurst. Durable anti-stiction coatings by molecular vapor deposition (mvd). In *NSTI Nanotech*, volume 2, pages 247–350. Molecular Vapor Deposition (MVD) is a trademark of Applied MicroStructures, Inc, 2005.

[27] Nanomaster. Nano-master atomic layer deposition systems. Brochure, N/a.

[28] Oxford instruments. Atomic scale processing ald, ale cvd process solutions. Brochure, 2019.

[29] SPTS technologies a KLA company. Mvd® 300 technology and applications. Brochure, N/a.

[30] E+R Vacuum Beneq. Mvd® 300 technology and applications. Brochure, N/a.

[31] Arradiance. Gemstar-8tm benchtop ald system. Brochure, N/a.

[32] Kurt J Lesker. Ald 150-lx atomic layer deposition system. Brochure, N/a.

[33] Veeco. Phoenix – batch production ald, 2023.

[34] Veeco. Savannah-thermal ald for r d, 2023.

[35] Picosun. Picosun® p-300b. Brochure, 2022.

[36] SVT associates. Northstar ald. Brochure, 2011.

[37] Martin Winter and Ralph J Brodd. What are batteries, fuel cells, and supercapacitors? *Chemical reviews*, 104(10):4245–4270, 2004.

[38] Xiaopeng Chen, Weixiang Shen, Thanh Tu Vo, Zhenwei Cao, and Ajay Kapoor. An overview of lithium-ion batteries for electric vehicles. In *2012 10th International Power & Energy Conference (IPEC)*, pages 230–235. IEEE, 2012.

[39] Chao-Yang Wang, Teng Liu, Xiao-Guang Yang, Shanhai Ge, Nathaniel V Stanley, Eric S Rountree, Yongjun Leng, and Brian D McCarthy. Fast charging of energy-dense lithium-ion batteries. *Nature*, 611(7936):485–490, 2022.

[40] Hiroki Moriwake, Akihide Kuwabara, Craig AJ Fisher, and Yuichi Ikuhara. Why is sodium-intercalated graphite unstable? *Rsc Advances*, 7(58):36550–36554, 2017.

[41] Wei Luo, Fei Shen, Clement Bommier, Hongli Zhu, Xiulei Ji, and Liangbing Hu. Na-ion battery anodes: materials and electrochemistry. *Accounts of chemical research*, 49(2):231–240, 2016.

[42] Wei-Jun Zhang. A review of the electrochemical performance of alloy anodes for lithium-ion batteries. *Journal of Power Sources*, 196(1):13–24, 2011.

[43] M Stanley Whittingham. Lithium batteries and cathode materials. *Chemical reviews*, 104(10):4271–4302, 2004.

[44] Xiaosong Huang. Separator technologies for lithium-ion batteries. *Journal of Solid State Electrochemistry*, 15(4):649–662, 2011.

[45] Derek Pletcher. *A first course in electrode processes*. Royal Society of Chemistry, 2019.

[46] Klaus Schmidt-Rohr. How batteries store and release energy: Explaining basic electrochemistry. *Journal of chemical education*, 95(10):1801–1810, 2018.

[47] Toshiaki Ohtsuka, Atsushi Nishikata, Masatoshi Sakairi, and Koji Fushimi. *Electrochemistry for corrosion fundamentals*. Springer, 2018.

[48] Ahmad Mayyas, Karim Moawad, Assia Chadly, and Emad Alhseinat. Can circular economy and cathode chemistry evolution stabilize the supply chain of li-ion batteries? *The Extractive Industries and Society*, 14:101253, 2023.

[49] Bloomberg NEF. Race to net zero: The pressures of the battery boom in five charts, 2022.

[50] David Archer and Stefan Rahmstorf. *The climate crisis: An introductory guide to climate change*. Cambridge University Press, 2010.

[51] Roland Berger. The lithium-ion (ev) battery market and supply chain. Website presentation, 2022.

[52]

[53] Stephen E Kesler, Paul W Gruber, Pablo A Medina, Gregory A Keoleian, Mark P Everson, and Timothy J Wallington. Global lithium resources: Relative importance of pegmatite, brine and other deposits. *Ore geology reviews*, 48:55–69, 2012.

[54] U.S Geological Survey. Mineral commodity summaries 2022. Technical report, National Minerals Information Center, 2022.

[55] Peter Greim, AA Solomon, and Christian Breyer. Assessment of lithium criticality in the global energy transition and addressing policy gaps in transportation. *Nature communications*, 11(1):4570, 2020.

[56] Pankaj K Choubey, Kang-Sup Chung, Min-seuk Kim, Jae-chun Lee, and Rajiv R Srivastava. Advance review on the exploitation of the prominent energy-storage element lithium. part ii: From sea water and spent lithium ion batteries (libs). *Minerals Engineering*, 110:104–121, 2017.

[57] Brian Taylor. Study says progress needed in lithium-ion battery recycling, 2022.

[58] US Geological Survey. Average lithium carbonate price from 2010 to 2022, 2023.

[59] US Geological Survey. Sodium-ion batteries on the horizon: Where do they challenge lithium-ion?, 2023.

[60] Michael D Slater, Donghan Kim, Eungje Lee, and Christopher S Johnson. Sodium-ion batteries. *Advanced Functional Materials*, 23(8):947–958, 2013.

[61] Ashish Rudola, Ruth Sayers, Christopher J Wright, and Jerry Barker. Opportunities for moderate-range electric vehicles using sustainable sodium-ion batteries. *Nature Energy*, 8(3):215–218, 2023.

[62] Clement Bommier, Xiulei Ji, and P Alex Greaney. Electrochemical properties and theoretical capacity for sodium storage in hard carbon: insights from first principles calculations. *Chemistry of Materials*, 31(3):658–677, 2018.

[63] Sanjay Nanda, Abhay Gupta, and Arumugam Manthiram. Anode-free full cells: a pathway to high-energy density lithium-metal batteries. *Advanced Energy Materials*, 11(2):2000804, 2021.

[64] Johannes Betz, Georg Bieker, Paul Meister, Tobias Placke, Martin Winter, and Richard Schmuch. Theoretical versus practical energy: a plea for more transparency in the energy calculation of different rechargeable battery systems. *Advanced energy materials*, 9(6):1803170, 2019.

[65] Tingzhou Yang, Dan Luo, Yizhou Liu, Aiping Yu, and Zhongwei Chen. Anode-free sodium metal batteries as rising stars for lithium-ion alternatives. *Iscience*, 2023.

[66] Francesco Mazzali, Marcin W Orzech, Arturas Adomkevicius, Ambra Pisanu, Lorenzo Malavasi, Davide Deganello, and Serena Margadonna. Designing a high-power sodium-ion battery by in situ metal plating. *ACS Applied Energy Materials*, 2(1):344–353, 2018.

[67] E Irisarri, A Ponrouch, and MR Palacin. Hard carbon negative electrode materials for sodium-ion batteries. *Journal of The Electrochemical Society*, 162(14):A2476, 2015.

[68] Ruiguo Cao, Kuber Mishra, Xiaolin Li, Jiangfeng Qian, Mark H Engelhard, Mark E Bowden, Kee Sung Han, Karl T Mueller, Wesley A Henderson, and Ji-Guang Zhang. Enabling room temperature sodium metal batteries. *Nano Energy*, 30:825–830, 2016.

[69] Ashish Rudola, Satyanarayana R Gajjela, and Palani Balaya. High energy density in-situ sodium plated battery with current collector foil as anode. *Electrochemistry Communications*, 86:157–160, 2018.

[70] Jiaolong Zhang, Shuo Wang, Wenhui Wang, and Baohua Li. Stabilizing sodium metal anode through facile construction of organic-metal interface. *Journal of Energy Chemistry*, 66:133–139, 2022.

[71] Zhi Wei Seh, Jie Sun, Yongming Sun, and Yi Cui. A highly reversible room-temperature sodium metal anode. *ACS central science*, 1(8):449–455, 2015.

[72] Yanying Lu, Qiu Zhang, Mo Han, and Jun Chen. Stable na plating/stripping electrochemistry realized by a 3d cu current collector with thin nanowires. *Chemical Communications*, 53(96):12910–12913, 2017.

[73] Chaozhi Wang, Ying Zheng, Zhe-Ning Chen, Rongrong Zhang, Wei He, Kaixuan Li, Sen Yan, Jingqin Cui, Xiaoliang Fang, Jiawei Yan, et al. Robust anode-free sodium metal batteries enabled by artificial sodium formate interface. *Advanced Energy Materials*, page 2204125, 2023.

[74] Olusola John Dahunsi, Siyuan Gao, Jacob Kaelin, Bomin Li, Iddrisu B Abdul Razak, Bowen An, and Yingwen Cheng. Anode-free na metal batteries developed by nearly fully reversible na plating on the zn surface. *Nanoscale*, 15(7):3255–3262, 2023.

[75] Solomon T Oyakhire, Wenbo Zhang, Andrew Shin, Rong Xu, David T Boyle, Zhiao Yu, Yusheng Ye, Yufei Yang, James A Raiford, William Huang, et al. Electrical resistance of the current collector controls lithium morphology. *Nature communications*, 13(1):3986, 2022.

[76] Sanjay Nanda, Abhay Gupta, and Arumugam Manthiram. A lithium–sulfur cell based on reversible lithium deposition from a li2s cathode host onto a hostless-anode substrate. *Advanced Energy Materials*, 8(25):1801556, 2018.

[77] Tesfaye Teka Hagos, Balamurugan Thirumalraj, Chen-Jui Huang, Ljalem Hadush Abrha, Teklay Mezgebe Hagos, Gebregziabher Brhane Berhe, Hailemariam Kassa Bezabh, Jim Cherng, Shuo-Feng Chiu, Wei-Nien Su, et al. Locally concentrated lipf6 in a carbonate-based electrolyte with fluoroethylene carbonate as a diluent for anode-free lithium metal batteries. *ACS applied materials & interfaces*, 11(10):9955–9963, 2019.

[78] Tamene Tadesse Beyene, Bikila Alemu Jote, Zewdu Tadesse Wondimkun, Bizualem Wakuma Olbassa, Chen-Jui Huang, Balamurugan Thirumalraj, Chia-Hsin Wang, Wei-Nien Su, Hongjie Dai, and Bing-Joe Hwang. Effects of concentrated salt and resting protocol on solid electrolyte interface formation for improved cycle stability of anode-free lithium metal batteries. *ACS applied materials & interfaces*, 11(35):31962–31971, 2019.

[79] AD Pelton. The cu- na (copper-sodium) system. *Bulletin of Alloy Phase Diagrams*, 7(1):25–27, 1986.

[80] Yun-Jung Kim, Sung Hyun Kwon, Hyungjun Noh, Seongmin Yuk, Hongkyung Lee, Hyun soo Jin, Jinhong Lee, Ji-Guang Zhang, Seung Geol Lee, Hwanuk Guim, et al. Facet selectivity of cu current collector for li electrodeposition. *Energy Storage Materials*, 19:154–162, 2019.

[81] Seulki Chae, Jiyong Soon, Hyejeong Jeong, Tae jin Lee, Ji Heon Ryu, and Seung M Oh. Passivating film artificially built on lini0. 5mn1. 5o4 by molecular layer deposition of (pentafluorophenylpropyl) trimethoxysilane. *Journal of Power Sources*, 392:159–167, 2018.

[82] Lei Dong, Liu RuiXian, Jianmin Feng, CongLai Long, Guizhi Wang, Huari Kou, MengLi Zhao, L Dong, Xifei Li, and Dejun Li. Improved high-rate performance of na3v2 (po4) 3 with an atomic layer deposition-generated al2o3 layer as a cathode material for sodium-ion batteries. *Materials Letters*, 205:75–78, 2017.

[83] Andrew J Loebl, Christopher J Oldham, Christina K Devine, Bo Gong, Sarah E Atanasov, Gregory N Parsons, and Peter S Fedkiw. Solid electrolyte interphase on lithium-ion carbon nanofiber electrodes by atomic and molecular layer deposition. *Journal of The Electrochemical Society*, 160(11):A1971, 2013.

[84] Lin Chen, Justin G Connell, Anmin Nie, Zhennan Huang, Kevin R Zavadil, Kyle C Klavetter, Yifei Yuan, Soroosh Sharifi-Asl, Reza Shahbazian-Yassar, Joseph A Libera, et al. Lithium metal protected by atomic layer deposition metal oxide for high performance anodes. *Journal of Materials Chemistry A*, 5(24):12297–12309, 2017.

[85] Mingpeng Yu, Aiji Wang, Yinshu Wang, Chun Li, and Gaoquan Shi. An alumina stabilized zno–graphene anode for lithium ion batteries via atomic layer deposition. *Nanoscale*, 6(19):11419–11424, 2014.

[86] Vanchiappan Aravindan, KB Jinesh, Rajiv Ramanujam Prabhakar, Vinayak S Kale, and Srinivasan Madhavi. Atomic layer deposited (ald) sno2 anodes with exceptional cycleability for li-ion batteries. *Nano Energy*, 2(5):720–725, 2013.

[87] Hongliang Zhao, Hanxi Gao, Biqian Li, Zhifan Song, Tao Hu, and Fengqin Liu. Atomic layer deposition of v2o5 on nitrogen-doped graphene as an anode for lithium-ion batteries. *Materials Letters*, 252:215–218, 2019.

[88] Fernando A Soto, Asma Marzouk, Fedwa El-Mellouhi, and Perla B Balbuena. Understanding ionic diffusion through sei components for lithium-ion and sodium-ion batteries: Insights from first-principles calculations. *Chemistry of Materials*, 30(10):3315–3322, 2018.

[89] Lina Gao, Juner Chen, Qinlong Chen, and Xueqian Kong. The chemical evolution of solid electrolyte interface in sodium metal batteries. *Science Advances*, 8(6):eabm4606, 2022.

[90] Changyuan Bao, Bo Wang, Peng Liu, Hao Wu, Yu Zhou, Dianlong Wang, Huakun Liu, and Shixue Dou. Solid electrolyte interphases on sodium metal anodes. *Advanced Functional Materials*, 30(52):2004891, 2020.

[91] Lin Zhou, Zhen Cao, Jiao Zhang, Qujiang Sun, Yingqiang Wu, Wandi Wahyudi, Jang-Yeon Hwang, Limin Wang, Luigi Cavallo, Yang-Kook Sun, et al. Engineering sodium-ion solvation structure to stabilize sodium anodes: universal strategy for fast-charging and safer sodium-ion batteries. *Nano Letters*, 20(5):3247–3254, 2020.

[92] Dmitrii A Rakov, Fangfang Chen, Shammi A Ferdousi, Hua Li, Thushan Pathirana, Alexandr N Simonov, Patrick C Howlett, Rob Atkin, and Maria Forsyth. Engineering high-energy-density sodium battery anodes for improved cycling with superconcentrated ionic-liquid electrolytes. *Nature materials*, 19(10):1096–1101, 2020.

[93] Julian JA Kreissl, Daniel Langsdorf, Boryslav A Tkachenko, Peter R Schreiner, Jürgen Janek, and Daniel Schröder. Incorporating diamondoids as electrolyte additive in the sodium metal anode to mitigate dendrite growth. *ChemSusChem*, 13(10):2661–2670, 2020.

[94] Shiyang Wang, Yulin Jie, Zhihao Sun, Wenbin Cai, Yawei Chen, Fanyang Huang, Yang Liu, Xinpeng Li, Ruiqi Du, Ruiguo Cao, et al. An implantable artificial protective layer enables stable sodium metal anodes. *ACS Applied Energy Materials*, 3(9):8688–8694, 2020.

[95] Wei Luo and Liangbing Hu. Na metal anode:“holy grail” for room-temperature na-ion batteries?, 2015.

[96] Kang Xu. Electrolytes and interphases in li-ion batteries and beyond. *Chemical reviews*, 114(23):11503–11618, 2014.

[97] Yang Zhao, Lyudmila V Goncharova, Andrew Lushington, Qian Sun, Hossein Yadegari, Biqiong Wang, Wei Xiao, Ruying Li, and Xueliang Sun. Superior stable and long life sodium metal anodes achieved by atomic layer deposition. *Advanced materials*, 29(18):1606663, 2017.

[98] Sung Chul Jung, Hyung-Jin Kim, Jang Wook Choi, and Young-Kyu Han. Sodium ion diffusion in al2o3: A distinct perspective compared with lithium ion diffusion. *Nano letters*, 14(11):6559–6563, 2014.

[99] Bing Zhao, Bobo Li, Zhixuan Wang, Chuxiong Xu, Xiaoyu Liu, Jin Yi, Yong Jiang, Wenxian Li, Ying Li, and Jiujun Zhang. Uniform li deposition sites provided by atomic layer deposition for the dendrite-free lithium metal anode. *ACS applied materials & interfaces*, 12(17):19530–19538, 2020.

[100] Chengcheng Zhao, Xiao Yao, Hao Yang, Xiaoxia Jiao, and Lina Wang. Hierarchical porous carbon nanofibers with lithiophilic metal oxide crystalline grains for long-life li metal anodes. *Composites Communications*, 26:100789, 2021.

[101] Wan-Jing Yu, Fan Liu, Lili Zhang, Zhiyuan Liu, Sumei Wang, and Hui Tong. Lithiophilic zno confined in microscale carbon cubes as a stable host for lithium metal anodes. *Carbon*, 196:92–101, 2022.

[102] Paul JD Whiteside, Jeffrey A Chininis, and Heather K Hunt. Techniques and challenges for characterizing metal thin films with applications in photonics. *Coatings*, 6(3):35, 2016.

[103] Cheng Gong, Chunming Huang, Justin Miller, Lanxia Cheng, Yufeng Hao, David Cobden, Jiyoung Kim, Rodney S Ruoff, Robert M Wallace, Kyeongjae Cho, et al. Metal contacts on physical vapor deposited monolayer mos2. *ACS nano*, 7(12):11350–11357, 2013.

[104] Barbara Putz, C May-Miller, Volker Matl, Bernhard Völker, DM Többens, Christopher Semprimoschnig, and MJ Cordill. Two-stage cracking of metallic bi-layers on polymer substrates under tension. *Scripta Materialia*, 145:5–8, 2018.

[105] M Seipenbusch and A Binder. Structural stabilization of metal nanoparticles by chemical vapor deposition-applied silica coatings. *The Journal of Physical Chemistry C*, 113(48):20606–20610, 2009.

[106] Heeyeon Kim and Sang Heup Moon. Chemical vapor deposition of highly dispersed pt nanoparticles on multi-walled carbon nanotubes for use as fuel-cell electrodes. *Carbon*, 49(4):1491–1501, 2011.

[107] Yingjiu Zhang, Qi Zhang, Yubao Li, Nanglin Wang, and Jing Zhu. Coating of carbon nanotubes with tungsten by physical vapor deposition. *Solid state communications*, 115(1):51–55, 2000.

[108] Junling Lu, Jeffrey W Elam, and Peter C Stair. Synthesis and stabilization of supported metal catalysts by atomic layer deposition. *Accounts of chemical research*, 46(8):1806–1815, 2013.

[109] Titta Aaltonen, Mikko Ritala, Timo Sajavaara, Juhani Keinonen, and Markku Leskelä. Atomic layer deposition of platinum thin films. *Chemistry of materials*, 15(9):1924–1928, 2003.

[110] Emil Roduner. Understanding catalysis. *Chemical Society Reviews*, 43(24):8226–8239, 2014.

[111] Ermanno Filippi and Cristina Pizzolitto. The past and the future of catalysis and technology in industry: a perspective from casale sa point of view. *Catalysis Today*, 387:9–11, 2022.

[112] Xiao Jiang, Xiaowa Nie, Xinwen Guo, Chunshan Song, and Jingguang G Chen. Recent advances in carbon dioxide hydrogenation to methanol via heterogeneous catalysis. *Chemical reviews*, 120(15):7984–8034, 2020.

[113] Bo You and Yujie Sun. Innovative strategies for electrocatalytic water splitting. *Accounts of chemical research*, 51(7):1571–1580, 2018.

[114] Christian Berggren and Thomas Magnusson. Reducing automotive emissions—the potentials of combustion engine technologies and the power of policy. *Energy Policy*, 41:636–643, 2012.

[115] Volodymyr A Yartys, Mykhaylo V Lototskyy, Vladimir Linkov, Sivakumar Pasupathi, Moegamat Wafeeq Davids, Ivan Tolj, Gojmir Radica, Roman V Denys, Jon Eriksen, Klaus Taube, et al. Hydride4mobility: an eu horizon 2020 project on hydrogen powered fuel cell utility vehicles using metal hydrides in hydrogen storage and refuelling systems. *international journal of hydrogen energy*, 46(72):35896–35909, 2021.

[116] MA Aminudin, SK Kamarudin, BH Lim, EH Majilan, MS Masdar, and N Shaari. An overview: Current progress on hydrogen fuel cell vehicles. *International Journal of Hydrogen Energy*, 48(11):4371–4388, 2023.

[117] Bruno G Pollet, Iain Staffell, and Jin Lei Shang. Current status of hybrid, battery and fuel cell electric vehicles: From electrochemistry to market prospects. *Electrochimica Acta*, 84:235–249, 2012.

[118] Mohammad Hossein Ahmadi, Amin Mohammadi, Fathollah Pourfayaz, Mehdi Mehrpooya, Mokhtar Bidi, Antonio Valero, and Sergio Uson. Thermodynamic analysis and optimization of a waste heat recovery system for proton exchange membrane fuel cell using transcritical carbon dioxide cycle and cold energy of liquefied natural gas. *Journal of Natural Gas Science and Engineering*, 34:428–438, 2016.

[119] Mahmood Chahartaghi and Behrad Alizadeh Kharkeshi. Performance analysis of a combined cooling, heating and power system with pem fuel cell as a prime mover. *Applied Thermal Engineering*, 128:805–817, 2018.

[120] Zhi Qiao, Chenyu Wang, Yachao Zeng, Jacob S Spendelow, and Gang Wu. Advanced nanocarbons for enhanced performance and durability of platinum catalysts in proton exchange membrane fuel cells. *Small*, 17(48):2006805, 2021.

[121] Yi Yu, Zhengkai Tu, Haining Zhang, Zhigang Zhan, and Mu Pan. Comparison of degradation behaviors for open-ended and closed proton exchange membrane fuel cells during startup and shutdown cycles. *Journal of Power Sources*, 196(11):5077–5083, 2011.

[122] Zhongxin Song, Mohammad Norouzi Banis, Hanshuo Liu, Lei Zhang, Yang Zhao, Junjie Li, Kieran Doyle-Davis, Ruying Li, Shanna Knights, Siyu Ye, et al. Ultralow loading and high-performing pt catalyst for a polymer electrolyte membrane fuel cell anode achieved by atomic layer deposition. *ACS Catalysis*, 9(6):5365–5374, 2019.

[123] Dustin Banham and Siyu Ye. Current status and future development of catalyst materials and catalyst layers for proton exchange membrane fuel cells: an industrial perspective. *ACS Energy Letters*, 2(3):629–638, 2017.

[124] Liang Su, Wenzhao Jia, Chang-Ming Li, and Yu Lei. Mechanisms for enhanced performance of platinum-based electrocatalysts in proton exchange membrane fuel cells. *ChemSusChem*, 7(2):361–378, 2014.

[125] Alfredo Ursua, Luis M Gandia, and Pablo Sanchis. Hydrogen production from water electrolysis: current status and future trends. *Proceedings of the IEEE*, 100(2):410–426, 2011.

[126] Armin Laube, André Hofer, Simon Ressel, Antonio Chica, Julien Bachmann, and Thorsten Struckmann. Pem water electrolysis cells with catalyst coating by atomic layer deposition. *international journal of hydrogen energy*, 46(79):38972–38982, 2021.

[127] Maximilian Bernt, Alexandra Hartig-Weiß, Mohammad Fathi Tovini, Hany A El-Sayed, Carina Schramm, Jonas Schröter, Christian Gebauer, and Hubert A Gasteiger. Current challenges in catalyst development for pem water electrolyzers. *Chemie Ingenieur Technik*, 92(1-2):31–39, 2020.

Chapter 3

Materials and methodology

In this work, coating, characterisation and testing of MVD thin films has been performed using a number of different techniques, which are detailed in the following section

3.1 materials and preparation

3.1.1 Coin cell parts

Coin cells were source from Cambridge energy solutions- cell sets included; male and female outer casing, cone spring and 0.5mm spacers which were made from stainless steel 316L (these can be seen in figure 3.2. The parts were all sonicated for 30 minutes in acetone, then 30 mins in IPA and then 30 mins DI water. These were then left to dry in a vacuum Oven at $70^{o}C$ for 24 hours before being transferred to the glovebox environment and then stored under a dry argon atmosphere.

3.1.2 Copper foil

Copper foil was cleaned with acetone, IPA, methanol and DI water using dry particle free tissues. The Copper foil was then cut into circular electrodes using a precision disk cutter (MTI corporations). The electrodes were then left in an Oven to dry at $70^{o}C$ for 24 hours. Samples were then transported to the glove box for assembly into coin cells. This solvent cleaning method is similar to other research groups [1].

3.1.3 Celgard separator

Celgard separator (25 micron thickness by Pi- KEM limited) were cleaned with IPA, methanol then DI water, using dry particle free tissues. They were then cut using a precision cutter and placed into a vacuum oven at $70^{o}C$ for 24 hours before being transferred to the glovebox environment and then stored under a dry argon atmosphere.

3.1.4 Sodium preparation

Sodium was obtained from sigma Sigma Aldrich - The sodium came stored in an oil based substance. Before testing the oil was removed with a hexane wash and then stored in a separate basin of fresh hexane ($<$10ppm water measured by karl fisher titration see section 3.1.7) in preparation for testing. This was all performed inside an argon filled glovebox. Before testing, sodium metal was mechanically sheared to remove any surface contamination and oxidation before being incorporated into cells.

3.1.5 Lithium preparation

Lithium was obtained from Sigma Aldrich. The lithium came as precut discs stored under argon. Discs were further punched to the correct size before the surface was mechanically sheered to remove any surface contamination and thereforee expose fresh lithium.

3.1.6 Making the electrolyte

Throughout this work, the electrolyte utilized was 1M Sodium hexafluorophosphate ($NaPF_6$) (99.99% PURATREM Strem chemicals), dissolved in ethylene glycol dimethyl ether (Diglyme) (Sigma Aldrich), and the measured water content was $<$10ppm by (measured by Karl fisher titration see section 3.1.7 for details on this). Diglyme was selected as a solvent due to its comparable ionic conductivity to commonly used carbonate-based electrolytes, as demonstrated by Seh *et al.* This group compared $NaPF_6$ in glyme-based electrolytes to $NaPF_6$ in carbonate-based electrolytes [2]. Not only does Diglyme outperform alternative solvents in plating and stripping systems, but it also offers advantages such as a higher thermal stability, lower flammability, and reduced volatility, making it a promising candidate for next-generation batteries [2]. $NaPF_6$ was chosen as the salt due to its superior solvation properties, storage kinetics, and safety advantages compared to other commonly used salts like $NaClO_4$. This superiority stems from the weak interactions between Na^+ cations and $PF6^-$ anions, rendering it one of the most promising candidates for the industrialization of sodium-ion batteries [3].

For the lithium anode free cells (chapter 4), Lithium bis(trifluoromethanesulfonyl)imide (LiTFSI) salt was obtained from Sigma aldrich and made up to 1M in Dimethyl carbonate (DOL)/ Dimethoxyethane (DME) with a 1:1 ratio of each which is a typical electrolyte in this field [4]. 5% lithium nitrate $LiNO_3$ was added to improve the SEI and cycling performance which is typical for lithium metal based batteries in this cofiguration [5].

The salts were initially dried using a shlenk line connected to a hotplate at 150^oC for 24 hours before being transferred to an argon filled glovebox with $<$1ppm water, The solvent was further left to dry overnight by adding molecular sieves. Solvent water content was measured using Karl fisher titration, if the water content was $<$10ppm this was deemed acceptable to begin mixing. The Salt and solvent were subsequently added together using equation 3.1 to calculate the correct molarity. Where M is the desired molarity, V is the volume of solvent, m is the mass of salt and Mr is the molar mass of the salt. The mixture was left on a hotplate at 100^oC for 24 hours whilst being agitated by a magnetic stirrer to ensure complete mixing. Karl fisher titration was performed on the resulting solution and water content $<$10ppm was considered an acceptable level which could be used. Molecular sieves were then Incorporated into the Electrolyte to ensure any remaining water was removed.

$$M = \frac{m.1000}{V.Mr} \tag{3.1}$$

3.1.7 Karl fisher titration

Karl Fisher titration is a well know technique for determining the moisture content of liquids. the process works by the reaction of iodine with water. The amount of water present can be calculated when the uptake of iodine stops. Two methods for determination of water content in ppm include the volumetric and coulometric methods. The tool used was a C10S Coulometric KF Titrator by Mettler Toledo and works by Coulometric

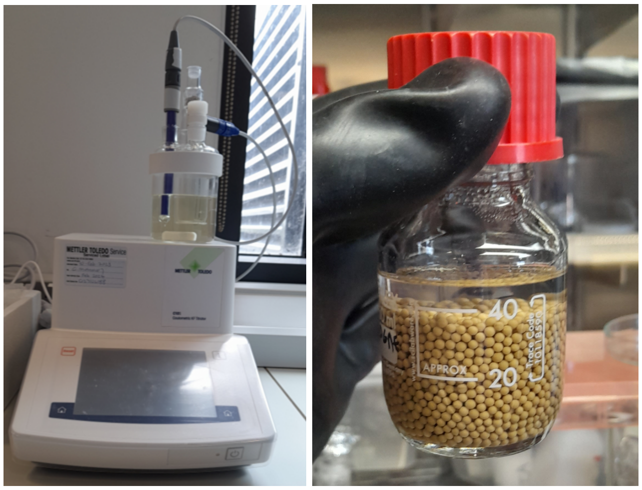

Figure 3.1: Image (left) showing Karl Fisher titration setup used to determine water content of the electrolyte. Image (right) shows electrolyte with molecular sieves in container.

titration [6]. Figure 3.1 left shows the Karl fisher used shows right highlights the electrolyte with molecular sieves.

3.2 Battery section

3.2.1 coin cells assembly

Significant time was spent manufacturing coin cells for insitu testing of materials. The coin cells of interest were a 2032 stainless steel set which consisted of a male and female casing, cone spring, 3 x 0.5mm spacers, the sample electrode, a celgard separator and a counter electrode. The manufacturing process involves several steps and different pieces of equipment. The schematic for coin cell manufacture can be seen in figure 3.2. The most common type of cell used was the (copper- sodium/lithium) half cell, but cell format can vary slightly depending on the experiment.

To make the cell, a cube of sodium is removed from oil and washed in a solution of dry hexane and shaved using a razor to remove any oxide contamination. It is then rolled from a cube into a flat sheet using a syringe plunger and cut into a disk of desired shape using a leather punch. It is then placed on the female case. after this, 60 microlitres of dry electrolyte were placed on the sodium using a pipette. The cut

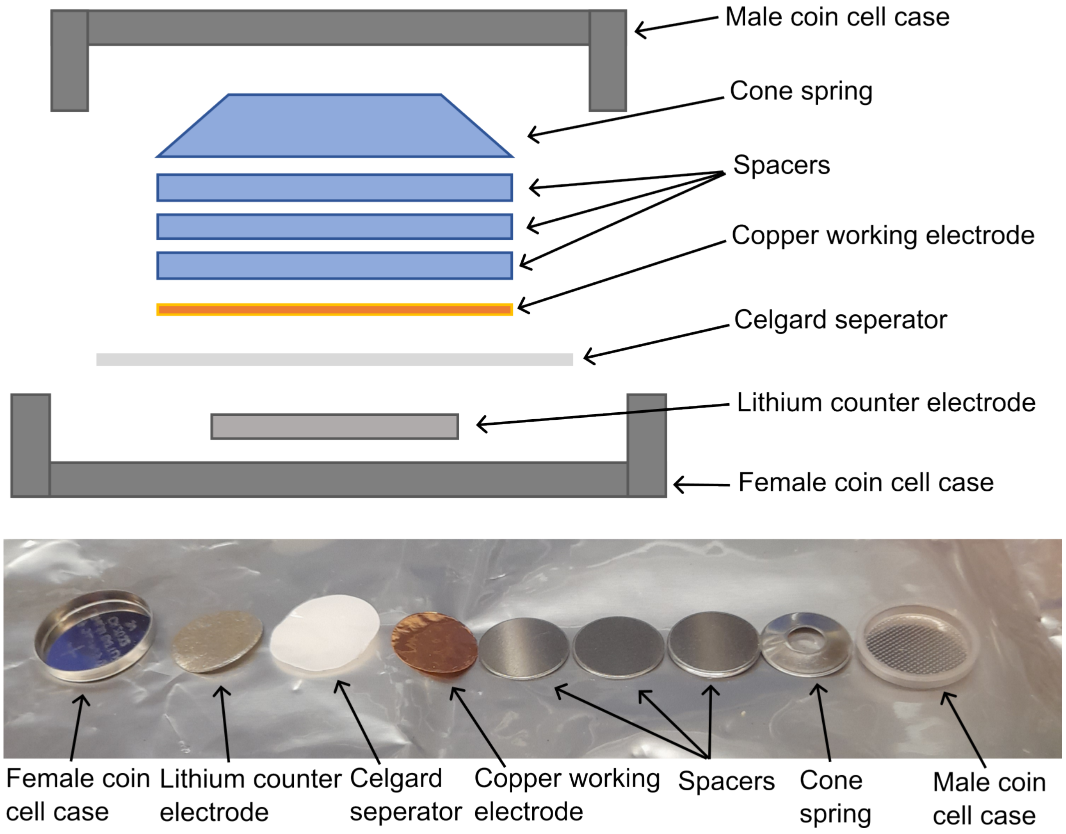

Figure 3.2: Diagram showing schematic representation of the coin cell format used throughout this thesis vs the real components layed out ready to be assembled

celgard separator was then placed on the sodium and consequently wetted with electrolyte. 60 microlitres of dry electrolyte were placed ontop of the separator. The working electrode is now placed on the celgard using tweezers. Three 0.5mm spacers were then stacked ontop of the spacers using a suction tool from RS components. A cone spring was then mounted on the spacers using tweezers. Once all the parts were in place, the male coin cell case was slotted to complete the cell layout. The cell is now placed in a manual coin cell press and crimped together with a force of $70kg/cm^2$. Cells were then removed from glovebox cleaned, then labelled, then left to rest for 24 hours to ensure the separator is adequately soaked in electrolyte before electrochemical testing.

3.2.2 Molten lithium infusion into ZnO coated carbon electrodes

Carbon scaffolds used for chapter 5 were sourced from HCP030N, Shanghai Hessen Electrical Co, LTD inspired by the following research undertaken by Zhao et al. 2030 coin cells used in this thesis were also used by the group so it was assumed current collectors would be mechanically robust enough to withstand cycling conditions [7].

The electrodes were infused with lithium before they were cycled. This was done by melting lithium metal onto a sheet of Teflon and increasing the temperature to 200^oC which is above the melting point of lithium at 181^oC. The electrodes were then simply placed onto the molten liquid and were left for the required amount of time for them to appear soaked with lithium. The lithiated electrodes were then removed from the molten mass and allowed to cool. They were then incorporated directly into a coin cell vs a lithium counter electrode for testing.

3.3 electrochemical testing methods and equipment

3.3.1 Redox reactions

The term redox stands for reduction-oxidation and refers to the process of electron transfer between two electrochemically dissimilar materials. A redox reaction between two materials will only occur if certain conditions are met. These can be determined by equation 3.2 which represent the Gibbs free energy equation where n is the number of moles, F is the Faraday constant and Ecell is the equilibrium cell voltage. If the value for delta G is positive, the desired reaction is thermodynamically unfavorable as the constituents are very stable so will not occur spontaneously. In order to get a reaction that is not spontaneous to occur, electrical current has to be supplied at the equilibrium cell voltage. On the contrary if delta G is negative the reaction is thermodynamically favourable therefore will occur spontaneously producing electrical current at the equilibrium potential.

$$\Delta G = -n.F.Ecell \tag{3.2}$$

The equilibrium potential represents the potential difference at which the electrochemical reaction reaches steady state. The equilibrium potential can be determined by subtracting the equilibrium potential of the cathode from that at the anode as seen in equation 3.3. For simplicity these values can be gathered from a standard electrode potentials database for the desired reaction vs the standard hydrogen electrode. These values however only take into account the potential at standard conditions which are performed at $25^{o}C$, 1 atmosphere pressure and 1M concentration of aqueous species. To calculate the equilibrium potential for your specific scenario, standard conditions are not always applicable [8].

$$Ecell = Ecathode - Eanode \tag{3.3}$$

$$pP + qQ + ne^{-} <=> xX + yY \tag{3.4}$$

$$E = E + \frac{2.3RT}{nF}.log\frac{(aP)^{p}.(aQ)^{q}}{(aX)^{x}(aY)^{y}} \tag{3.5}$$

To account for the potential variation in these conditions, equation 3.5 can be used, this is known as the Nernst equation. for the system highlighted in equation 3.4. R represents the molar gas constant, T represents the temperature of the system, n represents the valence of the ion, and F is the Faraday constant which is the charge carried by 1 mole of electrons. The Faraday constant has a value of 96485 coulombs per mole. aP,aQ,aX,aY represent the concentrations of the components in the reaction assuming the activity of each ion component equals one [8].

3.3.2 Chronopotentiometry

Chronopotentiometry, also known as galvanostatic charge-discharge, is a common technique used to repeatedly cycle coin cells. It works by applying a constant current to either the cathode or the anode electrodes of the cell, for a set period of time at a set charge rating. The current can then be reversed which forces the electrochemical reaction in the opposite direction thus reversing the reaction.

For this thesis all potentiometry experiments were conducted in 2032 coin cells. The current density J was calculated by equation 3.6 where I is the current in milliamps and A is the area of the counter electrode in cm^2.

$$J = \frac{I}{A} \tag{3.6}$$

To calculate the capacity, this equation can be further extended to equation 3.7 where t is the time in hours. X represents the capacity of plated active mass which is given in mAh/cm^2.

$$X = \frac{It}{A} \tag{3.7}$$

Typical potentiometry recipes consist of several parameters that need to be explained. The recipe consists of a cutoff potential which if reached will immediately start the next part of the recipe, both charge and discharge cycles have a cutoff voltage which is primarily present for safety and to prevent exceeding the operating potential window of the electrolyte (to prevent reduction and oxidation of this medium). As well as this, it is sometimes necessary to incorporate pause steps into the process to ensure conditions of the cell are kept as consistent as possible [8].

By collecting data this way an important parameter can be determined which is the Coulombic efficiency (CE). The CE is the ratio of charge applied during electrostripping of the active material (lithium or sodium) vs charge applied to electroplate material onto the electrode and is represented by equation 3.8. CE gives an indication of how efficient each battery cycle is during its life, a value of 100% would indicate a fully efficient charge/discharge process where all reduced material is subsequently oxidised. A CE lower then 100% could indicate parasitic reactions inside the cell are occuring, causing some of the active mass inside the cell to belost by forming irreversible compounds [9]. The current applied (a) and voltage response (b) can be seen in figure 3.3.

$$CE(\%) = \frac{Qdischarge}{Qcharge}.100 \tag{3.8}$$

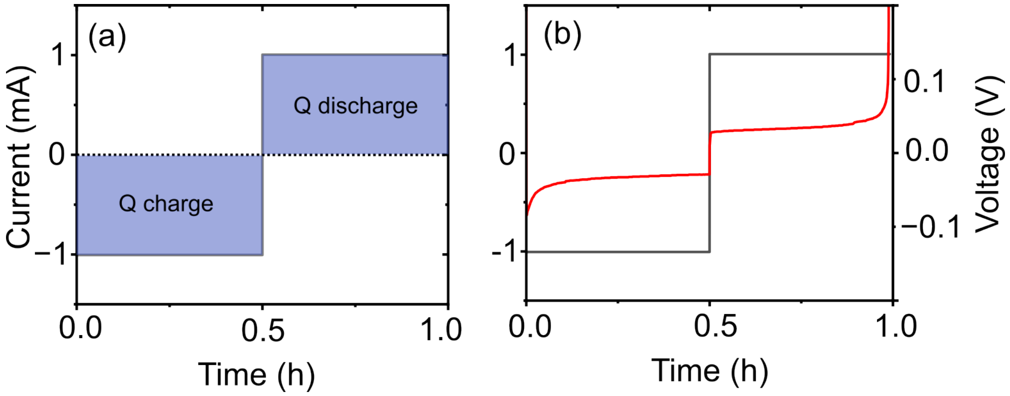

Figure 3.3: Graph showing show CE is calculated. (a) represents the constant application of current. (b) represents how the voltage response varys with time when the current is kept constant

As well as the CE the nucleation overpotential is an important parameter to be considered when testing cells. As defined by Zhang *et al* the Li/Na-metal nucleation overpotential is defined as the differnece between the bottom of the potential and the flat potential plateau, which reflects the metal nucleation barrier [10, 11, 12]. The value of the nucleation overpotential can give insight into the size and shape of the nuclei and can therefore ultimately affect the growth electrodeposition as suggested by Pei *et al* [13]. Figure 3.4 (a) site 1 highlights the metals nucleation overpotential region whilst site 2 highlights the growth region whereby the existing nuclei grow [13].

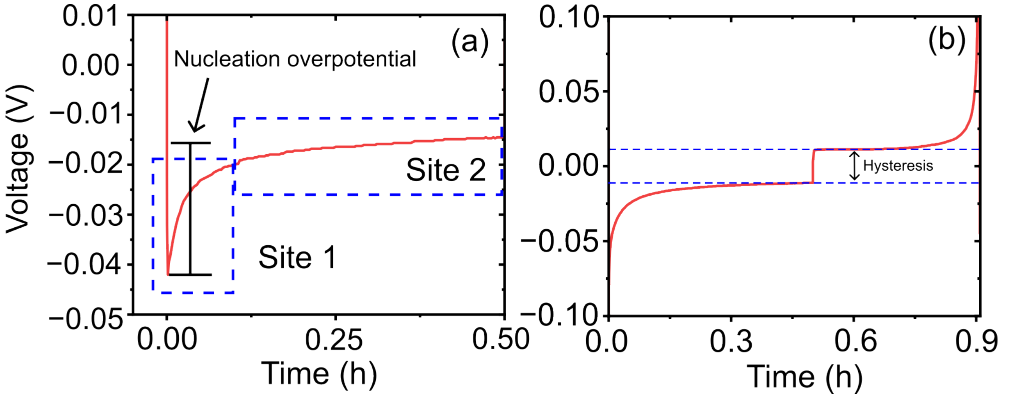

Figure 3.4: Graph showing an example (a) the nucleation overpotential and (b) the hysteresis

The hysteresis is also an important parameter when analysing battery data. Whilst hysteresis is not a common phenomena explored in eletrochemistry, it can give essential information to characterise battery cell cycling and arises due to insitu processes within the cell including sluggish kinetic processes (polarization) which represents the restriction of ion movement during cycling highlighted by van der ven *et al* [14]. For this work the hysteresis is defined as the voltage differnece between the growth overpotential of electrodeposition and electrostripping which is commonly employed in current research [2]. For this thesis, the value is determined using a novel python code (appendix section 8.5). Figure 3.4 (b).

All potentiometry experiments were conducted on a Basytec CTS LAB multichannel potentiostat as the multiple channels on this tool allowed for simultaneous testing of different cells. This particular system has an operating voltage up to 6V and 3A which is suitable for coin cell testing. The tool has a precision of 200nA when a cycling current of 1ma is applied. The Basytec is installed in conjunction with an environmental chamber in which the cells are placed, the chamber is maintained at 30 degrees celsius to make the temperature independent.

3.3.3 Cyclic Voltametry

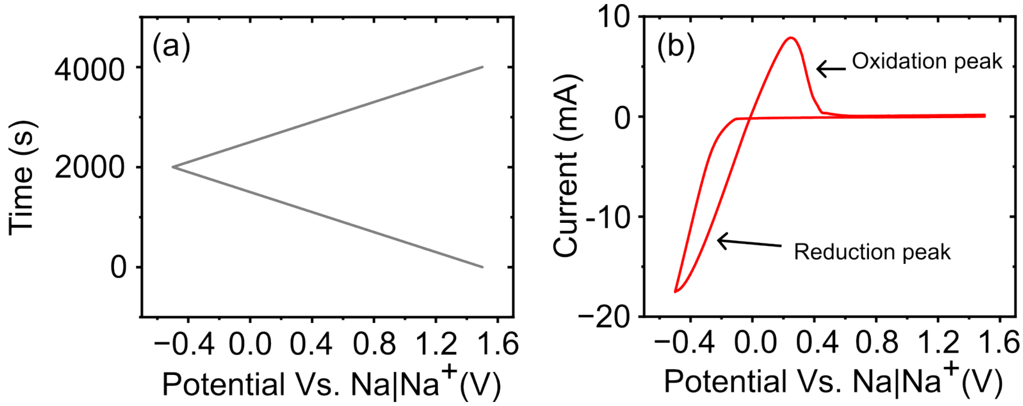

Figure 3.5: Cyclic voltamograms including (a) the linear potential sweep with time (b) the current response to the potential sweep of Na plating on the Cu electrode

Unlike potentiometry, Cyclic voltametry is a technique where a potential window is scanned at a specific rate highlighted by the user and the current response is measured. The purpose of this technique is to identify components of the oxidation and reduction reactions as well as the kinetics within the system. For redox processes that are typically present in secondary battery cells, reduction processes are found at the working electrode during the charging cycle which is signified by a peak in the negative sweep. Oxidation occurs on the discharge cycle which is signified by a peak on the positive sweep. Figure 3.5 (a) displays the voltage sweep whilst (b) highlights the current response.

Throughout this thesis both two electrode and three electrode cyclic voltametry are employed. 3 electrode measurements were performed using a sodium reference electrode and a glass fibre separator using an ECC-ref system (EL-CELL), whilst 2 electrodes were performed using the standard 2032 coin cells (Cambridge energy solutions) with the solid sodium counter electrode also acting as a reference electrode. The potential window and scan rates were set depending on the components of the cell. Cyclic voltametry was performed on an Ivium multistat.

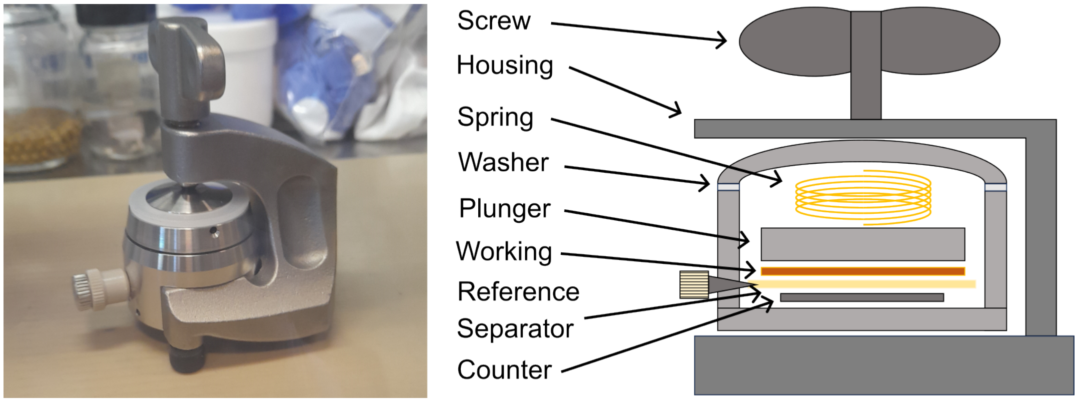

Figure 3.6: 3 electrode EL- cell used with a schematic highlighting the components of the cell

3.3.4 Platinum catalysis experiments propene oxidation

For propene oxidation experiments (chapter 7) ceramic monoliths supplied by Cardiff univerisity (consisting of cordierite with an aluminium washcoat) were tested for total propene oxidation using a gas mixture of 200 ppm of propene in air at a flow rate of 1.7 L/min. These are particularly harsh conditions and industrially relevant. Experiments were repeated 3 times. Further experiments were performed with a monolith that was reduced before testing. Propene oxidation was performed using a heat treatment at 500 C under a flow of 5% H_2/Ar gas mixture for 4 hours.

Figure 3.7: Image showing the MVD 300 by KLA and the exposed chamber in which the deposition takes place (right)

3.4 Coatings materials and methods

Molecular vapor deposition 300 (MVD 300)

The molecular vapor deposition (MVD 300) system is a deposition tool supplied by KLA corporations. The tool has the potential to do both ALD and MLD coatings as well as hybrid organic metallic films. Unlike many similar tools, the MVD has a large reaction chamber that is easy to access making it a potential candidate for batch production which is important in industries such as semiconductor processing where coatings for silicon wafers need to have a high throughput to meet consumer demand. The tool has 4 precursor delivery lines making it suitable for stacked film deposition as well as complex coatings that would require multiple precursors. Another feature of the MVD 300 is the remote plasma source that sits on-top of the chamber expanding the applications of the tool into plasma enhanced processing. Figure 3.7 (right) shows the MVD 300 tool, (left) shows the reaction chamber.

As process parameters are an important part of optimisation, the detailed working principles for a two stage ALD process will be highlighted here. Figure 3.8 shows an operational schematic showing the relevant pieces of hardware involved in the deposition process which will be refereced to in this section. The process works by evaporation of precursor materials from their constituent precursor ampules. In order to get the desired rate of evaporation, the ampules are covered by heating jackets with a thermocouple feedback system. This allows the temperature to be increased and decreased to regulate the rate of evaporation from the ampules depending on the application. As well as temperature, the rate of gas transfer can be controlled by implementation of an orifice restrictor into the cavity fill valve. The gaseous precursors then enters the vapor collection cavity through the cavity fill valve. The pressure inside the vapor collection cavity can be varied by a feedback system controlled by a manometer. This allows for control of the amount of precursor to be dosed into the chamber per cycle. Controlling precursor dosing is important, too little precursor being dosed would prevent all active sites in the chamber from being occupied affecting film quality. However too much precursor dosing could lead to an excess of precursor which would be wasted. Once the desired pressure of precursor has been reached in the vapor collection cavity, the cavity fill valve is closed and the vapor delivery valve is then opened dosing the chamber with its constituents. Once the vapor collection cavity reaches a pressure low point, the vapor delivery valve closes. The reaction time of the precursor inside the chamber can be varied. Because the process is determined by the kinetic movement of precursor molecules making contact with surface hydroxyl groups, it is important to allow enough time for all active sites to react with the dosed gas. Overly long reaction times can add time to the already long process as well as damage sensitive parts of the tool such as the manometers. This kinetic movement can also be controlled by temperature. The temperature of the VDM, chamber walls and door can be set by the user in the range of 35^oC to 150^oC. Whilst increasing the temperature can increase reaction kinetics, it also increase the energy consumption of the process and can damage temperature sensitive processes. Once the reaction is complete, any leftover precursor and bi products are purged from the chamber using Nitrogen gas. The processes highlighted can now be repeated with the second precursor to complete the fabrication of one mono layer of the deposited film. The process cycles described can be repeated to create a film of the desired thickness.

3.4.1 Methodology Al_2O_3 coatings

Aluminium oxide (Al_2O_3) is one of the materials being coated onto samples by the MVD. Although many prexursors exist for this material, the coating is applied by cycling precursor gases Tri methyl aluminium (TMA) (pegasus chemicals) and DI water by ligand exchange reaction in a thermal deposition mode. Whilst there are many factors that affect the quality of the material, the recipe being used was optimised by Burwell *et al* [15]. The chamber and door temperatures were set to 100^oC, the reaction time was set to 1 second, the VDM temperature and ampule temperatures were set to 100^oC and 50^oC respectively. The TMA dose

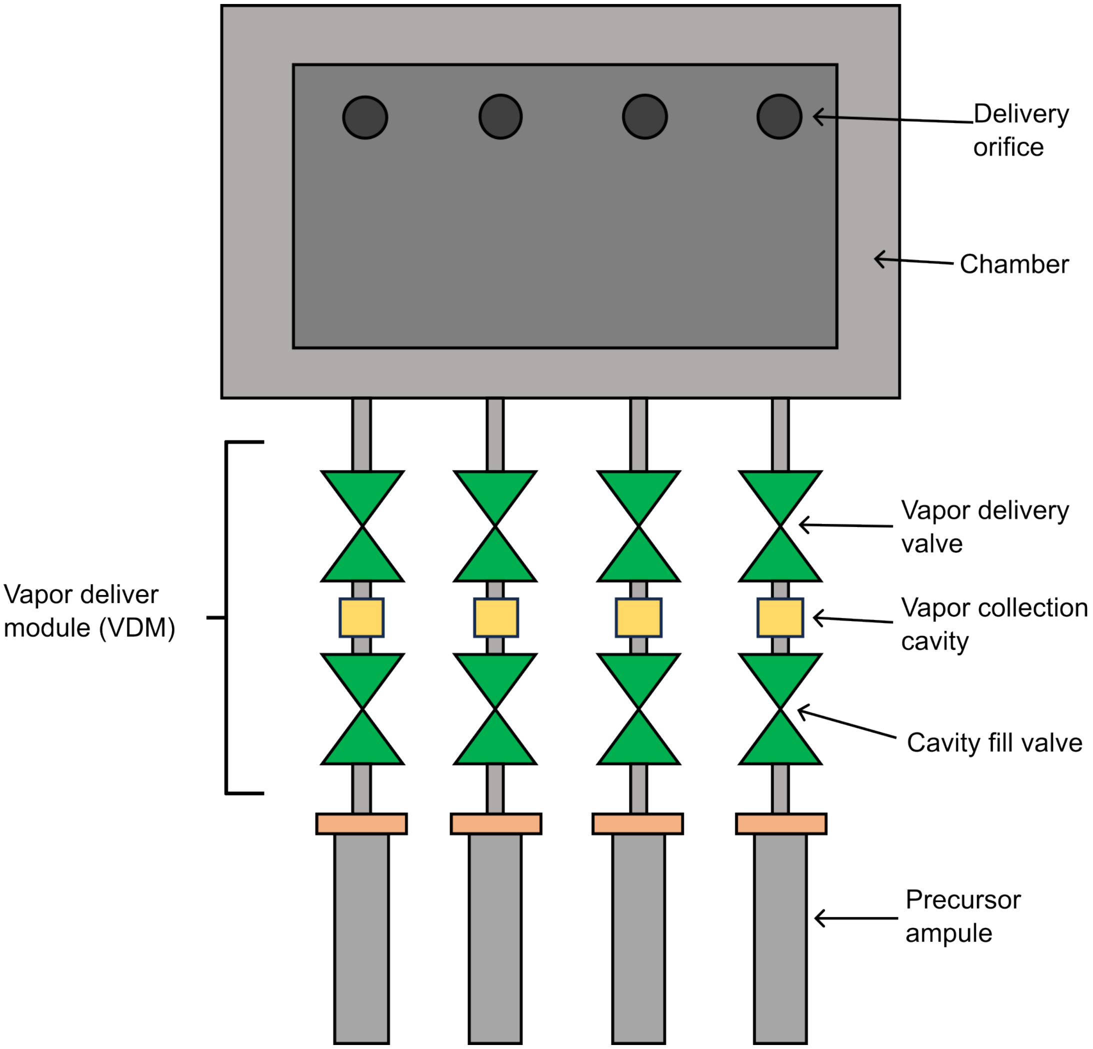

Figure 3.8: Schematic highlighting the different working parts of the MVD vapor delivery system

VDM pressure was 1.3 torr whilst water was 1.0 torr per cycle. The recipe was kept constant for all runs to keep this experimental variable independent. The growth per cycle (gpc) for this material was around 1.1 angstroms per cycle [15].

Several factors need to be considered when optimizing MVD coatings for specific applications. Firstly, surface hydroxyl active sites must be saturated by dosing the correct amount of precursor into the chamber for each cycle. This can be increased or decreased by changing the VDM pressure before opening the delivery valves in figure 3.8. This factor is very dependent on the total surface area of the substrate inside the chamber. If active sites are not fully saturated, the film can be defective containing pin holes. On the contrary, too much dosing can lead to trapped precursor molecules in the film. As well as precursor dosing, optimizing the temperature of deposition is also important. As well as considering the temperature tolerance of the sample, this variable can affect the thickness uniformity of the films across the surface of the substrate.[15]

3.4.2 Methodology ZnO coatings

For Zinc oxide coatings the precursors diethyl zinc (DEZ) (Pegasus chemicals) and water were cycled sequentially to grow zinc oxide epitaxially via a ligand exchange reaction. The recipe used includes; chamber and door temperatures set to 125^oC, the precursor reaction time set to 1 second, the VDM temperature was set to 125^oC and the ampule temperature was set to 35^oC. This recipe was kept constant for all runs. The precursor dose of DEZ was set to 1.4 torr and the water dose was set to 1.4 torr. Whilst results varied slightly, the GPC of ZnO deposition was around 2.1 Angstrom per cycle. This process, previously optimised by Rejnhard *et al*, was used in this work[16].

3.4.3 Methodology Pt coatings

For platinum metal deposition the precursors used were $MeCpPtMe_3$ (pegasus chemicals) with an oxygen plamsa step, the process works by combining a ligand exchange reaction and a subsequent combustion step. The recipe used includes; chamber and door temperature set to 150^oC, ampule temperature set to 65^oC. Plasma composition 1000 sccm O^2/5000 sccm Ar with a power of 2700 watts, the plasma exposure time was 10 seconds per step. The dose of $MeCpPtMe^3$ was 0.5 torr per cycle [16].

3.4.4 Thickness calculation

The coating of Al_2O_3 is epitaxial so occurs one atomic layer at a time time. Each complete MVD Al_2O_3 cycle coats roughly 1.1 angstrom of material, this is known as the growth per cycle. The thicknesses of the coating can be predicted from this. In practice, the GPC does vary very slightly so the value from the previous run is used to estimate the number of cycles required for the next run. As an example, if a 5nm coating is desired 45 MVD Al_2O_3 cycles need to be performed to obtain the desired film thickness.

Due to this variation, the estimated GPC was calculated from the thickness of the previous run by ellipsometry and analysed using the Cauchy model for transparent thin films [17]. With every run a piece of Si wafer was placed inside the chamber in order to perform accurate ellipsometry measurements on. A 1 point measurement was performed and Cauchy model fitted. The GPC was calculated using equation 3.9 where T= thickness of the film and N = the number of MVD cycles. The thickness was then adjusted to the new desired value (Tn) and the equation was rearranged as seen in equation 3.10 to find the new number of cycles. GPC = Growth per cycle, Tn = new desired thickness.

$$GPC = \frac{T}{N} \tag{3.9}$$

$$N = \frac{GPC}{Tn} \tag{3.10}$$

3.4.5 Kurt J Lesker physical vapour deposition (PVD) 75 system

The process of DC sputtering works by application of high voltage between a target material (cathode) and a sample (anode) which creates a strong electric field. Argon gas is then injected into the chamber and then ionized by the the electric field. These ions are then accelerated at high speed towards the target material resulting in the ejection of target atoms. These target atoms travel a random path to coat the walls of the chamber as well as the sample [18].

A Kurt J Lesker PVD 75 was used for this research to coat a piece of silicon with copper metal to determine the growth rate of Aluminum oxide on copper. Parameters to coat copper include using a 30 watt plasma with an Argon flow rate of 100 cubic centimeters per minute. The amount of deposited copper was determined by the SEM cross sectional imaging. Figure 3.9 shows a schematic image of the PVD process.

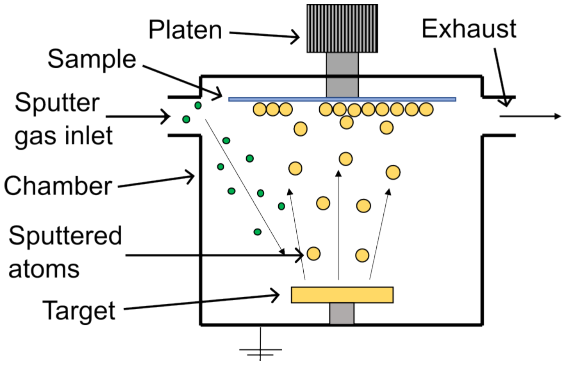

Figure 3.9: Schematic highlighting the components of the Kurt J Lesker PVD system

3.5 characterisation

3.5.1 Spectroscopic ellipsometry

Ellipsometry works by directing monochromatic light at the desired target material to be analysed, once this light reaches the target it is either reflected, transmitted, absorbed, or scattered depending on the optical properties of the material. This incident light then undergoes a change in Phase and Amplitude upon contact with the sample which is dependent on the thickness of the material being studied as well as the optical constants of the film. The output beam is then detected by the optical detector which can measure the phase and amplitude change. This change can be compared to relevant pre-programmed models of the corresponding material and an accurate calculation of the thickness of the material down to a few angstroms and up to micrometre can be determined. As well as this, ellipsometry can be used to gather other key data such as the Refractive index and the dielectric function tensor of materials. This allow the user to determine the quality of the materials analysed as well as the thickness [19].

Throughout the course of this work a J A Woolam M-2000 ellipsometer figure 3.10 (right) was used to identify the thickness of the substrates being coated by the MVD. To do this, an uncoated piece of Silicon wafer was premeasured to obtain thickness information about the native oxide layer on its surface. It was then placed into the MVD with the batch of samples to be processed and subsequently coated with the same thickness of coating as the sample material, for this thesis Al_2O_3 and ZnO were characterised using this method. A Cauchy optical model for transparent films was fitted to obtain the value for thickness.

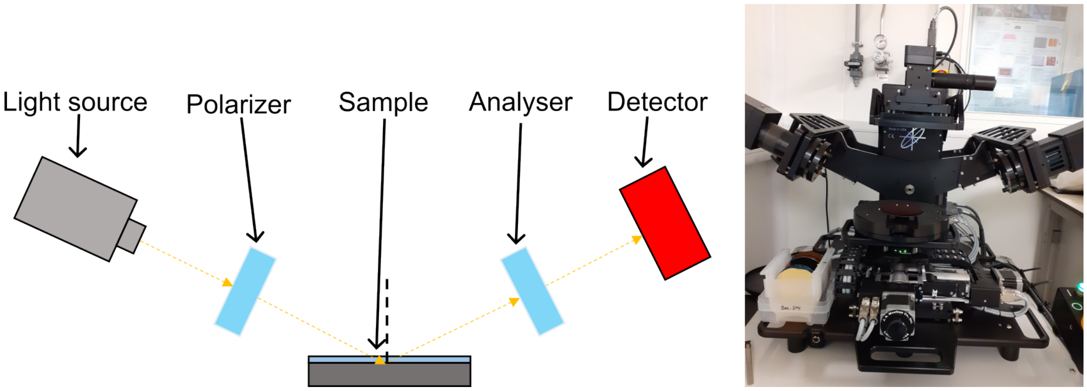

Figure 3.10: Schematic highlighting the components of a spectroscopic ellipsometer (left) image of the J.A. Woolam M-2000 ellipsometer (right)

3.5.2 X-ray photoelectron spectroscopy (XPS)

X-ray photoelectron spectroscopy (XPS) is both a quantitative and qualitative analysis technique used to obtain detailed information about the surface of a material up to a 10nm depth. However this value can vary depending on the specific type of machine. XPS can provide in depth information regarding the types of atoms present in a bulk compound as well as what those atoms are bonded to, which gives an indication of their chemical constituents. The technique can detect all atoms with the exception of hydrogen and helium due to only having 1 molecular orbital. XPS works by the photoelectric effect whereby a high frequency x-ray is emitted from a source and is focused onto the surface of the material to be analysed. The X-rays then excite electrons within the atoms of the materials. If the electron receives sufficient energy, it has the potential to be liberated from its valence band (K-shell) within the atom and becomes a photoelectron. The ejected photo electrons are randomly scattered around the chamber, some of which travel into the detector analyser where they are separated and quantified by their binding energy and kinetic energy which is characteristic of the material. Many other characteristics such as the formation of satellite peaks, multiple splitting and Auger lines can be used to identify chemical states within the bulk material [20].

For this thesis a Kratos Axis Supra XPS was utilised. Wide scan and high resolution spectra was obtained and processed in CASA XPS. All samples were coupled with a charge neutraliser to prevent sample charging and any charge corrections were performed with respect to carbon 1s where possible. For the depth profile study an argon etch gun set at 5KeV Ar^+ was used to remove material and high resolution spectra were

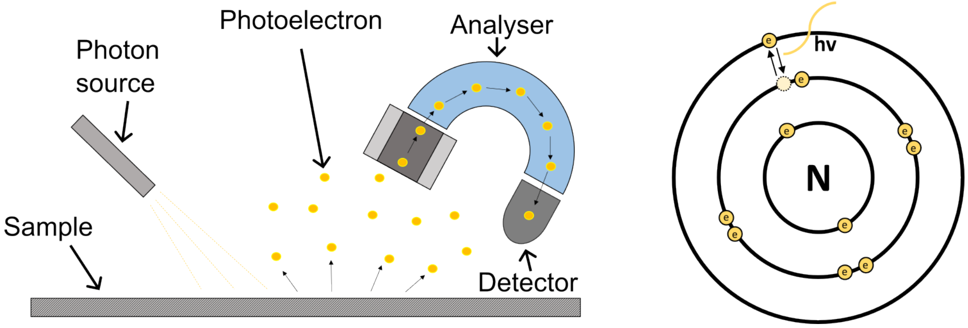

Figure 3.11: Schematic highlighting the components of a XPS tool

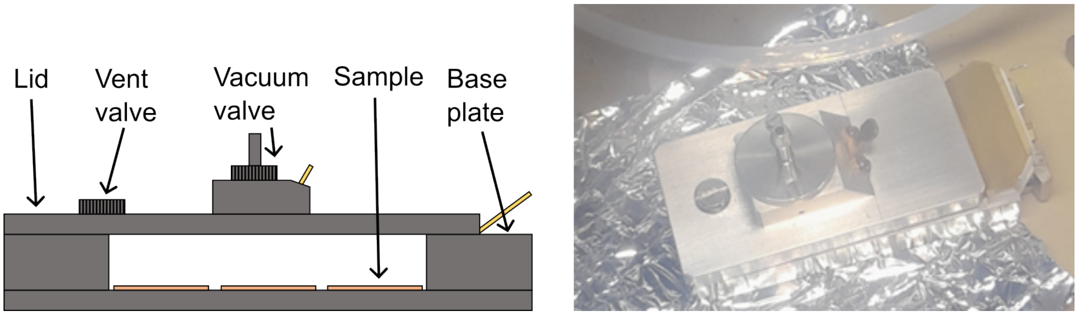

Figure 3.12: Schematic highlighting the XPS sample transfer holder (left), image showing the XPS sample transfer holder (right)

taken at regular intervals.

To record spectra of group 1 metals, a specialist sample holder was utilised to allow for transfer of samples from the inert atmosphere inside a glovebox to the Kratos Axis Supra XPS. To use this device, samples are loaded onto a platform (figure 3.12), the lid is then placed over the samples and a hand pump was used to create a vacuum seal. The samples can now be transferred from glovebox to the XPS. When loaded into the XPS and pumped down, due to the pressure differential, the lid will now naturally come off and spectra of the samples can be collected.

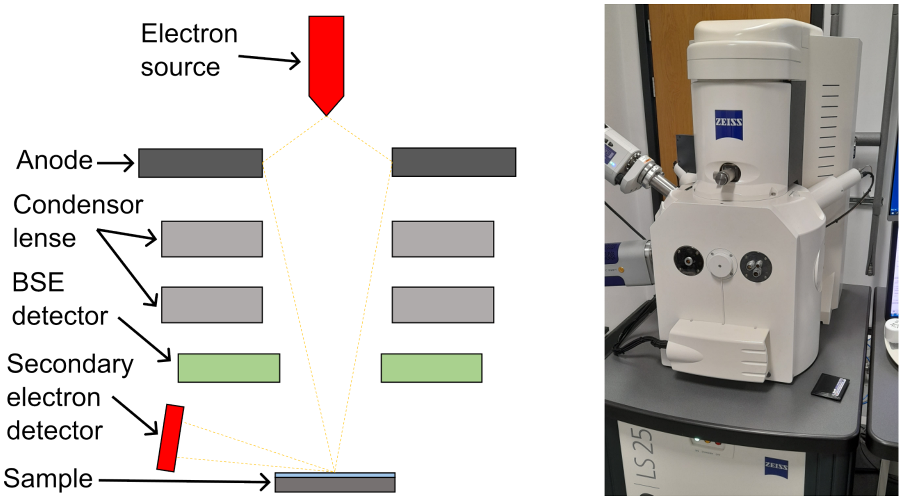

Figure 3.13: Schematic showing the components of an SEM (left), image showing the Zeiss Evo SEM used for the majority of SEM imaging in this thesis (right)

3.5.3 scanning electron microscopy(SEM)

Scanning electron microscopy (SEM), unlike optical microscopy works by focusing a narrow beam of electrons in substitution of conventional visible light. Initially electron are generated at the source which commonly comprises of a tungsten hairpin filament heated to 2500 degrees Celsius, these electrons have energies that vary between 2-40 keV. Lanthanum hexaboride (LaB_6) crystals can also be used as emitters. These electrons then reach a series of condenser lenses which cause them to be focused into a fine beam which can be manipulated to different parts of the sample by scan coils, see figure 3.13 for details. The electrons then penetrate the sample in a tear drop like pattern, the depth of penetration is dependent on the electron beam energy. Once electron interaction have taken place between the electrons from the filament and those within the various energy levels in the sample, various types of electrons are emitted from the samples. These include, secondary, Backscattered and Auger electrons as well as X-rays and some other wavelengths of light. Each type of scatter can be detected by various detectors within the sample chamber which can be displayed on a monitor generating images of the sample surface. The resolution of the images is dependent on the type of electron scatter being detected as well as the type of emitter used, for Tungsten filament SEMs detecting secondary electron the minimum feature size lies around 5 nm[21, 22].

The Hitachi s-4800 was one of two heavily used SEM systems throughout the course of this thesis. For this particular SEM, the maximum magnification possible lies is $1x10^6$ optical magnification with a

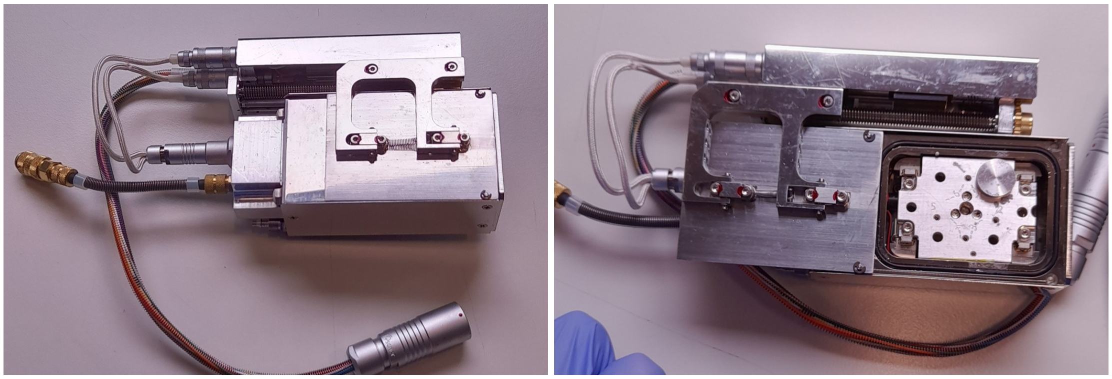

Figure 3.14: image showing the SEM holder used by Kammrath Weiss closed (left) and open (right)

resolution of down to 1nm. The beam can be accelerated from 0.5-30 KeV with an emission current range of between 1-20 micro amps. This SEM has a back scatter detector as well as a secondary electron detector. For the purpose of this work, the secondary electron detector was primarily used for images collected in this thesis.

The Zeiss Evo (figure 3.13 right) works by using Lanthanum Hexaboride crystal emitter (laB_6). Unlike the Hitachi s-4800, it has a chamber loading system instead of a loadlock. This particular system was used for work involving observation of sodium metal and other air sensitive compounds as it had a chamber modification allowing it to do so. Like the Hitachi images were taken primarily using the secondary electron detector.

Due to the reactivity of group 1 metals, a sample transfer holder was utilised to transfer disassembled cells from the inert Argon filled glovebox to the Zeiss Evo SEM. This particular holder was supplied by Kammrath Weiss. To use this device, samples are loaded onto SEM stubs which are consequently slotted into one of the 6 pin guiders seen on figure 3.14. The lid can then be closed using an electronic switch and the samples can now be transferred to the SEM. Once loaded, the lid can be opened again via and electrical feed through once the SEM has been pumped down to vacuum and the samples can be imaged.

3.5.4 Transmission electron microscopy (TEM)

To obtain the highest resolution images at high magnification TEM was employed. This was mainly employed for characterisation of nanoparticles. Unlike SEM, a TEM uses a high energy electron beam which

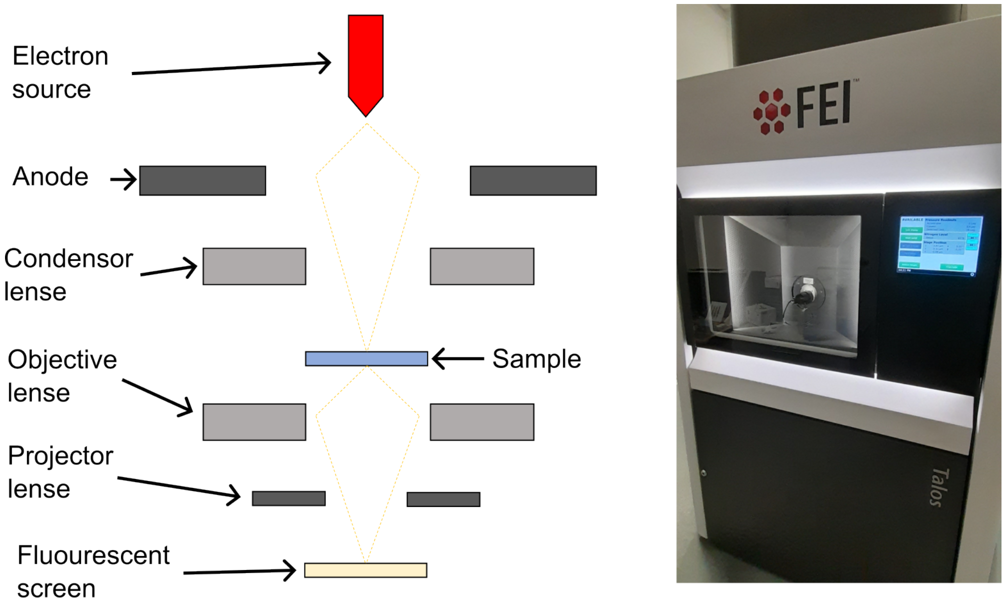

Figure 3.15: Schematic highlighting the structure of a TEM (left), image of TEM (right)

is focused onto an electron transparent sample. These electrons have an energy of 20KeV or higher. The electrons are focused into a narrow beam by a series of elctromagentic coils (figure 3.15) before being transmitted though the sample. Depending on the electron density of the specific areas on the sample, the transmitted electrons are scattered creating an image. This image is then projected onto a fluorescent screen where it can be captured and displayed for the user to interpret. The TEM utilised for the nanoparticles mounted on RGO TEM grids was the FEI Talos F200X [23].

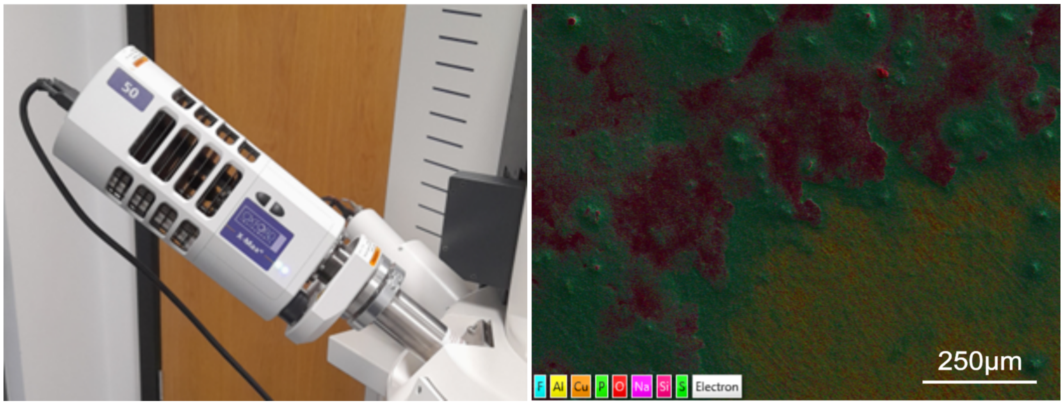

Figure 3.16: Image showing the oxford EDX used for mapping throughout this thesis (left), EDX map of an example sample (right), the different colors highlight different elements

3.5.5 Energy dispersive X-ray (EDX)

EDX is a spectroscopic technique that is usually coupled with an SEM system and is used to identify what elements are present within imaged material. Bombardment of a target sample with medium energy electrons causes atomic electrons within the sample structure to become excited into higher energy states. The excited electrons then relax back to their ground state shedding their excess energy as an X-ray. The excess energy primarily depends on the atoms from which they come from. As an example a characteristic X-ray emitted from atom x will have a different energy to atom y, this difference in energy can be used to characterise where the x-ray originated from and therefore its parent atom consequently. In reality this process is much more complicated. Unlike XPS previously mentioned, EDX is not sensitive to the surface as characteristic X-rays are generated in a region of about 2 microns in depth which exceeds the thickness of the thin films used in this thesis. Throughout this work, an OXFORD instruments EDX was used for all elemental mapping and points taken [24, 25]. Figure 3.16 shows the Oxford EDX and an example map created.

3.5.6 Focused ion beam (FIB)

Focused ion beam was used in conjunction with SEM to obtain high quality images of the sample cross section. Although for brittle crystalline substrates such as silicon this is not always necessary. For flexible substrates such as metal foils which are used extensively throughout this thesis it is highly applicable as a substitute for mechanical techniques for achieving a cross section such as cutting or shearing as these can

Figure 3.17: image showing the FIB lamellar cross section mounted ready for SEM analysis

damage thin films. The technique works by removal of a llamellar section from the sample by focusing an ion beam onto an area of around 5nm using a field ionisation source. The FIB used for this research was a Zeiss Crossbeam 550 Gemini2 FEG SEM column [26]. Figure 3.17 shows a FIB cross section lamellar to be imaged.

3.5.7 Optical microscopy

Optical microscopy was employed as a method for characterization of materials. Optical microscopy works by means of focusing white light onto the surface of the samples to observe topographical features present by focusing light through a series of lenses. Whilst the resolution of this technique is limited when compared to other techniques such as SEM the process for sample preparation is much more trivial than SEM and can generate images containing more contrasting colors. Throughout testing, a keyence VHX-1000 was employed to obtain optical microscope images of samples [27].

To observe group one metals electroplated onto copper substrates samples were sandwiched in between two glass microscope slides, they were then sealed using vacuum grease and epoxy resin before being removed from the glovebox for observation.

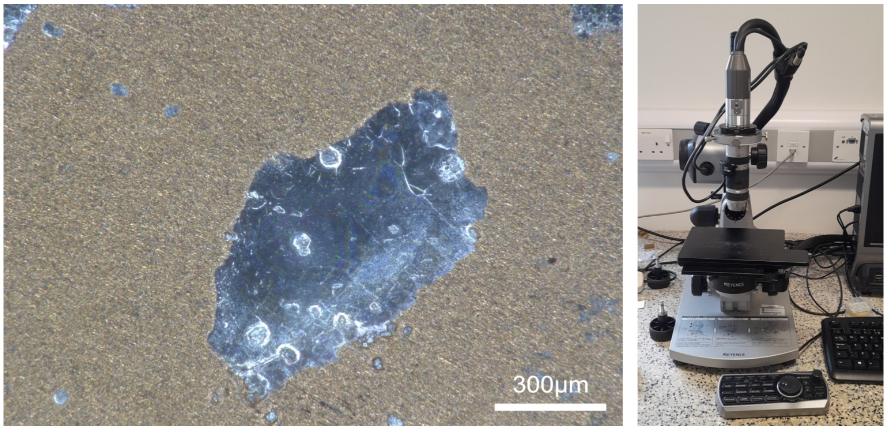

Figure 3.18: example microscope image take of group 1 metal deposition for this thesis (left), image of the Keyence microscope used for this thesis (right)

3.5.8 Insitu optical microscopy

To observe electrodeposition in real time, special equipment was used supplied by EL cell (ECC-Opto-Std-Aqu) which consists of a 3 electrode cell with a quartz viewing window allowing for analysis techniques such as optical microscopy and Raman spectroscopy to be incorporated into the process. For the work in this thesis the setup was coupled with optical microscopy to observe the electrodeposition of Sodium and Lithium onto anode materials in real time.

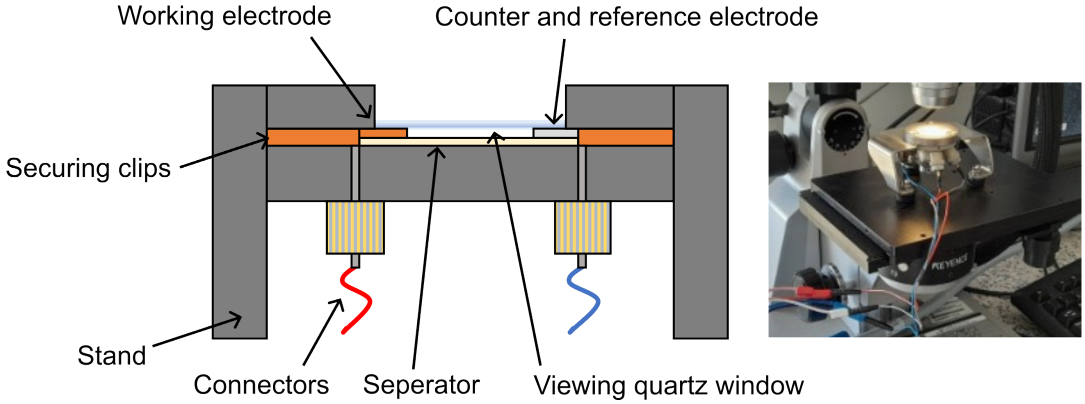

Figure 3.19: Schematic and image showing setup used for insitu optical microscopy experiments

Bibliography

[1] Solomon T Oyakhire, Wenbo Zhang, Andrew Shin, Rong Xu, David T Boyle, Zhiao Yu, Yusheng Ye, Yufei Yang, James A Raiford, William Huang, et al. Electrical resistance of the current collector controls lithium morphology. *Nature communications*, 13(1):3986, 2022.

[2] Zhi Wei Seh, Jie Sun, Yongming Sun, and Yi Cui. A highly reversible room-temperature sodium metal anode. *ACS central science*, 1(8):449–455, 2015.

[3] Fangyuan Cheng, Meilian Cao, Qing Li, Chun Fang, Jiantao Han, and Yunhui Huang. Electrolyte salts for sodium-ion batteries: Napf6 or naclo4? *ACS nano*, 2023.

[4] Tamene Tadesse Beyene, Hailemariam Kassa Bezabh, Misganaw Adigo Weret, Teklay Mezgebe Hagos, Chen-Jui Huang, Chia-Hsin Wang, Wei-Nien Su, Hongjie Dai, and Bing-Joe Hwang. Concentrated dual-salt electrolyte to stabilize li metal and increase cycle life of anode free li-metal batteries. *Journal of The Electrochemical Society*, 166(8):A1501–A1509, 2019.

[5] Xiang Li, Ruxin Zhao, Yongzhu Fu, and Arumugam Manthiram. Nitrate additives for lithium batteries: Mechanisms, applications, and prospects. *EScience*, 1(2):108–123, 2021.

[6] Steven K MacLeod. Moisture determination using karl fischer titrations. *Analytical chemistry*, 63(10):557A–566A, 1991.

[7] Bing Zhao, Bobo Li, Zhixuan Wang, Chuxiong Xu, Xiaoyu Liu, Jin Yi, Yong Jiang, Wenxian Li, Ying Li, and Jiujun Zhang. Uniform li deposition sites provided by atomic layer deposition for the dendrite-free lithium metal anode. *ACS applied materials & interfaces*, 12(17):19530–19538, 2020.

[8] Derek Pletcher. *A first course in electrode processes*. Royal Society of Chemistry, 2019.

[9] Guangyuan Zheng, Seok Woo Lee, Zheng Liang, Hyun-Wook Lee, Kai Yan, Hongbin Yao, Haotian Wang, Weiyang Li, Steven Chu, and Yi Cui. Interconnected hollow carbon nanospheres for stable lithium metal anodes. *Nature nanotechnology*, 9(8):618–623, 2014.

[10] Shao-Jian Zhang, Jin-Hai You, Zhiwei He, Jiajie Zhong, Peng-Fang Zhang, Zu-Wei Yin, Feng Pan, Min Ling, Bingkai Zhang, and Zhan Lin. Scalable lithiophilic/sodiophilic porous buffer layer fabrication enables uniform nucleation and growth for lithium/sodium metal batteries. *Advanced Functional Materials*, 32(28):2200967, 2022.

[11] Chengbin Jin, Ouwei Sheng, Yun Lu, Jianmin Luo, Huadong Yuan, Wenkui Zhang, Hui Huang, Yongping Gan, Yang Xia, Chu Liang, et al. Metal oxide nanoparticles induced step-edge nucleation of stable li metal anode working under an ultrahigh current density of 15 ma cm- 2. *Nano Energy*, 45:203–209, 2018.

[12] Kai Yan, Zhenda Lu, Hyun-Wook Lee, Feng Xiong, Po-Chun Hsu, Yuzhang Li, Jie Zhao, Steven Chu, and Yi Cui. Selective deposition and stable encapsulation of lithium through heterogeneous seeded growth. *Nature Energy*, 1(3):1–8, 2016.

[13] Allen Pei, Guangyuan Zheng, Feifei Shi, Yuzhang Li, and Yi Cui. Nanoscale nucleation and growth of electrodeposited lithium metal. *Nano letters*, 17(2):1132–1139, 2017.

[14] Anton Van der Ven, Kimberly A See, and Laurent Pilon. Hysteresis in electrochemical systems. *Battery Energy*, 1(2):20210017, 2022.

[15] Gregory Burwell, Klaudia Rejnhard, Jon Evans, Jacob Mitchell, Michael T Grimes, Matt Elwin, Ardalan Armin, and Paul Meredith. A low-temperature batch process for the deposition of high-quality conformal alumina thin films for electronic applications. *Advanced Engineering Materials*, 2023.

[16] Klaudia rejnhard. *Advanced Functional Coatings for Integrative Semiconductor Materials and Devices*. PhD thesis, Swansea university, 2022.

[17] Rizwan Ali, Muhammad Rizwan Saleem, Pertti Pääkkönen, and Seppo Honkanen. Thermo-optical properties of thin-film tio2–al2o3 bilayers fabricated by atomic layer deposition. *Nanomaterials*, 5(2):792–803, 2015.

[18] Ulf Helmersson, Martina Lattemann, Johan Bohlmark, Arutiun P Ehiasarian, and Jon Tomas Gudmundsson. Ionized physical vapor deposition (ipvd): A review of technology and applications. *Thin solid films*, 513(1-2):1–24, 2006.

[19] Harland Tompkins and Eugene A Irene. *Handbook of ellipsometry*. William Andrew, 2005.

[20] John F Watts and John Wolstenholme. *An introduction to surface analysis by XPS and AES*. John Wiley & Sons, 2019.

[21] Karen D Vernon-Parry. Scanning electron microscopy: an introduction. *III-Vs review*, 13(4):40–44, 2000.

[22] D. McMullan. Scanning electron microscopy 1928–1965. *Scanning*, 17(3):175–185, 1995.

[23] ANA REBEKA KAMŠEK. Transmission electron microscopy. 2020.

[24] David C Bell and Anthony J Garratt-Reed. *Energy dispersive X-ray analysis in the electron microscope*. Garland Science, 2003.

[25] Ashutosh Kumar Shukla and Siavash Iravani. *Green synthesis, characterization and applications of nanoparticles*. Elsevier, 2018.

[26] Cynthia A Volkert and Andrew M Minor. Focused ion beam microscopy and micromachining. *MRS bulletin*, 32(5):389–399, 2007.

[27] Ian M Watt. *The principles and practice of electron microscopy*. Cambridge University Press, 1997.

Chapter 4

Lithium anode free

4.1 introduction

As previously mentioned in section 2.2.4, the use of anode free batteries has many advantages over conventional batteries and will therefor be explored in this chapter.

For this chapter, copper is employed as a current collector material for lithium due to its high conductivity. Despite this, it binds relatively weakly to lithium and as a result there is a high nucleation overpotential required for electrodeposition. This high nucleation overpotential leads to small lithium deposits being formed on the copper which aggregate into high surface area lithium deposits during plating. These high surface area deposits are responsible for uncontrollable SEI growth which causes rapid consumption of the liquid electrolyte according to current research [1, 2, 3].

Al_2O_3 is a widely used material in this field and has been applied to anode free lithium ion batteries as well as coatings directly onto batteries with a solid lithium metal electrode, it is used to enhance the cycle life of half cells and full cells with the coated anode[4, 5]. Currently a few different theories exist as to why the layer effectively mitigates dendrite growth as highlighted in the literature review section 2.4.1. Chen et al suggest the presence of the layer enhances the wettability of the Li surface towards both carbonate and ether electrolytes, leading to a uniform and dense SEI formation and reduced electrolyte consumption during battery operation [5]. More recent suggestions by oyakhire et al who implemented Al_2O_3 as well as ZnO and SnO_2 by ALD onto copper electrodes for anode free batteries suggests that the lithium metal promotes sparse nucleation of lithium deposits. This sparse nucleation promotes lateral growth of lithium resulting in dense deposits with a low surface area. The group tests several coating and report that the SEI atop lithium in the presence of each coated copper substrate is chemically and structurally similar indicating that in this work the changes in lithium morphology stem from differences in substrate properties and not the SEI [4].

This chapter focuses on coating copper electrodes with Al_2O_3 by an MVD process. The aim of the chapter is to study any advantages the process may have over it's ALD predecessor given its advantages highlighted in chapter 2 . As well as this a selection of material thicknesses including uncoated, 2.5nm, 5.0nm, 10.0nm, 15nm, 20nm and 27.5nm of Al_2O_3 were selected to study the affect the thickness of this layer has on plating and stripping of lithium. Coin cells were cycled at $1mA/cm^2$ for 1hour giving a capacity of $1mAh/cm^2$. Hysteresis and coulombic efficiency were derived from python codes.

4.2 Deposition

Initially electrodes were incorporated into the MVD chamber using stainless steel baffles which were cleaned by sonication with Acetone, IPA and DI water respectively. Due to the minute size of the foil it was expected the nitrogen pulse and purge stages of the process would displace the samples which could affect the coating process as well as potentially damage the tool itself (if samples were to be displaced into the extraction etc). Figure 4.1 highlights the placement of samples into the MVD. It was found that to minimise chamber loading the stainless gauss lids could be removed without affecting the deposition. Deposition was performed in accordance with parameters from the materials and methodology section 3.4.1 which was optimised by Burwell et al, these parameters were used because the deposition of stoichiometrically perfect Al_2O_3 with lowest levels of carbon contamination whilst mainting the lowest temperature possible was achieved.[6].

4.3 Characterisation Al_2O_3 layer on Cu

Over the course of my EngD key characterisation has been performed. These include SEM, Cross sectional SEM, EDX, TEM, XPS and FIB. The following section focuses on characterisation of the Al_2O_3 layer deposited on the surface of the copper substrates that will be tested.

Figure 4.1: Image showing the experimental setup for how copper substrates were coated by MVD using stainless steel baffles to stop sample movement

4.3.1 Visual confirmation

It is evident that from a first glance the coating process was successful. Figure 1 shows the contrasting shades of deposition which is dependant on the thickness of material deposited. Figure 4.2 shows the varying levels of deposition from the uncoated samples up to the 27.5nm thickness. It is clear that as the layer increases in thickness the deposition becomes darker.

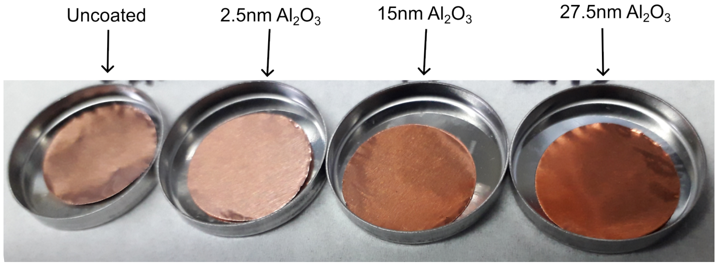

Figure 4.2: Image showing visually the change in thickness of Al_2O_3, as the thickness increases the sample appears darker

4.3.2 Ellipsometry

As well as cross sectional SEM, spectroscopic ellipsometry is another technique used for this film characterisation. As Al_2O_3 is optically transparent at the thicknesses we are working at accurate ellipsometry measurements could be taken of the coatings. Unfortunately due to the surface roughness of the copper substrate (which can be visualised by the cross sectional FIB lamellar seen in figure 4.3 (b)) substrate it was not possible to obtain reliable thickness data. Instead a small piece of polished silicon wafer was implemented in the same run as the copper electrodes to take measurements. 1 point measurements were taken by an J.A woolam M-2000 ellipsometer. For each point, 3 measurements were taken from 65^o-75^o angles in steps of 5^o. Film thickness was then extracted from a cauchy model and fitted using the CompleteEASE as highlighted in the methodology section 3.5.1.

4.3.3 SEM characterisation

To ensure growth rates of Al_2O_3 on copper were similar to that on the Si/SiO_2 substrate, 80nm of PVD Cu was deposited on an Si/SiO_2 wafer substrate. This was then coated with a 27.5nm layer of Al_2O_3 by MVD (thicker coatings were chosen to ensure they could be resolved by SEM). The sample was then cleaved and the cross section was observed by SEM. This was then compared to an Si/SiO_2 substrate that wasn't processed with 80nm of PVD copper by ellipsometry. Both samples were placed in the same MVD run. Figures 4.2 (c) shows the cross sectional SEM results as well. From the results the value generated by the cross sectional SEM results is 28.7nm. This Value is slightly different to expected value of 27.5nm which is put down to human error associated with the SEM measurements. It was concluded from this experiment that the growth of Al_2O_3 on Cu is similar to that on Si/SiO_2 so our method for characterisation is accurate.

Figure 4.3 (b) highlights the Al_2O_3 layer on the surface of the copper electrodes used for testing. The sample is extracted by SEM analysis of a lamellar cross section taken by focused ion beam. At a glance it is evident that the surface of the copper is highly non uniform which can be further justified by the top down SEM image of the copper substrate in figure 4.3 (a). Despite this apparent surface roughness, the MVD is able to conformally coat the distinct features on the copper which shows off the strengths of this deposition technique.

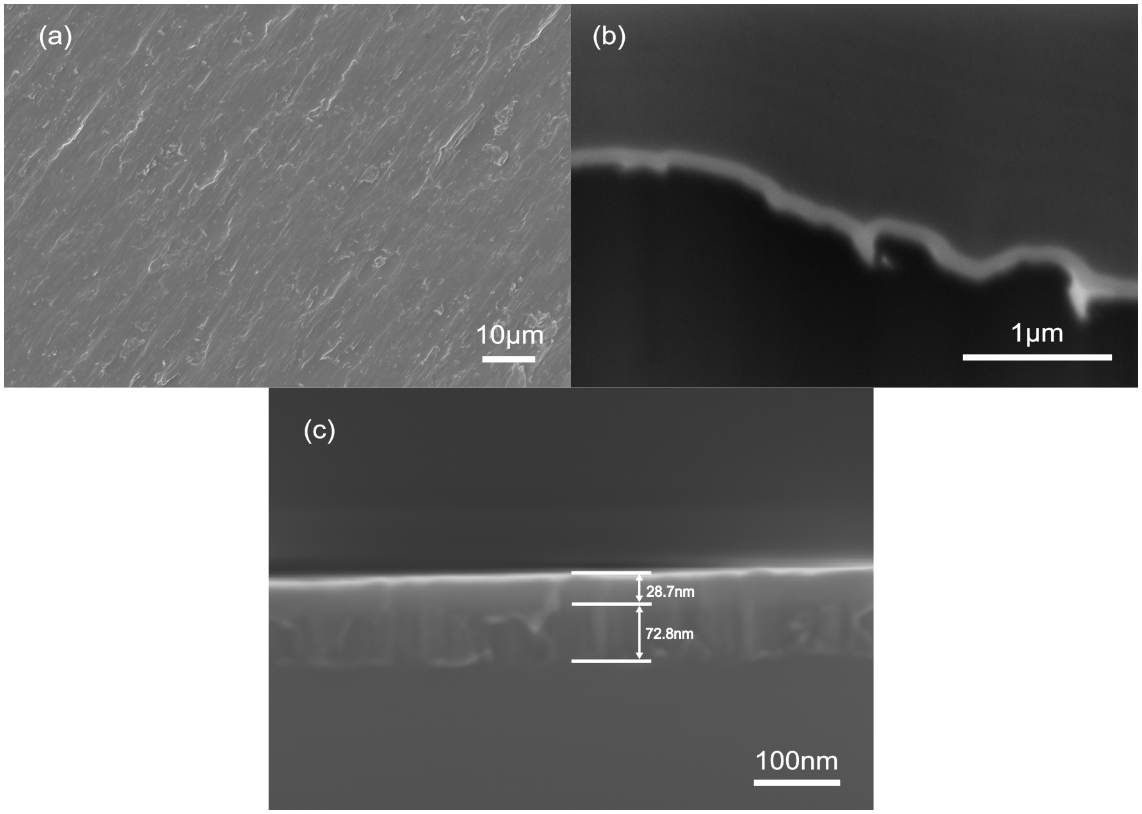

Figure 4.3: Images showing SEM of the various Al_2O_3 coated samples. (a) shows a top down images of the copper with the Al_2O_3 coated copper, (b) shows the FIB cross section of the Cu/Al_2O_3 substrate, (c) shows the cross section of an Si/(pvd)Cu/Al_2O_3 coated sample

4.3.4 Cross sectional EDX

figure 4.4 highlights the EDX spectra of the SEM image above in figure 4.3 (b). The image shows the bulk substrate of the material being copper (figure 4.3 (a)) and the contrasting layer ontop being Aluminium oxide. For the Aluminium and oxygen map it is clear that the concentration of these elements is higher at the point where the layer is present as the colours are more intense when compared to the surrounding background (figure 4.4 (c) and (d)). This proves the coating process was successful and the desired Al_2O_3 compound was deposited.

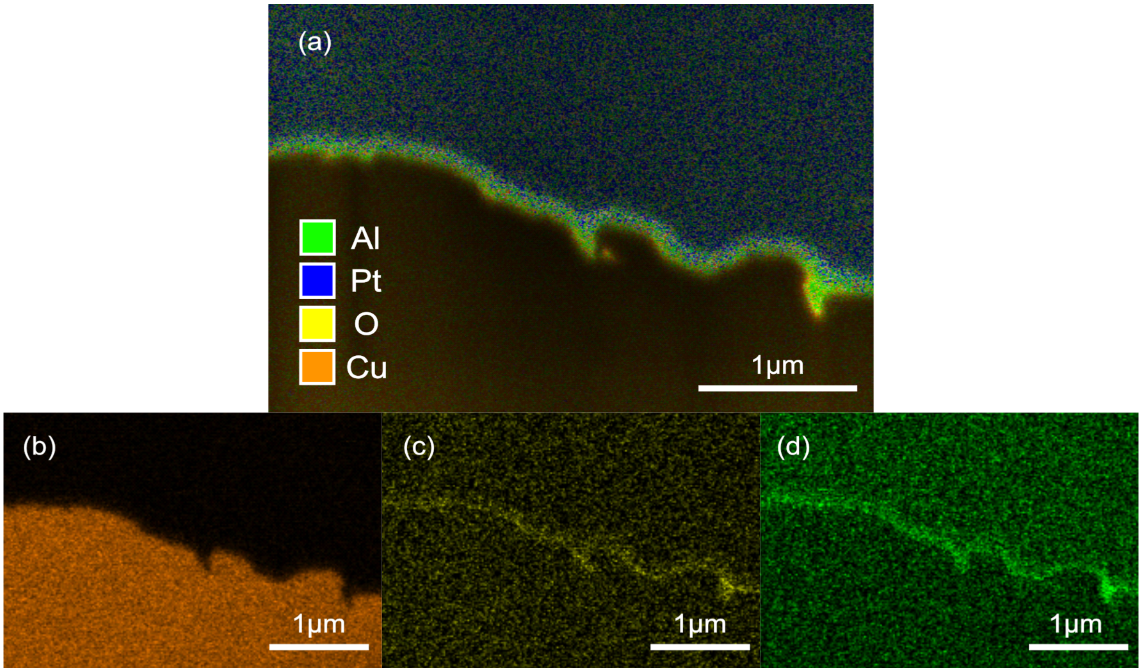

Figure 4.4: Figure showing (a) the EDX maps of the copper substrate with Al_2O_3 layer of the surface. (b),(c) and (d) shows the copper, Oxygen and Aluminium peaks respectably

4.3.5 XPS of Al_2O_3

As well as EDX, XPS spectra was also collected of the films at thicknesses including uncoated Cu, 2.5nm, 5.0nm, 10.0nm Al_2O_3. The overlayed results can be seen in figure 4.5 (b) and (c) which highlight the O1s and the overlayed Al2p and Cu3p peaks. To better highlight this, Figure 4.5 (d) shows the 5.0nm Al_2O_3 film on copper, this was chosen because it highlights both the Al2p and Cu3p due the 5.0nm film being very thin and the penetration depth of the XPS exceeding this as mentioned in the methodology section 3.5.2. This will allow us to gather information with regards to the Al2p peak and Cu3p peak at the same time. It is evident that only the Cu3p doublet peaks appear at 77.6eV (Cu3p3/2) and 80.0eV (Cu3p1/2) for the uncoated copper sample as no deposition has taken place. The spacing of 2.4eV is in accordance with work performed by Khalakhan et al[7]. It is worth noting that the peak position for this research is slightly different to the values in the paper which is likely due to differential charging effects between the underlying copper, Al_2o_3 and advantitious carbon layer on the surface, As Al_2O_3 is an electrical insulator so there is likely poor conduction into the copper [8, 9].The Al2p3/2 and Al2p1/2 peaks located at 74.8eV and 75.24eV (figure 4.5 (d)) corresponds to Al-O bonding [10]. From figure 4.5 (b) it is evident that as the thickness is increased from uncoated to 2.5, 5.0 then 10.0 nm respectively as the Cu3p peak becomes less intensive whilst the Al2p peak increases in intensity up to 10nm where the Cu3p no longer exists (due to the penetration depth of the XPS being 10nm), This indicates that the Al_2O_3 layer coated by MVD is very thin as expected and that our thickness measurements by elliposmetry are accurate.

Figure 4.5 (c) highlights the O1s peak at 5.0nm Al_2O_3. After fitting it is evident that the O1s peak predominately is made up of Al-O bonds at 531.8eV with a smaller peak at 533 which I expect belongs to the adventitious carbon layer that has been highlighted in figure 3.4 (a) [11, 10]. After quantifying the Al-O component of O1s peak and the Al-O belonging to the Al2p peak, an O:Al ratio of 1.51 was achieved which is near a stoichiometric perfect ratio for Al_2O_3 at 1.5 O:Al showing of the high quality of the process and repeatability with prior research [6]. C1s in figures 4.5(a) was suggestd to be adventitious carbon contamination, with C-C, C-O and C=O components present at 284.8, 286.6 and 289.1 eV. These values are very similar to those suggested by Jones et al [11].

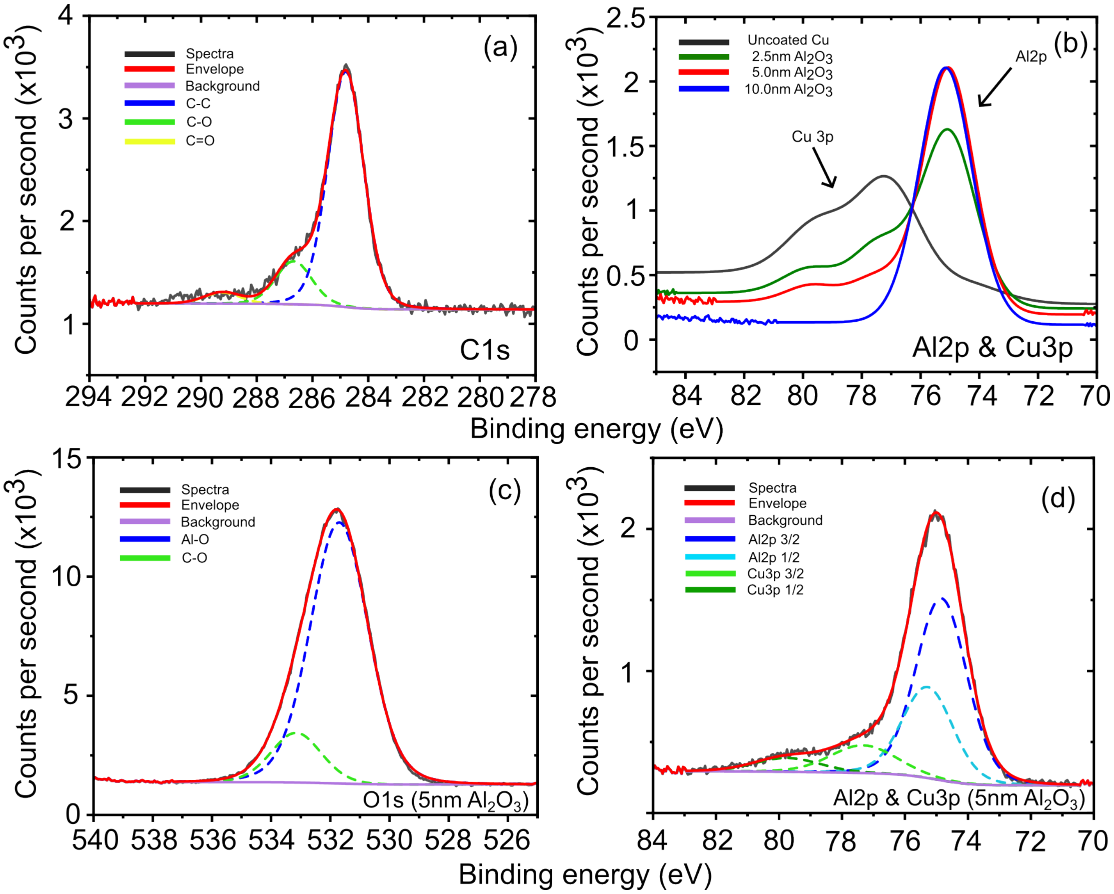

Figure 4.5: XPS spectra showing (a) the fitted C1s peak for a 5.0nm Al_2O_3 coated copper sample, (b) the overlayed Al2P and Cu3p peaks for bare, 2.5, 5.0 and 10.0nm Al_2O_3 coated samples, (c) the fitted O1s peak for a 5nm Al_2O_3 coated sample, (d) the fitted Al2p and Cu3p peak for a 5nm Al_2O_3 coated sample

4.4 Cycling half cells

From the characterisation it was concluded that Al_2O_3 coatings from the MVD are high quality due to their near stoichiometric perfect ratio, they also display good conformatlity determined from SEM. I expect that the thicknesses determined from ellipsometry are correct showing that thickness can be controlled accurately. Electrodes were then incorporated into half cells where they were tested.

For all cells cycled below a cycling rate of $1mA/cm^2$ was employed for 1 hour plating and 1 hour stripping giving a capacity of $1mAh/cm^2$. Thicknesses of Al_2O_3 including uncoated, 2.5, 5.0, 10.0, 15.0, 20.0 and 27.5nm Al_2O_3 were tested. To begin, the first cycle nucleation over potential data was gathered and presented in figure 5.1 (a) and is quantified in figure 5.1 (b) for easy comparison. Evidently the general trend shows an increase in the nucleation overpotential as the thickness of the coating increases which include values of 225, 220, 315, 327, 375, 537 and 436 mV respectively. Oyakhire et al show a similar trend testing 1, 2, 4 and 8nm Al_2O_3 respectively which shows a nucleation overpotential increase of 40, 40, 110 and 800 mV respectively (supplementary information of their paper). The group put this observation down to the increased electrical resistance of the thicker coating causing more sparse nucleation points for lithium. We used the same current and capacity as this group and a similar electrolyte 1 M lithium bis(trifluoromethanesulfonyl)imide (LiTFSI) in 1:1 DOL/DME with 1 wt% lithium nitrate additive albeit they have a lower concentration of lithium nitrate additive. [4].

The following section highlights the galvanostatic charge discharge cycling data for each separate thickness of Al_2O_3. For cycling, the Voltage cutoff for was set to 0.5V with plating and stripping times set to 30 minutes plating - 33 minutes stripping to ensure the working electrode was fully stripped. Exploded sub graphs were taken at the beginning middle and end of cycling to better observe how the response is throughout cycling. As well as this, values for the coulombic efficiency and hysteresis were taken with respect to cycle number as suggested in the materials and methodology section.

Figure 4.7 shows the results for the uncoated cell, the CE shows stable plating and stripping with values above 95% for the first 15 cycles, after this value the CE begins to fade. Figure 4.7 (c) shows the results for CE. The cell hits 80% CE at 27 cycles where the cell was deemed failed. The expected reason for this is that the dendritic growth is becoming more and more extensive constantly exposing fresh lithium to the electrolyte which is then consuming the lithium and converting it into irreversible products which cannot be

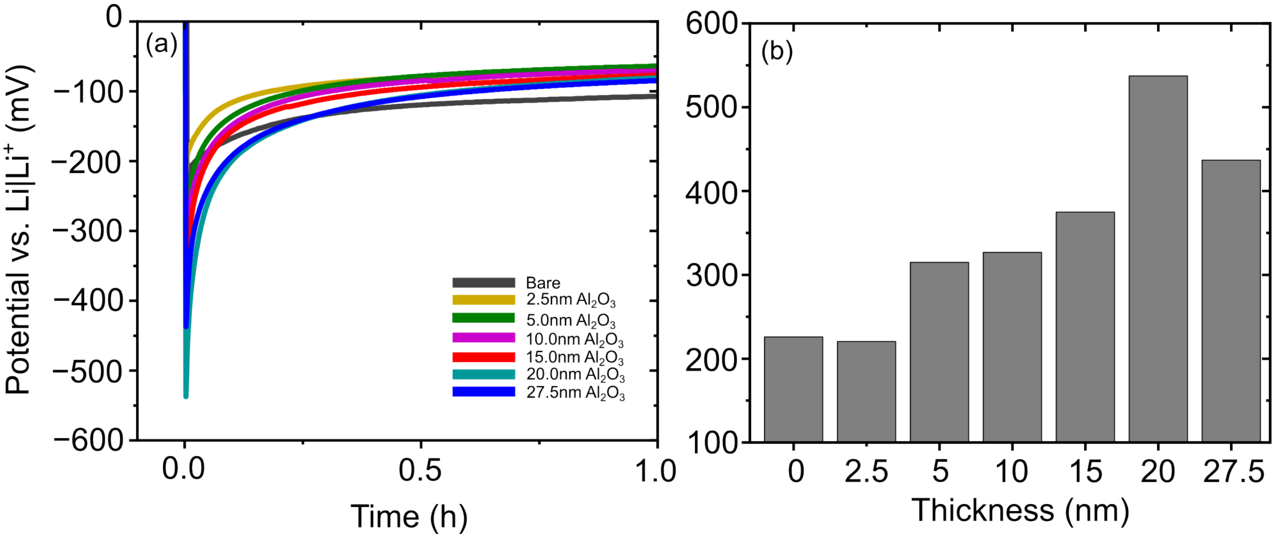

Figure 4.6: (a) graph showing the nucleation over-potential for lithium plating on bare, 2.5, 5.0, 10.0, 15.0,20 and 27.5nm Al_2O_3 (b) bar chart showing the comparison of the nucleation overpotential values

oxidised in the subsequent stripping cycle. After 33 cycles the CE appears to recover which was expected to be due to the solid metal counter electrode replacing the active mass that was lost during the period of CE fade, this recovery was not taken into consideration when assessing the cycle life of the cell as in a full cell setup where there is a finite amount of lithium in the cathode this would not occur. Figure 4.7 (c) shows the hysteresis of the cell. The hysteresis increases gradually which was expected to be due to the SEI layer becoming more and more extensive throughout cycling, this resistive layer thickens and therefor restrains the diffusion of lithium ions meaning a higher potential is required for the redox process to occur. Figure 4.7 (aiii) shows the explode charge discharge cycles towards the end of cycling, it is evident at this point that the plating and stripping is more noisy (jagged) which could highlight the severe presence on dendrites with the formation of dead lithium causing this response.

Figure 4.8 shows the results for the 2.5nm Al_2O_3 coated cell, unlike the uncoated cell which shows the decrease in CE which can be used to determine the failure of the cell, this one showed an abrupt hysteresis increase on the 31st cycle of the cell from roughly 70mV to 180mV. Figure 4.8 (aiii), this elevated hysteresis then remains for 3 further cycles before a noisy region appears at an elevated potential value. Huang et al note the overpotential is due to the resistance of the SEI layer protruding and fresh Li growth onto the

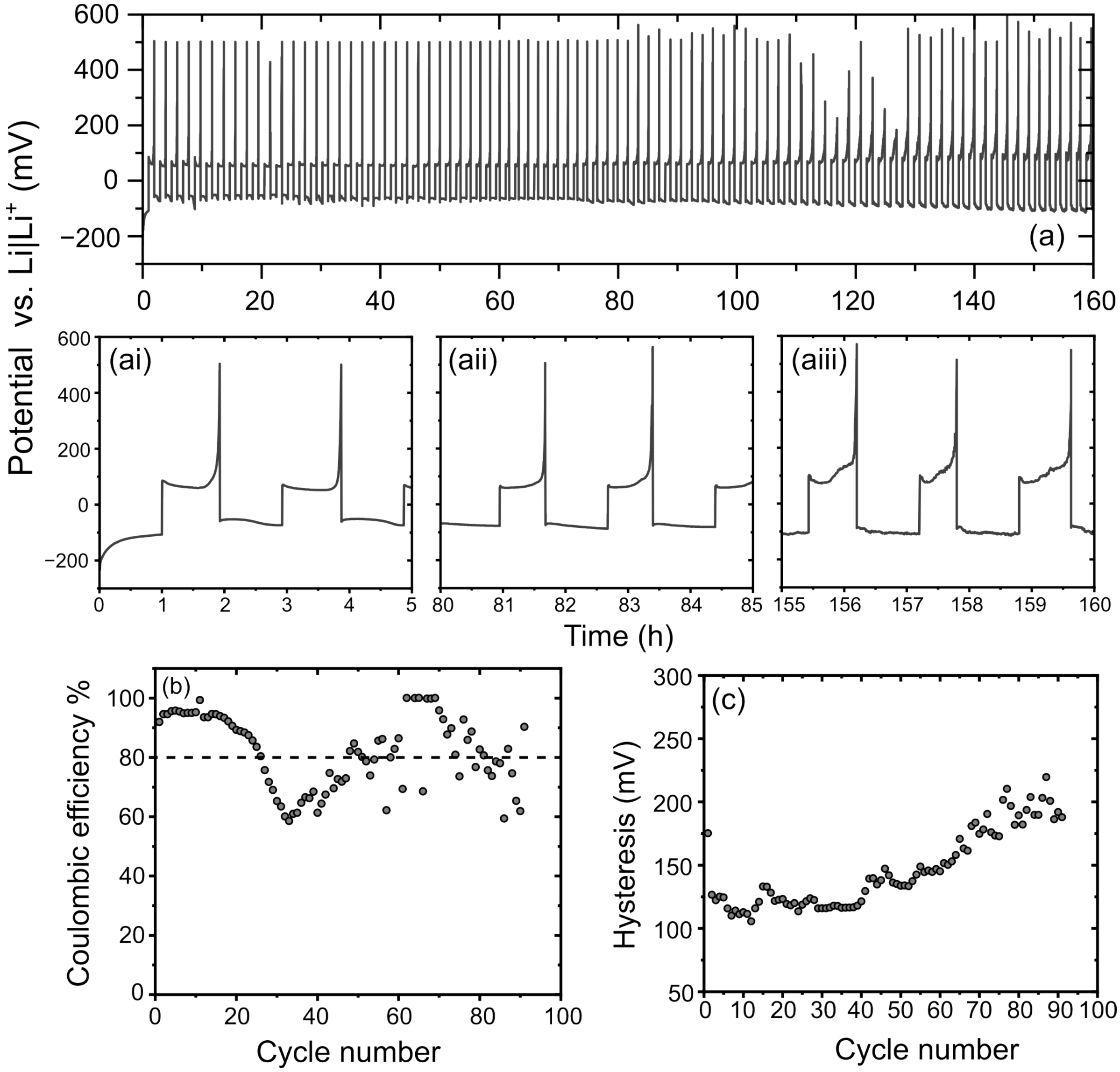

Figure 4.7: graphs a-aiii displaying charge-discharge data for uncoated Cu half cell. (b) graph showing CE data. (c) graph showing Hysteresis

Li surface which could suggest this is occurring in the case for this cell as well [12]. From this it was determined that the cell in this case has failed at 31 cycles. This cell was repeated (section 8.2) and the typical capacity fade which indicates cell failure at 38 cycles. which although slightly different to the figure 4.8 is still respectably close and fits the trend. The reason this cell wasn't used was because the first 5 cycles

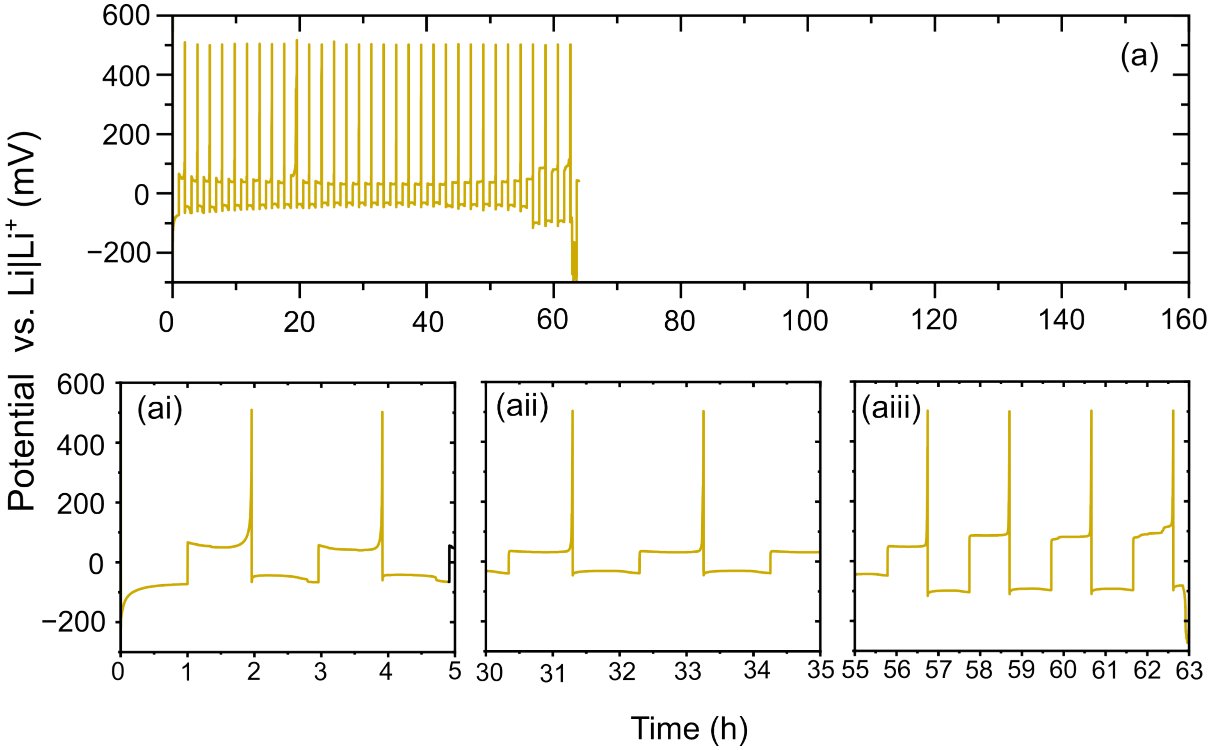

Figure 4.8: graphs (a-aiii) displaying charge-discharge data for uncoated 2.5nm Al_2O_3 coated half cell.

(ai) show an elevated hysteresis which stabilises, this could not be explained.

The 5nm Al_2O_3 coated sample shows an abrupt increase in hysteresis and an abrupt decrease in CE at 40 cycles which decreases below 80% at cycle number 46 which was determined as the cells failure point, this hysteresis increase coincides with the decrease in CE which suggests the two are related and further strengths the suggestion by huang et al that the increase in overpotential is due to the resistance of the SEI [12].

The 10nm Al_2O_3 coated cell shows a similar response to 5nm With an abrupt decrease in CE which begins at cycle number 58 reaches 80% at the 70th cycle which was the point for which cell failure was assumed.

The 15nm Al_2O_3 coated cell shows a more gradual decrease in CE which begins at cycle number 59 and reaches 80% at cycle number 114, this cell showed the longest cycles life out of all the thicknesses tested.

The 20nm Al_2O_3 coated cell shows a significant decrease in CE which begins at cycle number 77, this

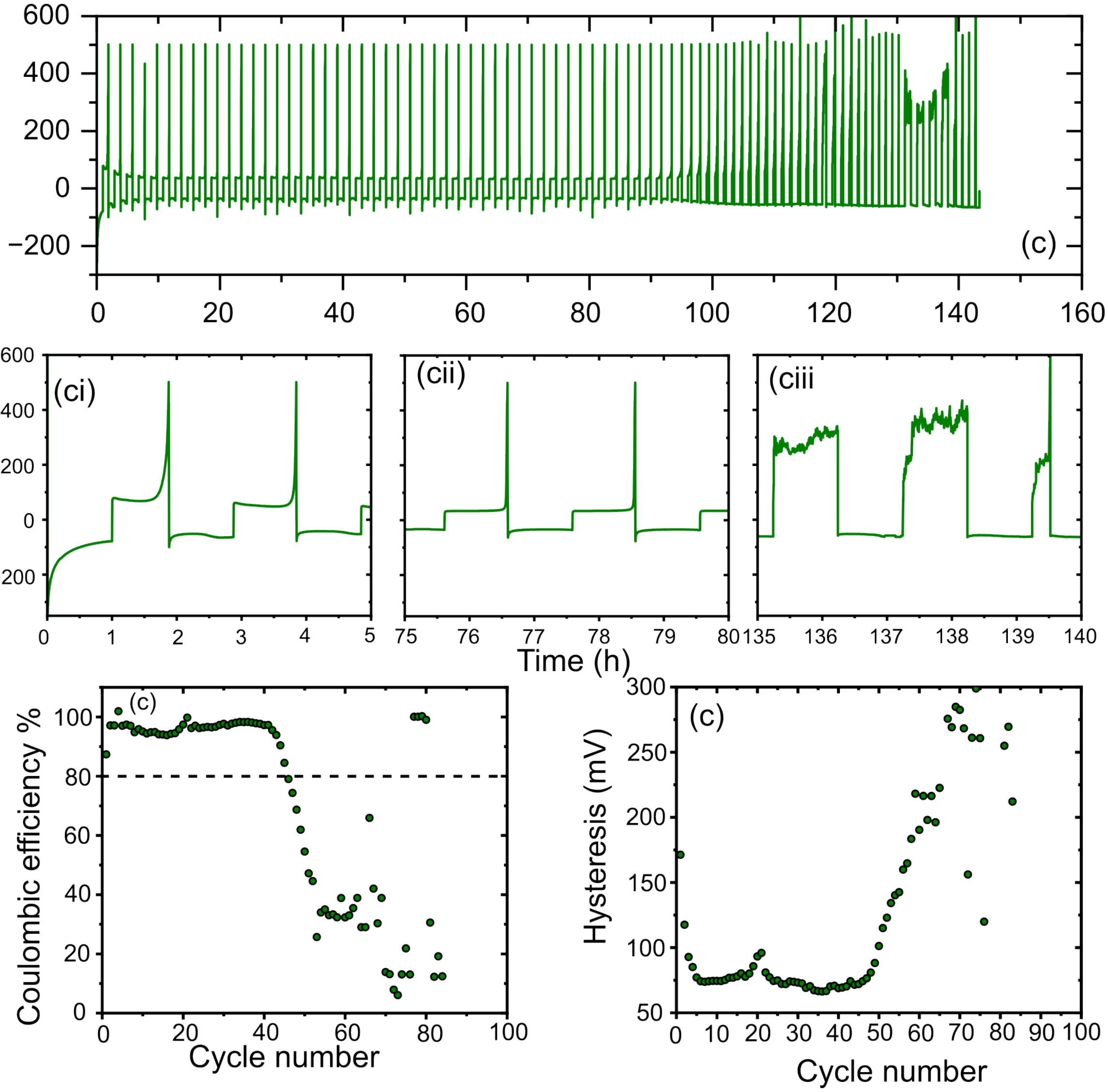

Figure 4.9: graphs (a-aiii) displaying charge-discharge data for uncoated 5.0nm Al_2O_3 coated half cell. (b) graph showing CE data. (c) graph showing Hysteresis

reaches 80% at around 87 cycles.

The 27.5nm cell was particularly interesting when compared to the other cells in this chapter. the cell appears to cycle well, maintaining a CE above 95% until cycle number 60 where the CE becomes more irratic and varies significantly between 95 and 100%. After the 82nd cycle, the CE hits 110% for 6 cycles

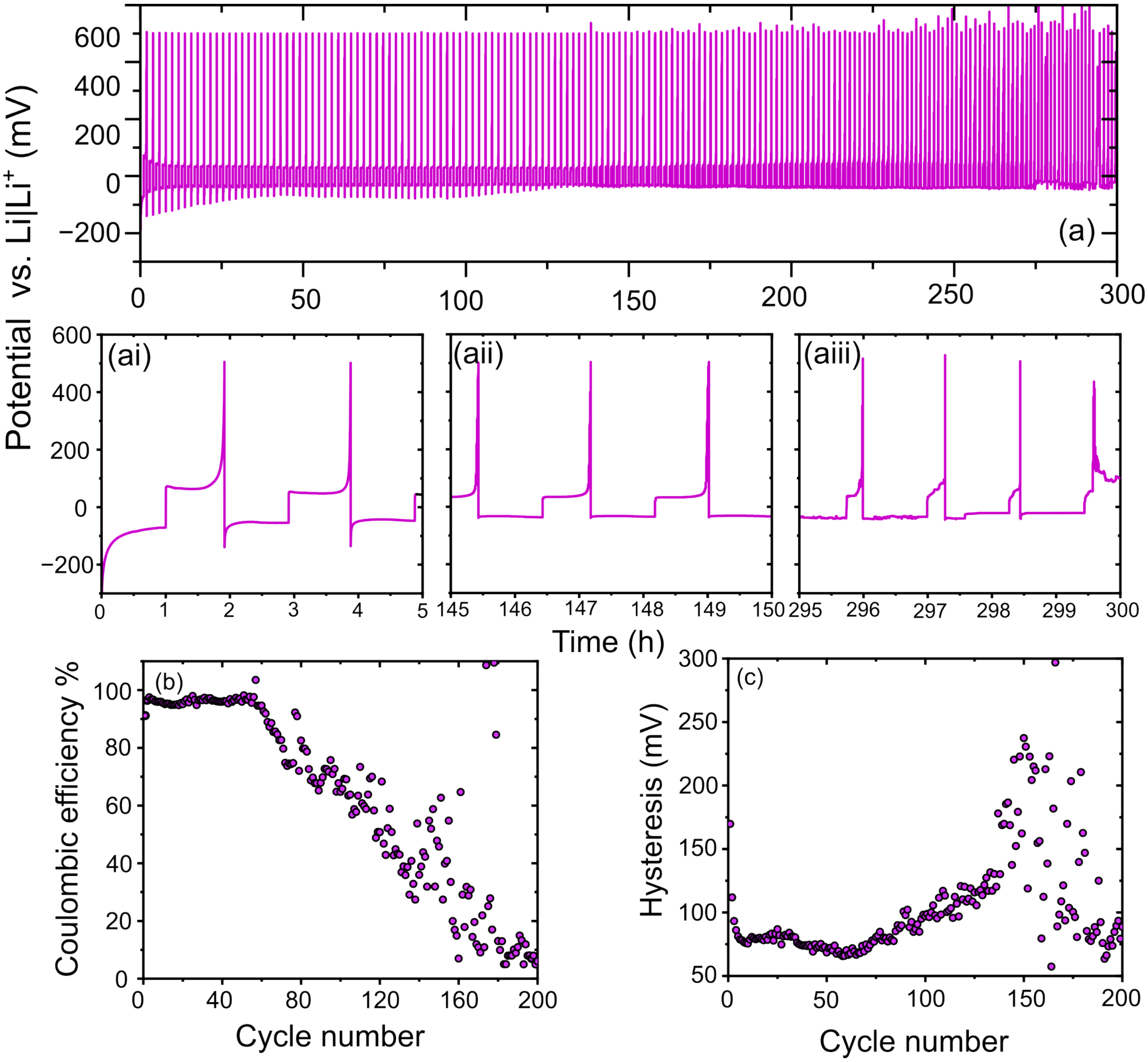

Figure 4.10: graphs (a-aiii) displaying charge-discharge data for uncoated 10.0nm Al_2O_3 coated half cell. (b) graph showing CE data. (c) graph showing Hysteresis

which is due to the time cutoff being reached before the voltage cutoff in this case (figure 4.13 (b)). After this point the CE becomes very erratic with some values exceeding 100% and other values being significantly lower. This CE being over 100% is not unheard of and has been reported several times in literature who put it down to incomplete stripping of lithium from the copper electrode and the presence of dead active mass forming inside the cell [13, 14]. Due to the inconsistent CE values, determining the failure point of the cell

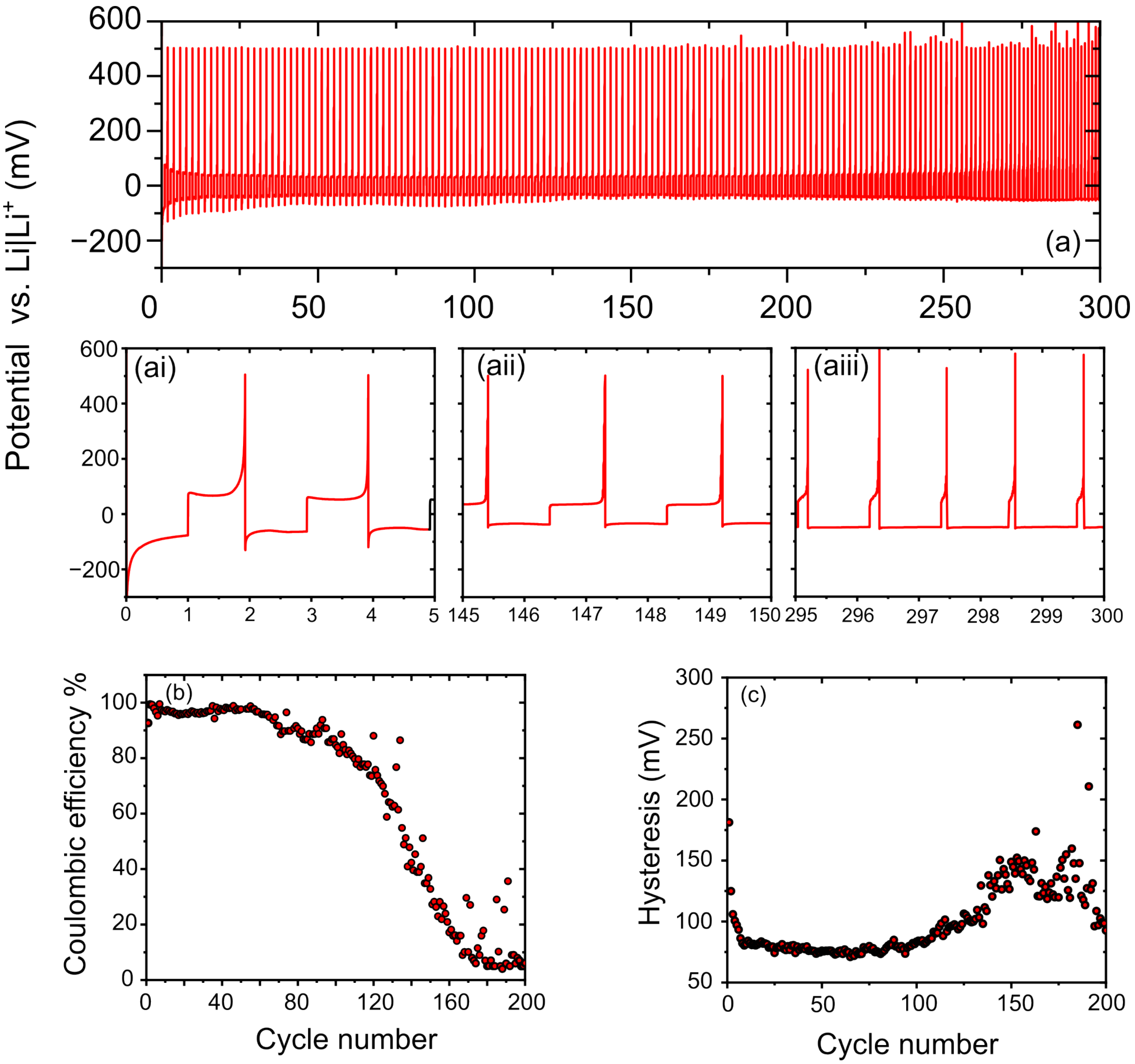

Figure 4.11: graphs (a-aiii) displaying charge-discharge data for uncoated 15.0nm Al_2O_3 coated half cell. (b) graph showing CE data. (c) graph showing Hysteresis

was not easy. If you take the first instance of the CE going below 80% the cycle life would appear to be 104 cycles however for this cell was determined finished when the CE exceeded 100% consistently at the 82nd cycle. The reason for this is due to the dead lithium inside the cell would be irreplaceable in a full cell system and would therefor lead to capacity loss which is not seen in a half cell due to the large pool of

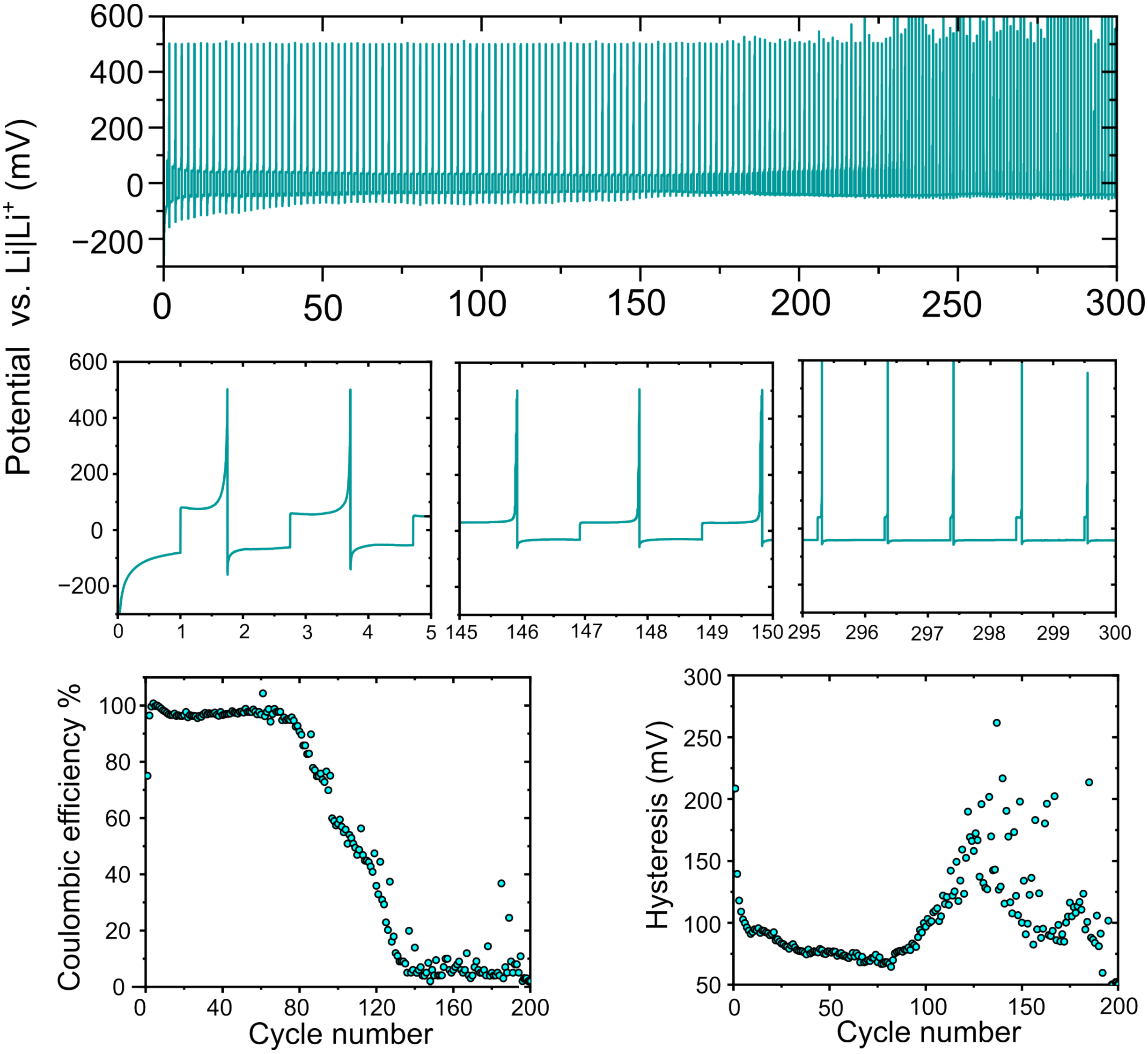

Figure 4.12: graphs (a-aiii) displaying charge-discharge data for uncoated 20.0nm Al_2O_3 coated half cell. (b) graph showing CE data. (c) graph showing Hysteresis

lithium available in the counter electrode.

Its worth noting that coatings as thick as 45nm were attempted (section 8.3) however it was not possible to get more the a few cycles out of them before failure therefor they were not included in the chapter.The was also mentioned by Oyakshire et al who were unable to achieve lithium plating on areas of copper at

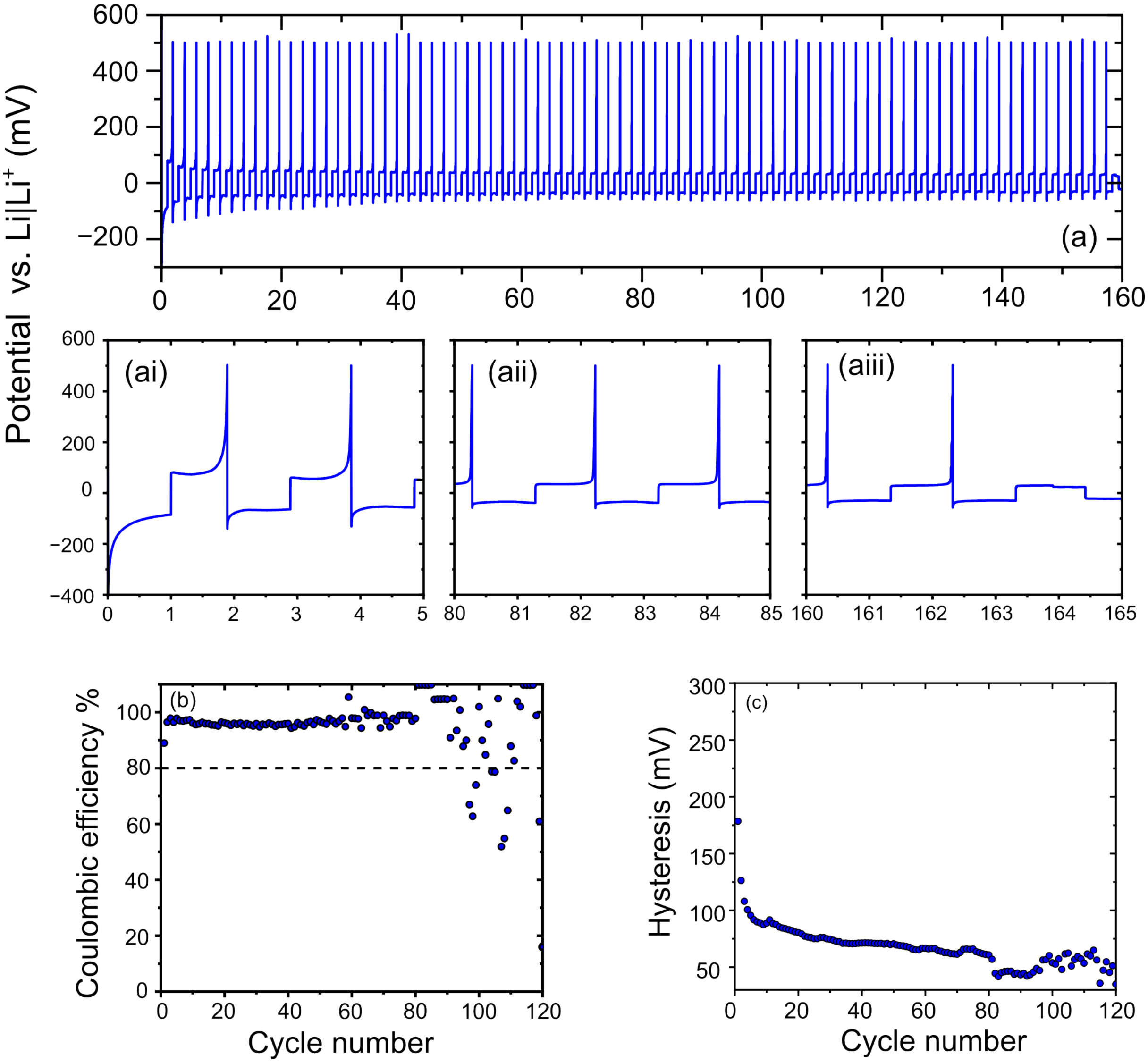

Figure 4.13: graphs (a-aiii) displaying charge-discharge data for uncoated 27.5nm Al_2O_3 coated half cell. (b) graph showing CE data. (c) graph showing Hysteresis

50nm Al_2O_3 in thickness.

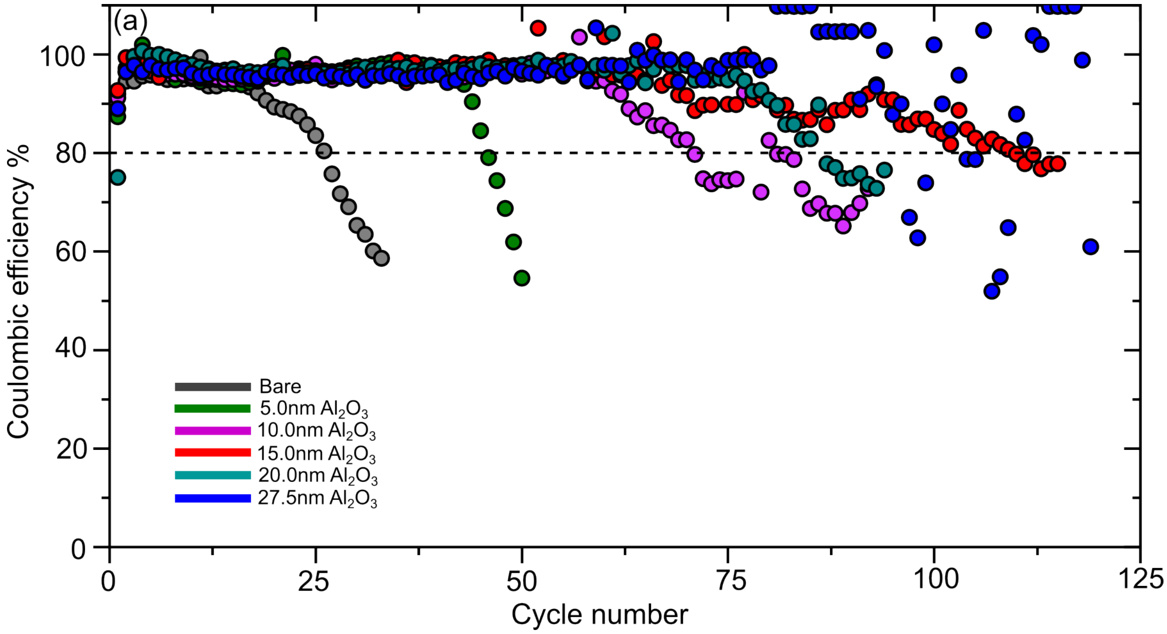

Figure 4.14: Figure showing the coulombic efficiency of uncoated Cu, 5.0, 10.0, 15.0, 20.0 and 27.5nm Al_2O_3 overlayed for ease of interpretation

Figure 4.14 (a) shows the coulombic efficiency data for each individual thickness overlayed for ease of comparison. Some data points after the cells reached 80% capacity have been removed to make interpretation more easy. The point at which cell failure occurred was plotted for comparison as a bar chart in figure 4.15. The points of failure are based on the coulombic efficiency unless specified otherwise. It is clear to see that from this data increasing the thickness of Al_2O_3 increases the cycle life of the cells up to 15nm Al_2O_3 after which the cycle life begins to decrease which could suggest a value around 15nm Al_2O_3 is an optimal coating thickness for this work.

Figure 4.16 shows the hysteresis overlayed. All cells show a high value of hysteresis in the first few cycle which then decreases and stabalise. It is evident that the uncoated cell hysteresis value plataues at a higher value between 100 and 150mV, this value then gradually increases for the remainder of cycling. For the Al_2O_3 coated cells, the hysteresis plateaus much lower between 50 and 100mV which suggests the coating is actually promoting a lower cell resistance which could be due to the SEI not forming at all or not being as extensive as the uncoated value which supports the suggestion that Al_2O_3 is acting as an artificial SEI in this case mentioned in section 2.4.2. Once the CE begins to decrease this value begins to increase

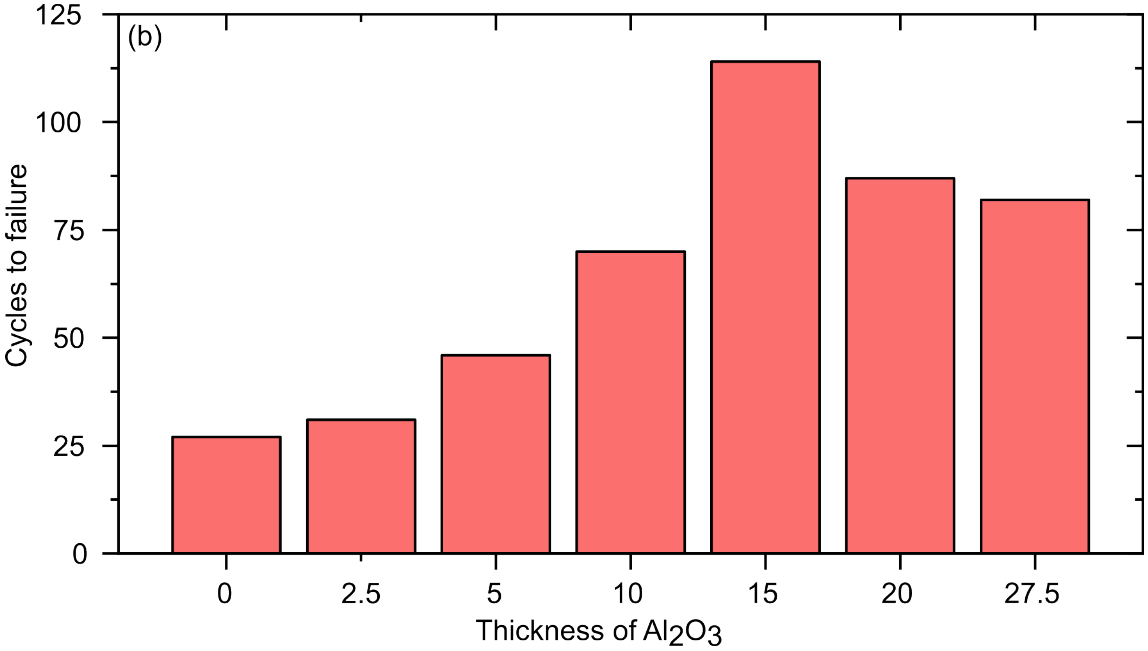

Figure 4.15: Bar chart showing the cycle life of each cell for ease of comparison

suggesting the coating is no longer functioning and uncontrollable SEI growth is occurring, The 27.5nm coating interestingly shows a very stable hysteresis compared to the other thicknesses but unfortunately suffers from incomplete stripping of the electrode which might suggest the cell fails differently to the other thicknesses.

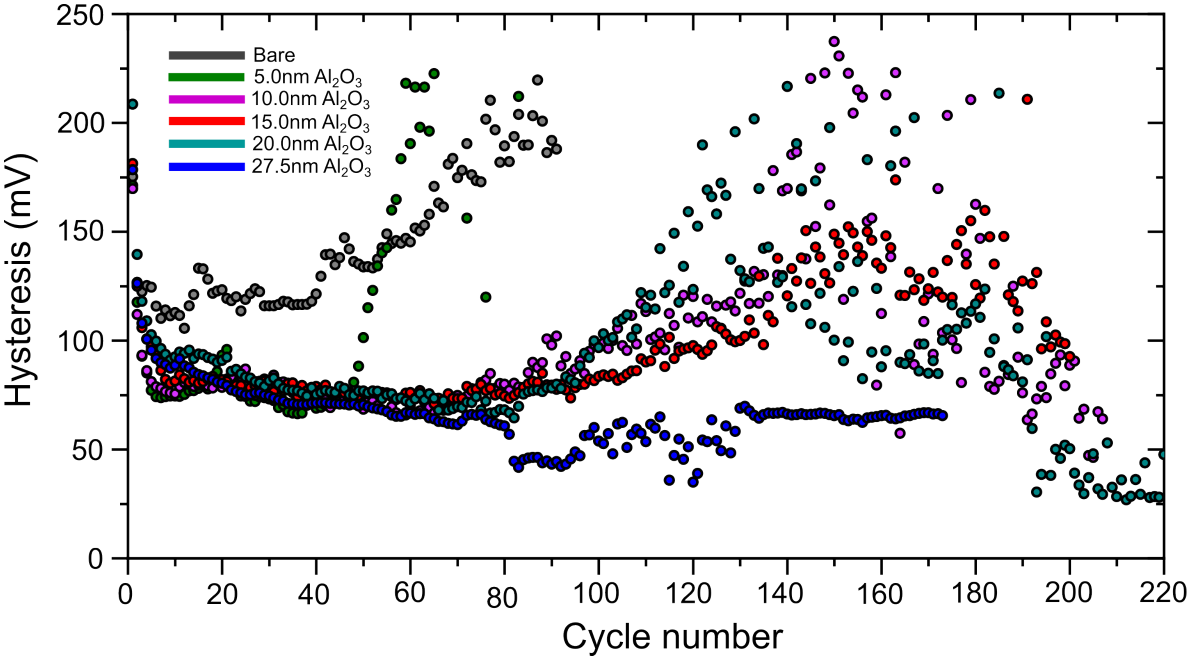

Figure 4.16: Figure showing the CE of uncoated Cu, 5.0, 10.0, 15.0, 20.0 and 27.5nm Al_2O_3 overlayed for ease of interpretation

4.4.1 Investigating how coating thickness affects the deposition of lithium

The following section aims to identify how the different thicknesses of Al_2O_3 coatings affect the deposition of lithium onto copper. To do this, thicknesses of copper including uncoated, 2.5nm, 5.0nmm, 15nm and 27.5nm Al_2O_3 were obtained and $1mAh/cm^2$ was deposited onto their surfaces at $1mA/cm^2$ to mimic the half cell work analysed prior to this, these are represented in figures 4.17 (a)-(e) respectively. The cells were then disassembled and were photographed using a camera before being incorporated into an SEM for higher magnification imaging.

Figure 4.17 (a) highlights deposition onto the uncoated copper cell. It is evident that the deposition is covering much more of the surface of the copper then coated cells and from looking under the SEM (ai) and (aii) this deposition appears to be mossy. The 2.5nm Al_2O_3 coatings also shows good coverage of the electrode within the area of the counter electrode (b). When looking under SEM (bi) and (bii) the deposition appears to be less conformal with the formation of mossy islands. at 5nm is evident that these islands are becoming more spatially resolved as the thickness of Al_2O_3 is increased. This data strengthens the the work performed by Oyakshire et al who mention the Al_2O_3 promotes spares nucleation of lithium during plating [4]. At 15nm and 27.5nm Al_2O_3 the clusters appear the most sparse out of all the thicknesses.

Unlike the work performed by Oyakshire et al who show non mossy lithium deposits, despite the lithium deposits evidently becoming more sparse with the thickness of the coating increasing they appear to still be growing mossy in the case for the work conducted in this section. After looking into this further I can suggest that the pressure distribution as a result of crimping the cell is not uniform and plays a large role in the deposition. Figure 4.18 shows SEM images take from the 27.5nm Al_2O_3 cell, the red highlighted box in figure 4.18 (aiii) indicates non mossy deposits towards the edges of the copper whilst the green box indicates central deposits that are clearly mossy, (ai) and (aii) highlight the central and edge regions in higher magnification respectably . It was noticed that around the edges of the copper substrate the deposits appeared to be non dendritic which was expected to be due to the pressure around the edges here to be different then around the centre region of the copper as a result of the circular geometry of the spring used. To further evidence this, some cells for the sodium ion work showed deposition around the edges of the sodium and not in the centre which suggests again pressure plays a role, this can be seen in appendix 8.4, it has also been mentioned in research by willow et al that pressure plays an important role in cell cycling [15]. It's possible that this mossy growth is leading to much higher surface area deposits of lithium which are responsible for the cycle life being much lower then the work performed by Oyakshire et al who achieved in excess of 300 cycles for their half cells and did not report mossy growth for their 8nm Al_2O_3 coated samples.

To make the pressure of crimping as consistent as possible, firstly the electrodes were weighed to ensure the weight of them was as consistent as possible. Given that the cut area was the same, for the weight to be the same, the thickness of the electrodes would have to be similar. As- well as this, mechanical crimping was stopped as soon as the pressure met the desired value on the dial, relaxation of the pressure did occur however this was assumed the same for every cell. Ideally, electrical crimping would have led to a reduction in the variation of pressure however, we did not have access to this apparatus. EIS could have been employed to determine general differences in pressure as the charge transfer is affected by pressure but it would not allow the determination of localised pressure differences over the electrode which is something seen for the cells in this thesis.

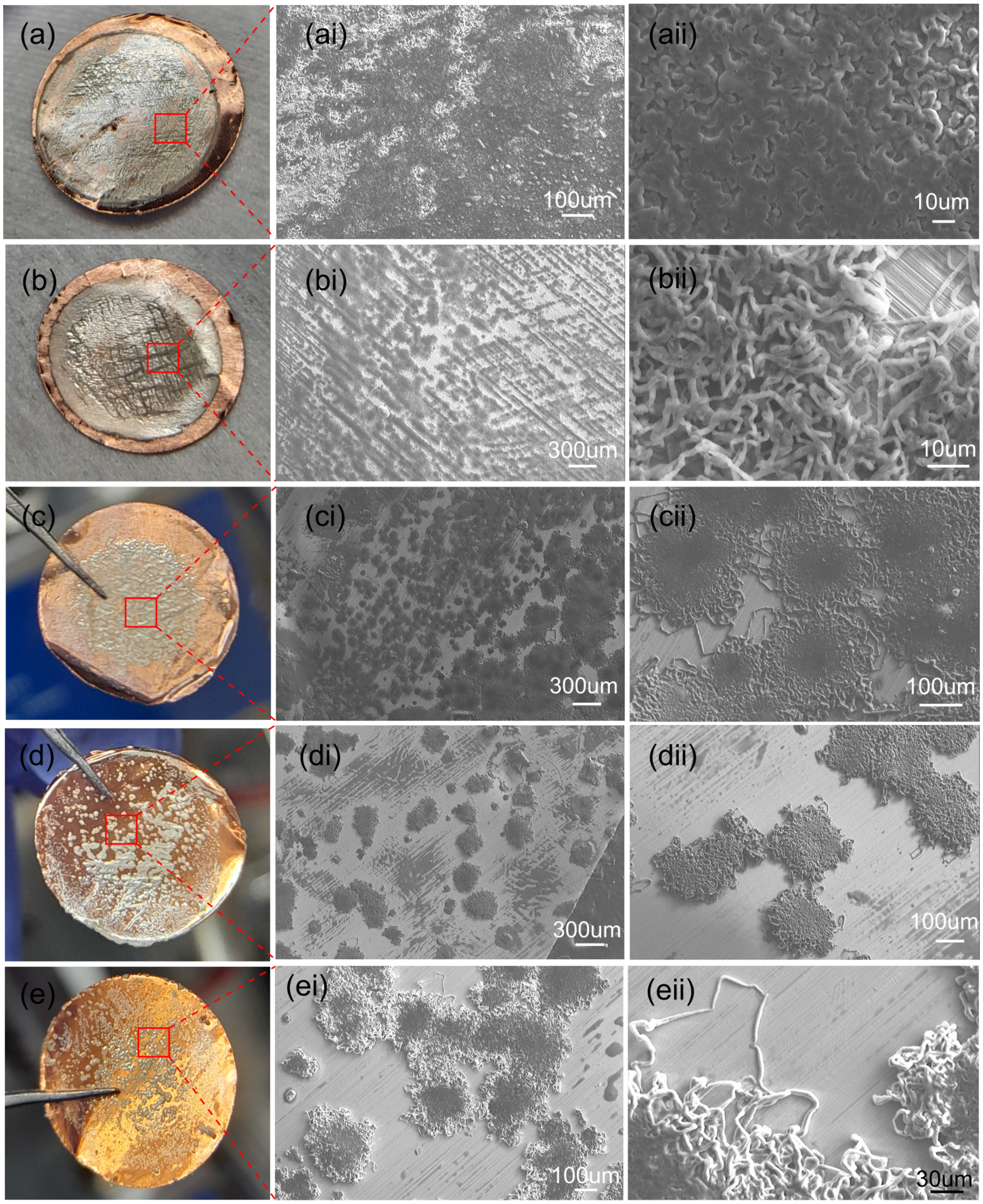

Figure 4.17: Optical and SEM images showing the $1mAh/cm^2$ of lithium plating at a current rate of $1mA/cm^2$ for Al_2O_3 coated copper half cells. These include thicknesses of (a)- (aii) bare copper, (b)-(bii) 2.5nm, (c)-(cii) 5.0nm, (d)-(dii) 15.0nm and (e)-(eii) 27.5nm Al_2O_3.

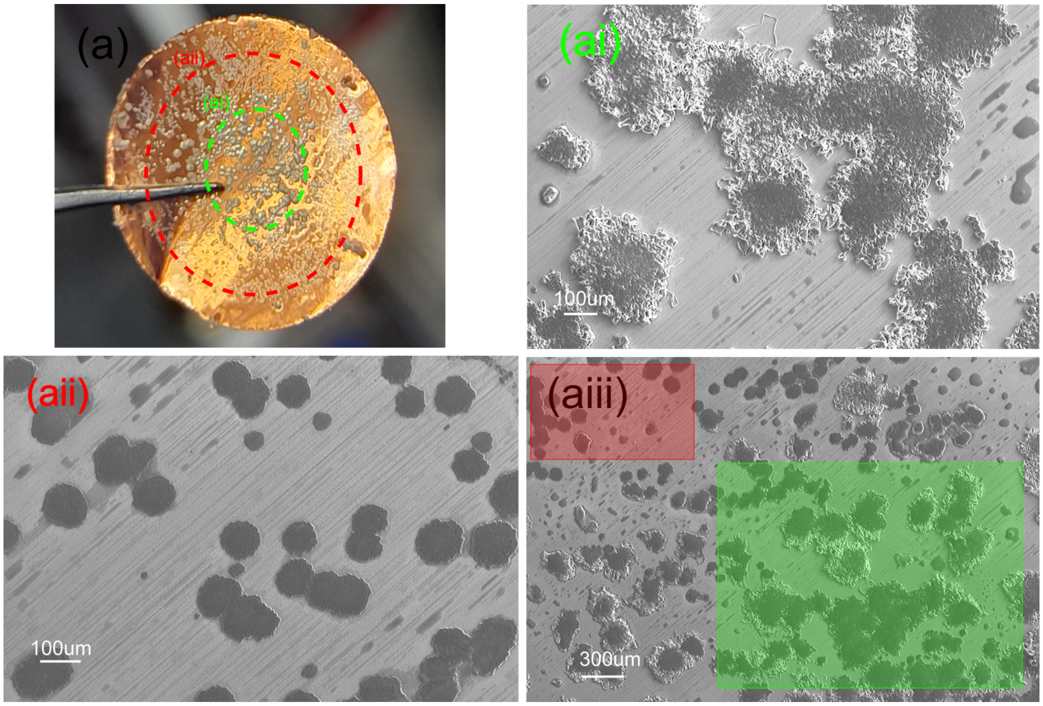

Figure 4.18: optical and SEM images showing how the deposition of lithium changes from non mossy to mossy depending on the location on the electrode. (a) shows optical image of copper with markers highlighting regions where plating is non mossy (red) and mossy (green). (ai) and (aii) show SEM images of areas take on the lines highlighted in (a). (aiii) shows low magnification SEM images of areas including regions of mossy and non mossy growth.

4.5 Conclusion and future work

The following chapter investigates the application of MVD Al_2O_3 onto copper for enhancing the cyclability of lithium ion anode free half cells. Whilst research exists in the area the chapter focuses on MVD deposition which has not been attempted to data and also focuses on determining an optimal coating thickness. Thicknesses including uncoated, 2.5, 5.0, 10.0, 15.0, 27.5 and 45nm were investigated. The results from the charge discharge data show the cycle life of the cells is increased by increasing the coating thickness up to 15.0nm Al_2O_3 after which the cycle life begins to decrease. To understand why, camera and SEM images were taken of the lithium plating on the copper which showed high surface area mossy lithium deposits over the surface area of the uncoated copper which lead to more severe uncontrollable SEI growth during cycling leading to cell failure by the mechanism highlighted in section 2.4.1. As the thickness of the Al_2O_3 increases, these deposits appear to become smaller with a lower surface area then the previous thickness which leads to less severe SEI growth from occuring and therefor increasing the cycle life of cells. Despite the presents of Al_2O_3, mossy growth was still observed and suggestions were made with regards to the inconsistent pressure distribution across the copper causing this due to the nature of the spring used during the cells crimping process. This inconsitency made it very difficult to compare the MVD to ALD tools used in other articles. Although cyclability was not the best seen in literature which was expected due to the mossy growth not reported in similar studies for Al_2O_3 coated cells, the mechanism for which the coating function supports work performed in recent studies published in nature [4].

To continue the work performed and address the weaknesses associated with it, this paragraph will highlight some future work and ideas which could be performed if more time and resources were available. Currently no suggestion has been made as to why the coating becomes less effective at thicker quantities therefor this will need to be addressed. To start a nucleation study could be performed on a 45nm Al_2O_3 coated copper sample to observe the distribution of lithium deposits, a personal hypothesis would be that perhaps very thick coatings limit the number of nucleation points on the copper due to fewer pinholes therefor physically preventing electrodeposition from taking place thus reducing the cycle life of the cell. Oyakshire et al patterned bare copper circular areas into 50nm Al_2O_3 coating and showed that the lithium plated on the bare copper circles and not on the Al_2O_3 coated areas, it was expected this phenomena was seen in this chapters results. [4, 16]. To strengthen the SEM study, additional areas on the surface on the copper will need to be observed and average particle sizes could be obbtsined to suggest how the coating changes these variables. As well as this, XPS depth studies would need to be performed to allow for a determination of the location of the Al_2O_3 layer. This will allow a better understanding as to how the layer is performing and would address some theories that exist suggesting the layer acts as an artificial SEI layer mentioned in the literature review. As well as focusing on the coating, the suggestion of the pressure having an affect on the deposition would need to be further explored to confirm its affect. This could be done by using different springs and spring orientations combined with SEM imaging similar those present in the above study. This could be combined with crimping the cells at different mechanical pressures as well. Additional work would be attempted with regards to testing larger areas of copper such as pouch cells to see the affect of plating lithium on larger area substrates which are more commercially relevant. Finally testing the cells in a full cell format vs standard cathode materials such as Lithium iron phosphate ($LiFePO_4$) could further indicate the commercial potential of MVD Al_2O_3 coatings for lithium anode free batteries. If the cathode has an areal capacity of 1mah/cm2 and is incorporated into a full cell. If the cell is fully charged, an areal capacity of 1mah/cm2 of lithium from the cathode will be plated onto the current collector. This assumes that the cathode, in a full-cell configuration, contains an equivalent areal capacity of lithium. This assumption is consistent with values reported in the literature and is considered reasonable for modeling and analysis purposes [17].

Bibliography

[1] Allen Pei, Guangyuan Zheng, Feifei Shi, Yuzhang Li, and Yi Cui. Nanoscale nucleation and growth of electrodeposited lithium metal. *Nano letters*, 17(2):1132–1139, 2017.

[2] Jiangyan Wang, William Huang, Allen Pei, Yuzhang Li, Feifei Shi, Xiaoyun Yu, and Yi Cui. Improving cyclability of li metal batteries at elevated temperatures and its origin revealed by cryo-electron microscopy. *Nature Energy*, 4(8):664–670, 2019.

[3] Kai Yan, Zhenda Lu, Hyun-Wook Lee, Feng Xiong, Po-Chun Hsu, Yuzhang Li, Jie Zhao, Steven Chu, and Yi Cui. Selective deposition and stable encapsulation of lithium through heterogeneous seeded growth. *Nature Energy*, 1(3):1–8, 2016.

[4] Solomon T Oyakhire, Wenbo Zhang, Andrew Shin, Rong Xu, David T Boyle, Zhiao Yu, Yusheng Ye, Yufei Yang, James A Raiford, William Huang, et al. Electrical resistance of the current collector controls lithium morphology. *Nature communications*, 13(1):3986, 2022.

[5] Lin Chen, Justin G Connell, Anmin Nie, Zhennan Huang, Kevin R Zavadil, Kyle C Klavetter, Yifei Yuan, Soroosh Sharifi-Asl, Reza Shahbazian-Yassar, Joseph A Libera, et al. Lithium metal protected by atomic layer deposition metal oxide for high performance anodes. *Journal of Materials Chemistry A*, 5(24):12297–12309, 2017.

[6] Gregory Burwell, Klaudia Rejnhard, Jon Evans, Jacob Mitchell, Michael T Grimes, Matt Elwin, Ardalan Armin, and Paul Meredith. A low-temperature batch process for the deposition of high-quality conformal alumina thin films for electronic applications. *Advanced Engineering Materials*, 2023.

[7] Ivan Khalakhan, Mykhailo Vorokhta, Xianxian Xie, Lesia Piliai, and Iva Matolínová. On the interpretation of x-ray photoelectron spectra of pt-cu bimetallic alloys. *Journal of Electron Spectroscopy and Related Phenomena*, 246:147027, 2021.

[8] Ayaka Fujimoto, Yasuhiro Yamada, Michio Koinuma, and Satoshi Sato. Origins of sp3c peaks in c1s x-ray photoelectron spectra of carbon materials. *Analytical chemistry*, 88(12):6110–6114, 2016.

[9] Sefik Suzer. Differential charging in x-ray photoelectron spectroscopy: a nuisance or a useful tool? *Analytical chemistry*, 75(24):7026–7029, 2003.

[10] Georgios P Gakis, Constantin Vahlas, Hugues Vergnes, Sandrine Dourdain, Yann Tison, Hervé Martinez, Jerôme Bour, David Ruch, Andreas G Boudouvis, Brigitte Caussat, et al. Investigation of the initial deposition steps and the interfacial layer of atomic layer deposited (ald) al2o3 on si. *Applied Surface Science*, 492:245–254, 2019.

[11] Daniel R Jones, Robert Phillips, William JF Gannon, Bertrand Rome, Michael EA Warwick, and Charles W Dunnill. Photocapacitive cds/wox nanostructures for solar energy storage. *Scientific Reports*, 9(1):11573, 2019.

[12] Chen-Jui Huang, Balamurugan Thirumalraj, Hsien-Chu Tao, Kassie Nigus Shitaw, Hogiartha Sutiono, Tesfaye Teka Hagos, Tamene Tadesse Beyene, Li-Ming Kuo, Chun-Chieh Wang, She-Huang Wu, et al. Decoupling the origins of irreversible coulombic efficiency in anode-free lithium metal batteries. *Nature Communications*, 12(1):1452, 2021.

[13] Yanying Lu, Qiu Zhang, Mo Han, and Jun Chen. Stable na plating/stripping electrochemistry realized by a 3d cu current collector with thin nanowires. *Chemical Communications*, 53(96):12910–12913, 2017.

[14] Wenbo Zhang, Philaphon Sayavong, Xin Xiao, Solomon T Oyakhire, Sanzeeda Baig Shuchi, Rafael A Vilá, David T Boyle, Sang Cheol Kim, Mun Sek Kim, Sarah E Holmes, et al. Recovery of isolated lithium through discharged state calendar ageing. *Nature*, 626(7998):306–312, 2024.

[15] Ashley Willow, Haytham EM Hussein, Sutthiphan Vajirakaphan, Aphidet Chasri, and Serena Margadonna. Improving in-situ sodium metal plating on copper foil through optimization of mechanical pressure: Towards high-performance anode-free sodium ion batteries. *Frontiers in Energy Research*, 10:888321, 2022.

[16] Julia Litvinov, Yi-Ju Wang, Jinnie George, Pawilai Chinwangso, Stanko Brankovic, Richard C Willson, and Dmitri Litvinov. Development of pinhole-free amorphous aluminum oxide protective layers for biomedical device applications. *Surface and Coatings Technology*, 224:101–108, 2013.

[17] Jean Pierre Mwizerwa, Changyong Liu, Kun Xu, Ning Zhao, Yide Li, Zhangwei Chen, and Jun Shen. Three-dimensional printed lithium iron phosphate coated with magnesium oxide cathode with improved areal capacity and ultralong cycling stability for high performance lithium-ion batteries. *Journal of Colloid and Interface Science*, 623:168–181, 2022.

Chapter 5

ZnO for lithiophillic carbon electrodes

5.1 introduction

Whilst the majority of the work conducted for this thesis included the application of Al_2O_3 for sodium and lithium anode free batteries other smaller studies were conducted utilising different MVD coatings and technologies. This chapter focuses on the use of 2d carbon current collectors which is lithiated with ZnO to reduce the local current density due to its large specific surface area. This also allows for homogeneous charge distribution for Li nucleation which as a consequence delays the growth rate of lithium dendrites. Due to the lithiophillic properties of ZnO mentioned in section 2.5 ZnO is implemented onto carbon based electrodes to improve the lithiophilicity and provide nucleation sites for the Li metal. Although similar experiments have been conducted in the field using ALD processes, this chapter focuses on the deposition by MVD. Due to the higher quoted aspect ratio of MVD which comes about due to it's novel deposition method, similar experiments were conducted to see if this process could offer any advantages to the nucleation site distribution and therefor the performance [1][2].

5.2 Deposition

MVD deposition of ZnO onto carbon electrodes was performed using precursors DEZ and water as highlighted in the materials and methodology section 3.4.2. The process parameters used included a VDM pressure of 1.4 torr and a water dose of 1.4 torr per MVD cycle, the chamber temperature was 125^oC, thickness calculations and quality were performed using ellipsometry. Due to the available time slot these process parameters were not optimised for our specific material and a standard process was selected based on the work performed in chapter 5 of Klaudia Rejnhards thesis [3].

5.3 characterisation

5.3.1 SEM

Carbon electrode material were cut into 16mm electrodes and coated with Zinc oxide using the stainless steel baffels to prevent samples from moving around inside of the chamber. thicknesses including 5nm, 15nm, 27.5nm and 50nm of zinc oxide were coated to asses how the thickness variable affects the quality of electrodeposition and electrostripping. Figure 1 (a) shows the electrodes after they have been coated. The 50nm appears blue, the 25nm appears a yellow color whilst the coating cannot be seen for the 5nm sample which gives the first indication that the coating process was successful, images showing similar results can be seen in the work performed by Zhao et al for comparison [1]. Figures 5.1 (b) shows the fibrous carbon electrode which has a high surface area and a high aspect ratio. Figures 5.1 (c) and (d) show the uncoated vs 50nm ZnO coated sample under SEM respectively. From figure 5.1 (d) it is evident that the ZnO is present on the fibre due to the formation of what appear to be islands which could correspond to the crystalline structure of ZnO, similar structure was observed by Klaudia Rejnhard [3].

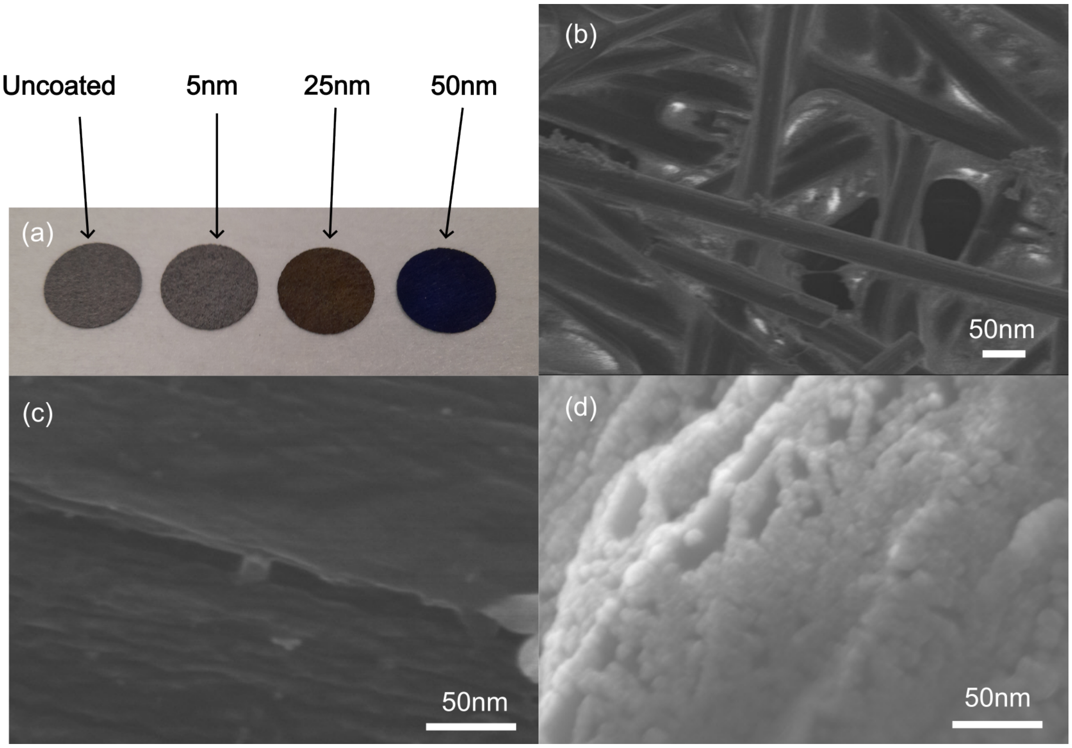

Figure 5.1: SEM and optical images showing the charaterisation of ZnO. (a) highlights the optical changes as the coating thickness is increased, (b) SEM showing the fibrous carbon structure of the electrodes uncoated, (c) SEM showing high magnification of an electrode fibre without any coating, (d) SEM showing the ZnO deposition onto the fibrous carbon electrode.

5.3.2 XPS

Figure 5.2 shows the XPS spectra of ZnO which includes C1s, O1s and Zn2p (a),(b),(c) respectively. The spectra was calibrated using the adventitious carbon peak at 284.8eV. The C1s peak is very weak and consists of 3 components at 284.8eV, 286eV and 289eV which align themselves with C-C, C-O and C=O bonds which are expected to belong to adventitious carbon contamination. Due to the fact that the carbon signal is so weak and that the ZnO is very thick, it is unlikely the underlying carbon from the electrode is present in the spectra so this was deemed contamination and not trapped carbon in the film. In the future it would be best to do a small adventitious carbon etch to remove this layer before starting the high resolution scans [4]. The O1s peak shows a strong signal at 530.4eV which aligns itself with the Zn-O peaks corresponding to literature. The smaller peak at 532.4eV was expected to belong to C-O bonds from the adventitious carbon layer [5, 6]. Figure 5.2 (c) highlights the Zn2p doublet with Zn2p1/2 at 1045 eV and Zn2p3/2 at 1022eV which are common locations for the Zn2p doublet in literature [7].

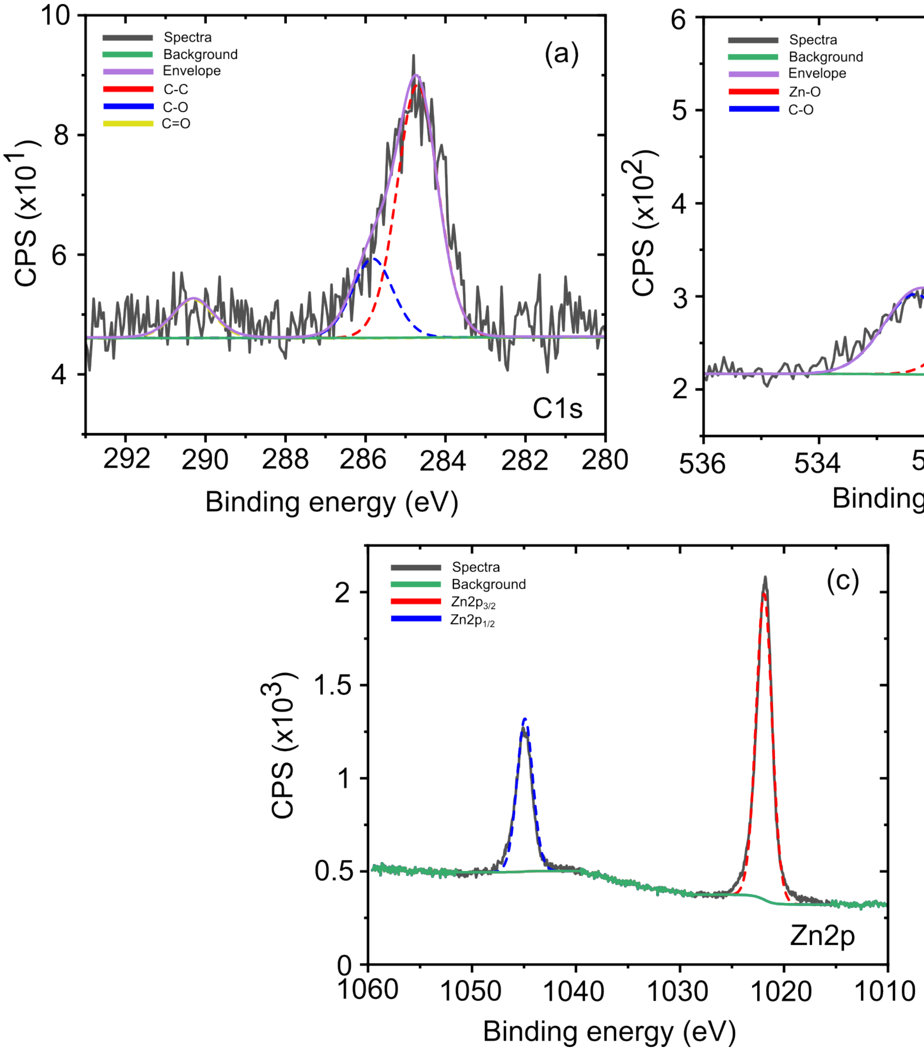

Figure 5.2: XPS showing the electrodes after being coated with MVD ZnO. (a) C1s spectra, (b) O1s spectra, (c) Zn2p spectra

5.4 electrochemical infusion of lithium into the carbon matrix insitu

Initially carbon samples were incorporated into a half cells as the working electrode vs a solid lithium counter electrode to asses how the ZnO coating affect the insertion of lithium into the matrix and to asses how feasible this process is. The cells were cycled galvanostatically at a current rate of $1ma/cm^2$ with a lithium loading of $1mah/cm^2$, the electroylte was 1 M LiTFSI in DOL/DME (1:1) with 5% $LiNO_3$ by weight. CE and hysteresis values were extracted and plotted. Figure 5.3 shows the results of the galvanostatic charge discharge experiments, cells tested were carbon fibre electrodes Uncoated, 2.5nm, 15.0nm and 27.5nm ZnO respectively. Figures 5.3 shows the results of the GCD experiments, for all samples the inital cycles (ai),(bi),(ci) and (di) seem to be particularly unstable with a very short stripping cycle, the uncoated cell (showing noise on the plating cycles) is particularly unstable which could be due to the fact no ZnO is present to assist with lithiation of the carbon, this generally takes around 40 cycles for all samples. After this, the plating and stripping appears to be stable with a low hysteresis (aii), (bii), (cii), (dii). Towards the end of cycling (aiii), (biii), (ciii) and (diii) cycling becomes unstable with an elevated hysteresis and the presents of noise on the charge and discharge, this is also met by a decrease in CE. I expect towards the end of cycling the dendritic growth begins and causes unstable growth of the SEI similar to that seen in chapter 4.

Figure 5.4 and 5.5 shows the CE data. From looking at the CE, the first thing to notice is for all samples, the value gradually increase from 0 to between 90 and 100% which takes around 40 cycles. As the samples are not lithiated prior to experimentation (unlike the molten infused experiments in the next section), This could be due to it taking 40 cycles to fully lithiate the ZnO coating to form Li-Zn alloy which has been previously highlighted by Outang et al who performed similar work [8]. As a similar response can be observed for the uncoated carbon electrode, I expect the phenomena could also be due to the formation of the SEI which is much more extensive due to the larger surface area electrodes when compared to (relatively) planer copper current collectors studied before [9]. Once fully lithiated, the CE remains consistent around 90-100% before fading for all samples figure 5.4 (a)-(d). For the uncoated sample, (figure 5.4 (a) this fade begins at around cycle 120 and reduces to 60% by cycle 160. For the 2.5nm ZnO coated sample figure 5.4 (b), the CE becomes irratic with a general downwards trend from cycle 80.During this erratic period, some cycles reach the upper time curoff causing a 100% CE. For the 15nm ZnO coated sample figure 5.4 (c), after 40 cycles the CE remains between 90 and 100% up to 210 cycles where it begins to fade rapidly to point where the cell was stopped, this cell performed the best out of the 4 samples. The thicker coating of 27.5nm

ZnO figure 5.4 (d) yields similar results to 15nm however the capacity fade begins slightly earlier at 180 cycles. Figure 5.5 shows the overlayed CE values for better comparison. From the GCD graphs it is evident that the fade in CE is accompanied by an increase in hysteresis seen in chapter 4. By taking the failure of the battery when the CE falls below 80% we can determine the cycle life for this work. The results can be seen in figure 5.5 which shows the uncoated cycle life at 128 cycles, 2.5nm ZnO at 144 cycles, 15.0nm ZnO at 224 cycles and 27.5nm at 192 cycles. It is worth noting that the initial low CE values at the start of cycling were disregarded for this analysis despite being a very important part to consider. The 2.5nm cell shows alot of variation in the CE before reaching 80% whilst the other cells CE decreases abruptly. The large difference between 2.5nm and 15nm could indicate the at 2.5nm the ZnO coating is not having that much of an affect on the cycling.

To discuss the results further it is possible that the optimal thickness of ZnO could be located between 5nm ZnO and 27.5nm as 15nm ZnO has the best performance in terms of CE fade and hysteresis increase. Despite this observation this technique was not considered feasible for large scale energy storage. The CE for the first 40 cycles for all samples increases gradually which suggests lithium is consumed initially forming the Li-ZnO as well as the solid electrolyte interphase. If a cathode was present in a full cell with a finite amount of lithium intercolated into the matrix, the capacity would likely decrease rapidly in the first few cycles in forming these layers making the battery sub optimal.

Figure 5.6 (d) - (f) highlights in-situ optical microscopy experiments showing the cycling of the carbon electrode coated with Zn-O at current rate of $1ma/cm^2$. As the cell is subject to negative current the electrode turns from blue to a silver coloration which is more obvious as the cell is left for longer at this current rate. figure 5.6 (d) shows the silver colouration is very local to the edge of the carbon electrode closest to the counter electrode. (e) shows the grey colour is very consistent over the surface of the electrode indicating that the lithiation is very consistent. (f) shows lighter grey patches appearing on the electrode, at this point bubbles of Argon appear in the cell from assembly, these are likely due to trapped argon on the porous electrode being replaced with lithium and therefor being forced out into the electrolyte.

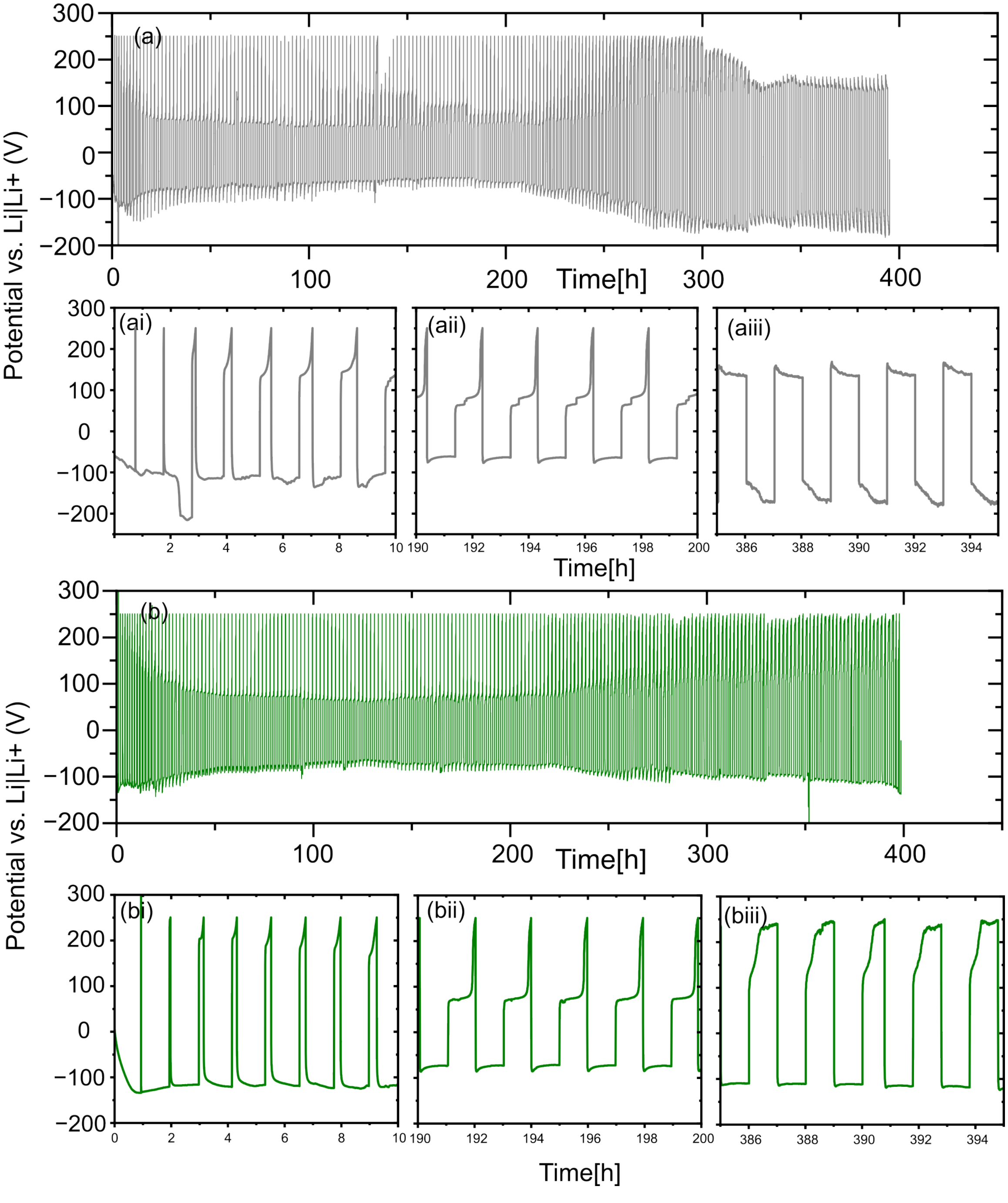
(a)
Potential vs. Li|Li+ (V)
300
200
100
0
−100
−200
0
100
200
300
400
Time[h]
(ai)
(aii)
(aiii)
2
4
6
8
10
190
192
194
196
198
200
386
388
390
392
394
Time[h]
(b)
(bi)
(bii)
(biii)
Time[h]

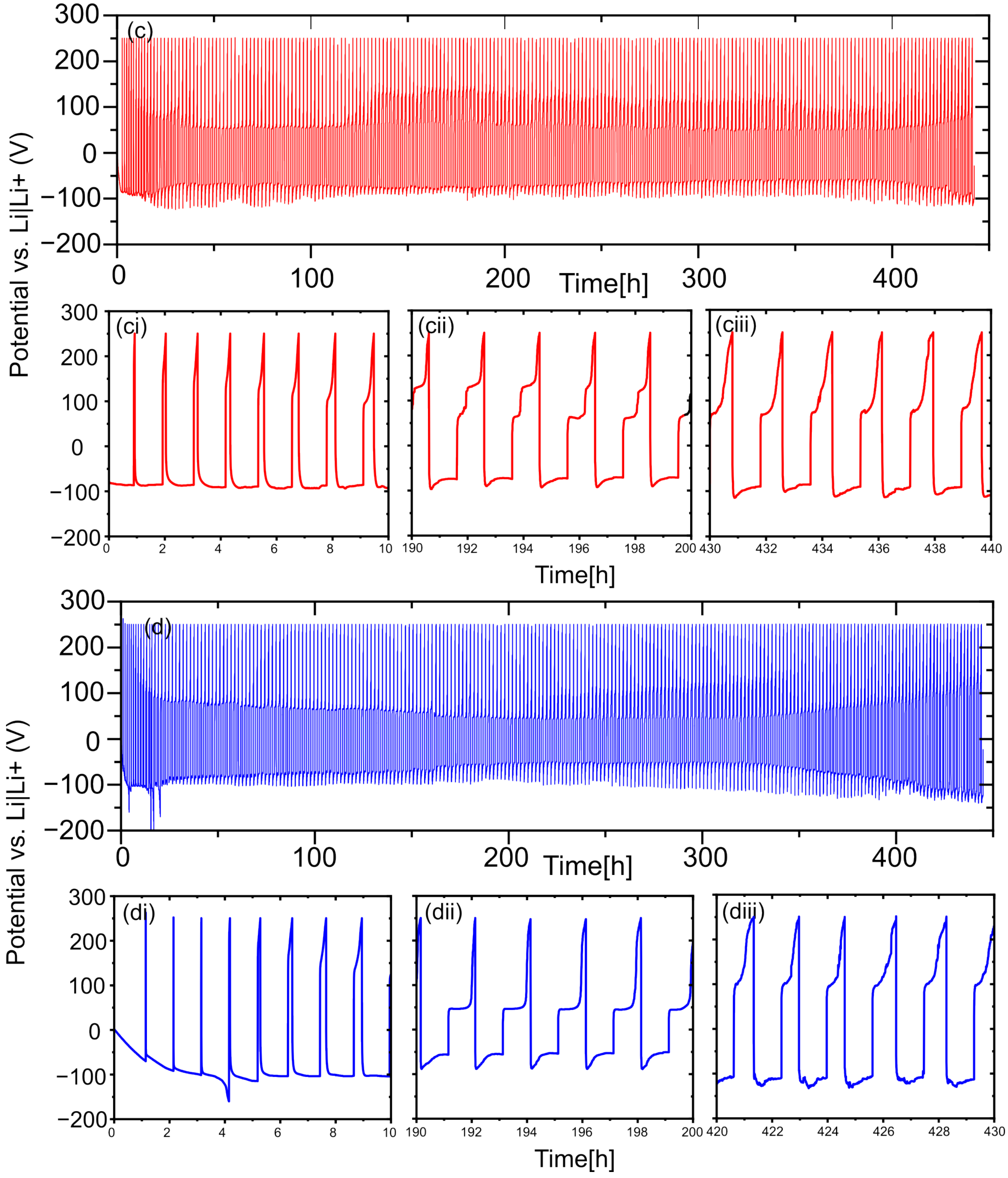

Figure 5.3: graphs showing the GCD of the MVD ZnO coated fibrous carbon electrodes of thicknesses including (a) uncoated, (b) 2.5nm ZnO, (C) 15.0nm ZnO and (d) 27.5nm ZnO

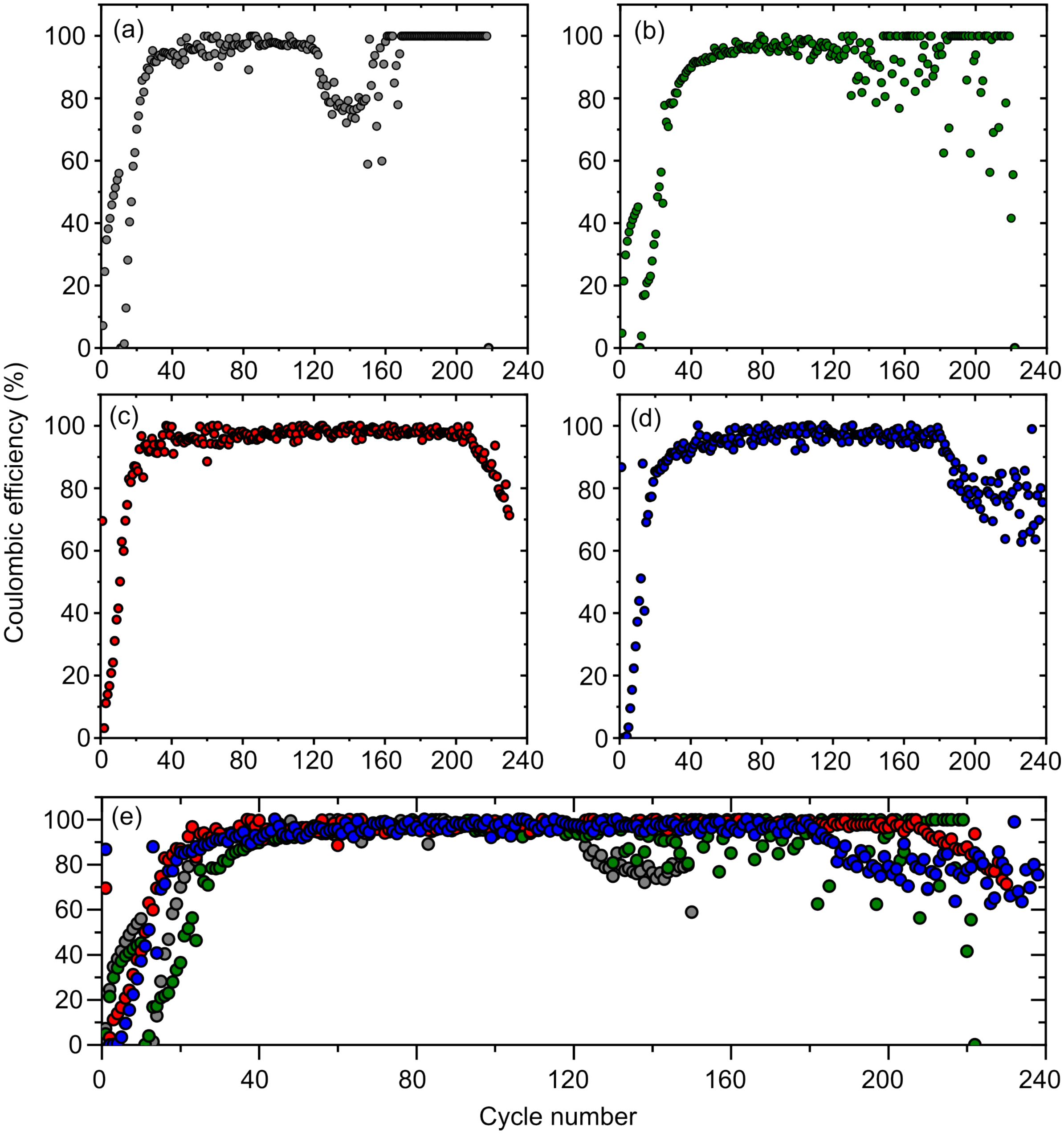

Figure 5.4: Graphs showing the CE data from the MVD ZnO coated fibrous carbon electrodes of thicknesses including (a) uncoated, (b) 2.5nm ZnO, (C) 15.0nm ZnO, (d) 27.5nm ZnO and (e) showing the overlayed data

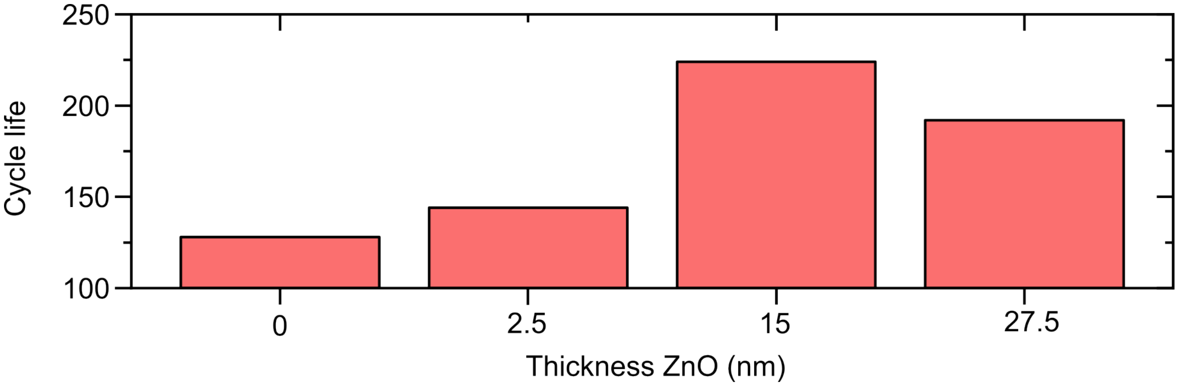

Figure 5.5: Bar chart showing the number of cycles to failure for the ZnO coated carbon half cells, failure was determined when the CE was less that 80%

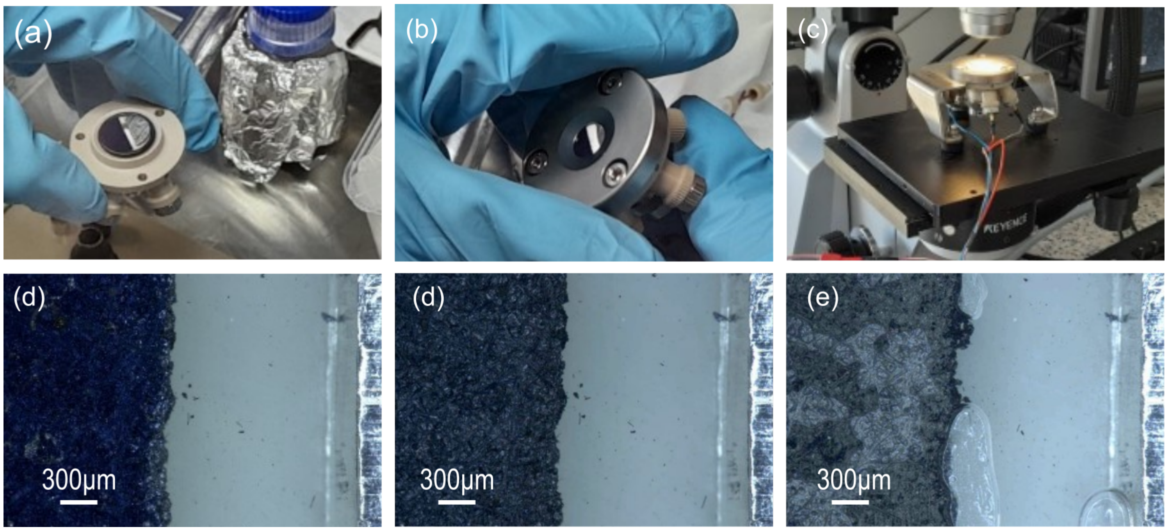

Figure 5.6: Microscope images showing the lithiation of ZnO coated carbon images (a),(b) and (c) show the experimental setup. Images (d),(e) and (f) show the lithiation at 0, 5minutes and 60 minutes respectively

5.5 Prelithiation of carbon by molten metal

To overcome the poor CE for initial cycling carbon was soaked in molten lithium to create a lithium rich electrode before being incorporated into a half cell. This technique is more industrial feasible as electrodes don't need to be incorporated into an electrochemical cell and this process can be done ex situ prior to cell manufacture.

5.5.1 Li infusion into carbon current collectors

Before cycling, lithium metal was infused into the carbon fibre matrix. Electrodes were placed in a molten pool of lithium seen in figure 5.7 (a) and the time taken for the lithium to diffuse into the electrode was taken (the endpoint of this experiment was determined by eye). The lithium was prepared as highlighted in the experimental section section (3.1.4). For the 50nm sample, the lithium diffusion was very efficient taking only 45 seconds to saturate. The 25nm sample took 2 minutes whilst the uncoated sample and 5nm coated sample did not fully saturate so were left for 24hours and used after this time regardless of the amount of lithium infused for comparison. From the results of this experiment the thicker the ZnO coating allows for more efficient saturation of lithium into the electrode. Three different samples of ZnO on coated carbon were tested including an Li-Li symmetric cell, a LiC-Li cell (uncoated carbon infused with lithium) and 50nm ZnOLiC-Li (lithiated zinc oxide coated carbon cell). The 50nm ZnO coated sample was selected for experiments as it appeared to become infused with lithium the fastest. The Li-Li control cell was used to compare directly to the infused samples.

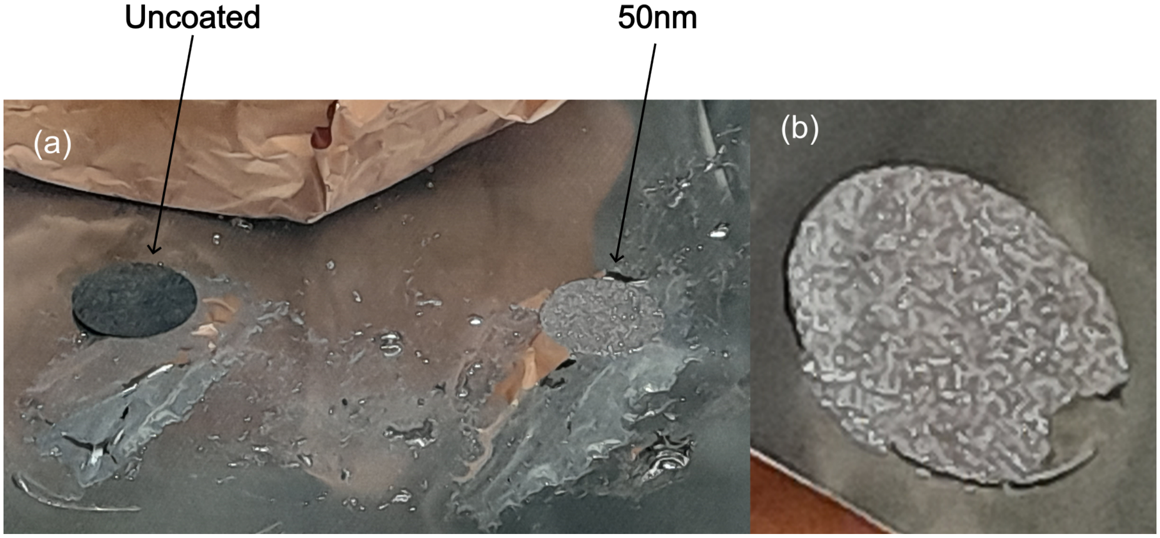

Figure 5.7: camera images highlighting the molten infusion of lithium into a fibrous carbon electrode (left) and a ZnO coated fibrous carbon electrode (right)

5.5.2 Charge-discharge lithium infused electrodes ZnO - DOL electrolyte

Lithiated electrodes were incorporated into 2032 coin cells in a LiC-Li format with the LiC as the working electrode. The electrolyte used was 1 M LiTFSI in DOL:DME (1:1). The cells were cycled at $1mA/cm^2$ for 1hour per half cycle which calculates to a capacity of $1mAh/cm^2$. Cells were initially precycled in a waterfall like style including 10 cycles of the following current densities and capacities; $0.05mAcm^2$ at $0.05mAh/cm^2$, $0.1mAcm^2$ at $0.1mAh/cm^2$, $0.25mAcm^2$ at $0.25mAh/cm^2$, $0.5mA/cm^2$ at $0.5mAh/cm^2$ and finally $1mA/cm^2$ at $1mAh/cm^2$ where they were left to cycle.

Figure 5.8 (a)-(c) shows the results of the charge discharge experiments separated whilst figure 5.8 (d) shows the overlayed results with some expanded areas to allow for better comparison of results. The first thing to notice is for the first 5 cycles (figure 5.8 (di)) precycling the response from the Li-Li and LiC-Li samples shows a square response with no sharp overpotentials, which suggests that plating and stripping is occurring in a relatively similar manner for the two samples, the 50nm coated sample shows a much larger hysteresis 55mV vs 20 and 25mv for the previous two samples respectively with a higher nucleation potential of -35mV. The hysteresis for the first 20 cycles is slightly higher for the ZnOC-Li then the Li-Li and LiC-Li samples. At 45 cycles figure 5.8 (diii) the potential response shows a sharp overpotential at the start and end of cycling which is observed similarly by Ouyang et al but not explained [8]. The hysteresis of all cells gradually decreases after the pre-cycling reaches $1mA/cm^2$ at 40 cycles and the sharp overpotentials become less prolifant to the point where the deposition is more square figure 5.8 (div)-(dvi). This can be more easily observed by figure 5.10 (a)-(d). At around 260 cycles, the hysteresis for the Li-Li and LiC-Li cells increase slightly figure 5.10 (d) before cells were stopped which could imply the onset of cell failure which is observed by Zhao and Ouyang et al [1, 8]. After 40 cycles the hysteresis of the ZnOC-Li is on average 5mV (by eye) less then the Li-Li and 10mV less then the LiC-Li cell throughout cycling as obtained by figure 5.10 (d).

To offer some explanation for this data, due to the hysteresis being higher at the start of cycling, it would suggest that the resistance within the cell is greater so a higher over-potential is required for cycling. The thick ZnO coating could be inhibiting ion movement into the electrode and therefor be responsible for this however given that the sample has been prelithiated this response was not expected. Typically the hysteresis

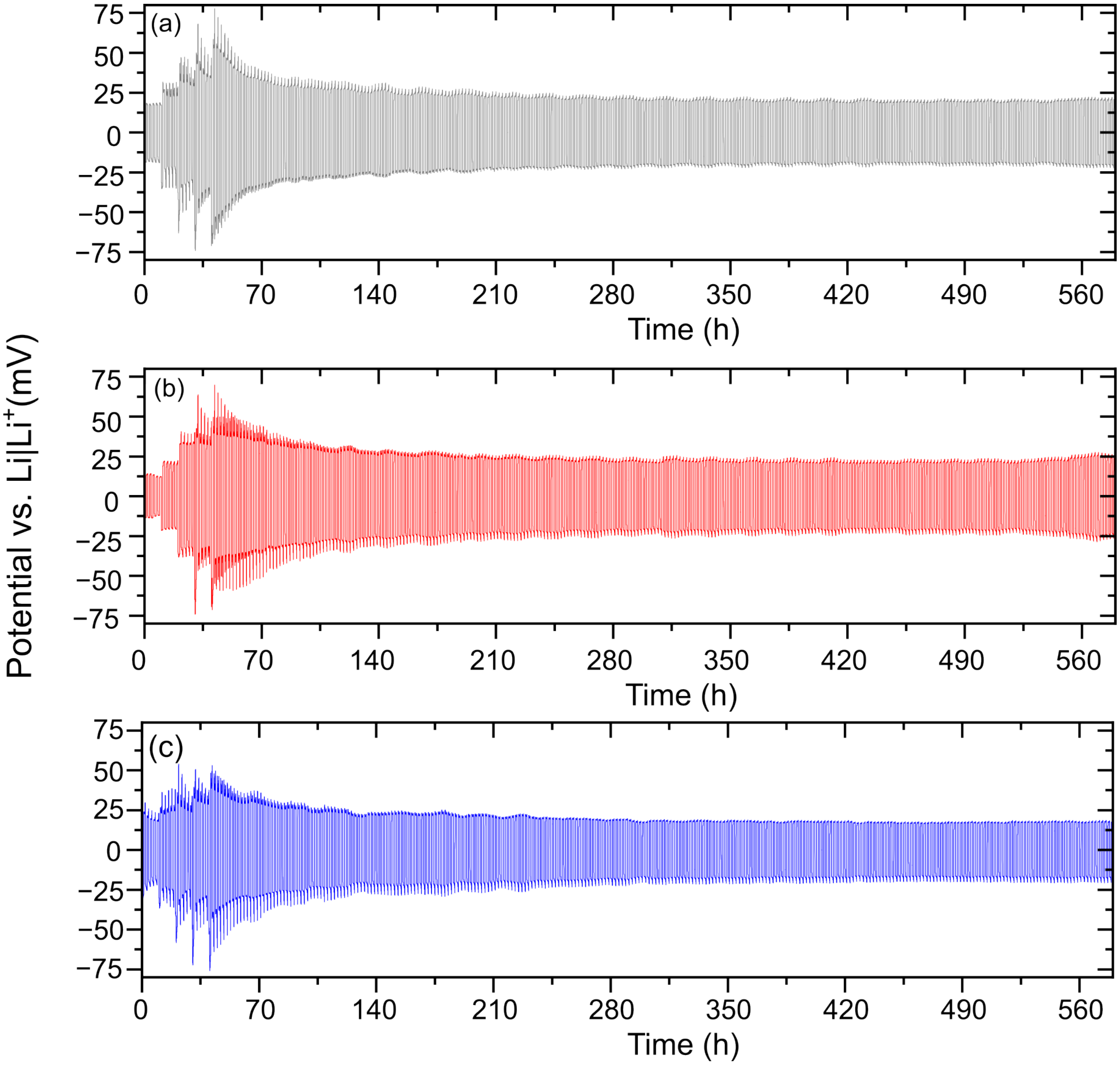

Figure 5.8: Graph showing GCD results of the molten lithium infused carbon samples in half cell format,(a) Li-Li cell, (b) LiC- Li cell, (c) 50nm ZnOLiC cell

is much higher throughout cycling for the Li-Li control as seen in the work by Ouyang et al [8]. Between 40 and 45 cycles as the current is increased during precycling, the hysteresis becomes slightly lower for the ZnO coated electrode and remains as such throughout the remainder of cycling figure 5.9 (d). The CE for the 3 samples shows a similar response and is consistent around 99.9% throughout cycling for all the samples figure 5.10 (a)-(d). The first cycle efficiency appears at 99.9% which is the same for all other samples, give

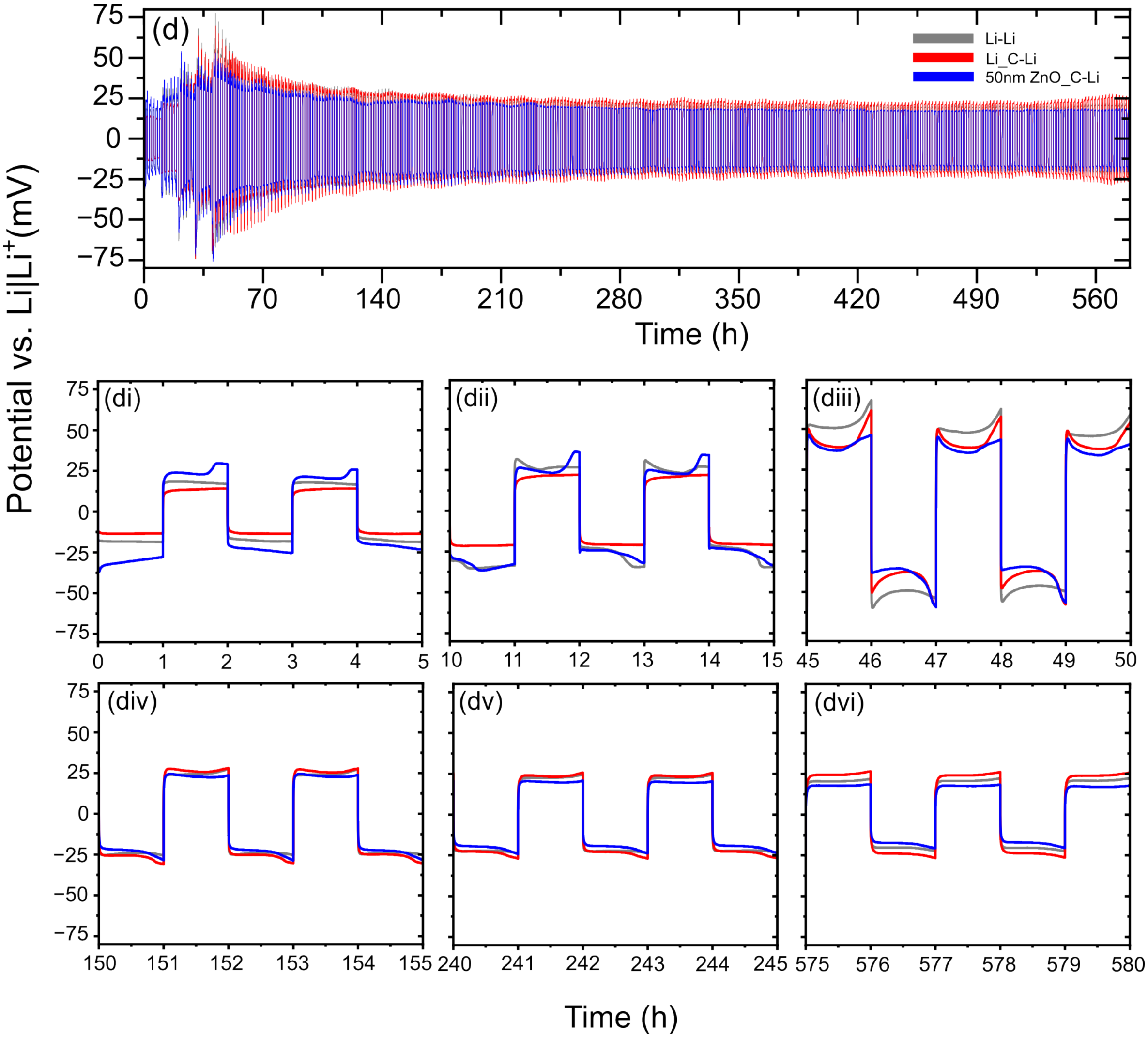

Figure 5.9: Overlayed GCD results of the molten lithium infused carbon samples with some exploded sections of the graph for more detailed analysis

that the working electrode is prelithiated any lost lithium will be replenished by the relatively infinite pool available which is not the case for the electrochemically infused samples where electrodes had no lithium at the start of cycling.

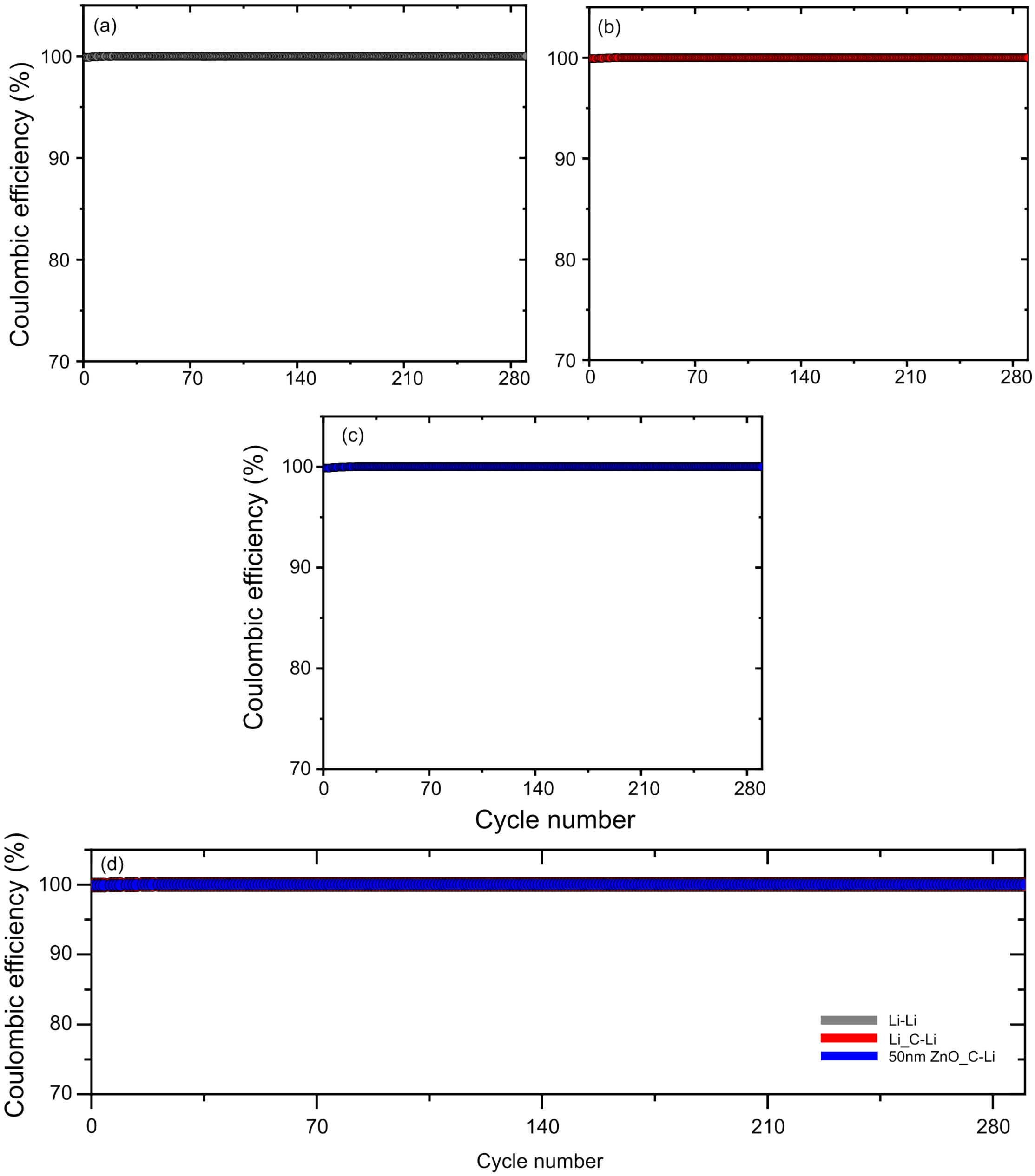

Figure 5.10: CE data from the Molten lithium GCD cycling. (a) Li-Li cell, (b) LiC-Li cell, (c) 50nm ZnOLiC cell and (d) which highlights the overlayed results

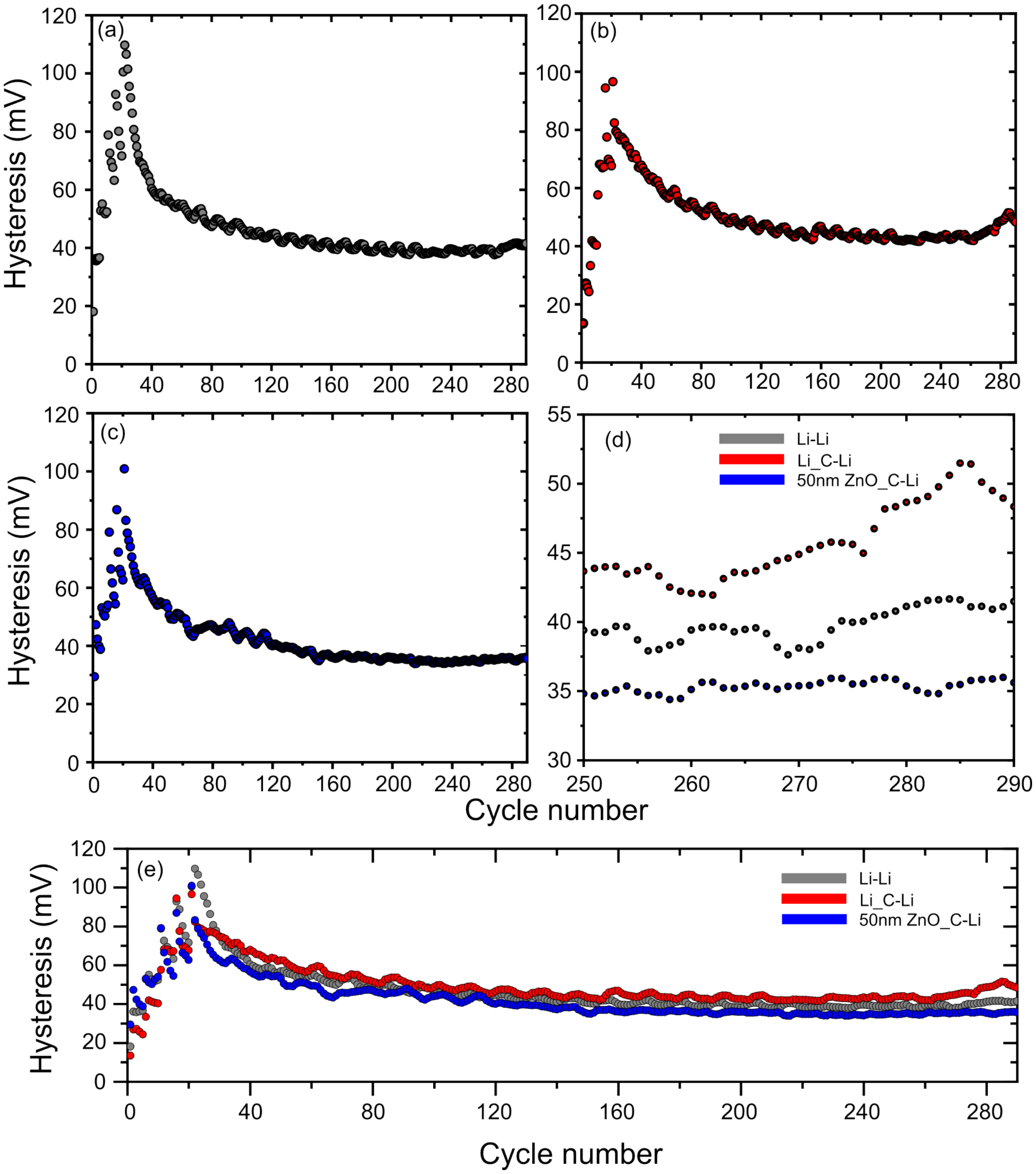

Figure 5.11: Hysteresis data from the Molten lithium GCD cycling. (a) Li-Li cell, (b) LiC-Li cell, (c) 50nm ZnOLiC cell, (d) overlayed hysteresis at the end of cycling and (e) which highlights the overlayed results

5.6 Conclusion and future work

From the data presented, electrochemical infusion of lithium into the carbon was deemed to be unfeasible due to poor CE after the first 40 cycles for all samples coated and uncoated which implies that when coupled with a full cell a proportion of the active mass would be lost in the first few cycles. To further justify this point cells, would need to be assembled vs a commercial cathode such a LFP which would lead the capacity to fading quickly. Despite this, after 40 cycles, all of the cells cycled with a CE above 90% for a period of time before failure. It was found that the 15.0nm coated ZnO cell cycled for the longest duration offering a closer insight into the optimal thickness of ZnO required for cycling cells in this format. To justify this further more cells would need to be cycled around this thickness as well as performing repeats. Although the lithium infused carbon experiments showed a high first cycle efficiency eliminating this problem, the results of plating and stripping were fairly consistent for all samples with a CE of 99.9% for Li-Li, LiC-Li and LiZnO-Li cells over 290 cycles. Furthermore the hysteresis was very consistent with only a 10mV reduction for the ZnO coated carbon sample. Unfortunately due to potentiostat time available samples were only cycled for 290 cycles (580 hours) and it appears that the hysteresis began to increase towards the end of cycling for the Li-Li cell and LiC-Li whilst remaining stable for the ZnOLiC-Li cell which could have been the beginning of the hysteresis increasing leading to cell failure like that observed by Zhao and Ouyang et al[1, 8]. In the future cells will be run for a longer duration. To conclude, given that molten infusion saturates the fibrous carbon matrix with lithium prior to cycling, it is likely that the surface of the electrode is no longer benefiting from the ZnO which is buried underneath and therefor the cell cycling appears very similarly to a conventional solid lithium electrode which explains why the results are very similar. The uncoated fibrous carbon electrode shows a slightly higher hysteresis potentially because the molten infusion was not complete and therefor more energy was required to insert lithium into the matrix however if this was the case, you'd expect to see a lower first cycle efficiency suggesting that despite taking longer, molten infusion for uncoated carbon was also successful.

To justify that the suggestions above future work would need to be performed. Firstly to observe the relative success of the molten infusion into the ZnO coated carbon fibre electrode and the uncoated carbon fibre electrode SEM imaging would need to be performed on the electrode after infusion to compare surface morphology. It would be expected that the surface morphology of the ZnO coated carbon and the solid electrode would have a similar appearance whilst the uncoated fibrous carbon electrode would have incomplete infusion thus some of the carbon strands may still be visible. As well as this, surface sensitive analysis such as XPS could be performed on the ZnO coated fibrous electrode to determine if the ZnO is lifting off of the surface during infusion. If this is the case, then the ZnO on the coating could be promoting dendrite free electrodeposition which has been reported previously by wei et al and therefor could explain the slightly lower hysteresis when compared to the solid lithium anode [10]. Further work could be performed by coupling ZnO coated carbon fibrous collectors with conventional cathodes to asses to performance of full cells a large area electrodes could be tested in pouch cells to push this work closer towards a commercial standpoint. As well as this, Scanning Electron Microscopy (SEM) was performed on the electrode surfaces to assess surface coverage. With additional time and resources, further experiments were planned to cut the electrodes and examine their cross-sections. This would allow for a more detailed structural analysis, This could be complemented by EDX to evaluate the elemental distribution and confirm the extent of material coverage throughout the electrode thickness. It was hypothesized that improved conformality of the deposited material may lead to more uniform coating along the carbon strands therefore enhancing lithiation uniformity. This could contribute to improved electrochemical performance and potentially longer cycle life compared to results reported in the literature, such as those by Zhao et al [1].

In summary whilst it is evident the ZnO coating is assisting with lithiation of fibrous carbon current collector, this work suggests for GCD experiments the molten infused electrodes does not offer any outstanding advantages to a solid metal electrode. Although Zhao et al compare a ALD ZnO coating to a ZnO chemical solution impregnation method (showing the ALD as a superior method), they do not compare their work to a solid lithium metal electrode like has been done in this case [1]. A possible solution to the electrochemical infusion issues regarding the first cycle efficiency of the cell could be to incorporate a solid electrolyte that does not react with the electrode. This would mean no SEI would form consuming the lithium and the benefits of fast lithiation of the electrode caused by ZnO could be beneficial to cell cycling.

Bibliography

[1] Bing Zhao, Bobo Li, Zhixuan Wang, Chuxiong Xu, Xiaoyu Liu, Jin Yi, Yong Jiang, Wenxian Li, Ying Li, and Jiujun Zhang. Uniform li deposition sites provided by atomic layer deposition for the dendrite-free lithium metal anode. *ACS applied materials & interfaces*, 12(17):19530–19538, 2020.

[2] Yayuan Liu, Dingchang Lin, Zheng Liang, Jie Zhao, Kai Yan, and Yi Cui. Lithium-coated polymeric matrix as a minimum volume-change and dendrite-free lithium metal anode. *Nature communications*, 7(1):10992, 2016.

[3] Klaudia rejnhard. *Advanced Functional Coatings for Integrative Semiconductor Materials and Devices*. PhD thesis, Swansea university, 2022.

[4] De Fang, Feng He, Junlin Xie, and Lihui Xue. Calibration of binding energy positions with c1s for xps results. *Journal of Wuhan University of Technology-Mater. Sci. Ed.*, 35:711–718, 2020.

[5] Leong G Mar, Peter Y Timbrell, and Robert N Lamb. An xps study of zinc oxide thin film growth on copper using zinc acetate as a precursor. *Thin Solid Films*, 223(2):341–347, 1993.

[6] VI Nefedov, Ya V Salyn, G Leonhardt, and R Scheibe. A comparison of different spectrometers and charge corrections used in x-ray photoelectron spectroscopy. *Journal of Electron Spectroscopy and Related Phenomena*, 10(2):121–124, 1977.

[7] PS Wehner, PN Mercer, and G Apai. Interaction of h2 and co with rh4 (co) 12 supported on zno. *Journal of Catalysis*, 84(1):244–247, 1983.

[8] Yan Ouyang, Can Cui, Yanpeng Guo, Yaqing Wei, Tianyou Zhai, and Huiqiao Li. In situ formed lizn alloy skeleton for stable lithium anodes. *ACS applied materials & interfaces*, 12(23):25818–25825, 2020.

[9] Seong Jin An, Jianlin Li, Claus Daniel, Debasish Mohanty, Shrikant Nagpure, and David L Wood III. The state of understanding of the lithium-ion-battery graphite solid electrolyte interphase (sei) and its relationship to formation cycling. *Carbon*, 105:52–76, 2016.

[10] Ying Wei, Henghui Xu, Hang Cheng, Weixin Guan, Jiayi Yang, Zhen Li, and Yunhui Huang. An oxygen vacancy-rich zno layer on garnet electrolyte enables dendrite-free solid state lithium metal batteries. *Chemical Engineering Journal*, 433:133665, 2022.

Chapter 6

Al_2O_3 coatings on copper for anode free sodium ion batteries

6.1 Introduction

This chapter of my thesis will be concentrating around applying a Al_2O_3 layer using the MVD onto a copper current collector (in this case metallic Cu) to promote stable electrodeposition and stripping of Na during charging and discharging of Na metal batteries configured in an anode free format, whereby a half cell is made of Cu as an anode and Na metals as a cathode. As mentioned in the literature review section 2.2.4, anode free technology can offer many advantages including an increase in volumetric energy density by reducing the cell size, reduced diffusion pathway for ions and a reduction in manufacturing cost due to removal of the carbon anode casting process. Despite this advantage, such technology is still hindered by uncontrollable dendrite growth leading to rapid consumption of the liquid electrolyte or catastrophic failure by short circuit. As well as this, changing the active material from lithium to sodium offer additional advantages such as Na's lower cost highlighted in section 2.2.2. Despite some promising technology in the area of anode free sodium ion batteries (section 2.2.5). No feasible solution has been created to solve current issues leading to a commercial product.

This chapter focuses on application of Al_2O_3 by MVD in an attempt to promote stable electrodeposition of sodium during the batteries charging/discharging cycles and negate the issues highlighted previously. Although Cu coated by Al_2O_3 by ALD coatings have been studying heavily for lithium anode free systems, attempts for applying Al_2O_3 coatings for a sodium anode free system have not been attempted to date. Furthermore, Al_2O_3 coated by an MVD process is novel in this field and offers advantages over its ALD counterparts which include a higher aspect ratio of coating, lower temperature deposition and a large easily accessed chamber capable of batch production (section 2.1.7). Samples used for this chapter were the same material with similar coating strategy performed as to that in chapter 4.

The chapter will include cycling half cells at $0.5mA/cm^2$ to asses the performance of the mechanism for the plating and stripping of sodium. Post mortem analysis will be conducted including EDX and SEM to asses the quality of electro-deposition and XPS etch studies will be conducted to asses the film after cycling has taken place. For this chapter, 3 copper samples with different amounts of MVD Al_2O_3 deposition were chosen including unocated, 15nm Al_2O_3 and 45nm Al_2O_3 coatings. The 15nm Al_2O_3 was selected due to its success in chapter 4 whilst unocoated and 45nm extremes were selected for comparison due to material availability. Although for chapter 4, 1ma/cm2 was selected to cycle the lithium cells as this was a common value seen in the literature and showed a respectable C rate of 1C when cycled at a capacity of 1mah/cm2. Whilst sodium cells were cycled at a similar rate initially, short circuiting highlighted in section 6.1.6 became too severe preventing cell cycling. Although this would mean the comparability of electrodeposition would not be possible, the plating looked very different with lithium depositing forming mossy islands and sodium depositing forming mounds and jagged lateral formations as seen in figure 6.4 and figure 6.8.

6.1.1 Nucleation overpotential

Figure 6.1 (a) highlights the first electroplating cycle for GCD experiments which is also refereed to as the nucleation overpotential, the value for the nucleation overpotential can be quantified more clearly in the bar chart in figure 6.1 (b). Similar to chapter 4 as the thickness of the Al_2o_3 increases, the nucleation overpotential increases which suggests more energy is required to seed nuclei onto the copper for thicker coatings. This makes sense as thicker coating would likely impede ion movement more as the coating thickness increases. While this is consistent with chapter 4, interestingly the plataue which signifies the nuclei growth region is significantly higher for the 45nm Al_2O_3 coated copper whilst being the lowest for

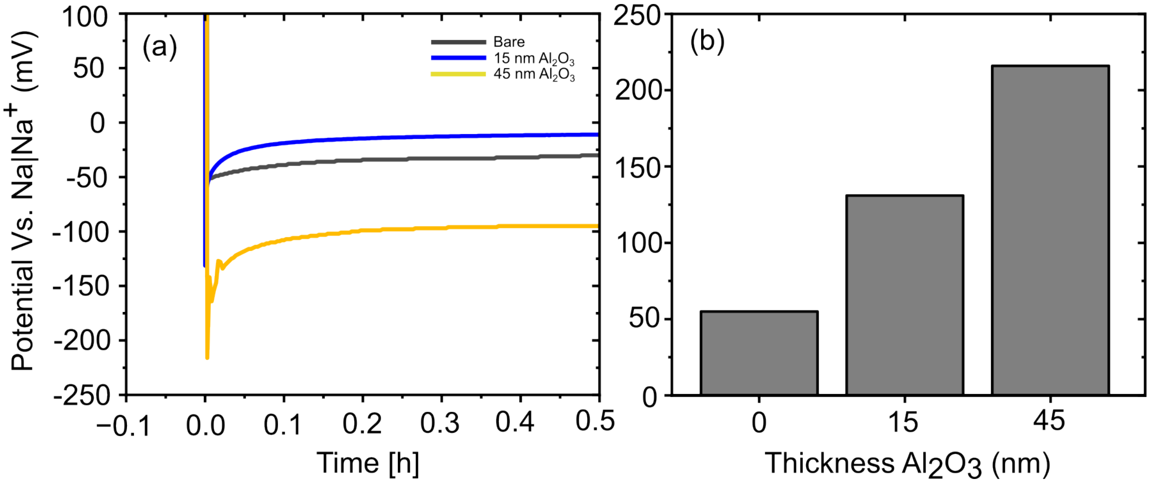

Figure 6.1: (a) figure showing the nucleation overpotential of sodium electrodeposition on uncoated, 15nm Al_2O_3 coated copper and 45nm Al_2O_3 coated copper, (b) bar chart highlighting overpotential values for each sample more clearly

the 15nm Al_2O_3 coated copper. This was expected to be due to the larger coating thickness.

6.1.2 Cyclic voltametry

Cyclic voltametry was performed in 3 electrode EL-cell with a sodium reference electrode. When a potential range was set from 0.5V-1.6V and a slow scan rate of 1mV per second was employed the reduction and oxidation peaks of sodium are very clearly observed. In the range -0.4-0.3V sodium reduction had occured which corresponds to the electrodeposition onto the copper. The process can be highlighted by equation 6.1.

$$Na^{+} + e^{-} -> Na \tag{6.1}$$

in the voltage window the oxidation process of sodium takes place which is represented by equation 6.2. It was concluded that from the CV only the reduction and oxidation of sodium takes place. Due to lack of other peaks or noise which typically occur when the electrolyte undergoes reduction or oxidation it was concluded that the electrolyte we had made was dry and stable.

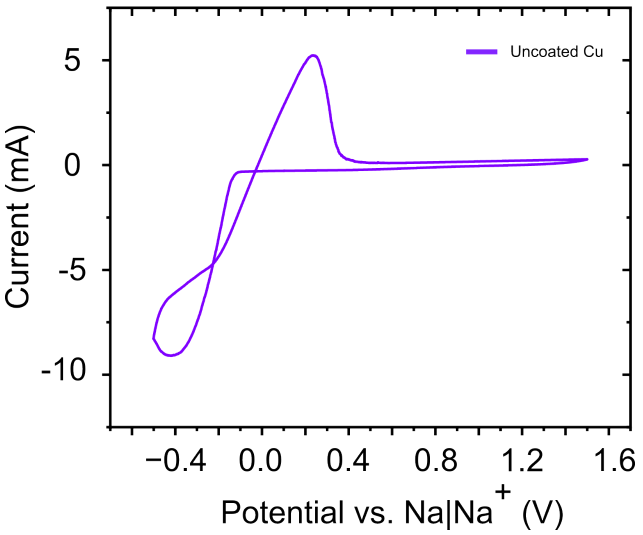

Figure 6.2: Graph showing 3 electrode CV of sodium electrodeposition and stripping on copper

The cross over points on the response indicate nucleation points of sodium onto copper.

$$Na- > Na^{+} + e^{-} \tag{6.2}$$

6.1.3 Charge-discharge

In this section samples were subject to GCD cycling. 15nm Al_2O_3 was selected due to it being the optimal thickness found for coated samples in the previous study and due to equipment availability, there was not enough of other thicknesses to complete the full study. The cells were cycled at $0.5ma/cm^2$ for 30 minutes giving an areal capacity of $0.25mAh/cm^2$. For each sample, 3 exploded views were taken of cycling including the first 5 cycles, 5 cycles whereby the cell had appeared to fail and the last 5 cycles.

Unlike the first chapter whereby the cell failure was determined by the CE decreasing below 80%, the sodium cells suffered heavily from inconsistent plating and stripping whereby on some cycles the electrode would not completely strip but would then continue to strip further during subsequent cycles making it difficult to predict the amount of remaining sodium left on the electrode at any particular point. CE values of up to 140% were witnessed in some instances which will be further explored later on in this chapter when only a voltage cutoff was employed at 0.5V. To prevent this from occurring, a time cutoff of 30 mins plating and 30minutes stripping was employed. This consequently meant that on some cycles the cutoff voltage was reached and some weren't in an inconsistent way.

For the sodium ion work at some point during cycling the hysteresis of all the cells seems to increase in value and remain permanently elevated. This was due to a phenomenon that occurs during the plating cycle of the cell. Due to the new increased potential required to drive the plating and stripping reaction, this was the point at which the cell was considered to no longer be cycling optimally and therefor no longer usable. To evidence this, huang et al report an jump in the plating voltage during the nuclei growth region which is illustrated as a dendrite growing in their insitu optical microscopy work [1].

Figure 6.3 shows the performance of the uncoated cell. The first cycle shows the stripping potential rising to meet the 0.5V cutoff then abruptly stopping at 300mV before reaching the time cutoff which makes the first cycle efficiency appear to be 100% in this case. After 74 hours figure 6.3 (@) (its worth noting that for some cycles stripping is cutoff by the voltage thus cutting the time meaning the cycles do not exactly line up with time) during plating there is what appears to be a jump on potential, after this the plating and stripping overpotentials occur at much higher values. Plating was stopped at around 175 hours.

To further understand the issues that are occurring, 2 cells were made and $0.25mAh/cm^2$ of sodium were plated at $0.5mA/cm^2$ to keep the consistency with the GCD experiment, these can be seen in figures 6.4. It is evident that the deposition is patchy and at a glance appears dendritic. I expect that due to these dendrites growing, the sodium is disconnecting from the electrode becoming dead sodium occasionally piercing the separator causing a short circuit like seen in the first cycle. The jump in hysteresis could be due to formation of high surface area deposits causing a more extensive SEI which is altering the charge transfer process at the electrode, this was assumed detrimental to cell cycling [1]. Looking at the SEM in figure 6.4 the deposition doesn't look mossy or dendritic like observed in the case for lithium electrodeposition but instead it grows laterally in a jagged type pattern which could explain why it is not covering the entire electrode and is forming inconsistent clusters. This doesn't appear to be the case for Al_2O_3 coated samples which will be explored next.

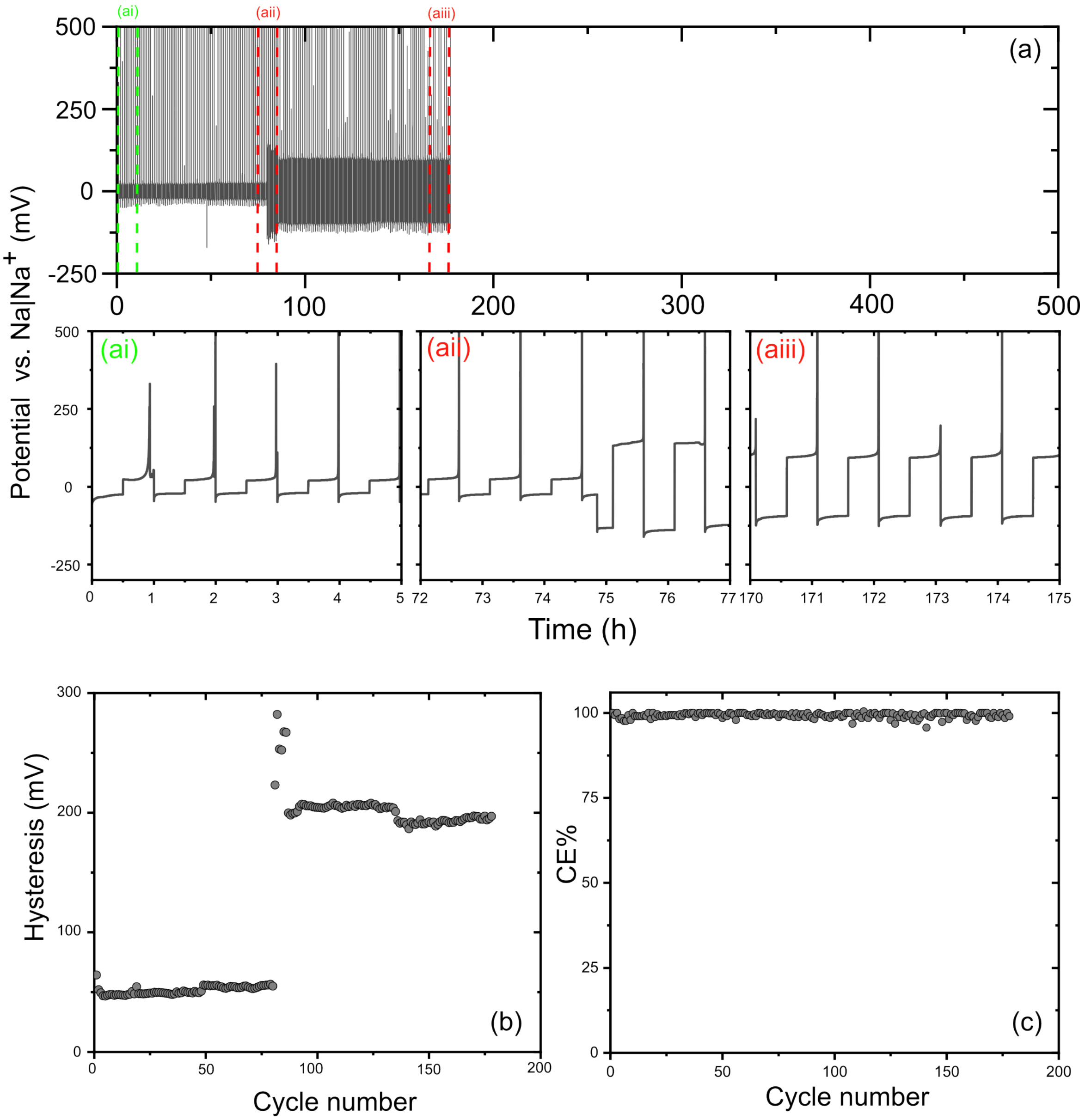

Figure 6.3: (a) Graphs highlighting the GCD results of sodium electrodeposition onto copper, (b) hysteresis and (c) CE

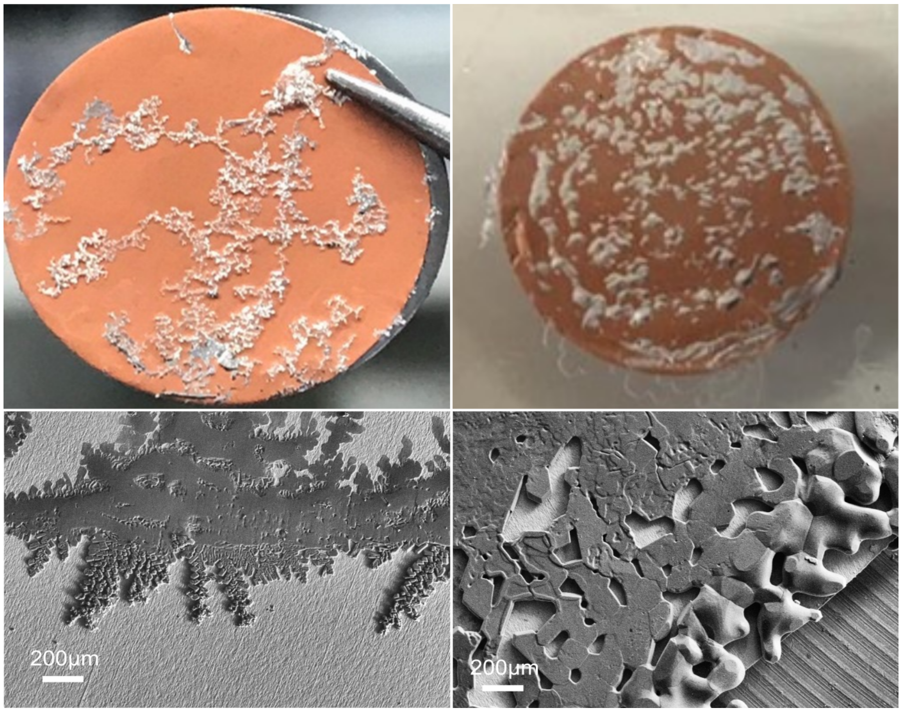

Figure 6.4: Photograph and SEM images of sodium electrodeposition onto an uncoated copper substrate

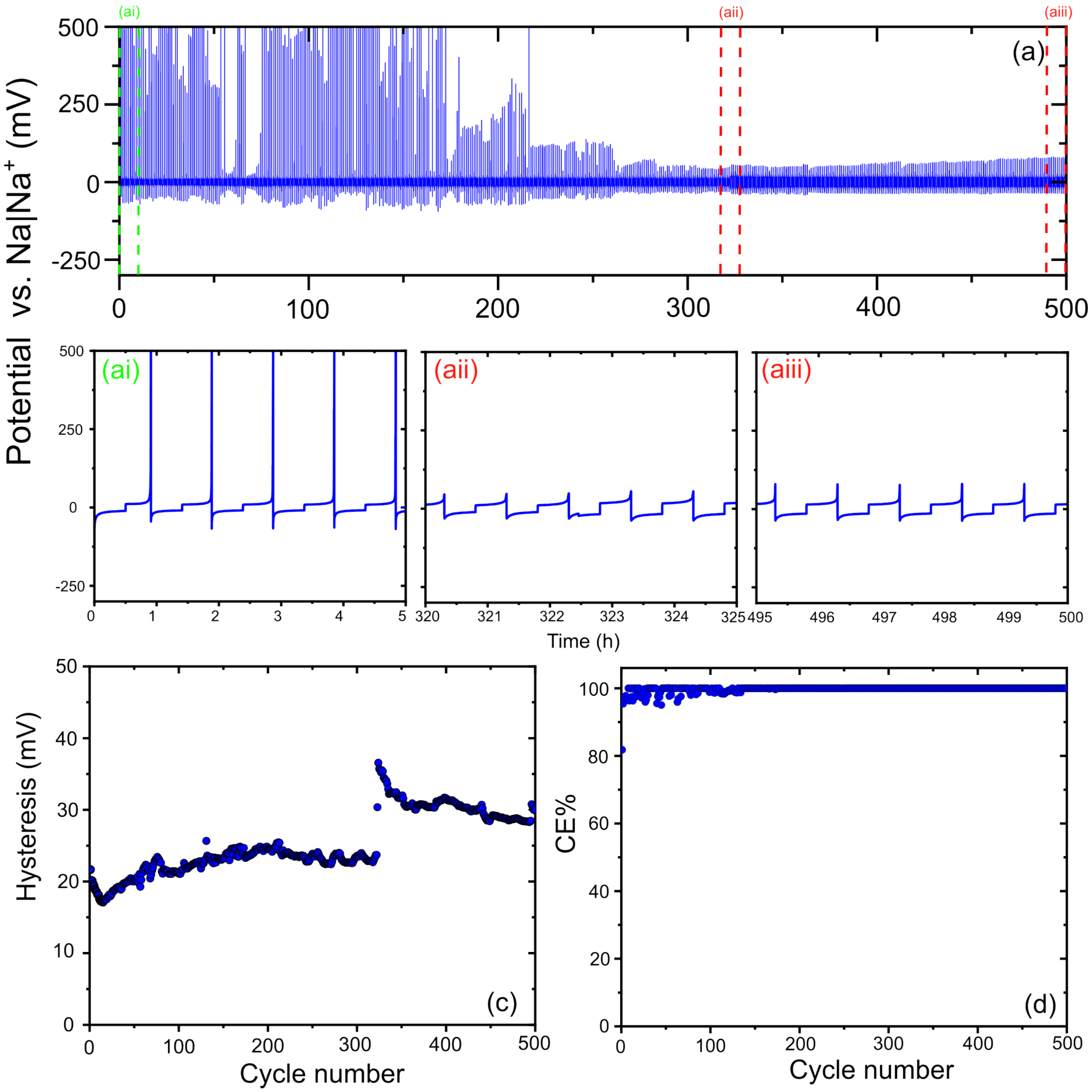

Figure 6.5: (a) Graphs highlighting the GCD results of sodium electrodeposition onto copper coated with 15nm Al_2O_3, (b) hysteresis and (c) CE

Figure 6.5 presents the findings obtained from the 15nm Al_2O_3 coated sample. Despite indications of inconsistent stripping, suggestive of the presence of residual sodium on the electrode, the onset of the jump in hysteresis is notably delayed, occurring between 322 and 323 hours. This delayed onset compared to the uncoated example suggests a higher degree of cycling stability.

To further corroborate this observation of stable cycling, a similar experiment was conducted on an 15nm Al_2O_3 coated cell, wherein $0.25mAh/cm^2$ was deposited at $0.5mA/cm^2$ for optical and SEM observation. Figure 6.6 (a) immediately reveals that the plating extends across a larger portion of the electrode's surface area and is not localized to specific regions. Additionally, Figures 6.6 (c) demonstrates a more uniform distribution of sodium plating, exhibiting lateral growth in all directions compared to the uncoated sample where plating appears jagged. This uniform growth pattern likely contributes to the improved coverage of sodium on Al_2O_3-coated copper samples.

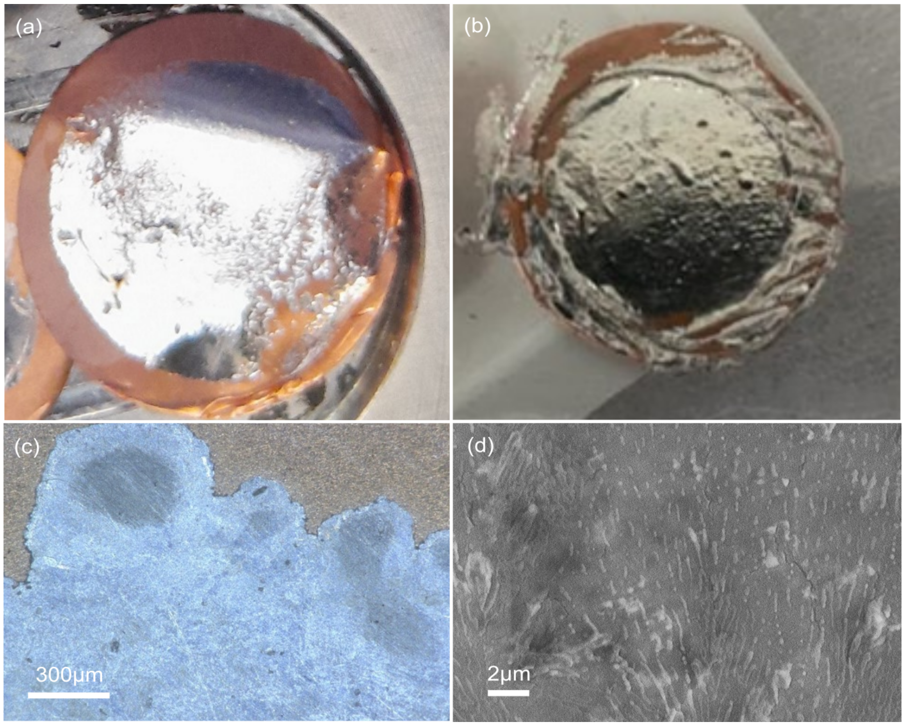

Figure 6.6: Photograph and SEM images of sodium electrodeposition onto a copper substrate with 15nm Al_2O_3 on the surface

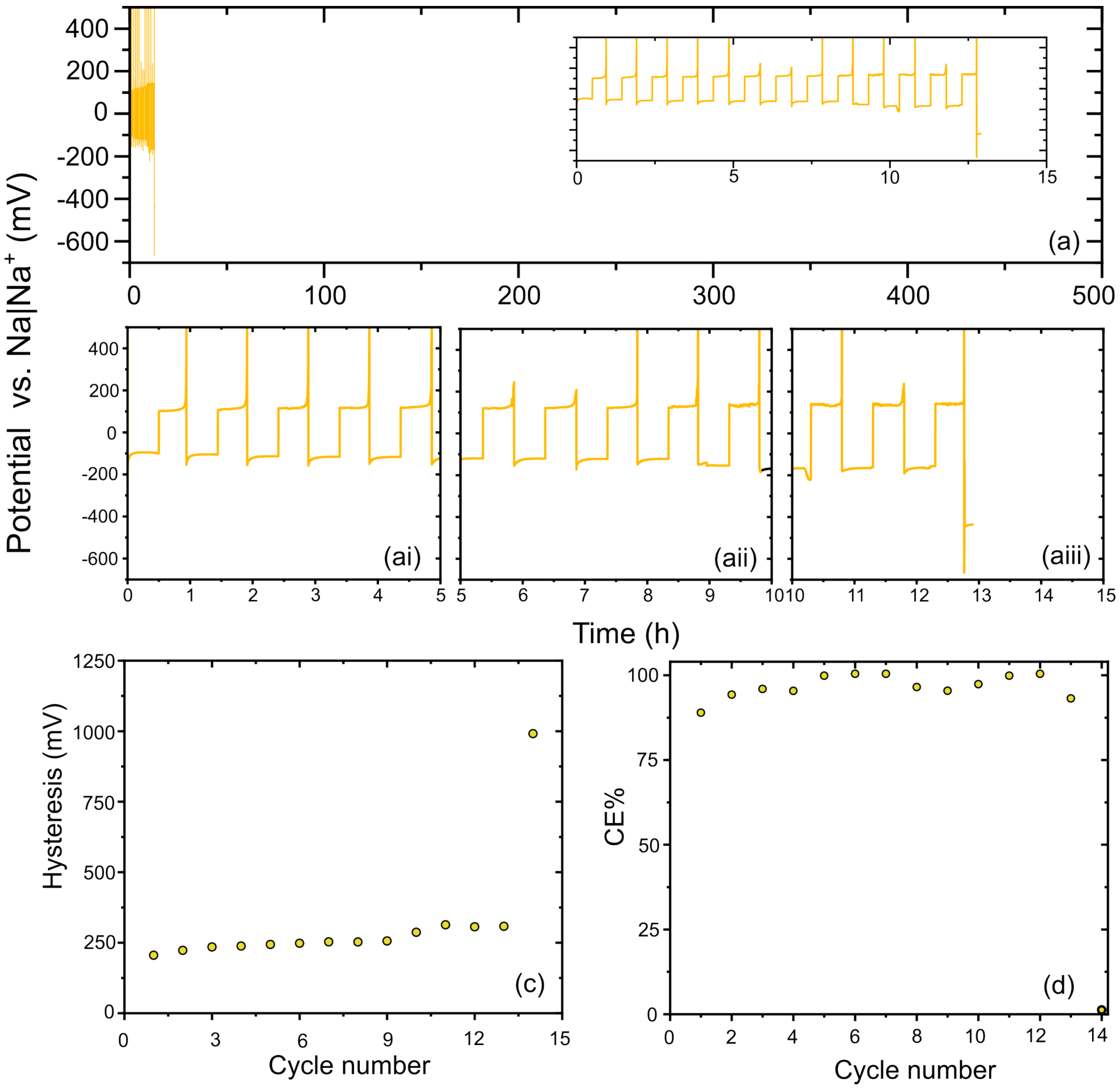

Figure 6.7: (a) Graphs highlighting the GCD results of sodium electrodeposition onto copper coated with 45nm Al_2O_3, (b) hysteresis and (c) CE

Figure 6.7 (a) shows the results obtained for the 45nm Al_2O_3 charge-discharge experiments, immediately it is evident that the overpotential for plating and stripping is occurring at a much higher value then the previous cells with some cycles not reaching the cutoff voltage. I expect that because the coating is much thicker then previous examples, the coating is acting as an obstacle for ion diffusion which means more energy is required for electrodeposition onto the copper to occur. After 13 hours of cycling the following cycles nucleation overpotential increases dramatically compared to previous cycling which is suggested where cell failure has occurred in conjunction with the other samples in the batch.

Looking at the plated sodium on figure 6.8, like the 15nm coated sample, there are no obvious signs of dendrites and the sodium is covering the electrode more consistently then the uncoated cell which suggests the Al_2O_3 coating is affecting the deposition. Despite this, the plating still appears to be much more non uniform then 15nm Al_2O_3 as the deposition appears to have areas on the electrode where the sodium is forming raised deposits. I expect these deposits are more likely to detached from the electrode forming dead sodium and ultimately leading to the failure of the cell.

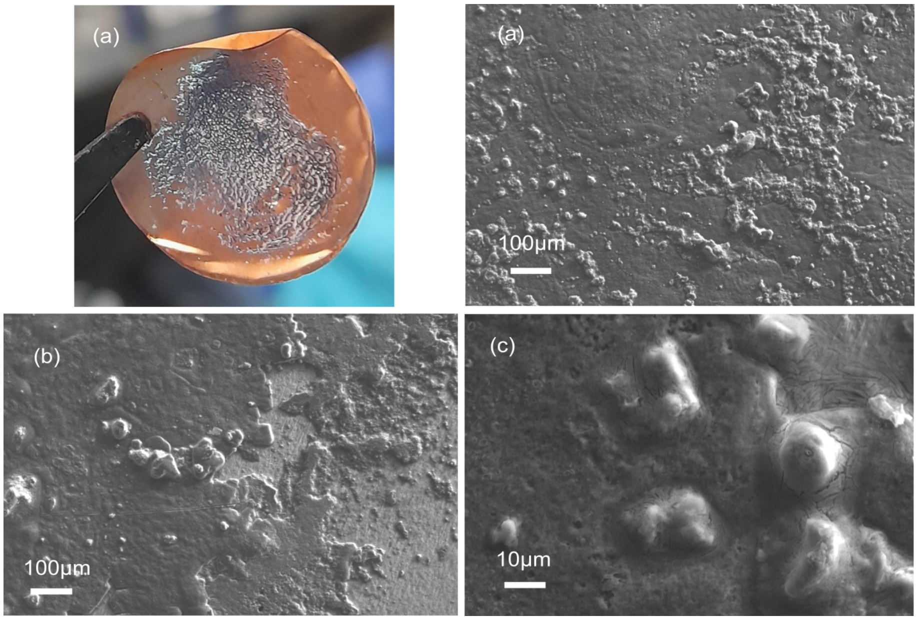

Figure 6.8: Photograph and SEM images of sodium electrodeposition onto a copper substrate with 45nm Al_2O_3 on the surface

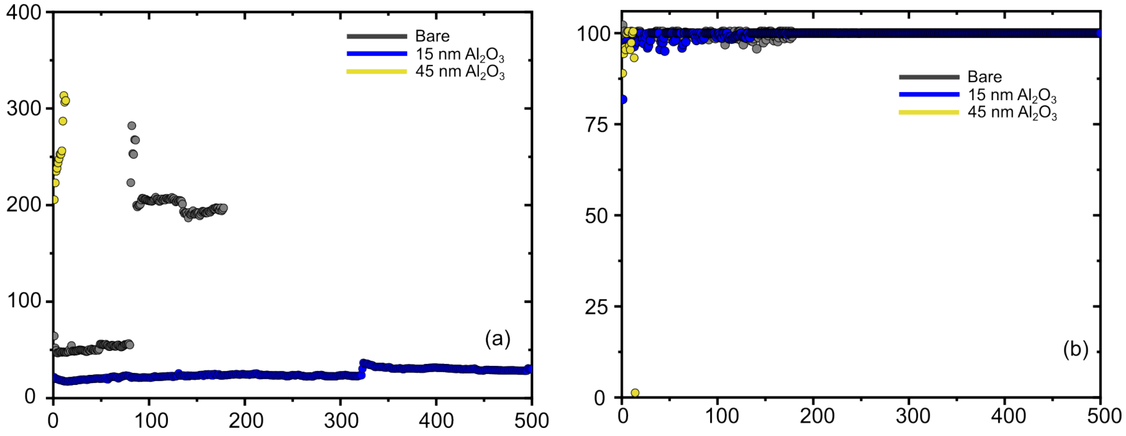

Figure 6.9: Figure showing (a) hysteresis of the 3 thickness overlayed (b) Coulombic efficiency of the 3 thicknesses overlayed

To directly compare the hysteresis of the 3 samples, it is evident that the hysteresis for the 45nm Al_2O_3 coating starts off at the highest value out of the 3 at 200mV and increases to 320mV during the short lifespan of the cell. The 15nm Al_2O_3 coated cell shows the lowest hysteresis at 20mV which increases to 30mV after the failure event. The uncoated cell shows a hysteresis of 50mV which increases to 200mV after the failure event. I expect that due to the higher surface area of the unocated and 45nm Al_2O_3 coated cell deposits, the SEI is more thick and is providing a thicker diffusion pathway for sodium ions contributing to this increased hysteresis. The more uniform deposition onto the 15nm Al_2O_3 coated sample means the SEI is more uniform and therefor hysteresis the lowest in this case. The CE is very difficult to interpret for this dataset due to the issues with regards to incomplete stripping of the electrode and the unknown capacity of sodium left on the electrode therefor will not be commented on.

6.1.4 A look into the reason for these charge discharge graphs

To study the plating in more detail in-situ optical microscopy was utilised. The idea is to observe optically how the electro-deposition was taking place on the copper to provide a greater understanding of the process.

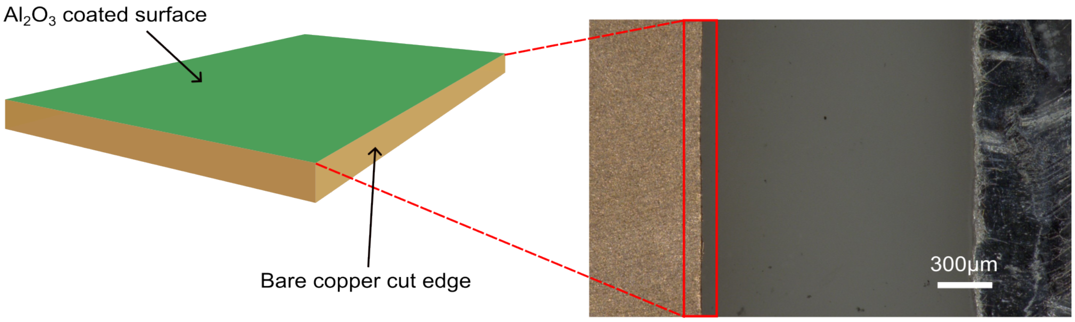

Figure 6.10: schematic showing the layout of the copper used for insitu- optical microscopy experiments

Figures 6.10 shows the setup used. A circular coated copper electrode with a 15nm Al_2O_3 coating was utilised and cut in half using a scalpel, this left the coating on the surface intact however would leave the cut edge with no coating present. This was then assembled into an optical cell (refer to methodology section 3.5.8) with the uncoated copper edge directly opposing the sodium counter electrode to mimic the coin cell scenario. The electrodes were placed ontop of a glass fibre separator which was wetted with 1molar $NaPF_6$ in diglyme. The spacing between the electrodes is roughly 1.5mm across the area images.

Figure 6.11 shows the process of electrodeposition at iterations onto the copper. Initially a current rate of $0.5 mA/cm^2$ was applied to the electrode. The area was taken to be that of the entire surface of the copper semicircle cut although due to the electrode being assembled this means the effective current density at the cut edge closest to the sodium will be much higher. The time was taken at increments of 300 seconds for 1800 seconds which is consistent with the electro deposition for the half cells previously. To better highlight the areas refereed to, an exploded image was created at 1800 seconds after the plating had finished and the different sites were marked.

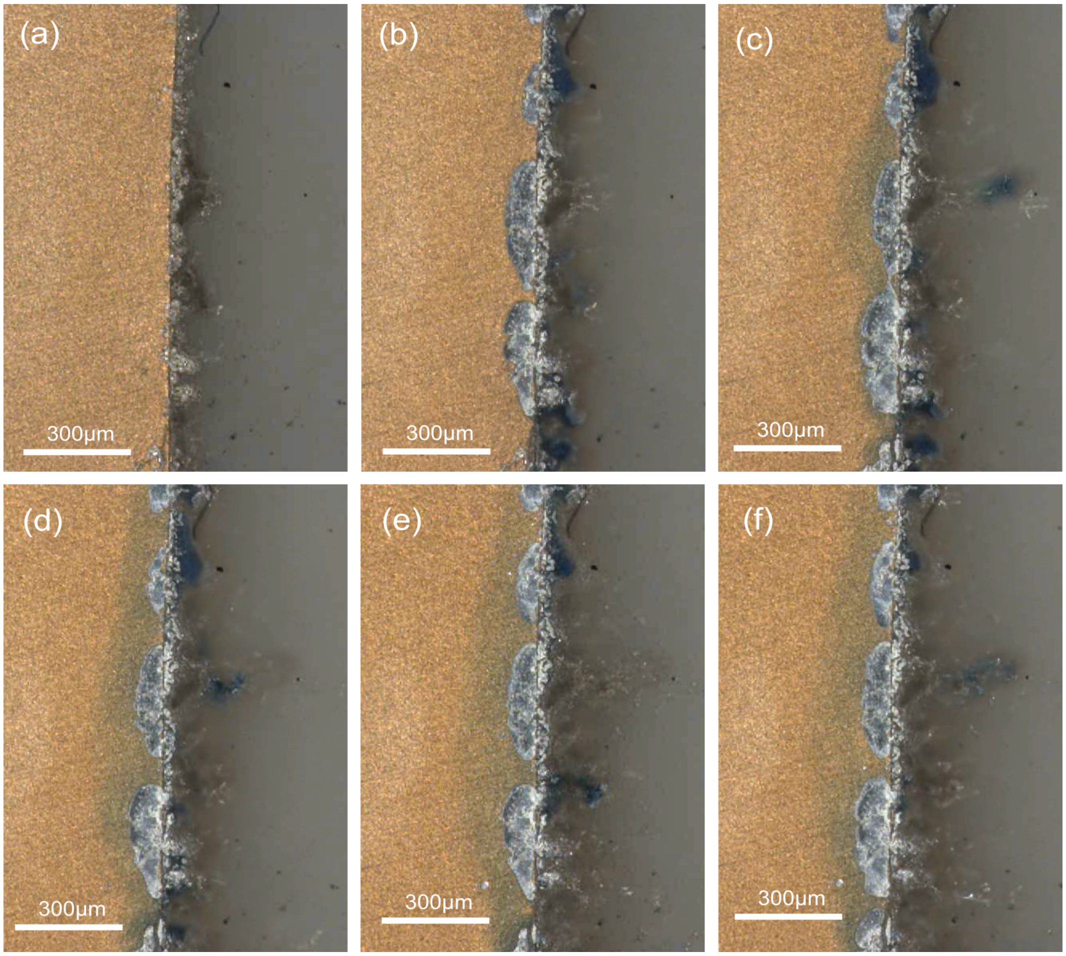

Figure 6.11: microscope images highlighting the deposition of sodium onto copper at 300 second intervals starting at 300 seconds (a), 600 seconds (b), 900 seconds (c), 1200 seconds (d), 1500 seconds (e) and ending on 1800 seconds (f).

At 300 seconds sodium is depositing on the cut edge of the copper which is not coated with Al_2O_3 as established by figure 6.10. The deposition at this point appears to be mossy and dendritic which follows on from the uncoated half cell in section 6.1.3. As the deposition progresses to 600 seconds figure 6.11 (b) plating appear to begin on the top surface around the edge of the copper. It is worth noting that throughout the rest of the cycling this changes however it does not become much larger. At 900 seconds figure 6.11 (c) a dark grey area began to appear next to where the sodium has started to deposit on top of the copper (site 3 figure 6.12), this becomes larger as the cycling progresses figures 6.11 (d)-(f). It was expected at this point that the sodium is diffusing through the Al_2O_3 layer which is enabled by the Al_2O_3s ability to rapidly conduct sodium via a Na-O bond making and breaking process as mentioned in the literature review [2]. At 1500 seconds (figure 6.11 (e)) interestingly a small piece of sodium appears in the grey area established at 900 seconds, this can be more easily seen as site 4 in figure 6.12. At this point I expect that the sodium has become very densely packed that it has actually appeared ontop of the Al_2O_3 which could explain the mechanism for how the coverage and uniformity for the 15nm samples is much greater then the uncoated copper sample. It is also worth noting that the dendrites initially observed at 300 seconds have grown significantly longer to around 300 micrometers on the uncoated copper edge (figure 6.12 site 1).

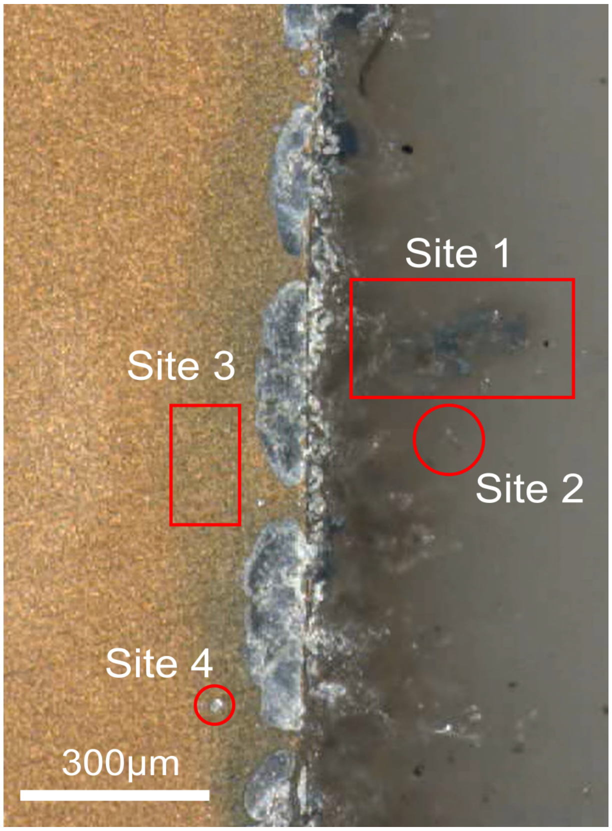

Figure 6.12: Image showing the exploded image of insitu optical microscopy experiment at 1800 seconds highlighting the different sites mentioned in the text

6.1.5 XPS crossectional analysis

To investigate the constituents of the sodium electrodeposition onto of copper, an experiment was designed that involves employing an XPS etch. The idea behind this is to etch through the various layers expected to be on the sample to identify where they might be present, how they might change and therefor the impact they may have on the cycling of the cells performed previously. One particular question that is important to answer in this experiment is the location of the Al_2O_3 layer with respect to the sodium electrodeposition which would allow the determination if it is acting as an artificial SEI or is enhancing the performance of the cell by other means.

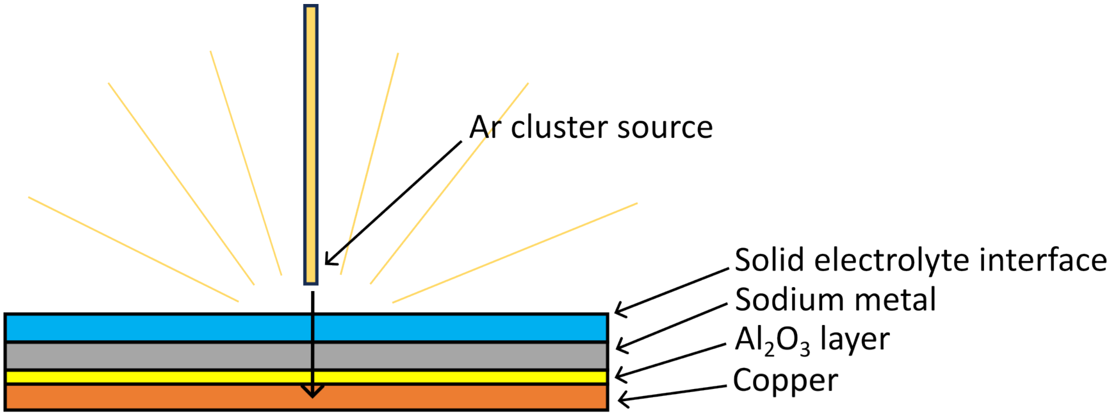

Figure 6.13: schematic highlight cross section of electrodeposition onto copper highlighting the different layers that are expected to be etched through

Figure 6.13 shows the expected structure of the sodium electrodeposition onto copper and therefor the layers that might need to be etched through. At the base is the copper substrate which will be the last peak to appear on our spectra. Above that is the MVD Al_2O_3 layer which is 15nm thick in this case (due to this having the best effect on the electrodeposition). Above that, the sodium metal layer is likely to be present. As mentioned before this might also be below the Al_2O_3 layer. Above the Na would likely be the SEI which will be comprised of inorganic Na-F and Na-O according to similar research [3]. After electrodeposition, electrodes were washed with dry diglyme to remove any residual salt using a pipette, this was repeated 3 times.

Although for the 15nm Al_2O_3 coated sample sodium plating on the surface of the electrode is most uniform out of the 3 samples tested, it is still not possible to determine the thickness for the specific sample and specific area on the sample being tested. For this reason a 5KeV Ar+ ion bombardment was selected which is the highest power ion bombardment capable for the XPS system available. An area was selected where plating covered the entire area where the etch will take place which can be highlighted in figure 6.14, the etch area can be seen highlighted in red. The etch was left to run for 24000 seconds which was the length of the available booked slot. High resolution Scans were performed of the Cu2p, Al2p, O1s and Na1s every 60 seconds. It was decided that these 4 peaks were essential to collect as they gave us the most information regarding the composition whilst not adding additional time onto the process which would reduce the depth of the etch.

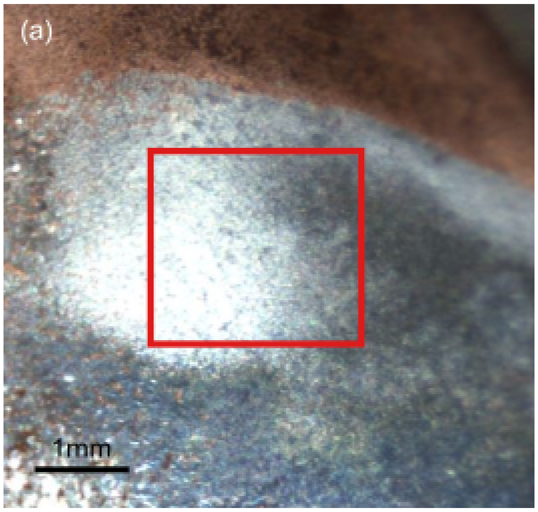

Figure 6.14: Microscope images with square highlighting the rough area for where the XPS etch took place.

The initial question that is important to consider is the location of the Al_2O_3 layer with respect to the copper as mentioned previously. To do this, data was taken with respect to the Al2P and Cu2P region of the spectra from the 24000 second Argon etch every 3000 seconds to highlight the components of the spectra at each stage of the etch. Firstly at 0 seconds (figure 6.15) there is no evidence of either a Cu2p doublet or Al2p peak which implies that these elements are not present at surface level which suggests the surface is covered with sodium and its potential compounds. At 6000 seconds a peak appears at around 70eV which strengthens up to 15000 seconds and remains throughout the study (this peak has not been identified as of yet and no literature gives any insight into it therefor, requires further research). After 9000 seconds of etching, it is evident that there is a weak response at 75.6eV which was expected to belong to the Al-O bond present in aluminium oxide. This suggests the beam has etched through the sodium and has reached the Al_2O_3 layer, this peak intensifies as the beam penetrates into the layer up to 15000 seconds where it remains consistent for the remainder of the study [4]. It needs to be mentioned that Al2p overlaps with Cu3p peak however due to no presence of Cu2p at 9000 and 12000 seconds it was assumed that peak present was in fact Al2p and not the underlying Cu2p. At 15000 seconds the first instance of the Cu2p doublet appears at 932.6eV (3/2) which I expect belongs to CuO which is likely present on the surface of the copper [5]. This peak intensifies throughout the rest of the study as the etch progresses further through the Al_2O_3 and into the Cu. As there is an Al2p peak between 9000-12000 and no Cu2p doublet until 15000 it would suggest that we are in the Al_2O_3 film here. To conclude I expect the Al_2O_3 layer and the copper to be very close to each other due to the appearance of the Al2p initially which is followed by the Cu2p 3000 seconds later. The fact that no Al2p is present on the surface of the sample also indicates that it is not lifting off the surface of the copper and therefor acting as an artificial SEI.

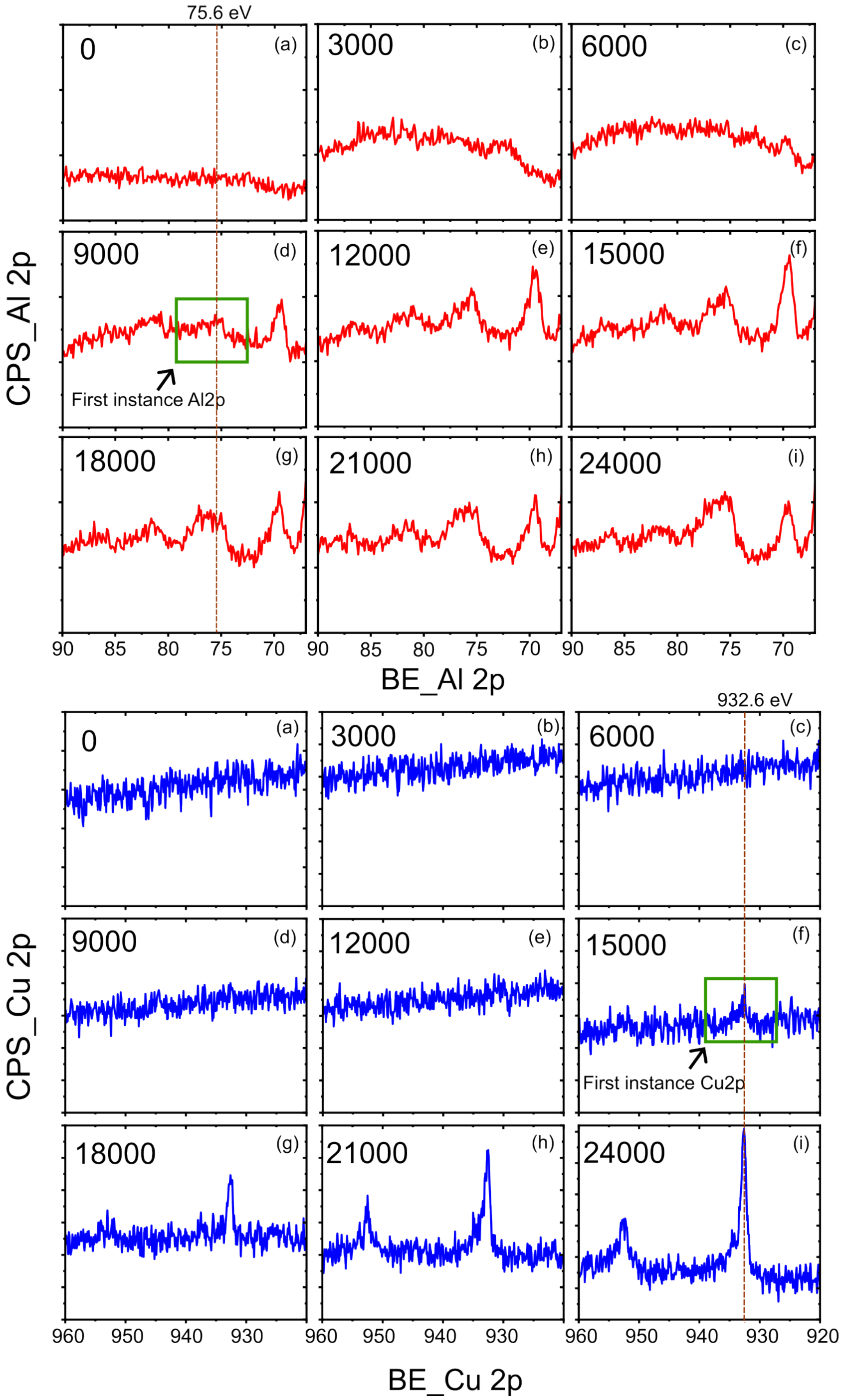

Figure 6.15: XPS spectra showing the Cu2p peak (blue) and Al2P peak (red) at 3000 second intervals throughout the XPS etch

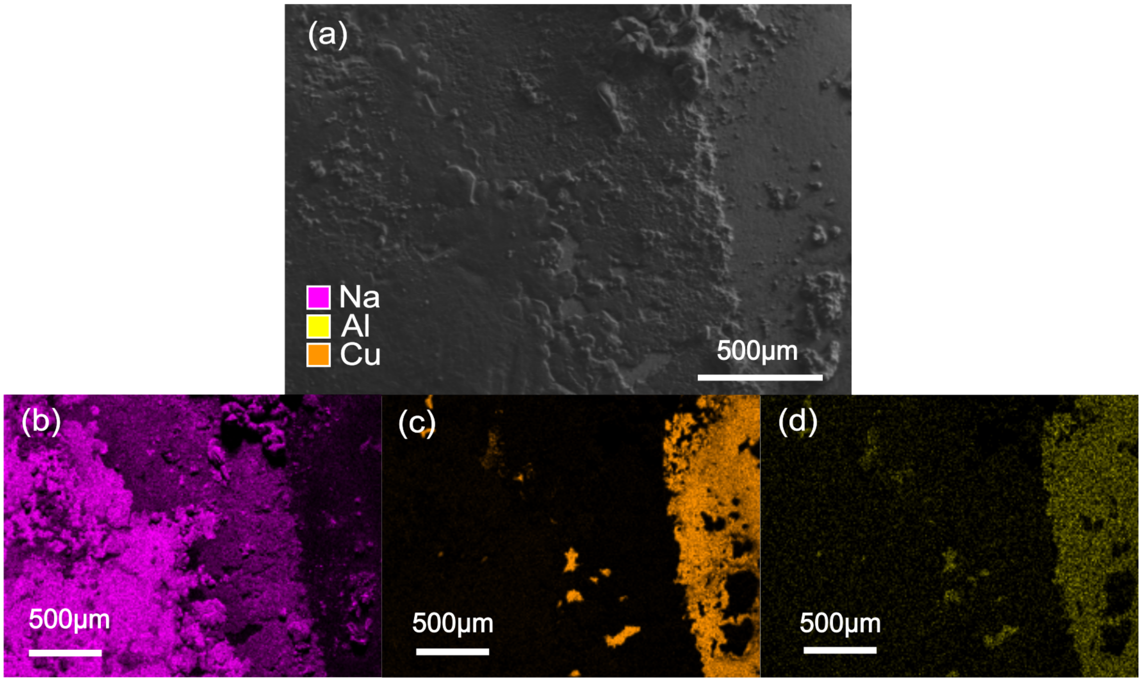

Figure 6.16: EDX image highlighting the elements including sodium, aluminium and copper on a 15nm Al_2O_3 coated copper sample which had sodium electro deposited onto it

To further strengthen this, an EDX map was taken of the edge of a sample with sodium plating ontop of an Al_2O_3 coated copper substrate. This can be seen in figure 6.16. The sample was rinsed by pipetting dry diglyme to remove the residual salt. Although EDX is by no means a surface sensitive characterisation techniques you can see the Al_2O_3 signal is the strongest where the deposition has not taken place around the edge of the copper and lines up perfectly with the copper signal. If the Al_2O_3 was on top of the sodium and therefor acting as an artificial SEI, you would expect the signal on the sodium to be similar to that on the copper. Again this should be taken lightly due to the penetration depth of incident electrons used for EDX.

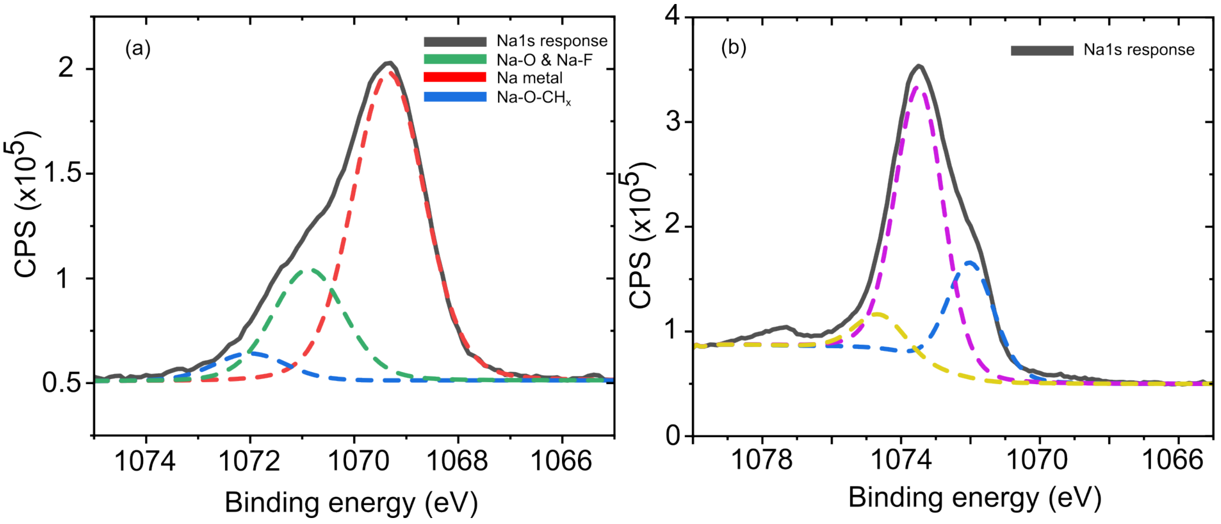

Figure 6.17: XPS spectra highlighting the Na1s peak at 0 seconds and 24000 seconds

To finish off this section, the Na1s peak was studied before the etch at 0 seconds and then after the etch at 24000 seconds. At 0 seconds the surface of the sodium is being analysed so constituents should allign with that of the SEI and potentially some sodium metal depending on the thickness of the SEI. Figure 6.17 (a) shows the results of the Na1s peak and components at 0 seconds. According to literature, the red peak corresponds to metallic sodium at 1069.5eV and the green at 1071eV which correspond to the NaO and NaF peak which are common constituents of the SEI for this cell format. It was surprising to see a strong presence of sodium metal at surface level as it would be expected predominantly to see Na-F and Na-O bonding which will correspond to the constituents of the SEI [3]. One article highlights the sodium peak at 1069.5eV and attributes it to sodium metal stuck in the micropores of their carbon based electrode so unless something similar is occurring in the SEI of the samples or if the SEI is very thin, it is likely due to differential charging effects [6]. The Na peak exists at 0 and 24000 seconds, this indicates that the sodium exists inside the Al_2O_3 which is expected as established by prior research [2]. To look at things in more detail, the Na-Na peak at 1069.5 decreases in intensity gradually where it is only very small at 24000 seconds. The Na-F, Na-O peak at 107eV reduces in intensity and becomes insignificant at 9000 seconds which could indicate that the SEI has been broken through at this point (followed by the appearance of the Al2p peak). Interestingly whilst not present at 0 seconds a peak at 1074eV appears at 3000 seconds and gets increasingly stronger as the etch progresses to 24000 seconds, This peak was left unidentified. For the Na1s peak after 24000 seconds it is important to mention that fitting is highly subjective due to the presence of what was expected to be differential charging caused by the different layers present. The different conductivity's of these layers will likely charge differently due to the different conductivity's associated with them due to long term exposure of samples to positively charged argon ions which therefore make this analysis subject to error [7].

6.1.6 Investigating the incomplete stripping dilemma

Throughout the anode free sodium ion and lithium ion chapters there has been the consistent occurrence of the CE exceeding 100% which is also an issue that arises in other studies whereby the charge/discharge mechanism of the battery is based on electrodeposition/stripping. The following section delves into this issue to provide some suggestions. Figure 6.18 (a) shows a section of and uncoated copper sample which was cycled by potentiometry to a voltage cutoff of 0.5 volts without a time cutoff, occasionally some cycles showed this issues with the stripping of sodium denoted as cycle X. In this example, the stripping approaches the 0.5V cutoff and falls short continuing with this noisy response (oscillations), one example of this can be seen in figure 6.18 (b). When this occurs, the coulombic efficiency radically goes over 100% (in the case of cycle X it goes as high as 140%)

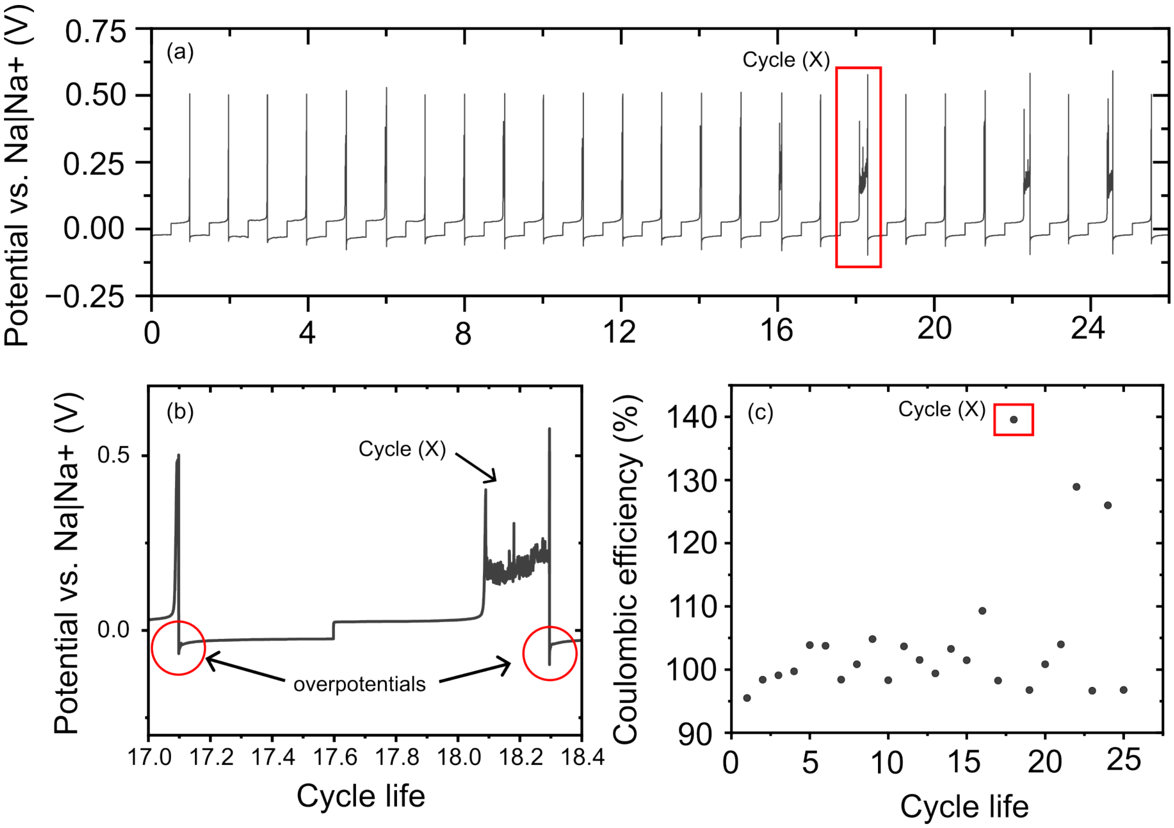

Figure 6.18: Figure showing (a) GCD response for uncoated copper with a voltage but no time cutoff, (b) zoomed in cycle highlighting oscillation and (c) CE response.

To understand why this is occurring a cell was manually stopped during stripping of sodium when this problem was occurring. It was then consequently opened to observe the electrode and its constituents. Figure 6.19 (b) shows the results of this experiment. It is evident that after the cell has been opened there are small deposits of sodium on the electrode despite the CE being over 100% so despite this observation incomplete stripping has occurred. This is either due to an excess of sodium building up from previous cycles or is due to dendrites piercing the separator causing a repeating short circuit as it rapidly touches and detaches from the electrode. After this has finished, the Na plating for the next cycle has a higher overpotential which is generally higher the longer the oscillation continues on for. The separator in the cell shows small deposits of sodium which I expect are dead sodium.

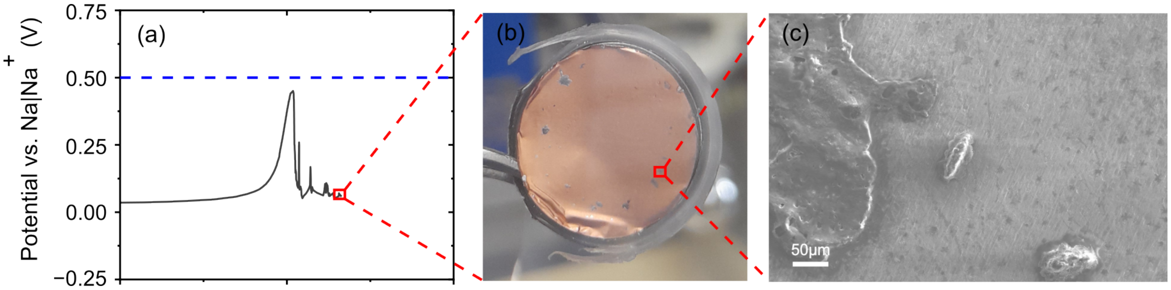

Figure 6.19: Figure showing (a) cell stopped on an oscillation, (b) opened and the electrode observed and (c) SEM analysis

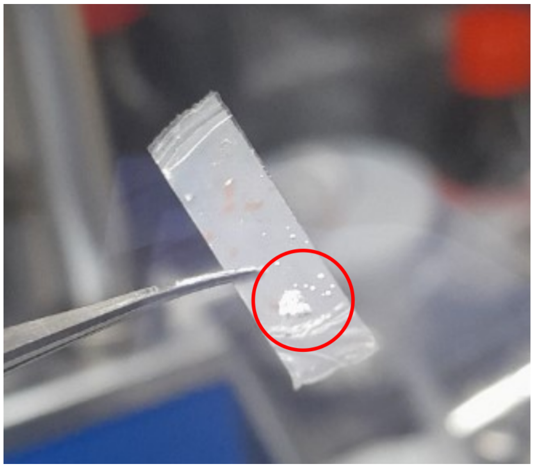

Figure 6.20: Image showing sodium deposits in the separator after sodium electrodeposition had occurred

A similar issue is observed for the Al_2O_3 coated samples which has a time and a voltage cutoff. Occasionally the electrode will reach the cutoff whilst sometimes it will not. This indicates that the plating and stripping process is still somewhat unstable and a varying amount of sodium is left on the electrode after each cycle making it very difficult to quantify the CE. However it is worth noting that the noisey response is not present for Al_2O_3 cells which may suggest the more uniform plating is preventing dendrite growth from occuring or at least mitigating it. This issue was recently reported by Zhang et al who suggest a process of calendar ageing after each cycle to recover this [8].

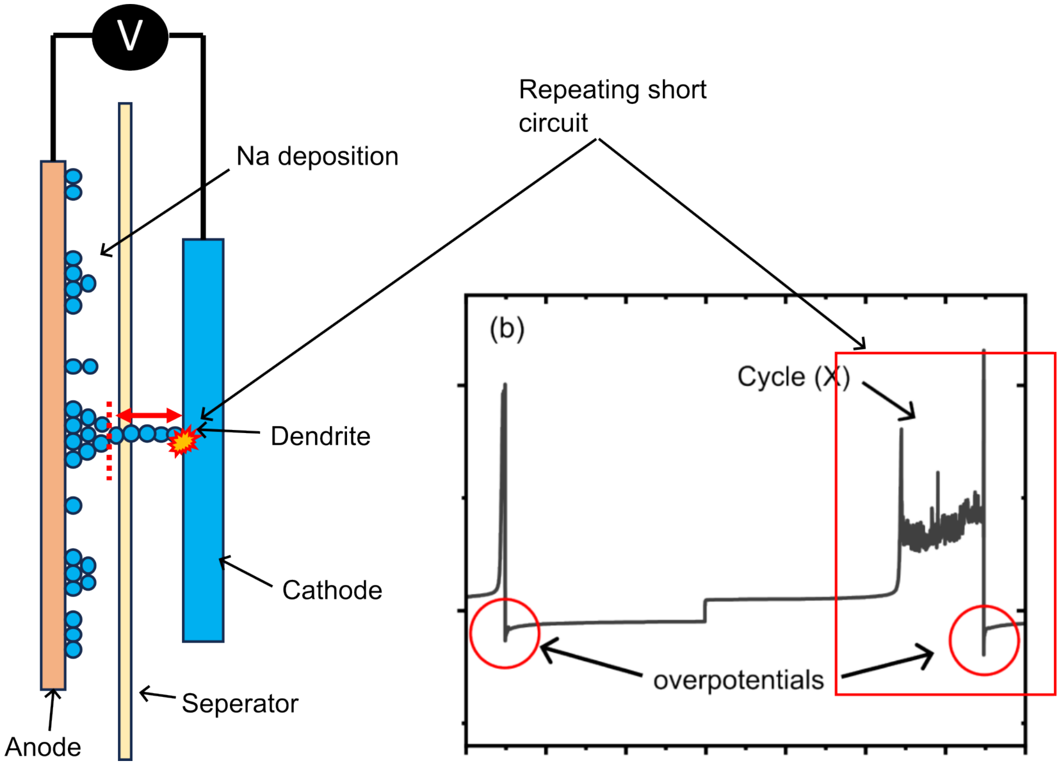

Figure 6.21: Schematic highlighting the idea for why the noisy response was observed on the stripping cycle of cell

Figure 6.21 highlights the schematic suggesting an explaination for the noisy response observed on the stripping of sodium from copper. When the dendrite touches the electrode, the potential drops. The current through the dendrite likely causes deformation of the dendrite leading to rapid attachment and detachment of sodium which causes this noisey response.

6.2 Conclusion and future work

The following chapter investigates the application of Al_2O_3 onto copper substrates for anode free sodium ion batteries. Although the concept has been attempted prior to this research for lithium anode free systems, sodium anode free systems have not been investigated. For this chapter different samples were studied including unocated copper, 15nm Al_2O_3 coated copper and 45nm Al_2O_3 coated copper. 15nm Al_2O_3 coated copper was selected due to being the most successful thickness in chapter 3. From performing GCD cycling and extracting data for hysteresis and CE, it was found that issues with regards to incomplete stripping of sodium from the electrode were especially prolifent for this data when compared to results in chapter 3, this made it very difficult to judge the cycle life of the cells from CE alone as after each cycle an inconsistent amount of sodium was left on the electrode so an accurate ratio for charge implemented for plating to charge implemented for stripping was not possible. Instead what was observed was an abrupt increase in the hysteresis of the cells during electrodeposition onto copper which from research suggests the formation of dendrites in the cell, the first instance whereby this occurs the cell was deemed finished. The uncoated cell exhibits a cycle life of 74 cycles before failure, the 15nm Al_2O_3 coated sample fails at 323 cycles and the 45nm Al_2O_3 sample fails after only 14 cycles.

As well as GCD analysis, cells were opened after individual plating cycles to observe the electrodeposition onto the electrodes. For uncoated cells it is evident the deposition is more patchy with sodium appearing to laterally spreading across the electrode as jagged chunks. For the 15nm Al_2O_3 coated electrode the sodium appears to cover the electrode more uniformly whilst being less patchy, under the microscope the deposition doesn't appear jagged like the uncoated electrode. The 45nm Al_2O_3 coated sample shows a good coverage of the electrode however the deposition is less uniform then the 15nm coated substrate with the appearance of raised sections of sodium. The deposition of sodium for the individual samples offers some explanation as to how cycling performs. The uncoated cell shows a relatively poor cycle life with the appearance of dendrites on the first cycle make the CE appear as 100% which suggests some sort of temporary short circuit is occurring. The 15nm Al_2O_3 doesn't appear dendritic from GCD which explains why the performance is better.

After conducting in-situ optical microscopy of GCD experiments, dendritic growth was observed on the uncoated cut edge of the copper. On the top surface coated with 15nm of Al_2O_3, the deposition appeared to diffuse across the surface smoothly, contrasting with the jagged patterns observed on the uncoated copper (as seen in the microscopy from figure 6.4). Additionally, a grey area appeared in front of the deposition atop the electrode, likely indicating ion diffusion through the Al_2O_3 film on the electrode surface. To delve deeper into this phenomenon, an XPS depth study experiment was conducted to pinpoint the location of the Al_2O_3 layer relative to the copper. This aimed to ascertain whether the layer was lifting off the electrode, as suggested in prior research. The results revealed that the Al2p peak appeared slightly before the Cu2p peak, indicating that the coating is closely bound to the copper. Furthermore, Na1s was detected throughout the entirety of the experiment, suggesting the presence of sodium within the film as well as on its surface, aligning with the observations from in-situ optical microscopy. If the Al_2O_3 film were located onto the sodium, an increase in the intensity of the Al2p peak followed by a decrease without any sign of the Cu2p peak would have been expected.

Experiments were also conducted to identify the issues regarding the noisy oscillation response present on the uncoated copper samples, during these noisy cycles the CE appears vastly over 100%. The cycling was stopped during one of these cycles and cells were opened to observe the working electrode. It was evident that during this noisy response small deposits of sodium appear on the electrode and in the separator which can only be suggested as dead sodium within the cell, it is not clear as to whether the deposits are penetrating the separator causing a short circuit which would suggest the sharp drop observed before reaching the 0.5V cutoff in this case which then rapidly oscillates, this may be dendrite breaking then coming back into contact with the electrode rapidly. If this was the case the CE could well go over 100% as charge ratios applied during GCD would no longer apply. Despite the CE being over the 100% there is still deposition on the working electrode signifying incomplete stripping of sodium anyhow.

To further strengthen this work in the future, a few aspects need to be addressed. Firstly although suggestions were made that the thickness of the 45nm Al_2O_3 coating was the reason for the elevated hysteresis and nucleation overpotential which ultimately led to poor cycling performance, no explanation was offered as to how this specifically caused cell failure. To identify this work would need to be performed looking specifically at how very thick coatings lead poor cycling performance, visually there appears to be coating on the electrode with 45nm Al_2O_3 which contradicts the lithium-ion chapter. Although the hysteresis is much higher for plating implicating that the kinetics of the reaction are sluggish, plating has still occurred on the electrode. It could be suggested that because the sodium ion has a much faster diffusivity in Al_2O_3 then lithium ion it may be able to diffuse through the coating and therefor plate onto the electrode allowing for some deposition to occur on copper for sodium metal but not lithium metal[2].

For the insitu optical microscopy, it would be interesting to see how the plating looks on the edge of the copper with the Al_2O_3 costing, this would allow us to identify visually whether the Al_2O_3 helps to mitigate dendrite growth in this case. To improve the XPS depth study, firstly continuing the etch for longer until the Na1s peak diminishes would allow certainty that the etch has passed through all of the layers present on the copper for sure. As well as this, to prevent the onset of differential charging it would be beneficial to stop the etch at regular intervals to allow for any charge to dissipate which would allow for better characterisation of the Na1s peak.

Recently after experimental work on this chapter had finished an article was published which suggested a solution to the issue regarding the CE increasing over 100% which suggests employing a calender ageing process on the discharge state of the cell to recover dead sodium within the cell. It would be interesting to see if this could be employed to the work in this chapter to combat this reoccurring issue and therefor potentially more efficiently compare cell performances [8].

Bibliography

[1] Chen-Jui Huang, Balamurugan Thirumalraj, Hsien-Chu Tao, Kassie Nigus Shitaw, Hogiartha Sutiono, Tesfaye Teka Hagos, Tamene Tadesse Beyene, Li-Ming Kuo, Chun-Chieh Wang, She-Huang Wu, et al. Decoupling the origins of irreversible coulombic efficiency in anode-free lithium metal batteries. *Nature Communications*, 12(1):1452, 2021.

[2] Sung Chul Jung, Hyung-Jin Kim, Jang Wook Choi, and Young-Kyu Han. Sodium ion diffusion in al2o3: A distinct perspective compared with lithium ion diffusion. *Nano letters*, 14(11):6559–6563, 2014.

[3] Zhi Wei Seh, Jie Sun, Yongming Sun, and Yi Cui. A highly reversible room-temperature sodium metal anode. *ACS central science*, 1(8):449–455, 2015.

[4] Ingemar Olefjord, HJ Mathieu, and P Marcus. Intercomparison of surface analysis of thin aluminium oxide films. *Surface and interface analysis*, 15(11):681–692, 1990.

[5] Mark C Biesinger. Advanced analysis of copper x-ray photoelectron spectra. *Surface and Interface Analysis*, 49(13):1325–1334, 2017.

[6] P-Y Brisson, H Darmstadt, M Fafard, A Adnot, G Servant, and G Soucy. X-ray photoelectron spectroscopy study of sodium reactions in carbon cathode blocks of aluminium oxide reduction cells. *Carbon*, 44(8):1438–1447, 2006.

[7] Ayaka Fujimoto, Yasuhiro Yamada, Michio Koinuma, and Satoshi Sato. Origins of sp3c peaks in c1s x-ray photoelectron spectra of carbon materials. *Analytical chemistry*, 88(12):6110–6114, 2016.

[8] Wenbo Zhang, Philaphon Sayavong, Xin Xiao, Solomon T Oyakhire, Sanzeeda Baig Shuchi, Rafael A Vilá, David T Boyle, Sang Cheol Kim, Mun Sek Kim, Sarah E Holmes, et al. Recovery of isolated lithium through discharged state calendar ageing. *Nature*, 626(7998):306–312, 2024.

Chapter 7

MVD platinum metal coatings

7.1 introduction

This chapter focuses on studying the growth of platinum by MVD and applying it to catalytic applications. The method for deposition involves the use of $MeCpPtMe_3$ along with an Ar/O_2 mixed plasma to combust the methyl ligands off the metal organic precursor. A TMA seed layer was used to improve the adhesion of the deposition to the substrate. Although this method for platinum deposition is common amongst plasma enhanced Atomic layer deposition (PeALD) systems a part of this study aims to see if the MVD and it's different method for precursor delivery can offer any advantage over its ALD predecessor which is due to the removal of the nitrogen carrier gas used during precursor injections as highlighted in section 2.1.5. The work from this chapter is a continuation of Klaudia rejnhards thesis who optimised the coating [1].

7.2 Characterisation of nanoparticles

Several methods were employed to characterise the nanoparticles grown by MVD including XPS, SEM and TEM. XPS was performed to determine the quality of the deposition whilst SEM and TEM were used to determine the particle size and distribution. Deposition was performed on several substrates including Si/SiO_2 wafer pieces, RGO TEM grids and monoliths. The initial study focused on assessing platinum deposition across a limited number of cycles. Deposits were applied to silicon wafer substrates, six samples with varying MVD cycle counts ranging from 5 to 35 were prepared. Figure 7.1 shows the SEM micrographs of these samples. Upon initial inspection, it is evident that at lower cycle counts, the deposition exhibits a particulate nature, particularly highlighted in figures 7.1 (a), (b), and (c) corresponding to 5, 15, and 20 cycles respectively. However, at 25 MVD cycles (figure 7.1 (d)), the deposition transitions from a particulate growth pattern to island-like formations. Images (e) and (f) show 30 and 35 MVD cycles and illustrate the progressive enlargement of these islands This is expected and has been proven in ALD studies [2, 3]. However, the study does not conclusively determine the threshold at which platinum forms a thin film. Further investigations involving more than 35 MVD cycles would be necessary to ascertain this critical transition point.

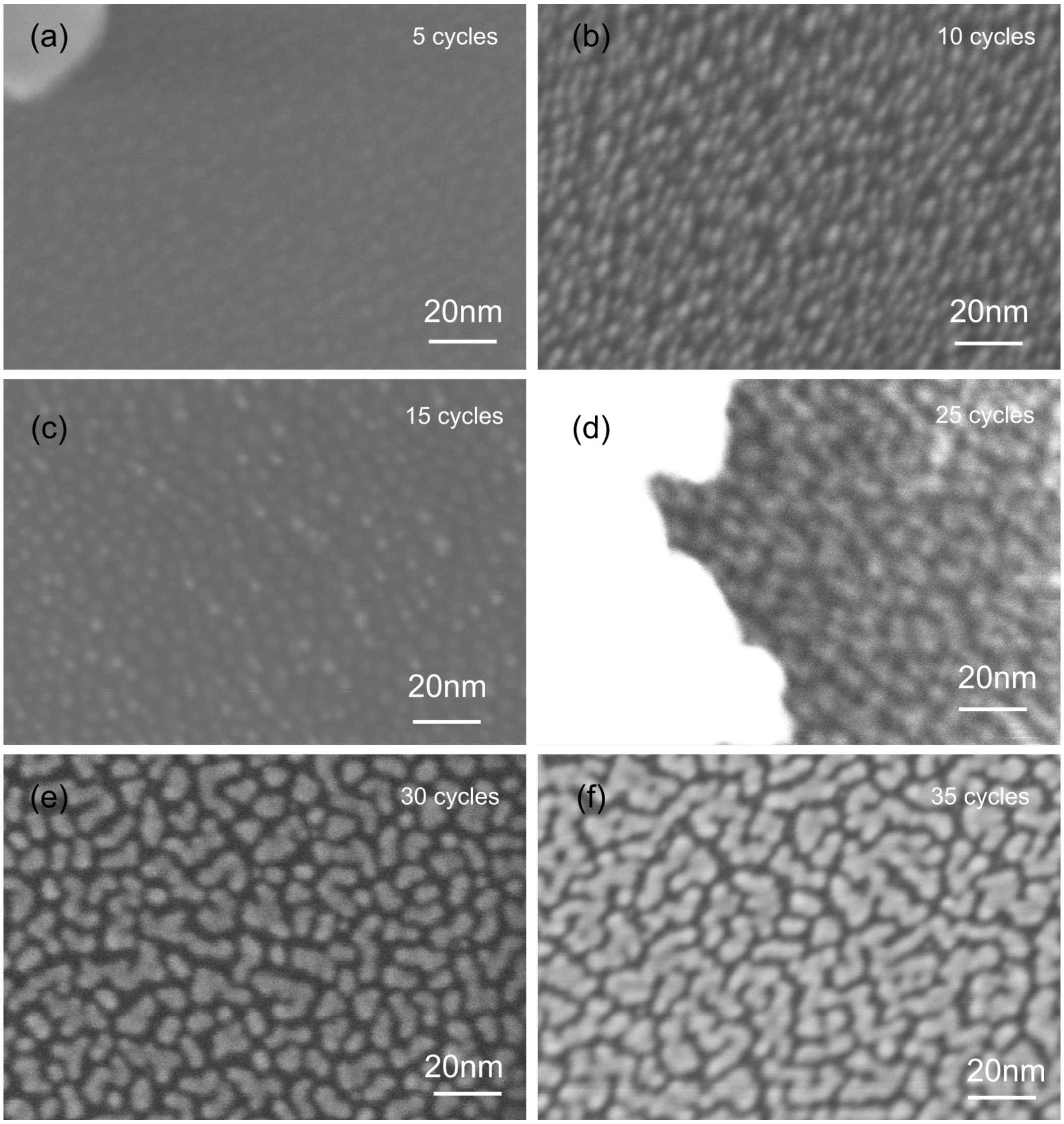

Figure 7.1: SEM images showing Platinum growth as a function of cycle number (a) 5 cycles, (b) 10 cycles, (c) 15 cycles, (d) 25 cycles, (e) 30 cycles and (f) 35 cycles respectively on Si/SiO_2 wafer pieces

7.2.1 TEM

In addition to SEM analysis, the nanoparticles underwent evaluation via TEM to achieve higher resolution imagery. Figure 7.2 presents the findings corresponding to 30 cycles ((a) and (b)) and 35 cycles ((c) and (d)) on reduced graphene oxide (RGO) TEM grids provided by Agar Scientific.

It's apparent that the nanoparticle growth on RGO substrates differs significantly from that on Si/SiO_2 substrates, despite undergoing identical treatment processes. The platinum metal deposits remain in the form of nanoparticles and have not yet transitioned into a percolated state like seen in the Si/SiO_2 coated samples analysed by SEM in figure 7.1 (e). These particles exhibit a notably dispersed distribution. Regrettably, due to time constraints, processing samples at lower numbers of deposition cycles was not performed. As well as imaging particles on RGO grids, particles were also observed on the surface of ceramic monoliths by TEM, this was achieved by crushing the monoliths and sprinkling them onto RGO TEM grids before incorporating them into the TEM column. Figure 7.3 shows the results of 35 MVD cycles deposited onto monoliths.

To explain why this difference in deposition is occurring one paper by richey et al highlights the effect sparse nucleation sites for precursor ligands and how this can lead to different deposition varying from growth of islands, nanoparticles or conformal thin films. Due to the difference in elemental composition between the Si/SiO_2 wafers compared to RGO TEM grids, the availability of surface nucleation sites may be different leading to the different observation in deposition [4]. Other effects can also take place which effect the growth as well including steric effects from the precursors ligands blocking active sites [5].

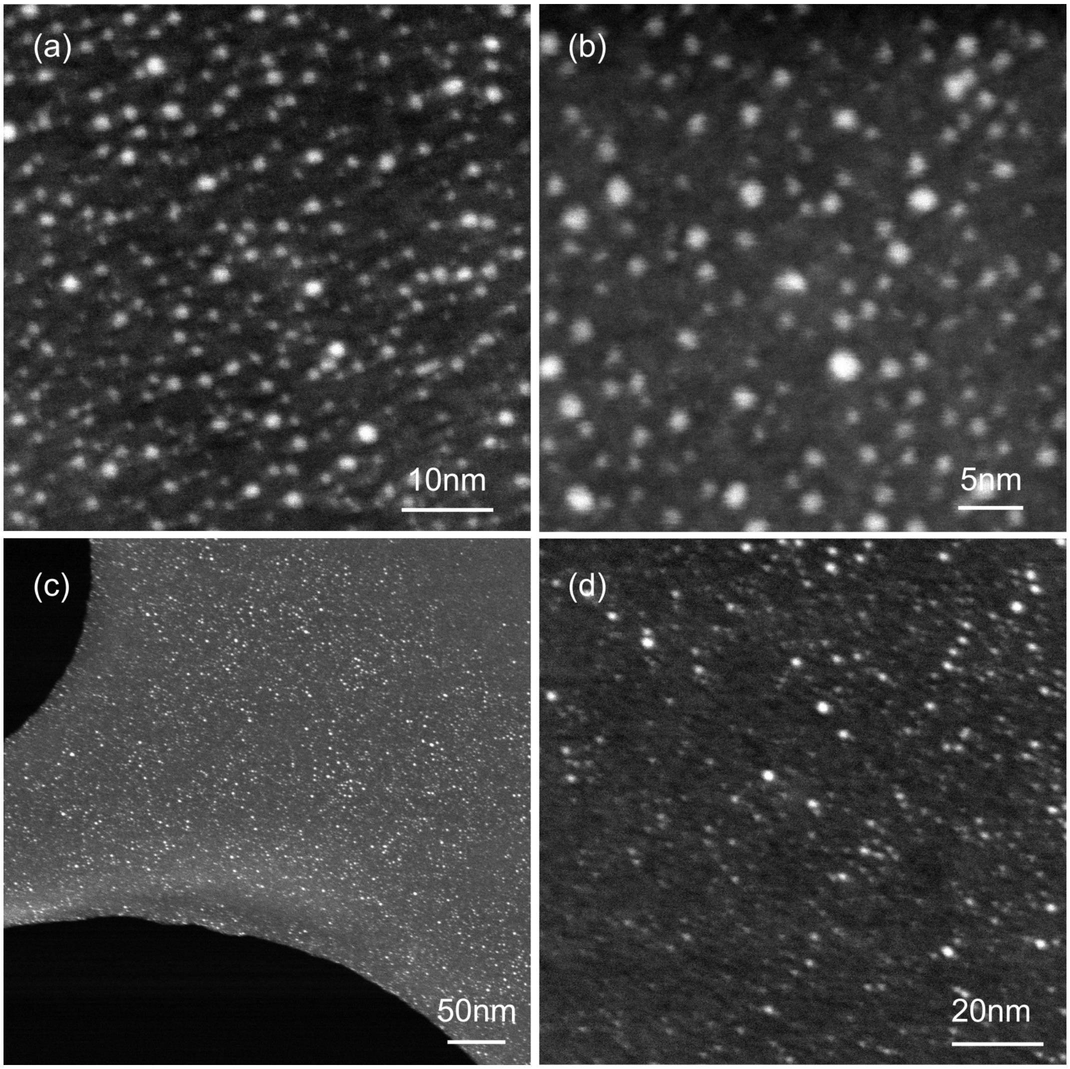

Figure 7.2: TEM images showing platinum nanoparticle deposition on RGO TEM grids. Images (a) and (b) show 30 cycles of deposition whilst images (c) and (d) show 35 cycles of deposition.

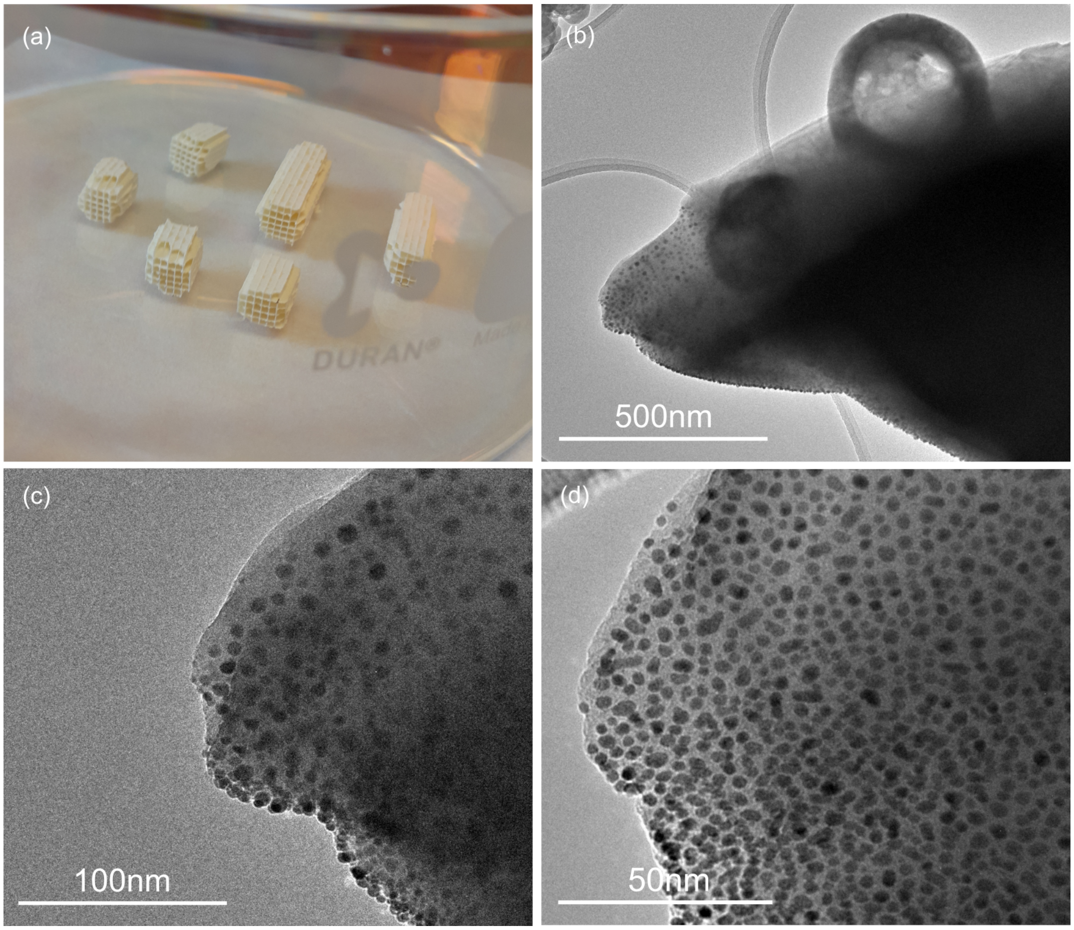

Figure 7.3: TEM and optical images showing platinum nanoparticle deposition to ceramic monoliths before being used for propene oxidation catalysis experiments. (a) images of the ceramic monoliths, (b), (c) and (d) TEM micrographs of the platinum nanoparticles deposited on the monoliths at different magnifications.

using an image thresholding technique in ImageJ software. This analysis was aimed at better understanding particle growth as a function of the number of molecular vapor deposition (MVD) cycles. For the 35-cycle run, it is evident that a significant number of particles have an area of $7nm^2$ or more, while for the 30-cycle run, the number of such particles is zero. This outcome aligns with expectations, as an increased number of MVD cycles generally leads to larger particles.

By examining the probability distribution, although more particles were counted for the 35-cycle run, the proportion of particles within the $0-1nm^2$ range is much lower then the 30-cycle run. In contrast, the proportion of particles within the $1-8nm^2$ range is higher across all bins for the 35-cycle run. This further supports the observation of a larger average particle size with 35 cycles of deposition. Additionally, the average particle area increased from $1.11nm^2$ for 30 cycles to 1.80 nm^2 for 35 cycles, representing a 62% increase in average particle area (equivalent to roughly a 12% increase per cycle).

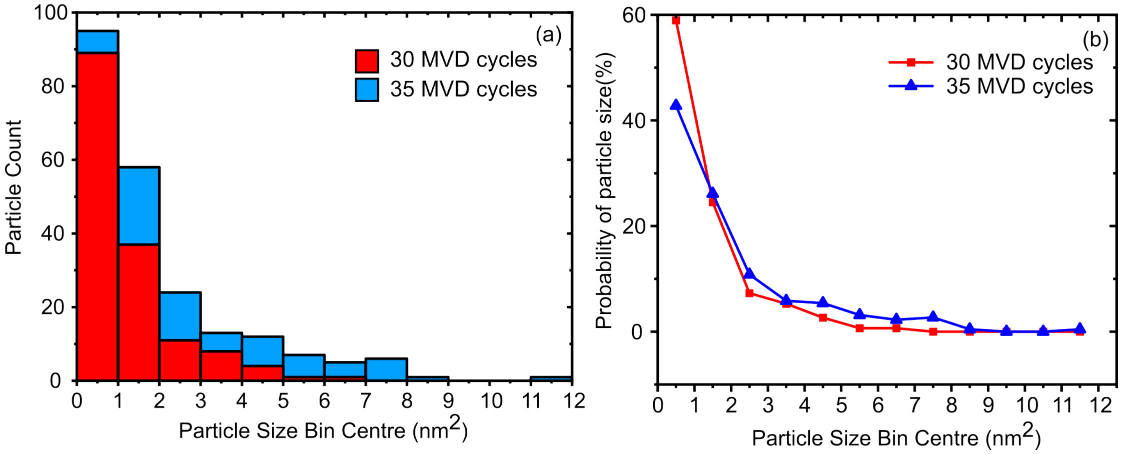

Figure 7.4: Graph showing PSD analysis of nanoparticles on RGO TEM grids (a) comparing 35 MVD cycles and 30 MVD cycles, (b) comparing probability distribution of particles

Figure 7.5 shows the particle size distribution (PSD) of nanoparticles on ceramic monoliths, derived from Figure 7.3. Despite undergoing the same number of deposition cycles, the average particle size is noticeably larger, with some particles exceeding $12nm^2$. This observation underscores how the choice of substrate can significantly influence nanoparticle growth, leading to variations in particle size. When comparing the average particle sizes to those reported in the literature, nanoparticles deposited on RGO TEM grids exhibit much smaller sizes than those achieved by other groups. In contrast, the particle sizes on the monolith material are more consistent with existing literature. The use of oxygen plasma in our deposition process allows for lower deposition temperatures compared to methods that employ oxygen and ozone gases.

More precursor material is deposited onto the substrate for each extra cycle which leads to the growth of larger particles. Initially, deposition occurs at active sites—typically surface hydroxyl groups—where nucleation begins. Rather than forming a continuous thin film, the growth follows a Volmer–Weber (island) growth mode, which occurs when the deposited material has a higher surface energy than the substrate. To minimize the overall surface energy, the material aggregates into discrete islands or particles. With each additional MVD cycle, these existing islands serve as preferential sites for further deposition promoting lateral and vertical particle growth and resulting in larger particle sizes[6],

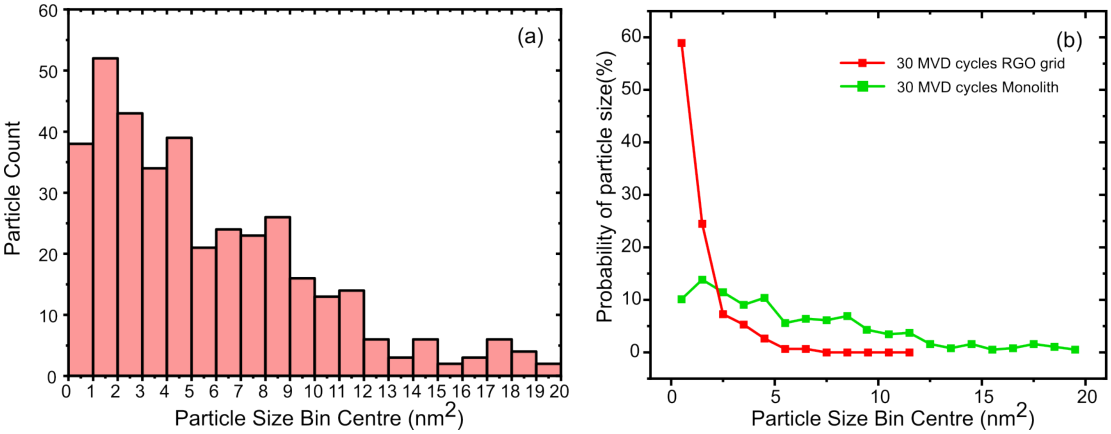

Figure 7.5: Graph showing PSD analysis of nanoparticles on ceramic monoliths. (a) highlights PSD, (b) highlights

Precursor gases	Number of ALD cycles	Temperature	Average particle size	Substrate	References
[(MeCp) PtMe3] and oxygen	5	320^oC	1.9nm	silica gel substrate	[7]
[(MeCp) PtMe3] and oxygen plasma	35	150^oC	0.8nm	RGO grids	This research
[(MeCp) PtMe3] and oxygen plasma	30	150^oC	0.6nm	RGO grids	This research
[(MeCp) PtMe3] and oxygen plasma	30	150^oC	1.6nm	Monolith material	This research
[(MeCp) PtMe3] and oxygen	30	250^oC	2.3nm	Bonded carbon layer	[8]
[(MeCp) PtMe3] and oxygen	10	325^oC	2.3nm	Silica gel	[9]
[(MeCp) PtMe3] and ozone	20	275^oC	1.9nm	3D porous Ni films	[10]

Table 7.1: Table showing how this research compares to platinum deposited by ALD for other studies

7.2.2 XPS

Figure 7.4 presents the XPS analysis of a 150°C run subjected to a 10-second plasma treatment. The spectra and samples were prepared by Klaudia Rejnhart and Greg Burwell. In Figure 4 (d), the prominent platinum 4f peak signifies the presence of platinum, exhibiting the characteristic 5/2 and 7/2 orbitals with peak energies measured at 71.24 eV for Pt4f7/2 and 74.66 eV for Pt4f5/2. This observation corroborates previous studies on platinum coatings conducted by PeALD [11]. Figure 7.4 (b) illustrates the carbon peak, with separate components at 284.8 eV (C-C) and 286 eV (C-O). While it could be suggested that these arise from trapped carbon species within the metal, they are typically associated with adventitious carbon. It was therefor inferred that the contribution from trapped carbon was negligible [12]. Figure 7.4 (c) shows the oxygen peak, with the peak at 532 eV aligning with the Pt-O bond, which is expected to be present on the surface of the platinum [13].

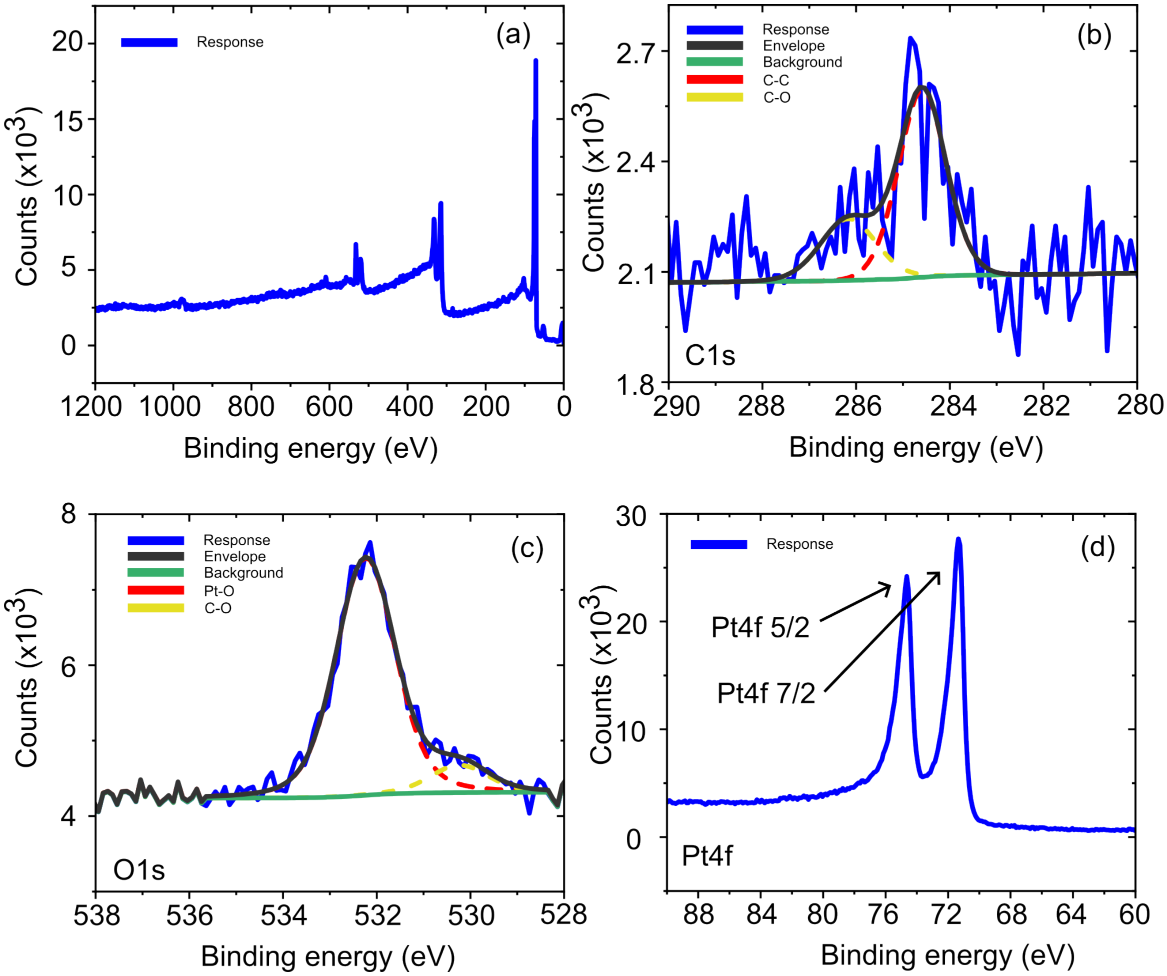

Figure 7.6: Graphs highlighting the results of the XPS of platinum nanoparticles (a) widescans, (b) C1s, (c) O1s and (d) Pt4f

7.3 Propene to CO_2 conversion

Working with Cardiff Catalysis Institute the monolith supported MVD platinum nanoparticles were tested for the total oxidation of propene to CO_2. 30 cycles of platinum were deposited onto monoliths. The TEM images present in figure 7.3 are of the monolith after treatment with MVD platinum. The Monoliths were crushed and the pieces were sprinkled onto a TEM grid (as images of complete samples are not possible in a TEM).

Figure 7.5 shows the results of the propene oxidation experiment. After deposition, the monoliths were packed into a furnace with a gas supply setup where the flow rate could be controlled. The gas supplied was propene in air at 200ppm at a flow rate of 1.7 l/minute. The reaction profile is shown in figure 7.5 Run 1. Whilst no oxidation took place without a platinum catalyst the Pt catalyst allowed for oxidation to begin at as low as 175^oC this increases to around a 89.4% conversion at 350^oC. The runs were repeated a further 2 times, it was found that after each collective run the Propene to CO_2 conversion increased to 92.4% on run 2 and then 93.8% on run 3 at 350^oC.

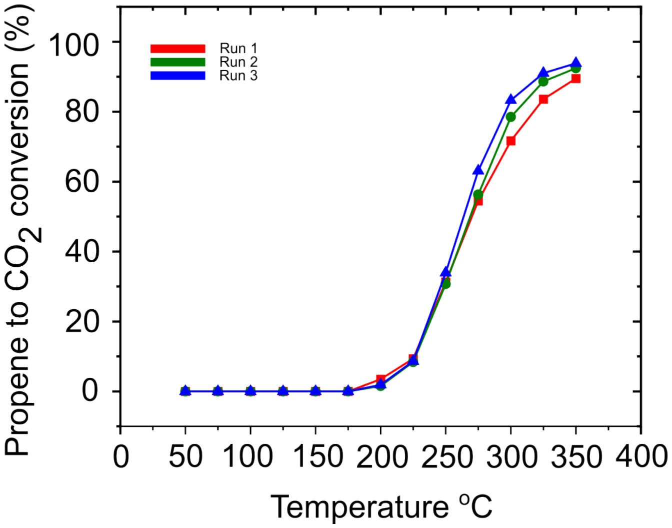

Figure 7.7: Graph highlighting the conversion of propene to CO_2. Sample were repeatedly tested highlighting the 3 consecutive runs.

Another piece of monolith was testing in a similar way but was first heat treated at 500^oC under a flow of

5% H_2/Ar for 4 hours which is expected to reduce the the Pt to Pt(0) and was run 3 times. Figure 7.4 shows the results of the experiment. Unlike the untreated run, the response of the 3 runs respectively are very similar. The conversion reaction for the treated monoliths starts at 125^oC which is roughly a temperature of 50^oC lower then the untreated monoliths. interestingly at 350^oC the conversion reaction peaks at around 85% which is roughly 9% lower then the untreated monoliths. However despite this the conversion at lower temperature is better, for example at 225^oC the untreated samples have a conversion of less then 10% whilst the treated samples are around 60%. Results are very similar for the 3 runs

For the untreated monoliths it is evident that the temperature of the experimental setup during the experiment is annealing the particles and increasing their effectiveness at reducing Propene to CO_2. for each subsequent run this is becoming more significant. The high temperature the nanoparticles are being subject to is likely changing them and increasing their activity. For the runs performed after temperature treatment, the particles have been fully reduced which is why the catalytic activity does not increase anymore as the subsequent addition of runs are performed. The nanoparticles being reduced would imply the XPS analysis suggesting the presence of Pt-O at 532eV (figure 7.4(c)) is correct.

To provide a comparison to literature, Li et al performed similar propene oxidation experiments using Pt nanoparticles suspended on Al_2O_3 with a average size of 3.4nm. These particles were created by solution impregnation using an double solvent approach into an Al-based MOF. The nanoparticles in the gamma Al_2O_3 support showed values for T-50 at 250^oC and T-90 at 264^oC. The results from the treated monolith show a T-50 at 225^oC which indicates a better conversion at lower temperatures compared to this literature article (These were chosen as they yield the least variation between runs) [14].

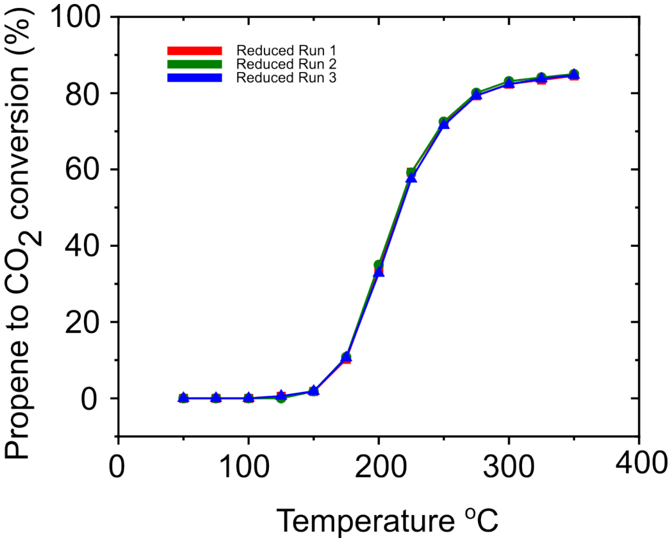

Figure 7.8: Graph showing the Propene to CO_2 oxidation of platinum nanoparticles after being reduced in a furnace at 500^oC

7.4 Conclusion and future work

To conclude, this chapter highlights the application of platinum nanoparticles deposited by MVD as a catalyst for propene oxidation for the first time. The results from the SEM and TEM characterisation highlight that the particles are well dispersed and size tuneable depending on the number of MVD cycles. Ceramic monoliths showed a 89.4% conversion of propene to CO_2 at 350^oC. Better still, when annealed at 500^oC the nanoparticles showed a conversion of around 60% at 225^oC compared to the untreated monoliths which had a conversion of 10% at these temperatures.

Unfortunately, due to time constraints and tool availability this particular chapter was not explored in as much detail as hoped, therefor it is important to highlight the future work that was planned and experiments that would be needed to strengthen results. Firstly only one MVD deposition was applied to monoliths (30 cycles). Giving a very narrow set of data to explore. To optimise performance, the various numbers of MVD cycle employed in the initial SEM study on Si/SiO^2 substrates would need to be employed onto the monoliths and separately tested. This would allow for an optimal number of cycles required to get the highest proportion of propene to CO_2 at the lowest temperature possible potentially saving money and time.

Although the results from this test were very promising, the data doesn't suit the title of this thesis well. The long term plan as highlighted in the literature review section 2.7.2 - 2.7.4 includes the application of MVD nanoparticles to carbon based electrodes for PEM electrolysis and hydrogen fuel cell applications. Work was planned with Cardiff university and professors Andrea Folli who suggested applying the nanoparticles to ITO glass initially and later down the line materials that align with real work electrolyser electrodes.

Bibliography

[1] Klaudia rejnhard. *Advanced Functional Coatings for Integrative Semiconductor Materials and Devices*. PhD thesis, Swansea university, 2022.

[2] Adriaan JM Mackus, Noémi Leick, Layton Baker, and Wilhelmus MM Kessels. Catalytic combustion and dehydrogenation reactions during atomic layer deposition of platinum. *Chemistry of Materials*, 24(10):1752–1761, 2012.

[3] Steven T Christensen, Jeffrey W Elam, Byeongdu Lee, Zhenxing Feng, Michael J Bedzyk, and Mark C Hersam. Nanoscale structure and morphology of atomic layer deposition platinum on srtio3 (001). *Chemistry of Materials*, 21(3):516–521, 2009.

[4] Nathaniel E Richey, Camila De Paula, and Stacey F Bent. Understanding chemical and physical mechanisms in atomic layer deposition. *The Journal of chemical physics*, 152(4), 2020.

[5] Riikka L Puurunen, Wilfried Vandervorst, Wim FA Besling, Olivier Richard, Hugo Bender, Thierry Conard, Chao Zhao, Annelies Delabie, Matty Caymax, Stefan De Gendt, et al. Island growth in the atomic layer deposition of zirconium oxide and aluminum oxide on hydrogen-terminated silicon: Growth mode modeling and transmission electron microscopy. *Journal of applied physics*, 96(9):4878–4889, 2004.

[6] Kim-Hue T Dinh, Huong T Thuy Ta, Ngoc Linh Nguyen, Viet Thong Le, Viet Huong Nguyen, and Hao Van Bui. Dimension control of platinum nanostructures by atomic layer deposition: From surface chemical reactions to applications. *Chemistry of Materials*, 35(6):2248–2280, 2023.

[7] Xinhua Liang, Yun Zhou, Jianhua Li, and Alan W Weimer. Reaction mechanism studies for platinum nanoparticle growth by atomic layer deposition. *Journal of Nanoparticle Research*, 13:3781–3788, 2011.

[8] Zhongxin Song, Mohammad Norouzi Banis, Hanshuo Liu, Lei Zhang, Yang Zhao, Junjie Li, Kieran Doyle-Davis, Ruying Li, Shanna Knights, Siyu Ye, et al. Ultralow loading and high-performing pt catalyst for a polymer electrolyte membrane fuel cell anode achieved by atomic layer deposition. *ACS Catalysis*, 9(6):5365–5374, 2019.

[9] Jianhua Li, Xinhua Liang, David M King, Ying-Bing Jiang, and Alan W Weimer. Highly dispersed pt nanoparticle catalyst prepared by atomic layer deposition. *Applied Catalysis B: Environmental*, 97(1-2):220–226, 2010.

[10] He Chen, Jin-Tao Chen, Lin Shao, Lei Wang, Xian-Zhu Fu, and Jing-Li Luo. Minimum and well-dispersed platinum nanoparticles on 3d porous nickel for highly efficient electrocatalytic hydrogen evolution reaction enabled by atomic layer deposition. *Applied Surface Science*, 494:1091–1099, 2019.

[11] Mao-Lin Shi, Jing Xu, Ya-Wei Dai, Qian Cao, Lin Chen, Qing-Qing Sun, Peng Zhou, Shi-Jin Ding, and David Wei Zhang. Plasma enhanced atomic layer deposited platinum thin film on si substrate with tma pretreatment. *Vacuum*, 140:139–143, 2017.

[12] De Fang, Feng He, Junlin Xie, and Lihui Xue. Calibration of binding energy positions with c1s for xps results. *Journal of Wuhan University of Technology-Mater. Sci. Ed.*, 35:711–718, 2020.

[13] JLG Fierro, JM Palacios, and F Tomas. An analytical sem and xps study of platinum–rhodium gauzes used in high pressure ammonia burners. *Surface and interface analysis*, 13(1):25–32, 1988.

[14] Chuanqiang Li, Siyuan Liu, Fengkai Yang, Yangyang Zhang, Zhengyuan Gao, Xiaoya Yuan, and Xuxu Zheng. Synthesis of γ-al2o3–supported pt nanoparticles using al-based metal-organic framework as medium and their catalytic performance for total propene oxidation and selective nitrobenzene hydrogenation. *Materials Chemistry and Physics*, 240:122146, 2020.

Chapter 8

Summary

8.1 Summary of research

Research conducted in this work applied the KLA MVD 300 technologies to two prominent industries including batteries and catalysis. For batteries, Al_2O_3 and ZnO were implemented onto copper and carbon fibre electrodes respectively and were made into anode free cells which is a promising technology offering a higher volumetric energy density and fast charging capabilities. Lithium was investigated as the batteries active material initially due to its prolifent use in battery technology. Sodium was also investigated as a low cost alternative. For catalysis, Pt metal was deposited onto monolith material, their efficacy was determined by there ability to reduce propene gas into CO_2, these tests were only preliminary and more suitable applications which included depositing the nanoparticles on electrodes for hydrogen fuel cell technology were planned but never accomplished.

MVD deposition differs from conventional ALD as it does not require a nitrogen carrier gas for precursor delivery. This allows for high quality films to be deposited at low temperatures with an impressive aspect ratio of 3500:1 which is higher then other tools analysed (table 2.1). As well as this, the MVD has a large open chamber allowing for batch production capability which opens up potential industrial scalability. This thesis aims to utilise the MVDs bespoke deposition method to see if it offers any advantages over ALD in the fields highlighted above.

Chapter 4 highlights the application of Al_2O_3 onto copper current collectors for lithium anode free half cells. Anode free batteries offer distinct advantages over conventional batteries including a higher volumetric energy density and lower manufacturing cost (section 2.2.4). Unfortunately, the technology comes with detrimental issues which primarily include dendritic growth of lithium on the charge cycle. This leads to unstable SEI formation and short circuiting on some occasions. Whilst a conformal Al_2O_3 coating has been shown by many research groups to stabalise the electrodeposition of lithium leading to cells with a longer cycle life, a viable explanation as to why this occurs is not clear, with many research groups offering different ideas (section 2.4). This chapter aimed to explore these ideas as well as to identify an optimal thickness. The results of the study showed the best cycle life at 15nm Al_2O_3. To explain the reason for this, electrodepositon was performed onto electrodes which were then opened. It was evident that increasing the thickness of the Al_2O_3 promoted more sparse nucleation of lithium. These results were similar to a recently published study by Oyakhire et al. Despite the promising results, half cells we made did not outperform cells in the study despite the similar cell setup used so it cannot be said that MVD has offered any advantages for this particular application [1].

Chapter 5 highlights the application of ZnO onto 3D carbon fibre current collectors. The advantages of this particular type of cell is the very high surface area of the electrode reduces the localised current density. This allows for much higher discharge/charge rates which offers the ability for fast charging, this is important for modern day electric vehicles. The application of ZnO allows for more efficient lithiation of these electrodes and due to the electrodes porous structure, MVD coatings are very suitable for this application. Results from the experiments showed that despite the improved lithiation the ZnO offered, the first cycle efficiency loses were very large due to the higher surface area which, when incorprated into a full cell, would render the cells useless after the first few cycles. Although pre saturation of electrodes can be performed prior to cell assembly using molten lithium infusion, this adds a process step to the manufacture of cells. It also creates a structure similar to a solid metal electrode which negates the advantages of the original cell design.

Chapter 6 highlights the application of Al_2O_3 onto copper current collectors for sodium anode free half cells. Whilst the cell design offers the same advantages as the lithium anode free cells, sodium is low cost alternative to lithium. The application of Al_2O_3 for this cell design was novel and therefore was explored to see if the advantages seen in lithium systems could also be observed for sodium. Three cells were tested including uncoated, 15nm and 45nm Al_2O_3. Half cells showed inconsistent plating and stripping throughout the experiments which made it difficult to quantify the point of cell failure. However, from the hysteresis and cycle life,it was concluded that the 15nm Al_2O_3 cells offered a better cyclability then the uncoated and 45nm Al_2O_3 cells. In-situ optical microscopy and XPS characterisation suggested that the Al_2O_3 facilitated the diffusion of sodium through the coating allowing for more uniform radial growth of nuclei, spreading the sodium across the electrode more uniformly. The uncoated copper showed a more jagged deposition which did not cover the electrode well. This was likely due to the lack of Al_2O_3. Within the chapter the inconsistent plating and stripping was investigated. It was found that completely stripping the electrode after plating could not be performed consistently. Despite this being a prolifent problem for this cell type, it has been recently acknowledged by research groups who offer solutions [2]. It was found that the presence of noise on the stripping was exclusive to uncoated cells and suggestions were made that it was due to soft short circuiting caused by sodium dendrites. The same effect was not observed for Al_2O_3 coated samples.

Chapter 7 highlights the application of platinum metal deposition by MVD and applies it to catalysis scenarios. The MVDs reaction mechanism works by the pulsing and purging of precursor gases allowing for nanoparticle deposition with a very high level of size control on a variety of different substrates. The work intended to apply nanoparticles to electrodes for hydrogen fuel cell technology. However, due to time constraints, only preliminary characterisation and testing was performed. Nanoparticles were applied to ceramic monoliths for propene oxidation experiments. The nanoparticles deposited by MVD showed a better conversion of propene to CO2 at low temperature then particles that were made by solution impregnation. This showed that MVD nanoparticles could compete with those produced by more traditional methods. Future work in this field would lean towards application of nanoparticles to ITO glass. This would provide more relevant tests which would then lead to deposition onto carbon to be applied to materials that aligned more closely with real world electrolysers.

8.2 industrial scalability

As well as research into the coatings, a small section in the introduction (section 1.3) was provided, highlighting the potential to meet the throughput requirements for a lithium sulphur battery company called OXIS energy. It was suggested that with the correct cassette and handling tools, one MVD tool with the optimised coating could be enough to coat twice the required output of anodes which proves that despite the very slow coating process, it would still be industrially relevant for battery technology.

Bibliography

[1] Solomon T Oyakhire, Wenbo Zhang, Andrew Shin, Rong Xu, David T Boyle, Zhiao Yu, Yusheng Ye, Yufei Yang, James A Raiford, William Huang, et al. Electrical resistance of the current collector controls lithium morphology. *Nature communications*, 13(1):3986, 2022.

[2] Wenbo Zhang, Philaphon Sayavong, Xin Xiao, Solomon T Oyakhire, Sanzeeda Baig Shuchi, Rafael A Vilá, David T Boyle, Sang Cheol Kim, Mun Sek Kim, Sarah E Holmes, et al. Recovery of isolated lithium through discharged state calendar ageing. *Nature*, 626(7998):306–312, 2024.

Chapter 9

Appendix

9.1 Table showing target markets for ALD tools (table 2.1)

A	High-K dielectrics, Hydrophobic coatings, Passivation layers, High aspect ratio diffusion barriers for Cu interconnects, Conformal coatings for microfluidic applications, Fuel cells (e.g single metal coatings for catalyst layers)
B	Dielectric layers, Diffussion barriers
C	Surface energy control layers (Antistiction, hydrophillic), Barrier coatings (corrosion, mosisture barrier), Adhrsion coatings, Dielectric layers and optical coatings (antireflection). Fields include MEMs and packaging.
D	Flexible electronics, batteries and solar
E	Clean energy, Energy storage, sensors, Microelectronics, nanotechnology, optoelectronics and catalysts.
F	R & D, Electronics, MEMs, Energy storage, Solar encapsulation, Nanophotonics, Biomedical and more.
G	Highly accurate film deposition on flat and 3D substrates alike.
H	R & D and industry.
I	Batch processisng in MEMs and 3 dimensional component production.
J	High-k dielectrics, Nanocoatings, Surface modification layers, Corrosion protection layers, Moisture barrier layers, Device encapsulation, MEMs and photonic crystals.

Table 9.1: Table showing application of ALD systems highlighted in table 2.1

9.2 2.5nm Al_2O_3 repeat Li- Cu

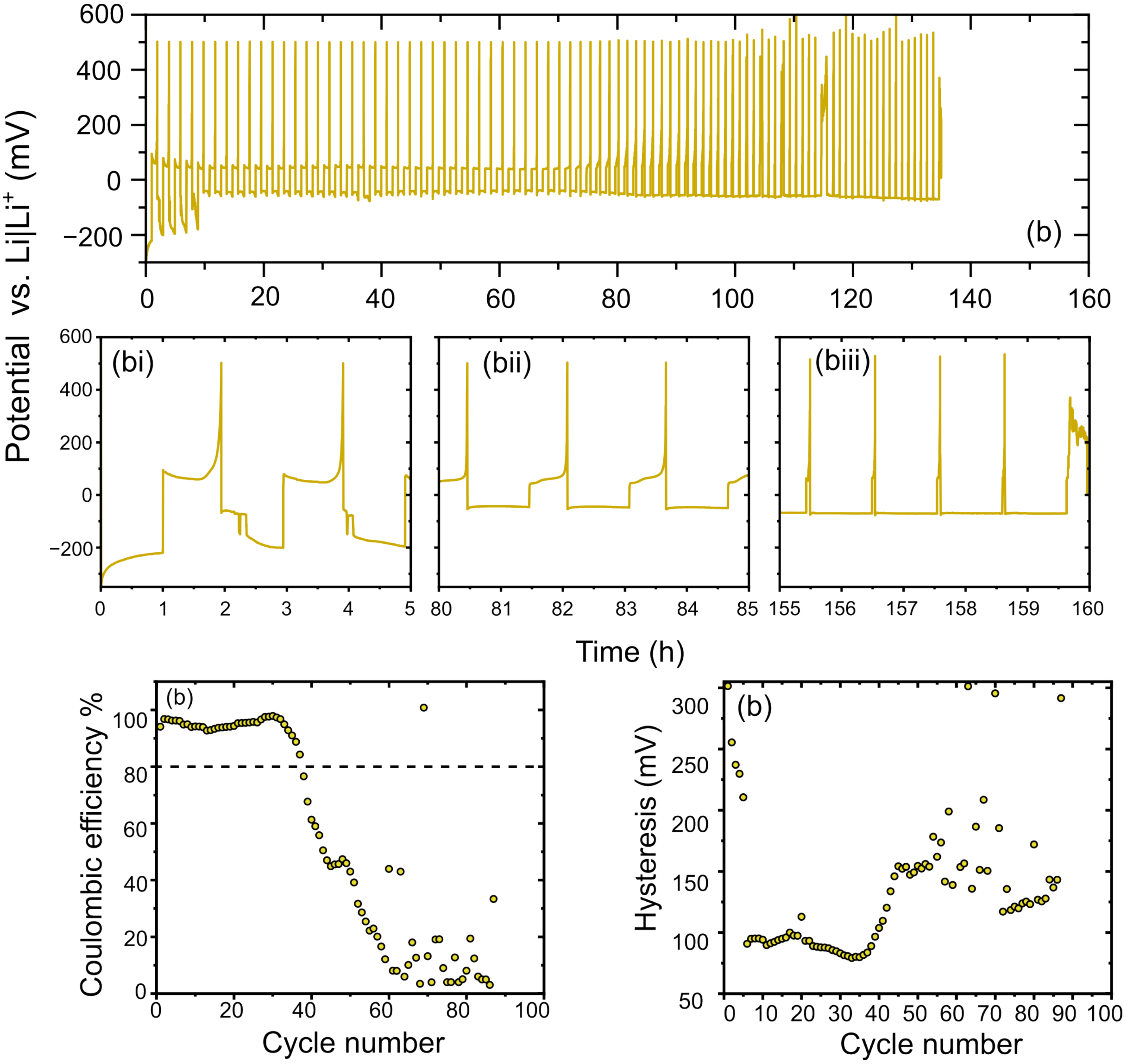

Figure 9.1: repeat results - (a) Graphs highlighting the GCD results of sodium electrodeposition onto copper coated with 2.5nm Al_2O_3, (b) hysteresis and (c) CE

9.3 45nm Al_2O_3 coated half cell charge discharge

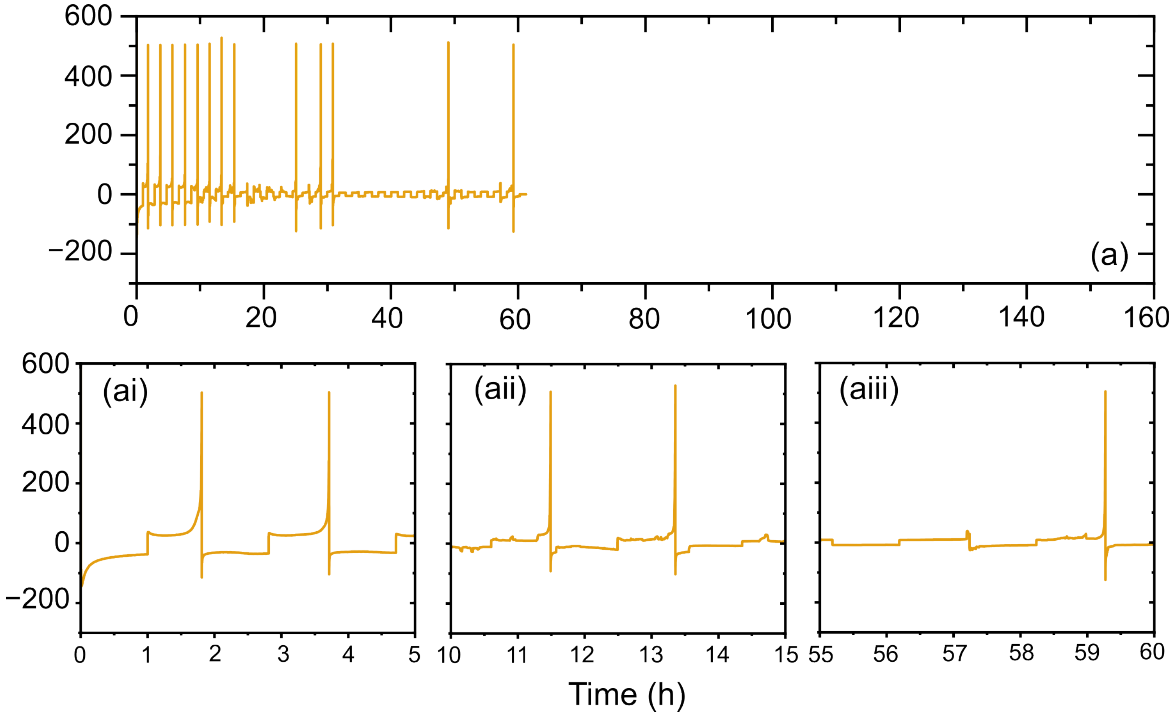

Figure 9.2: figure highlighting the 45nm Al_2O_3 cycled by GCD vs lithium counter electrode

9.4 sodium electrodeposition onto copper around edges

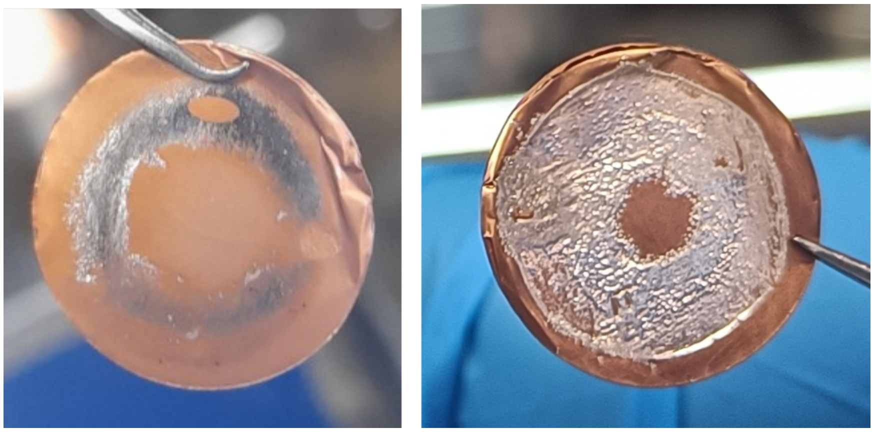

Figure 9.3: Images highlighting the electrodepsoition of active mass around the edge of copper substrates

9.5 Python code - for obtaining values for CE and hysteresis

Listing 9.1: Python example

```
import pandas as pd
import numpy as np

data = pd.read_excel('C:Data■file.xlsx')
data=data.to_numpy()

timenew=data[:,0]
volts=data[:,1]
current=data[:,2]

#Part 1: Finding potential difference and hysteresis

#Gets the indices of the start of each cycle
i = np.where(current == 0)
current[i] = −0.001
cross = np.where(np.diff(np.sign(voltsnew)))[0]

#Separates charge and discharge cycles
negvol=[]
posvol=[]
negvol.append(volts[0:cross[0]])
#(first cycle is negative)

for i in range(0,len(cross)):
    if i > len(cross)−2:
        break
    if (i % 2) == 0:
        posvol.append(volts[cross[i]+1:cross[i+1]+1])
```

```
    else:
        negvol.append(volts[cross[i]+1:crosss[i+1]+1])

#Finds the average voltage of the cycle plateaux
avvolneg=[]
avvolpos=[]

for i in range(0,len(negvol)):
    samplei=negvol[i]
    constnegvol=[]
    for j in range(100,len(samplei)):
        if j+1 > len(samplei)-1:
            break
        if abs(samplei[j] - samplei[j+1]) < 0.1:
            constnegvol.append(samplei[j])
    avneg=statistics.mean(constnegvol)
    avvolneg.append(avneg)

for i in range(0,len(posvol)):
    samplei=posvol[i]
    constposvol=[]
    for j in range(0,len(samplei)-(int(0.2)*len(samplei))):
        if j+1 >len(samplei)-1:
            break
        if abs(samplei[j] - samplei[j+1]) < 0.1:
            constposvol.append(samplei[j])
    avpos=statistics.mean(constposvol)
    avvolpos.append(avpos)

avvolneg=np.array(avvolneg)
avvolpos=np.array(avvolpos)
```

```
#Finds potential difference and hysteresis
pd = avvolpos - avvolneg
hysteresis = avvolpos + avvolneg

#Part 2: Finding coulombic efficiency

#Separating currents of charge and discharge cycles
negcur=[]
poscur=[]
negcur.append(current[0:cross[0]])
#(first cycle is negative)

for i in range(0,len(cross)):
    if i > len(cross)-2:
        break
    if (i % 2) == 0:
        poscur.append(current[cross[i]+1:cross[i+1]+1])
    else:
       negcur.append(current[cross[i]+1:cross[i+1]+1])

#Separating times of charge and discharge cycles
negtime=[]
postime=[]
negtime.append(timenew[0:cross[0]])

for i in range(0,len(cross)):
    if i > len(cross)-2:
        break
    if (i % 2) == 0:
        postime.append(timenew[cross[i]+1:cross[i+1]+1])
```

```
    else:
        negtime.append(timenew[cross[i]+1:cross[i+1]+1])

#Finding charge of cycle (integrate current wrt time)
negcharges=[]
poscharges=[]

for i in range(0,len(negcur)):
    negcuri=negcur[i]
    negtimei=negtime[i]
    for j in range(0,len(negtimei)-1):
        if negtimei[j+1] == negtimei[j]:
            negtimei[j]=negtimei[j]-(0.00001*(j+1))
    negcharges.append(integrate.simpson(negcuri, negtimei))

for i in range(0,len(poscur)):
    poscuri=poscur[i]
    postimei=postime[i]
    for j in range(0,len(postimei)-1):
        if postimei[j+1] == postimei[j]:
             postimei[j]=postimei[j]-(0.00001*(j+1))
   poscharges.append(integrate.simpson(poscuri, postimei))

poscharges = np.array(poscharges)
negcharges = np.array(negcharges)

coulombic_efficiency = (poscharges / -negcharges) * 100
```

9.6 List of Conferences

- M2a annual conference - April 2020 poster
- M2a annual conference - April 2021 poster
- M2a annual conference - April 2022 poster
- M2a annual conference - April 2023 presentation (runner up)
- Bath electrochemistry conference - June 2023 presentation (first place prize)
- BIOMATSEN Turkey - April 2024 presentation
- Solid State Battery Summit Chicago - August 2024 poster